ABSTRACT

Title of dissertation: LOW-DIMENSIONAL MODELS FOR FLUID FLOW

Virginia L Kalb, Doctor of Philosophy, 2004

Dissertation directed by: Associate Research Professor Anil Deane
Institute of Physical Science and Technology

Despite the temporal and spatial complexity of fluid flow, model dimensionality can often be greatly reduced while both capturing and illuminating the nonlinear dynamics of the flow. This dissertation follows the methodology of direct numerical simulation (DNS) followed by Proper Orthogonal Decomposition of temporally sampled DNS data to derive temporal and spatial eigenfunctions. The DNS calculations use Chorin's projection scheme; 2-d validation and results are presented for driven cavity and square cylinder wake flows. The flow velocity is expressed as a linear combination of the spatial eigenfunctions with time-dependent coefficients. Galerkin projection of these modes onto the Navier-Stokes equations obtains a dynamical system with quadratic nonlinearity and explicit Reynolds number (Re) dependence. Truncated to retain only the most energetic modes produces a low-dimensional model for the flow at the decomposition Re. This dissertation demonstrates that these low-dimensional models reproduce the flow dynamics, but

with small errors in amplitude, phase, and particularly long term dynamics. A new stabilization algorithm is presented that projects the error onto the derived temporal eigenfunctions, then modifies the dynamical system coefficients to significantly reduce these errors. Its effectiveness is demonstrated with low-dimensional dynamical systems for driven cavity flow in the periodic regime, quasi-periodic flow at Re 10000, and the wake flow. This dissertation also addresses the task of obtaining more useful models that are valid over a range of Reynolds numbers. Straightforward Re-based parameter continuation applied to extrapolate the model proves inadequate for successful flow prediction. A new concept of parameterizing the dynamical system coefficients is introduced that utilizes the kinetic energy transfer between modes as a function of Re to predict the flow dynamics correctly. Results for the driven cavity flow include a minimal four-mode dynamical system that captures the flow dynamics for Re up to 10000. A four-mode dynamical system for the square cylinder wake flow demonstrates accurate amplitude predictions for Re up to 100. The most robust low-dimensional models are obtained by further including a model for the frequency variation with Re. Low-dimensional models that incorporate spatial mode changes with Re are developed and quantitatively assessed for both test flows.

LOW-DIMENSIONAL MODELS FOR FLUID FLOW

by

Virginia L Kalb

Dissertation submitted to the Faculty of the Graduate School of the
University of Maryland, College Park in partial fulfillment
of the requirements for the degree of
Doctor of Philosophy
2004

Advisory Commmittee:

Associate Research Professor Anil Deane, Chair/Advisor
Associate Professor James Baeder
Professor David Levermore
Professor Dianne O'Leary
Assistant Professor Benjamin Shapiro

Acknowledgements

The direction of this dissertation has been influenced by several key people. Dr. John Maddocks, now at the Swiss Federal Institute of Technology, first introduced me to the fascinating area of bifurcation phenomena and parameter continuation. At the time, however, I didn't have knowledge of applications where this type of analysis would be useful. After his departure from the University, I had the good fortune to meet my current advisor, Dr. Anil Deane. His research interests include complex bifurcation phenomena and a limitless supply of appropriate problems in fluid dynamics. Finally, Dr. Jian-Guo Liu's course in computational fluid dynamics demystified the Navier-Stokes equations and gave me the concepts and confidence needed to write my own code.

Special thanks to Dr. Dianne O'Leary, UMD Computer Science, and Dr. David Gilsinn, NIST, for their steadfast support, encouragement, and advice. My supervisor, Edward Masuoka, NASA Goddard Space Flight Center, truly knows how to encourage his employees to higher achievements. The Laboratory for Terrestrial Physics of the Earth Sciences Branch at Goddard has supported me throughout this effort, and I am grateful.

Last but not least, my husband Thomas Goff has both assembled my hardware[1] and kept them up and running through more than my share of problems.

[1] current reincarnations: WhiteRabbit, 1.8 GHz AMD Athlon and MadHatter, 3 GHz Intel Pentium 4 SMP

Contents

List of Figures

List of Tables

1 Introduction

1.1 Overview

Despite the temporal and spatial complexity of fluid flow, the dimensionality of models can often be greatly reduced while both capturing and illuminating the nonlinear dynamics of the flow. This dissertation examines a methodology to achieve this goal, depicted in Figure (1.1), with the explicit goal of extending the resultant low-dimensional model to encompass a parameterized family of flow problems.

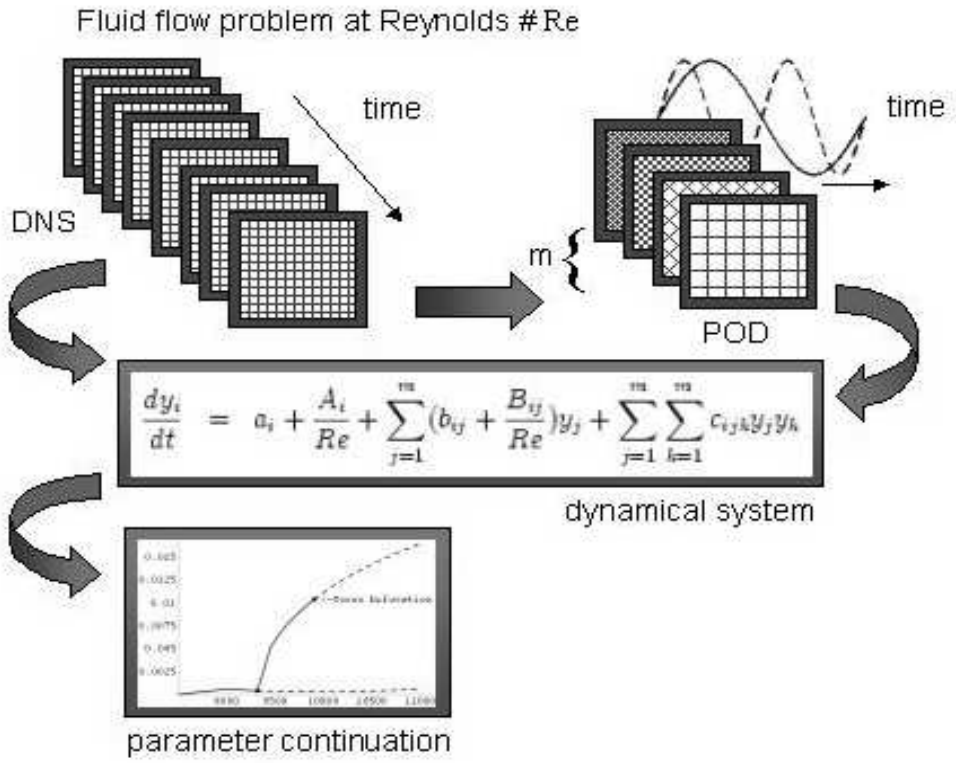

Figure 1.1: Overview. A full-field data set is collected from DNS for ingest into the POD, leading to a dynamical system. After truncation, parameter continuation techniques can be applied.

The next two chapters of this dissertation provide a review of relevant techniques, and their implementation and application to the 2-d driven cavity flow and the 2-d flow past a square cylinder. Chapter 2 discusses direct numerical simulation of the Navier-Stokes equations and Chapter 3 covers the Proper

Orthogonal Decomposition. The heart of the dissertation is contained in chapters 4 - 6.

- Chapter 4 derives the dynamical system from the POD and introduces a new stabilization scheme to significantly improve its ability to reproduce the temporal behavior of the fluid flow upon which it is based.

- Chapter 5 discusses parameter continuation techniques, applies them to the driven cavity flow and square cylinder wake flow, and develops a method of parameterizing the dynamical system coefficients for markedly improved extrapolation results.

- Chapter 6 introduces the concept of a separate spatial model derived from the Reynolds number dependence of the spatial eigenfunctions, and demonstrates its effectiveness at extending the predictive capability of a low-dimensional spatial model for the driven cavity flow and the square cylinder wake flow.

1.2 Background

The Navier-Stokes equations have proven to be an effective mathematical formulation for fluid flow. As nonlinear partial differential equations, however, they are not easy to solve. Known exact solutions are few and dependent on special symmetries of the problem. Thus, computational fluid dynamics (CFD) is a major tool for investigating fluid flow via these equations. Many options exist for solutions via direct numerical simulation (DNS) which can produce highly accurate results. The computational price tag continues to drop as computers get faster and cheaper, but there are compelling reasons why DNS alone is unsatisfactory:

- "One never has enough computer time to produce, or human time to interpret and evaluate, a "complete" picture of the solutions to a

system of reasonable dimension ... Preliminary analyses to locate interesting parameter ranges and regions of phase space are crucial. Naturally, numerical simulation can prompt and suggest such analyses, and hence they should proceed hand in hand.

- The very nature of chaotic dynamical systems, their sensitive dependence on initial conditions, immediately renders numerical approximations suspect. While rigorous results (shadowing lemmas) do imply that numerical solutions faithfully track true solutions in certain cases, in general we have no such guarantees ... the symmetric systems that we deal with are particularly sensitive to symmetry-breaking induced by numerical approximation, and one can obtain quite misleading results, including seemingly clear evidence of chaos, where in truth only regularity reigns.
- Numerical simulations and numerical analysis, the mathematical theory underlying them, typically deal with finite time integrations, while the realm of dynamical systems theory includes asymptotic, infinite time properties and phenomena such as attractors. From this viewpoint the two approaches are complementary." [1]

One route to extract a higher level of information from numerical or experimental data is to look for the major patterns or coherent structures in the flow. The field of pattern recognition has historically used the Karhunen-Loève (KL) expansion, which is the foundation for the Proper Orthogonal Decomposition (POD), to accomplish this same goal. This decomposition represents the flow field as a linear combination of spatial and temporal basis functions derived from the statistics of the sampled flow field (snapshots). Moreover, it orders the modes by their importance in the flow reconstruction, so that significant data reduction can be achieved by neglecting the later terms with negligible loss in the accuracy of the

representation. This process alone allows one to see the important structures in the flow. No information can be gleaned about flow transitions away from the modeled parameterization, however.

A further step is needed to gain dynamical information from the POD. This can be done by first replacing the flow variables in the Navier-Stokes equations by their POD, leaving the Reynolds number $(Re)^2$ as a parameter. Next, for example, take the Galerkin projection onto the spatial basis functions. The result is a set of ordinary differential equations in time, a dynamical system whose solution at the Reynolds number of simulation is an approximation to the temporal basis functions. Potentially, much more information can be obtained by doing a parameter continuation on the Reynolds number (Re), however. This is the key to investigating flow transitions since now they are equivalent to bifurcation phenomena in the dynamical system.

This area of research has been active since J. L. Lumley introduced the application of POD to the study of turbulence in the late sixties [2]. Coherent structures had long been observed in turbulent flow experiments, such as the Von Kármán vortex street behind a circular cylinder. It originates in the laminar flow regime and persists well into turbulence where "markedly periodic vortex shedding remains a characteristic of the flow up to the highest Reynolds number ($\sim 10^7$) at which observations have been made." [3] Numerous papers attest to the success of low-dimensional models derived from POD for many fluid flow problems. A comprehensive review of work in this field as well as a complete explanation of the techniques involved can be found in *Turbulence, Coherent Structures, Dynamical Systems and Symmetry* by P. Holmes, J. L. Lumley, and G. Berkooz, published in 1996 [1].

[2]The ratio of inertial force and viscous force and a measure of dynamic similarity.

Given the POD's beginnings in probability and statistics fields, its utility in turbulent flows is apparent. Less obvious, however, is its use as a nonlinear dynamics tool applied to non-turbulent flow regimes to extract the spatial and temporal characteristics of the flow. When the POD is applied to a spatiotemporal data set of an evolving flow, it simultaneously derives spatial and temporal orthogonal modes which are coupled. This bi-orthogonality was noted by N. Aubry [4] and can be mathematically defined as the representation of a flow field $\mathbf{u}(\mathbf{x}, t)$ in terms of basis functions $\theta_i(t)$ and $\mathbf{\Phi}_i(\mathbf{x})$ such that:

$$\begin{aligned} \mathbf{u}(\mathbf{x}, t) &= \sum_i \lambda_i \theta_i(t) \mathbf{\Phi}_i(\mathbf{x}) \,, \\ \text{with } \lambda_1 &\geq \lambda_2 \geq \cdots \geq 0 \,, \\ \text{and } \langle \theta_i, \theta_j \rangle &= \langle \mathbf{\Phi}_i, \mathbf{\Phi}_j \rangle = \delta_{ij} \,. \end{aligned}$$

Typically, the orthogonality of the temporal modes is ignored since the main objective is the dynamical system based on the spatial modes. However, this property is used to advantage in this dissertation.

The first paper to apply these tools to flows in complex geometries was published in 1991 by A. E. Deane *et al.* [5]. That paper constructed low-dimensional models for flow in a periodically grooved channel and for flow past a circular cylinder. Two-dimensional simulations yield a steady flow which gives way to a periodic flow at a critical Reynolds number specific to the problem. Both flows were studied in the periodic regime and both proved amenable to representation via low-dimensional models at the Reynolds number simulated. A far more difficult problem tackled in the Deane *et al.* paper, however, was predicting the flow properties for a range of Reynolds numbers from the models.

Parameter continuation of these low-dimensional models remains a challenge and this dissertation looks at new strategies for addressing it in both the temporal and

spatial domains. Two 2-dimensional flows will be considered in detail: square driven cavity flow and flow past a square cylinder. The driven cavity flow is far simpler to simulate, and certain factors such as its relatively unchanging mean flow make it an attractive subject for POD, yet it offers rich dynamical behavior. The square cylinder wake flow exemplifies bluff body wake flows while offering simplified discretization for finite differences. The square shape of the body also means that the points at which the flow separates from the body are fixed for a range of Reynolds numbers (up to 100) [6]. This in turn implies little change in the distribution of pressure in that range [7]. These factors help to isolate the changes in the wake flow as the Reynolds number increases.

A recent publication by W. Cazemier, *et al.* [8] derived a low-dimensional model for the two dimensional driven cavity flow at $Re = 22000$, where the flow appears to be chaotic. Their 80-dimensional dynamical system was studied in depth and a bifurcation diagram was presented. The transitions of the dynamical system in the Reynolds number range $8000 - 12000$ were compared with their DNS results. While agreement is good, the bifurcation diagram contains complicated transitions that were unconfirmed by their DNS results. In fact, there is little consensus in the literature about the flow transitions. In contrast, my work seeks to understand and characterize the temporal and spatial eigenfunctions and the resultant changes that need to occur in the dynamical system as a function of Re in order to achieve consistency with DNS results and provide valid low-dimensional temporal and spatial models.

Deane's results for the wake flow found that the dynamical system is extremely sensitive to the Reynolds number, probably due to shape changes that occur in the flow as the Reynolds number changes. B. Noack and H. Eckelmann [9] have also looked at low-dimensional models for this flow, and were able to extend the extrapolation range by use of a weighting factor in the inner product of the Galerkin

projection onto their predefined and scaled a priori basis functions. However, far more modes are required (~ 200 vs ~ 8), and the comparison to DNS results at a particular Reynolds number is unsatisfactory. This dissertation circumvents this issue by taking a fresh look at the implications of the bi-orthogonal decomposition and addressing the temporal and spatial problems separately.

In pursuit of this same goal of a longer range of model fidelity, E. A. Christensen, *et al.* [10], have proposed two modifications to the POD method: weighted POD allows weighting of certain snapshots by including them on the POD calculation multiple times; predefined POD augments the empirically derived modes with predefined modes based on a priori knowledge. They applied these methods to the rotating driven cavity and found model improvement over a longer range of Reynolds numbers. This indirectly addresses the redistribution of kinetic energy that occurs among the POD modes as the Reynolds number changes. This is an important concept, but is explored in this dissertation as an explicit scaling of the dynamical system inspired by the bi-orthogonal decomposition, not by altering the POD.

Direct numerical simulation was done using my own code which implements the Chorin projection method [11] via finite difference discretization on a staggered grid. Chapter 2 describes this method in detail. Appendix B addresses a few options considered for the discretization in more detail. A critical component in my implementation is the solution of Poisson's equation for pressure. Symmetric transforms can be used as the heart of a fast Poisson solver, and these transforms can be implemented via Fast Fourier Transform (FFT). At the time I developed my code, a new and faster FFT package became available, **FFTW** [14]. Modules for doing the symmetric transforms were not a part of the early releases of this software, so I wrote my own. A full description and timing results are in Appendix A.

As the first and most time-consuming link in the chain of calculations, the DNS is a very important component. Lack of accuracy here will cascade through the system, rendering the results worthless. Thus, comprehensive benchmarking of the code has been done, and results are presented in Chapter 2, section 2.11.

Finding the optimal basis for a linear decomposition of a data set is relevant to many fields in mathematics and science. The Karhunen-Loève method was initially proposed (independently) by Karhunen [15] in 1946 and Loève [16] in 1955, The method is known by different names depending on the field of study [17]. Principal component analysis, Proper Orthogonal Decomposition, empirical eigenfunction decomposition, and singular value decomposition are a few of the alternate names for equivalent procedures. It continues to be a viable topic for research and application, *e.g.*, [18], [19]. Chapter 3 describes this method and its utility in fluid dynamics. The application of POD to the driven cavity flow and wake flow are detailed in Chapter 3, sections 3.6 and 3.7, respectively.

The method of constructing the dynamical system from the POD is presented in Chapter 4, along with the specific dynamical systems derived for the driven cavity flow and the square cylinder wake flow. It is important to note that although the POD representation is a linear combination of modes, the nonlinearity of the Navier-Stokes equations is manifested in the shape of these modes, and the resulting dynamical system appropriately exhibits this nonlinearity. Since the dynamical system must neglect higher order modes, it typically needs some sort of closure or stabilization method to accurately evolve the number of steps needed for parameter continuation. A new stabilization method is introduced which exploits the bi-orthogonality of the POD.

Chapter 5 discusses parameter continuation and defines a new scheme to extend the viable range of Reynolds number for a low-dimensional model. By considering the energy transfer between modes as a function of Reynolds number and its impact

on the dynamical system coefficients, far better extrapolation results can be obtained. The methodology is applicable to a class of flow problems, independent of spatial complexity and is illustrated for the driven cavity flow and the flow past a square cylinder.

Although the POD gives excellent information about the temporal and spatial structure of a fluid flow, the tools presented thus far using dynamical systems only address the temporal evolution of the fluid flow with Reynolds number. This is not a new observation; Morkovin [20] and Wallace *et al.* [21] noted this shortcoming in 1988 and 1990, respectively, in the context of open turbulent flows. Chapter 6 examines the spatial counterpart of parameter continuation, looks at possible methods for extending the range of low-dimensional spatial models, and gives specific low-dimensional models parameterized by Reynolds number for the driven cavity flow and flow past a square cylinder, albeit for a limited range of Reynolds numbers.

Chapter 7 completes the dissertation with a summary, conclusions and a discussion of future work.

2 Direct Numerical Simulation and Validation of the Navier-Stokes Equations for Viscous Incompressible Flow

2.1 Mathematical model

The mathematical model for the flow problems under consideration consists of the non-dimensionalized Navier-Stokes equations for incompressible flow:

$$\frac{\partial \mathbf{u}}{\partial t} = -\nabla p - (\mathbf{u}\cdot\nabla)\mathbf{u} + \frac{1}{Re}\Delta\mathbf{u}\,, \tag{2.1}$$

$$\nabla\cdot\mathbf{u} = 0\,, \tag{2.2}$$

where $\mathbf{u} = \binom{u}{v}$ is the velocity vector, p is the static pressure, and Re is the Reynolds number. The unknowns are the velocity field and pressure, but the model does not include an evolution equation for pressure, nor are boundary conditions for pressure usually available. This mandates a numerical algorithm compatible with these constraints. The most direct way to solve for the pressure is to take the divergence of Equation (2.1) and simplify using the incompressibility constraint, Equation (2.2), to obtain a Poisson equation for pressure.

2.2 Algorithm

One method of solution that utilizes the pressure Poisson equation is the projection method proposed independently by A. Chorin in 1968 [11] and by R. Temam [12] in 1969. This is a fractional step method based on the Helmholtz-Hodge Decomposition Theorem [22].

Helmholtz-Hodge Decomposition Theorem *A vector field* $\mathbf{u}$ *on domain* D *can be uniquely decomposed in the form* $\mathbf{u} = \mathbf{u}^\star + \nabla p$ *where* $\mathbf{u}^\star$ *has zero divergence and is parallel to* ∂D*; that is,* $\mathbf{u}^\star\cdot\mathbf{n} = 0$ *on* ∂D*.* ($\mathbf{n}\cdot\partial D = 0$)*.*

Let $\mathcal{P}$ be the orthogonal projection operator which maps $\mathbf{u}$ onto its divergence-free part $\mathbf{u}^\star$. Note that $\mathcal{P}(\nabla p) = 0$. Applying the projection operator to the Navier-Stokes equations with $\mathbf{u} = \mathbf{u}^\star + \nabla p$ and Euler time-stepping leads to the following algorithm:[3]

For example, using Euler time-marching:

$$\frac{\mathbf{u}^\star - \mathbf{u}^n}{\triangle t} = -(\mathbf{u}^n \cdot \nabla)\mathbf{u}^n + \frac{1}{Re}\Delta \mathbf{u}^n , \tag{2.3}$$

$$\Delta p^{n+1} = \frac{1}{\triangle t}\nabla \cdot \mathbf{u}^\star , \tag{2.4}$$

$$\frac{\mathbf{u}^{n+1} - \mathbf{u}^\star}{\triangle t} = -\nabla p^{n+1} . \tag{2.5}$$

The sum of equations (2.3) and (2.5) is a discrete form of Equation (2.1). Equation (2.3) is solved for $\mathbf{u}^\star$. The pressure field is determined from a Poisson equation (2.4) with homogeneous Neumann boundary conditions [13]. Finally, the new velocity field is determined via Equation (2.5). For a finite difference solution, this method works best on a staggered grid where pressure is defined at the grid points, u is offset in y by $\frac{\triangle y}{2}$ and v is offset in x by $\frac{\triangle x}{2}$.

An advantage of this splitting method is that it does not require external boundary conditions for pressure. This method has its origins in the Marker and Cell (MAC) method developed in 1965 [23] which featured the staggered grid and a Poisson equation for pressure. The projection method coincides with the MAC method in the interior of the domain, but differs on the boundary. Many variants of these methods have been successfully used *e.g.* Kim and Moin, 1985 [24].

The Poisson equation, Equation (2.4), can be solved using one of three strategies: traditional iterative methods such as ADI or SOR; multigrid methods; or a direct solver based on spectral methods. Of these, multigrid methods have recently been widely used because of their excellent speed of convergence, accuracy,

[3]Boundary conditions are problem-specific, and will be discussed in a subsequent section.

and flexibility with regard to boundary conditions. Spectral methods are used here because of their speed, ease of implementation and they are ideal for the uniform staggered grid and otherwise second order discretization.

2.3 Discretization

The mathematical model and choice of algorithm are compatible with a myriad of discretization techniques and solution methods. A compromise must be made as to cost of implementation, accuracy, computational efficiency, and ease of data visualization and interpretation. For instance, higher order methods involve more nodes, consequently increasing computation time. Non-uniform grids and unstructured grids both increase flexibility of node placement, but at an increased cost of code development time for simulation and data visualization. Second order methods constitute a good compromise for these issues [26], and obtain accuracy comparable to the benchmark calculations of Ghia *et al.* for the driven cavity and Sohankar *et al.* for the square cylinder wake flow. This is demonstrated in Chapter 2, section 2.11. A further requirement for this particular application is the compatibility of the discretization with the Proper Orthogonal Decomposition code and the dynamical system computations. For these reasons, my implementation uses finite differencing discretization on a uniform staggered grid and follows the algorithm outlined above with the following differences: I use 4^{th} order Runge Kutta time marching. This was found to be a good choice for the sensitive temporal evolution cases which include quasi-periodic behavior discussed later. I have allowed discretization of the convective term $(\mathbf{u} \cdot \nabla)\mathbf{u}$ to be a run-time choice of either central differencing or modified upwinding. Central differencing works well on closed flows where there is no global directionality, and mixed upwinding is preferable for open flows where there is a dominant direction. Modified upwinding is implemented

by:

$$\frac{du_n}{dx} \approx \frac{u_{n+1} - u_{n-1}}{2\triangle x} + \frac{q(u_{n-1} - 3u_n + 3u_{n+1} - u_{n+2})}{3\triangle x}, \tag{2.6}$$

which is of order 3 in $\triangle x$ when $q = .5$ [25].

2.4 Grid

The staggered grid is advantageous for several reasons:

- The pressure and diffusion terms in the Navier-Stokes equations can be approximated by central finite differences without interpolation.
- Strong coupling between the velocities and pressure helps to avoid oscillations in pressure.
- Numerical approximation on a staggered grid conserves kinetic energy [26].

For the driven cavity flow, the pressure grid used is 256 x 256, $\triangle x = \triangle y = \frac{1}{256}$. A few grid refinement studies were done at 512 x 512, $\triangle x = \triangle y = \frac{1}{512}$, for flow validation and are presented with benchmarking results in section 2.11. The grid for flow past a square cylinder requires more care. Sohanker *et al.* [27],[28], have done sensitivity studies to determine the proper domain size for moderate Reynolds numbers to avoid numerical artifacts due to insufficient upstream and downstream distances from the cylinder and blockage (extent above and below the cylinder). Based on these studies, the domain in Figure (2.1) was used ($\triangle x = \triangle y = \frac{1}{32}$):

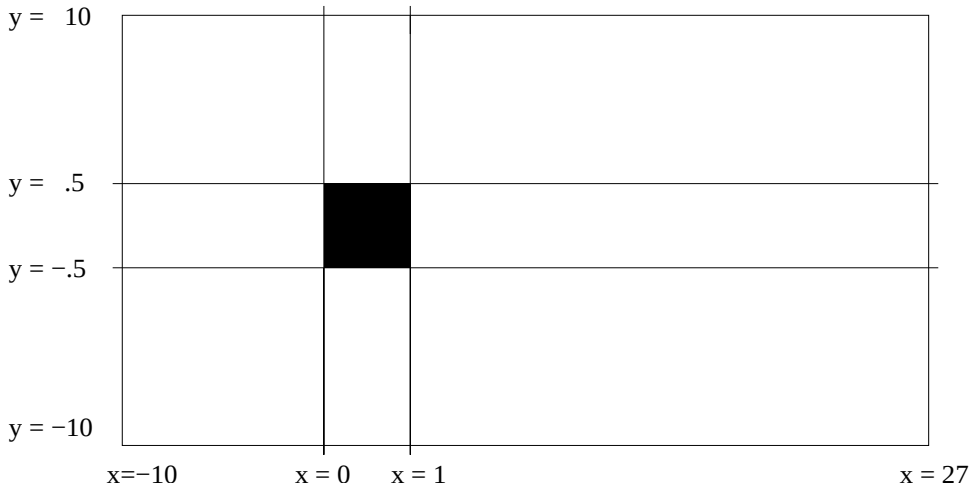

Figure 2.1: Cartesian coordinates of the computational domain for the flow past a square cylinder (not to scale).

2.5 Solving Poisson's equation for pressure

On a staggered grid with Neumann boundary conditions, the pressure Poisson equation can be very efficiently solved using the quarter cosine-wave transform. At the time this code was developed, fast symmetric transforms were not available, so I wrote my own based on the **FFTW** [14] fast Fourier transform package. Given the broader context of my work done in this area, this material is presented in depth in Appendix A. The **FFTW** authors recently implemented their own versions for the symmetric transforms and now include it as part of their software package.

2.6 Boundary conditions

Three types of boundary conditions have been implemented for this work:

- Dirichlet boundary conditions are used for prescribed inflow conditions and for the wake flow horizontal boundaries. For inflow, u values are on the boundary and are set to the desired value. The u values do not lie on the horizontal boundaries, however, so boundary values are set such that the average across the boundary is the desired value. It should be noted that it is also common to use free-slip ($\frac{du}{dy} = 0, v = 0$) on the horizontal wake boundaries. Given a sufficiently large computational domain, it should not be a significant factor and I felt that the Dirichlet formulation was more compatible for ingest into the POD to ensure that the boundary terms are incorporated into the mean flow.

- no-slip (u and v vanish at the boundary) is used for wall boundaries. This is done by setting the normal velocity component to 0 (since these grid points lie on the wall), and setting the tangential velocity component to minus the value of that velocity component at the adjacent interior point (in the normal direction) so that the average value at the wall is 0.

- outflow (the outflowing mass flux should equal the inflowing mass flux) is needed for channel, wake, and step flows. The common method of implementing outflow by specifying zero normal gradient in u and v is fine for steady flows, but was not found to be satisfactory for unsteady wake flows. The simple device of linearly extrapolating u and v to the outflow boundary preserves the vortical structure in the wake flow and does a fine job of conserving mass flux.

2.7 Stability constraints

The use of the 4^{th} order Runge Kutta method for time marching permits the time step to be governed by the usual stability conditions for convection and diffusion, even using centered differencing at high Reynolds numbers, since the stability region for convection with higher order Runge-Kutta methods includes a portion of the imaginary axis [29]:

$$\frac{2\Delta t}{Re} < \left(\frac{1}{\Delta x^2} + \frac{1}{\Delta y^2}\right)^{-1}, \tag{2.7}$$

$$|u_{max}|\Delta t < \sigma\,\Delta x\,, \tag{2.8}$$

$$|v_{max}|\Delta t < \sigma\,\Delta y\,, \tag{2.9}$$

where σ, the Courant-Friedrichs-Levy number, must be less than one to ensure that no information travels a distance greater than the mesh spacing in time $\triangle t$. I conservatively used $\sigma = 0.45$ for the driven cavity and $\sigma = 0.4$ for the square cylinder.

2.8 Automated detection of periodic flow

Since it is necessary to precisely compute the periodicity of the flow, the code has an option to track the correlation coefficient at each (fixed) time step with the

initial flow field. Computation stops when the run-time specified number of periods has been counted. Once an approximation to the period has been calculated, a subsequent simulation is run with the time step set to the period divided by the number of snapshots desired for the POD. This feature makes it easier to get a mean flow averaged on periodic boundaries and to get equally spaced snapshots for the POD.

2.9 Domain decomposition

The square cylinder wake flow requires domain decomposition to split the computational domain into the rectangular regions necessary for the solution of the Poisson equation for pressure by transform methods. I use a straightforward implementation of the alternating Schwarz method, where the number of iterations required for convergence is bounded independently of the mesh refinement and depends only on the amount of geometric overlap [30]. For the square cylinder, the domain has been partitioned into four rectangles with external domain boundaries on three of the four sides for each domain and bordering the square on the fourth side. This decomposition assures physical boundary conditions on three of the four sides for each domain.

This has been handled in a flexible way by the definition of two data structures. The DOMAIN data structure keeps track of the relative position and spatial extent of the rectangle within the entire computational domain. It also stores information specific to the Poisson solver for that rectangle. A pair of data structures of type OVERLAP is allocated for each pair of overlapping rectangles. The Poisson solver is iterated until the values of the specified overlap region pairs agree within a specified tolerance. The code has been written so that it is easy to solve problems for computational domains with any rectangular obstacle, from L-shaped cavities to full square obstacles. The backfacing step has also been solved with an actual step

with this code as well (as opposed to the common method of using a rectangular domain and specifying the expected inflow where the step would occur).

2.10 Visualization

The use of a uniform grid has made visualization of the results quite straightforward. I have written code in *Mathematica* to compute the stream function $\Psi(x, y)$ and vorticity $\omega(x, y)$. If u and v are the horizontal and vertical velocities of the flow field, then the stream function is defined by:

$$\frac{\partial \Psi}{\partial x} = -v\,, \quad \frac{\partial \Psi}{\partial y} = u\,,$$

and the vorticity by

$$\omega(x, y) = \frac{\partial v}{\partial x} - \frac{\partial u}{\partial y}\,.$$

The stream function is well defined since the incompressibility constraint (Equation (2.2)) guarantees that the integrability condition ($\frac{\partial^2 \Psi}{\partial x \partial y} = \frac{\partial^2 \Psi}{\partial y \partial x}$) is satisfied. A streamline is defined as a continuous line within the fluid whose tangent at any point is in the direction of the velocity at that point at a fixed time t. The stream function is so named because it is constant along a streamline. For a steady flow, the streamlines actually show the path of the fluid flow, but they only indicate the instantaneous flow direction for non-steady flow.

The vorticity is equivalently defined as $\boldsymbol{\omega} = curl\,\mathbf{u}$, but for two-dimensional flow, the x and y components of the vector field $\boldsymbol{\omega}$ are zero. This formulation gives insight into the physical meaning of vorticity, however, by considering its relationship with the concept of circulation, Γ. The circulation around a closed curve C is defined by:

$$\Gamma = \oint_C \mathbf{u} d\mathbf{s}\,,$$

where $d\mathbf{s}$ is an element of contour on C. Rewriting this equation using Stokes theorem ($\int_C \mathbf{u}\, d\mathbf{s} = \int_A (curl\, \mathbf{u}) \cdot dA$),

$$\Gamma = \int_A \boldsymbol{\omega} \cdot dA\,,$$

where A is any surface bounded by C. Thus, vorticity at a point equals the circulation per unit area [46]. For clockwise rotation in 2-d flow, $\frac{\partial u}{\partial x} > 0$ and $\frac{\partial v}{\partial y} < 0$, so we see that the negative vorticity corresponds to clockwise circulation.

2.11 Validation

Since the Navier-Stokes equations in general do not admit to an analytic solution, one must turn to experimental data and respected numerical benchmark calculations of others in the field. Two-dimensional fluid flow is an acceptable approximation to a physical fluid flow when the flow is parallel along one axis. Unfortunately, this is not the case for the driven cavity flow for Reynolds numbers above 1000. Koseff and Street ([40], [41]) have shown that the flow is three-dimensional, and two- dimensional simulations produce significantly different results. Thus, the 2-d driven cavity flow must be viewed as a numerical problem, and consensus of diverse methods of solution is the best one can do for validation of results. Fortunately, there is an abundance of numerical results for this problem, and comparisons are presented in this chapter.

In contrast, the wake produced by a two-dimensional body (extruded in the missing axis) has been studied experimentally for decades, particularly for circular cylinders. Robichaux [60] cites particularly relevant data for the flow past a square cylinder at $Re\,100$, illustrating agreement for both numerical and experimental results.

This section presents validation of the code done in several ways:

- comparison of computed solution with a known analytic solution,
- numerical solution of standard steady flow problems (driven cavity, L-shaped cavity, Poiseuille flow, flow past a backfacing step) for comparison with published results,
- computation of a spectral element solution of the L-shaped cavity flow for comparison with this code in the transient regime,
- comparison with the literature for square cylinder wake flow,
- grid refinement for several flow problems.

2.11.1 Exact solution

It is useful to use an exact solution as a first test of a new code. This will immediately reveal gross errors in the code, and also permit verification of the order of accuracy. The following two-dimensional test problem works well for this purpose:

$$\begin{aligned} \text{domain}\,\Omega &= [0,2\pi]\times[0,2\pi]\,, \\ u_{exact}(x,y,t) &= -\sin^2(x)\,\sin(2y)\,e^{-t}\,, \\ v_{exact}(x,y,t) &= \sin(2x)\,\sin^2(y)\,e^{-t}\,, \\ p_{exact}(x,y) &= -\frac{1}{4}\,\sin(2x)\sin(2y)\,e^{-t}\,, \\ Re &= 4\,, \end{aligned}$$

is the solution to the Stokes equation: [4]

$$\begin{aligned} \frac{\partial \mathbf{u}}{\partial t} &= -\nabla p + \frac{1}{Re}\Delta\mathbf{u} \\ \nabla\cdot\mathbf{u} &= 0\,, \end{aligned}$$

with boundary conditions $\mathbf{u}\equiv 0$ on $\partial\Omega$.

[4] The Stokes equations are for low Reynolds number flow where convection can be ignored.

Since the code to be tested incorporates the convection terms, a forcing term (equal to -convection term) was added to permit the $\mathbf{u} = \binom{u}{v}$ to be used as a solution to the Navier-Stokes equations. Tables (2.1) - (2.4) summarize the results for the options used, namely fourth-order Runge-Kutta time-stepping, and central or mixed upwind discretization of the convective terms. As expected, the results demonstrate approximately second order spatial accuracy.

The numerical solution was evolved in time from 0 to 1 for geometrically increasing grid sizes from 8×8 to 128×128. The accuracy was quantitatively measured by the following for grid $n \times n$:

$$
\begin{aligned}
\mathrm{L}^1 \text{ error in } u &= \sum_{j=1}^{n+2} \sum_{i=1}^{n+1} |u(x_i, y_j) - u_{exact}(x_i, y_j)| / ((n+1)(n+2)) \,, \\
\mathrm{L}^1 \text{ error in } v &= \sum_{j=1}^{n+1} \sum_{i=1}^{n+2} |v(x_i, y_j) - v_{exact}(x_i, y_j)| / ((n+2)(n+1)) \,, \\
\mathrm{L}^1 \text{ order} &= (\ln(\mathrm{L}^1\text{error } @ \, \frac{n}{2}) - \ln(\mathrm{L}^1\text{error } @ \, n) / \ln(2) \,, \\
\mathrm{L}^2 \text{ error in } u &= \sum_{j=1}^{n+2} \sum_{i=1}^{n+1} (u(x_i, y_j) - u_{exact}(x_i, y_j))^2 / ((n+1)(n+2)) \,, \\
\mathrm{L}^2 \text{ error in } v &= \sum_{j=1}^{n+1} \sum_{i=1}^{n+2} (v(x_i, y_j) - v_{exact}(x_i, y_j))^2 / ((n+2)(n+1)) \,, \\
\mathrm{L}^2 \text{ order} &= (\ln(\mathrm{L}^2\text{error } @ \, \frac{n}{2}) - \ln(\mathrm{L}^2\text{error } @ \, n) / \ln(2) \,, \\
\mathrm{L}^\infty \text{ error in } u &= \mathrm{Max}_{j=1}^{n+2} \, \mathrm{Max}_{i=1}^{n+1} \, |u(x_i, y_j) - u_{exact}(x_i, y_j)| \,, \\
\mathrm{L}^\infty \text{ error in } v &= \mathrm{Max}_{j=1}^{n+1} \, \mathrm{Max}_{i=1}^{n+2} \, |v(x_i, y_j) - v_{exact}(x_i, y_j)| \,, \\
\mathrm{L}^\infty \text{ order} &= (\ln(\mathrm{L}^\infty\text{error } @ \, \frac{n}{2}) - \ln(\mathrm{L}^\infty\text{error } @ \, n) / \ln(2) \,.
\end{aligned}
$$

Comparison of numerically computed u and v with exact solution

n	L^1 error	L^1 order	L^2 error	L^2 order	L^∞ error	L^∞ order
8	$1.2719\,10^{-2}$		$1.6352\,10^{-2}$		$3.0861\,10^{-2}$	
16	$1.5540\,10^{-3}$		$2.1770\,10^{-3}$		$5.3450\,10^{-3}$	
32	$6.8700\,10^{-4}$	1.1776	$9.6300\,10^{-4}$	1.1767	$2.4310\,10^{-3}$	1.1366
64	$1.9700\,10^{-4}$	1.8021	$2.7300\,10^{-4}$	1.8186	$6.8800\,10^{-4}$	1.8211
128	$5.1000\,10^{-5}$	1.9496	$7.1000\,10^{-5}$	1.9430	$1.7700\,10^{-4}$	1.9587

Table 2.1: u results, central differencing of convection terms.

n	L^1 error	L^1 order	L^2 error	L^2 order	L^∞ error	L^∞ order
8	$1.2820\,10^{-2}$		$1.6455\,10^{-2}$		$3.1345\,10^{-2}$	
16	$1.5630\,10^{-3}$		$2.1460\,10^{-3}$		$5.3020\,10^{-3}$	
32	$6.8600\,10^{-4}$	1.1880	$9.6000\,10^{-4}$	1.1605	$2.4240\,10^{-3}$	1.1292
64	$1.9700\,10^{-4}$	1.8000	$2.7300\,10^{-4}$	1.1413	$6.8700\,10^{-4}$	1.8190
128	$5.1000\,10^{-5}$	1.9496	$7.1000\,10^{-5}$	1.9430	$1.7700\,10^{-4}$	1.9566

Table 2.2: v results, central differencing of convection terms.

n	L^1 error	L^1 order	L^2 error	L^2 order	L^∞ error	L^∞ order
8	$3.5930\,10^{-3}$		$5.3090\,10^{-3}$		$1.5697\,10^{-2}$	
16	$3.9750\,10^{-3}$		$5.5000\,10^{-3}$		$1.2884\,10^{-2}$	
32	$1.0020\,10^{-3}$	1.9881	$1.4070\,10^{-3}$	1.9668	$3.4730\,10^{-3}$	1.8913
64	$2.3900\,10^{-4}$	2.0678	$3.3200\,10^{-4}$	2.0834	$8.3000\,10^{-4}$	2.0650
128	$5.7000\,10^{-5}$	2.0680	$7.9000\,10^{-5}$	2.0713	$1.9600\,10^{-4}$	2.0823

Table 2.3: u results, mixed upwind differencing of convection terms.

n	L^1 error	L^1 order	L^2 error	L^2 order	L^∞ error	L^∞ order
8	$3.2280\,10^{-3}$		$4.7470\,10^{-3}$		$1.4897\,10^{-2}$	
16	$3.9270\,10^{-3}$		$5.4430\,10^{-3}$		$1.2690\,10^{-2}$	
32	$1.0010\,10^{-3}$	1.9720	$1.4040\,10^{-3}$	1.9549	$3.4620\,10^{-3}$	1.8740
64	$2.3900\,10^{-4}$	2.0664	$3.3100\,10^{-4}$	2.0846	$8.3000\,10^{-4}$	2.0604
128	$5.7000\,10^{-5}$	2.0680	$7.8000\,10^{-5}$	2.0853	$1.9600\,10^{-4}$	2.0823

Table 2.4: v results, mixed upwind differencing of convection terms.

2.11.2 Driven cavity flow

The 2-d square driven cavity flow may be the most popular benchmarking choice in CFD, and for good reason. The spatial domain couldn't be simpler and the boundary conditions are unambiguous and easy to implement: no-slip on the three walls and a driven top edge at constant unit velocity. A common feature of non-turbulent two-dimensional driven cavity flow is a large rotating eddy occupying the central portion of the cavity. Cascades of counter-rotating eddies occupy the lower left and right corners. At high Reynolds numbers (≥ 5000), a top left eddy forms.

Extensive benchmarking results for $Re \leq 10000$ are available from Ghia *et al.* [42]. However, Ghia's work found a steady state up to $Re\,10000$. More recent publications, (*e.g.* Cazemier [8]), and my own results suggest that the flow in fact undergoes two bifurcations before $Re\,10000$. For this reason, the benchmarking results presented here are restricted to steady flow. Grid refinement has been done for key nonsteady flows used in this work to validate the later results derived from the nonsteady flow. Corroboration of the nonsteady driven cavity flows with current literature is presented when available, and is also mentioned in context in later chapters.

Figure (2.2) depicts the stream function and vorticity for the steady square driven cavity flow at $Re\,1000$ calculated on a 256×256 staggered grid. The black dots on the stream function plot mark the locations of the primary vortex near the center, and the bottom corner vortices. Red indicates negative values, and blue is used for positive values.

Ghia *et al.* [42] used a vorticity-stream function formulation of the Navier-Stokes equations (discussed in Appendix A, Equation (A.7)) with a multigrid solution method on a uniform grid of 128×128 to resolve this same flow. Second-order central differencing was used for all second-order derivatives, and upwinding for the

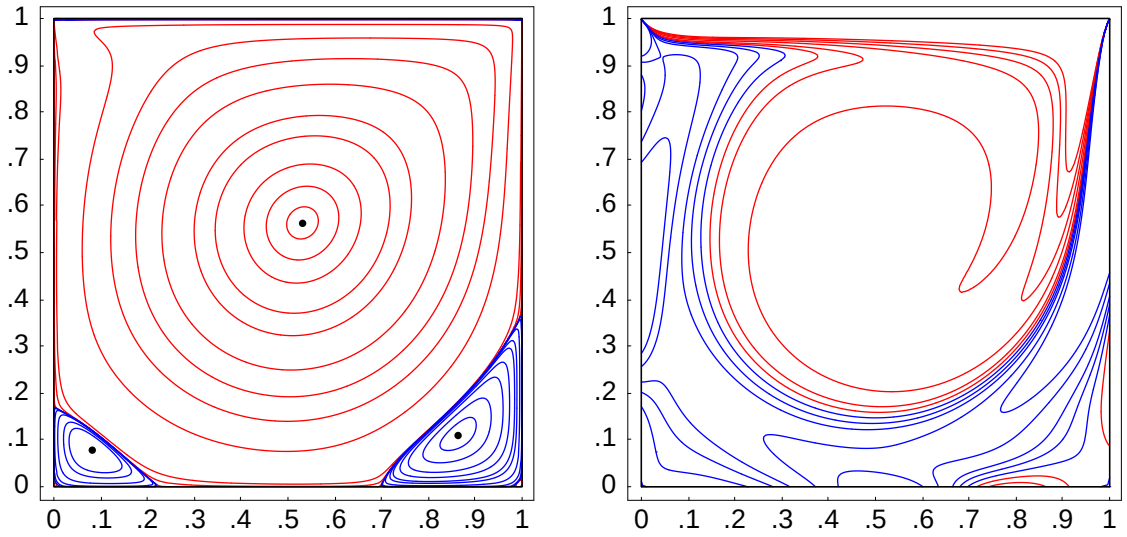

Figure 2.2: Driven cavity flow at Re 1000 solved on a 256×256 staggered grid. Negative values are red, positive values are blue.

convective terms. The multigrid technique allows local grid refinement by defining progressively finer grids in selected regions as needed. A more recent publication by Botella and Peyret [43] obtained a highly accurate solution for this flow by a Chebyshev collocation method. The velocity is approximated with a polynomial of at most degree N in both spatial directions, its values defined on the $(N+1) \times N+1)$ Gauss-Lobatto grid. The pressure is defined as a polynomial of degree two less, and is calculated at the $(N-1) \times (N-1)$ inner nodes. The published results used for comparison here are for the highest resolution reported at $N = 160$. Special attention was paid to the lid corner singularities where the velocity is discontinuous. Their boundary condition for the lid, however, was $u \equiv -1$, opposite to convention. This necessitates a mirroring of x coordinates and negating of u values for comparison with results from lid velocity $u \equiv +1$. Figure (2.3a) plots the u velocity component along the vertical center line of the cavity in black. The red dots show this information for the locations in Ghia *et al.* [42], and the green dots show $-u$ for the locations in Botella *et al.* [43]. Figure (2.3b) shows the v velocity component along the horizontal center line of the cavity in black. The

red dots show this information for the locations in Ghia *et al.* [42], and the green dots show the same for $1 - x$, where x is as published in Botella *et al.* [43]. Table (2.5) compares vortex properties of the discernible vortices in the flow. Blanks denote unreported, presumably undetected, vortices. The algorithm that I used for vortex detection is a simple point-wise search for local extrema of Ψ and $-\Psi$ [5] with the criteria that the point value must be less than that of all eight neighbors. Thus, the reported locations are only of order $\triangle x$.

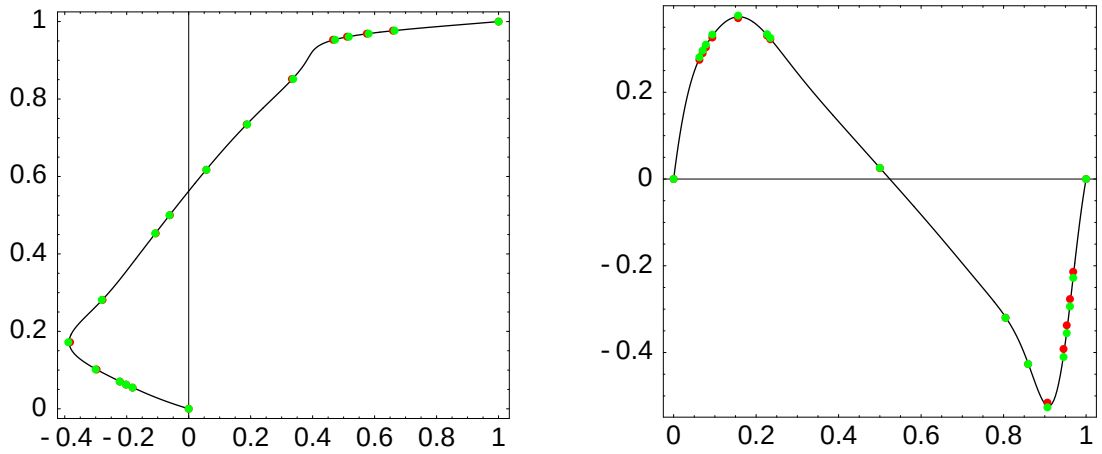

(a) u along vertical center line (plotted (u, y)). (b) v along horizontal center line (plotted (x, v)).

Figure 2.3: Comparison of solutions to the driven cavity flow at $Re\,1000$: black = 256×256, red dots = Ghia *et al.*, green dots = Botella *et al.*

One anomaly: the vorticity values published in Ghia *et al.* are inexplicably the negative of mine. The primary vortex is a good test case for sign. From Figure (2.3)(a) we see graphically that $\frac{du}{dy} > 0$. Figure (2.3)(b) illustrates that $\frac{dv}{dx} < 0$. Using the definition of vorticity $\omega = \frac{dv}{dx} - \frac{du}{dy}$, the vorticity at the primary vortex must be negative. This is logical as well, since clockwise rotation makes physical sense for a lid moving to the right. This is in agreement with my results. Thus, the tables which follow will have a sign discrepancy which I cannot resolve, for all Reynolds numbers.

[5] At extrema of f(x,y), the x and y derivatives vanish. For the stream function, this means u and v are zero, which is one way of indentifying a vortex.

primary vortex	source	x	y	Ψ	ω
	Ghia *et al.*	0.5313	0.5625	-0.117929	2.04968
	Botella *et al.*	0.5308 [3]	0.5652	-0.1189366 [4]	-2.067753 [4]
	256×256	0.5313	0.5625	-0.118087	-2.04902
bottom "left" secondary	source	x	y	Ψ	ω
	Ghia *et al.*	0.0859	0.0781	$2.31129\ 10^{-4}$	-0.36175
	Botella *et al.*	0.0833 [3]	0.0781	$2.334528\ 10^{-4}$ [4]	0.3522861 [4]
	256×256	0.0820	0.0781	$2.28889\ 10^{-4}$	0.342020
bottom "right" secondary	source	x	y	Ψ	ω
	Ghia *et al.*	0.8594	0.1094	$1.75102\ 10^{-3}$	-1.15465
	Botella *et al.*	0.8594 [3]	0.1118	$1.729717\ 10^{-3}$ [4]	1.109789 [4]
	256×256	0.8633	0.1094	$1.72278\ 10^{-3}$	1.08109
bottom "left" tertiary	source	x	y	Ψ	ω
	Ghia *et al.*	—	—	—	—
	Botella *et al.*	0.0048 [3]	0.0048	$-6.39880\ 10^{-9}$ [4]	—
	256×256	0.0039	0.0039	$-7.81250\ 10^{-9}$	$-1.02400\ 10^{-3}$
bottom "right" tertiary	source	x	y	Ψ	ω
	Ghia *et al.*	0.9922	0.0078	$-9.31929\ 10^{-8}$	$8.52782\ 10^{-3}$
	Botella *et al.*	0.9923 [3]	0.0077	$-5.03944\ 10^{-8}$ [4]	—
	256×256	0.9922	0.0078	$-4.68750\ 10^{-8}$	$-9.21600\ 10^{-3}$

Table 2.5: Comparison of vortex properties for the driven cavity flow at $Re\,1000$.

Figure (2.4) depicts the stream function and vorticity contours for the steady square driven cavity flow at $Re\,5000$ calculated on a 256×256 staggered grid. The black dots on the stream function plot mark the locations of the primary vortex near the center, and the bottom corner vortices. The top left vortex is now a flow feature, and the cascade of vortices in the lower right corner is more in evidence. Comparison with Ghia *et al.* [42] on the same grid size (the only known available comparison flow) follows in Figure (2.5) and Table (2.6). As before, red indicates negative values, and blue is used for positive values for the contours. Stream function contours are at $-1.0 \times 10^{-10}, -1.0 \times 10^{-7}, -1.0 \times 10^{-5}, -1.0 \times 10^{-4}, -.01, -.03, -.05, -.07, -.09, -.1, -.11, -.115, -.1175, 1.0 \times 10^{-}8, 1.0 \times 10^{-7}, 1.0 \times 10^{-6}, 1.0 \times 10^{-5}, 5.0 \times 10^{-5}, 1.0 \times 10^{-4}, 2.5 \times 10^{-4}, 5.0 \times 10^{-4}, 1.0 \times 10^{-3}, 1.5 \times 10^{-3}, 3.0 \times 10^{-3}$. Vorticity contours are at $-5, -4, -3, -2, -1, -.5, -.25, -.1, 0, .5, 1, 2, 3$.

[3] 1 - published value for lid velocity reversal

[4] negated from published value for lid velocity reversal

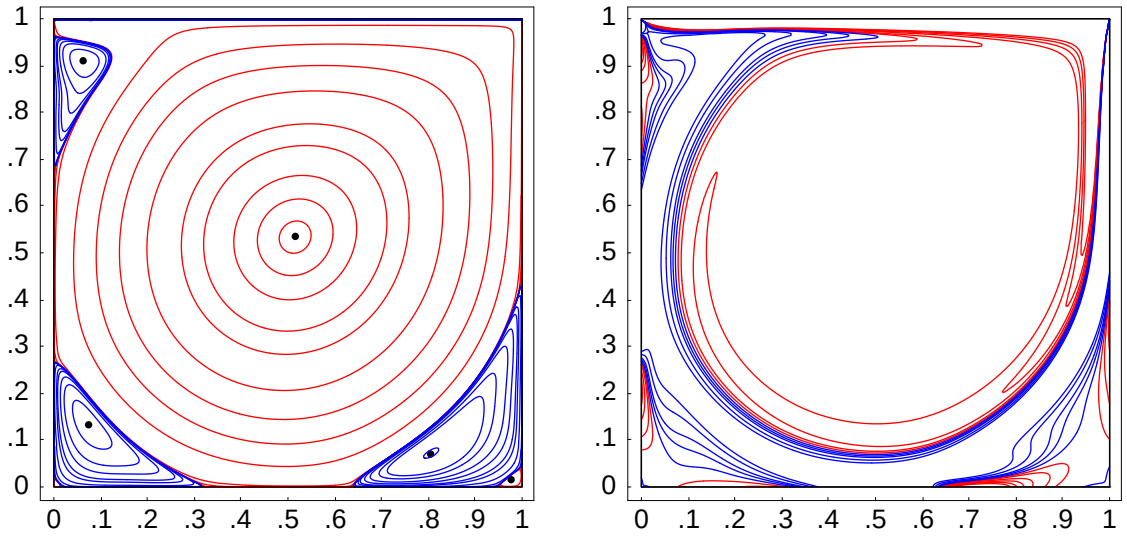

Stream function. Vorticity

Figure 2.4: Driven cavity flow at $Re\,5000$ solved on a 256×256 staggered grid. Negative values are red, positive values are blue.

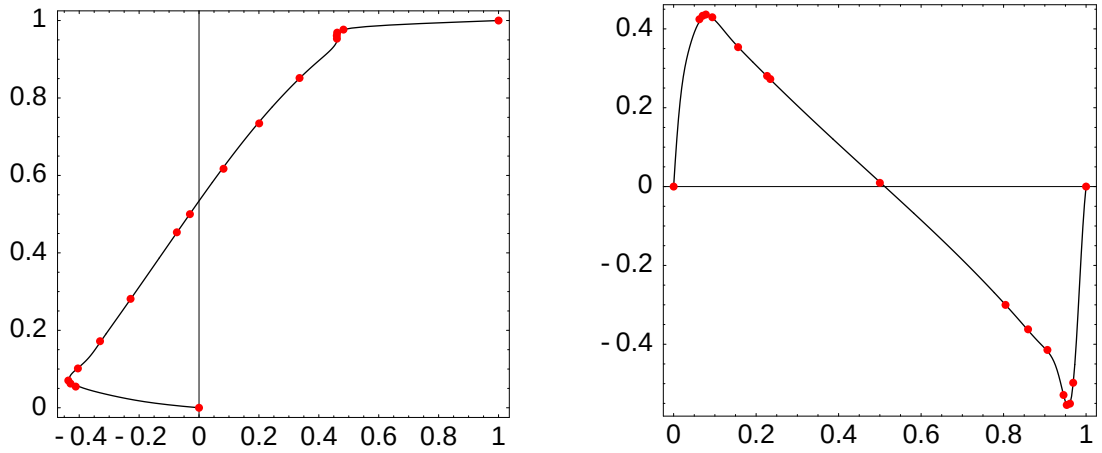

(a) u along vertical center line (plotted (u, y)). (b) v along horizontal center line (plotted (x, v)).

Figure 2.5: Comparison of solutions to the driven cavity flow at $Re\,5000$: black = 256×256, red dots = Ghia *et al.*

primary vortex	source	x	y	Ψ	ω
	Ghia *et al.*	0.5117	0.5352	-0.118966	1.86016
	256×256	0.5156	0.5352	-0.118036	-1.86163
top left vortex	x	y	Ψ	ω	
	Ghia *et al.*	0.0625	0.9102	$1.45641\ 10^{-3}$	-2.08843
	256×256	0.0625	0.9102	$1.42007\ 10^{-3}$	1.97120
bottom left secondary	source	x	y	Ψ	ω
	Ghia *et al.*	0.0703	0.1367	$1.36119\ 10^{-3}$	-1.53055
	256×256	0.0742	0.1328	$1.33268\ 10^{-3}$	1.38854
bottom right secondary	source	x	y	Ψ	ω
	Ghia *et al.*	0.8086	0.0742	$3.08358\ 10^{-3}$	-2.66354
	256×256	0.8047	0.0703	$3.05071\ 10^{-3}$	2.71053
bottom left tertiary	source	x	y	Ψ	ω
	Ghia *et al.*	0.0117	0.0078	$-7.08860\ 10^{-8}$	$1.88395\ 10^{-2}$
	256×256	0.0078	0.0078	$-6.05469\ 10^{-8}$	$-1.04960\ 10^{-2}$
bottom right tertiary	source	x	y	Ψ	ω
	Ghia *et al.*	0.9805	0.0195	$-1.43226\ 10^{-6}$	$3.19311\ 10^{-2}$
	256×256	0.9766	0.0156	$-1.35742\ 10^{-6}$	$-2.89280\ 10^{-2}$

Table 2.6: Comparison of vortex properties for the driven cavity flow at $Re\,5000$.

Figure (2.6) shows the stream function and vorticity for the steady square driven cavity flow at Re 7500 calculated on a 256×256 staggered grid. Stream function contours are at $-1.0 \times 10^{-10}, -1.0 \times 10^{-7}, -1.0 \times 10^{-5}, -1.0 \times 10^{-4}, -.01, -.03, -.05, -.07, -.09, -.1, -.11, -.115, -.1175, 1.0 \times 10^{-}8, 1.0 \times 10^{-7}, 1.0 \times 10^{-6}, 1.0 \times 10^{-5}, 5.0 \times 10^{-5}, 1.0 \times 10^{-4}, 2.5 \times 10^{-4}, 5.0 \times 10^{-4}, 1.0 \times 10^{-3}, 1.5 \times 10^{-3}, 3.0 \times 10^{-3}$. Vorticity contours are at $-5, -4, -3, -2, -1, -.5, -.25, -.1, 0, .5, 1, 2, 3$. A grid refinement was also done for comparison on a 512×512 grid. The black dots on the stream function plot mark the locations of the primary vortex near the center, and the bottom corner vortices. The top left vortex is now a flow feature, and the cascade of counter-rotating vortices in the lower right corner is more in evidence. Again, comparison with Ghia *et al.* [42] (the only known available comparison flow), also on a 256×256 grid, follows in Figure (2.7) and Table (2.7).

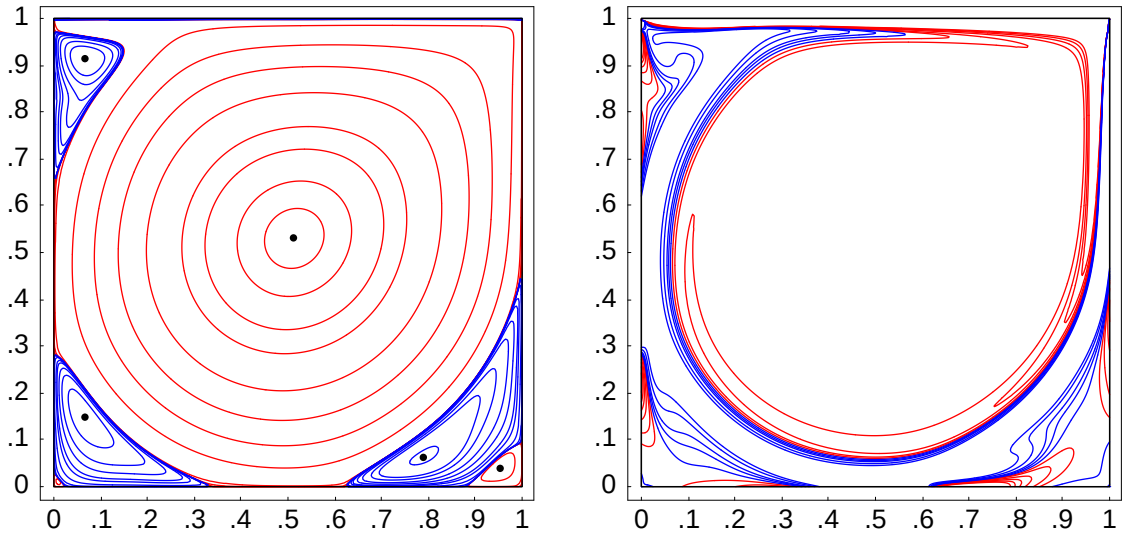

Figure 2.6: Driven cavity flow at Re 7500 solved on a 256×256 staggered grid. Negative values are red, positive values are blue.

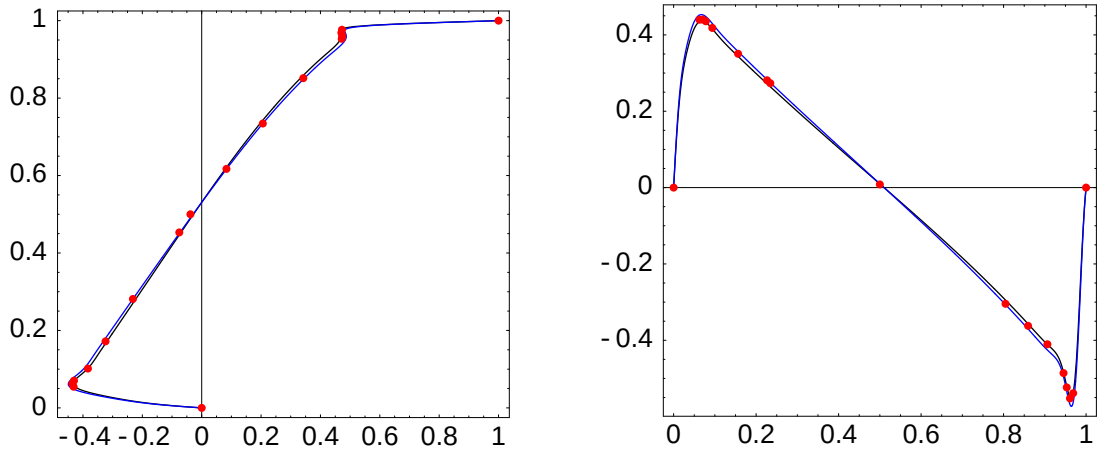

(a) u along vertical center line (plotted (u,y)). (b) v along horizontal center line (plotted (x,v)).

Figure 2.7: Comparison of solutions to the driven cavity flow at Re 7500: black = 256×256, blue = 512×512 grid, red dots = Ghia *et al.*

primary vortex	source	x	y	Ψ	ω
	Ghia *et al.*	0.5117	0.5322	-0.119976	1.87987
	256×256	0.5117	0.5313	-0.116837	-1.83859
	512×512	0.5137	0.5313	-0.121588	-1.93280
top left vortex	source	x	y	Ψ	ω
	Ghia *et al.*	0.0664	0.9141	$2.04620\ 10^{-3}$	-2.15507
	256×256	0.0664	0.9141	$2.05639\ 10^{-3}$	2.12403
	512×512	0.0664	0.9121	$2.11954\ 10^{-3}$	2.20826
bottom left secondary	source	x	y	Ψ	ω
	Ghia *et al.*	0.0645	0.1504	$1.46709\ 10^{-3}$	-1.78511
	256×256	0.0664	0.1484	$1.47007\ 10^{-3}$	1.71136
	512×512	0.0645	0.1523	$1.51950\ 10^{-3}$	1.85549
bottom right secondary	source	x	y	Ψ	ω
	Ghia *et al.*	0.7813	0.0625	$3.28484\ 10^{-3}$	-3.49312
	256×256	0.7891	0.0625	$3.21609\ 10^{-3}$	3.25581
	512×512	0.7910	0.0645	$3.22543\ 10^{-3}$	3.23533
bottom left tertiary	source	x	y	Ψ	ω
	Ghia *et al.*	0.0117	0.0117	$-1.83167\ 10^{-7}$	$1.72980\ 10^{-2}$
	256×256	0.0117	0.0078	$-1.66016\ 10^{-7}$	$-0.89600\ 10^{-2}$
	512×512	0.0098	0.0117	$-1.9043\ 10^{-7}$	$-1.28000\ 10^{-2}$
bottom right tertiary	source	x	y	Ψ	ω
	Ghia *et al.*	0.9492	0.0430	$-3.28148\ 10^{-5}$	$1.41058\ 10^{-1}$
	256×256	0.9531	0.0391	$-3.18379\ 10^{-5}$	$-1.35168\ 10^{-1}$
	512×512	0.9512	0.0410	$-3.28115\ 10^{-5}$	$-1.53600\ 10^{-1}$

Table 2.7: Comparison of vortex properties for the driven cavity flow at Re 7500.

The periodic nature of the flow at $Re\,8500$ on grid 256×256 was confirmed by grid refinement at 512×512. Fourier analysis of history points for the flows found dominant frequencies of 2.64 and 2.76, respectively. This translates to periodicity of about 2.38 and 2.28, respectively ($\frac{2\pi}{freq}$). Pan and Glowinski [44] obtained similar results for this flow at $Re\,8500$ using a projection/wave-like equation method. They report a period of 2.27. The flow at $Re\,8500$ was also studied by Kupferman [45] using a pure stream function formulation, and reported periodic flow of period 2.5.

The quasi-periodic nature of the flow at $Re\,10000$ exhibited on a grid of 256×256 was verified on a 512×512 grid. This was done in the frequency domain by looking at a Fourier analysis of history points along the diagonals of the cavity. The independent frequencies are 1.61 and 2.62 for the 256×256 grid, and 1.73 and 2.74 for the higher resolution grid. These results are consistent with other published results which are presented in context later on.

2.11.3 Poiseuille flow

Another classic fluid flow which is very handy for benchmarking purposes is the fully developed two-dimensional flow between two infinitely long parallel plates. This is one of the few fluid flow problems with an analytic solution. The incoming fluid moves at a constant velocity and the flow has a steady state solution for Reynolds numbers below about 2510 [46]. The flow is driven by a constant pressure gradient P in the direction of the flow, and reaches steady state when the viscous drag along the channel walls balances this force. If the plates are located at $\pm h$, the velocity profile of the fully developed flow has a parabolic profile:

$$\begin{aligned} v(x,y) &\equiv 0\,, \\ u(x,y) &= \frac{PRe}{2}(h^2 - y^2)\,. \end{aligned}$$

Assuming incoming velocity of $u \equiv 1$ and $v \equiv 0$, the pressure gradient can be determined by equating the inflow mass flux to the outflow mass flux:

$$\int_{-h}^{+h} dy = \int_{-h}^{+h} u(y)dy \Rightarrow \frac{PRe}{2} = \frac{3}{2h^2}\,.$$

Figure (2.8) shows the actual and expected u velocity profile for Reynolds number 100 at the outflow boundary. The boundary condition used was a simple linear extrapolation. Table (2.8) verifies second order accuracy in $\triangle x$ for this implementation of the outflow boundary condition.

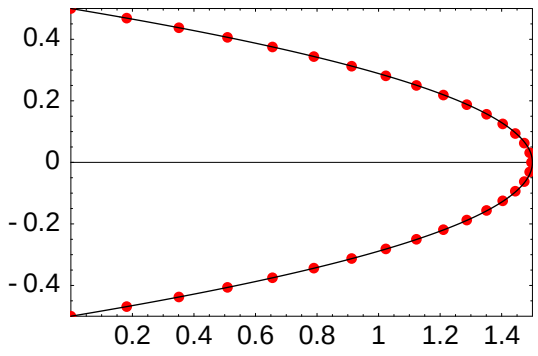

Figure 2.8: Poiseuille flow at $Re\,100$. Red = numerically computed, black = expected parabolic profile.

N	L^1 error	L^1 order	L^2 error	L^2 order	L^∞ error	L^∞ order
8	$1.62897\,10^{-1}$		$3.13700\,10^{-2}$		$4.58880\,10^{-2}$	
16	$0.85273\,10^{-1}$	0.933801	$0.82875\,10^{-2}$	1.92038	$1.92038\,10^{-2}$	1.94364
32	$0.43468\,10^{-1}$	0.972139	$0.21508\,10^{-2}$	1.94605	$0.32020\,10^{-2}$	1.89743

Table 2.8: Poiseuille flow: u at outflow results.

2.11.4 L-shaped cavity

The L-shaped driven cavity flow is a good test for domain decomposition, as well as for comparison with the literature. Oosterlee *et al.* [47] have published benchmarking results for this steady flow for $Re\,100$ and $Re\,1000$ at several grid refinements. Figure (2.9) shows the computational domain for this problem and the lines (a) and (b) which are referenced in later figures. Figure (2.10) illustrates the stream function contours at $Re\,100$ and Figure (2.11) show the same for $Re\,1000$. Figure (2.12) compares the u velocity component at $Re\,100$ along the vertical line (a) in Figure (2.9) (left) and the v velocity component along the horizontal line (b) in Figure (2.9) (right) for grids 128×128 and 256×256 and Oosterlee *et al.* published values at 256×256. Figure (2.13) compares the u velocity component at $Re\,1000$ along the vertical line (a) in Figure (2.9) (left) and the v velocity component along the horizontal line (b) in Figure (2.9) (right) for grids 128×128 and 256×256 and Oosterlee *et al.* published values at 512×512. Finally, Tables

(2.9) and (2.10) compare the location of vortices at several resolutions for $Re\,100$ and $Re\,1000$, respectively.

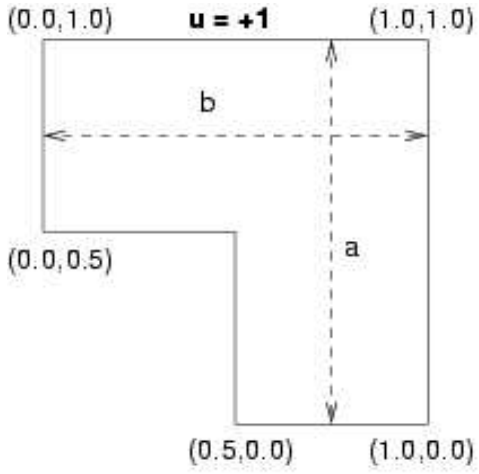

Figure 2.9: Computational domain for the L-shaped driven cavity flow.

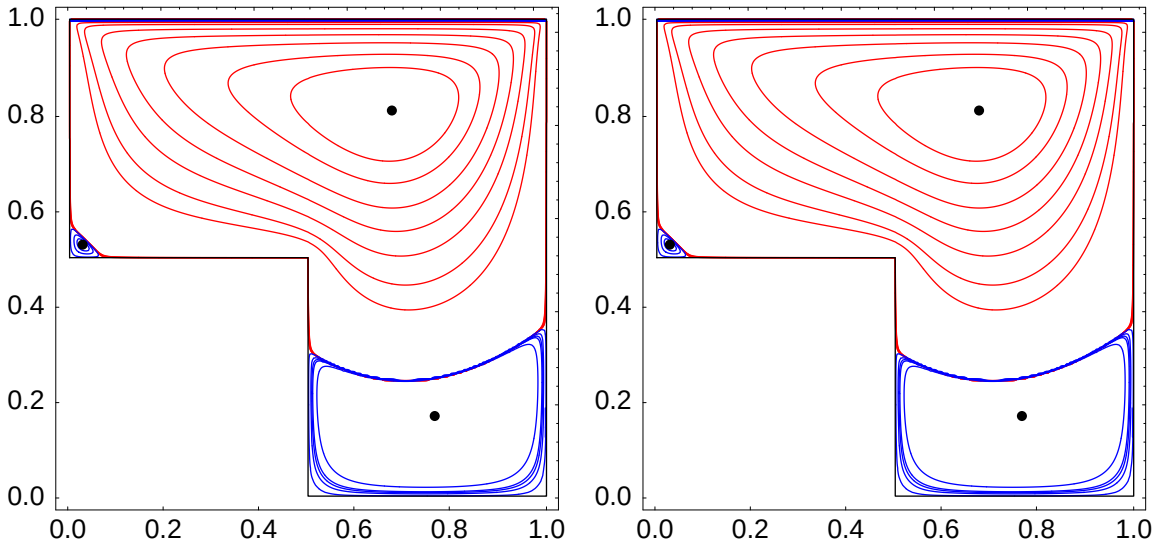

128×128 256×256

Figure 2.10: Stream function contours for $Re\,100$

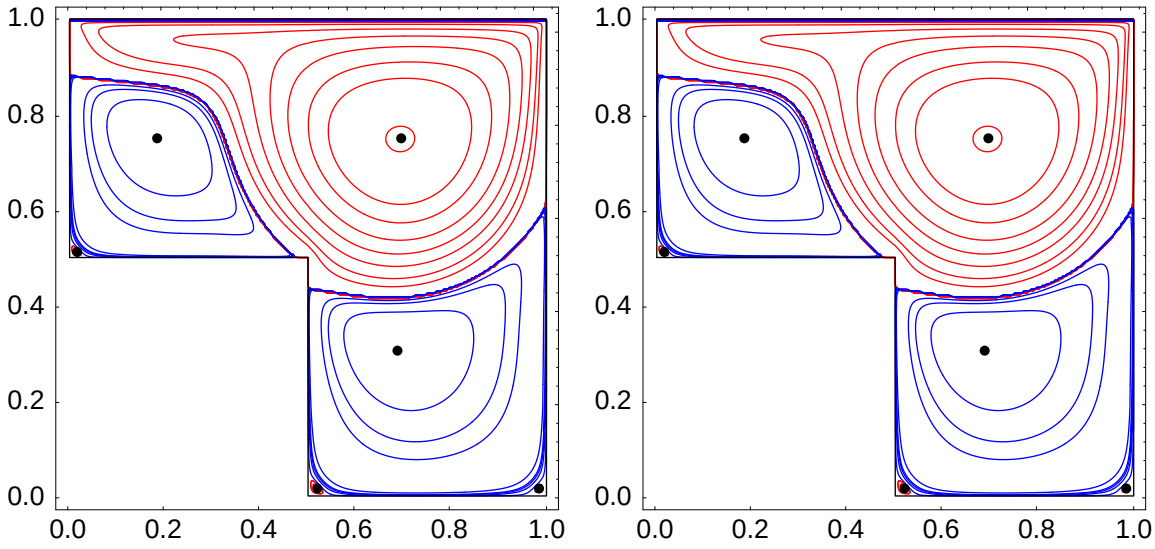

128×128 256×256

Figure 2.11: Stream function contours for Re 1000

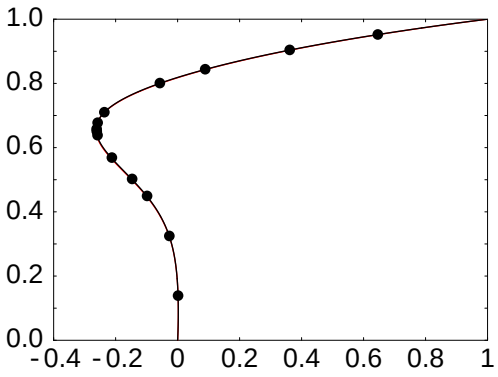

u along vertical line a, plotted (u, y).

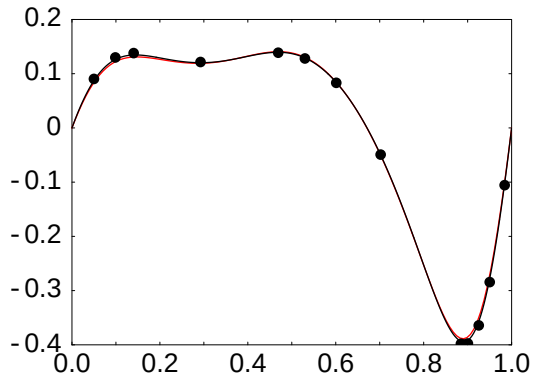

256×256 v along horizontal line b, plotted (x, v).

Figure 2.12: Comparison with Oosterlee *et al.* for Re 100. Red line = 128×128, black line = 256×256, black dots = published values @ 256×256 [47].

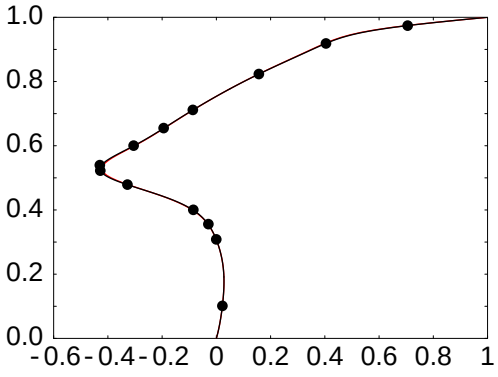

u along vertical line a, plotted (u, y).

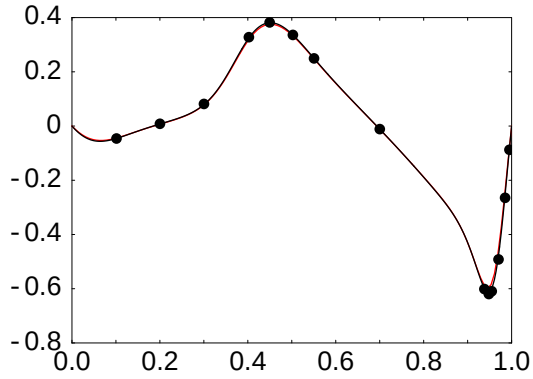

256×256 v along horizontal line b, plotted (x, v).

Figure 2.13: Comparison with Oosterlee *et al.* for Re 1000. Red line = 128×128, black line = 256×256, black dots = published values @ 512×512 [47].

top right vortex	source	x	y	Ψ
	Oosterlee *et al.*, 128×128	0.6763	0.8092	-8.0915 10^{-2}
	128×128	0.6719	0.8047	-8.0809 10^{-2}
	Oosterlee *et al.*, 256×256	0.6734	0.8127	-8.0859 10^{-2}
	256×256	0.6758	0.8086	-8.0882 10^{-2}
bottom right vortex	source	x	y	Ψ
	Oosterlee *et al.*, 128×128	0.7643	0.1747	2.6312 10^{-4}
	128×128	0.7656	0.1641	2.5102 10^{-4}
	Oosterlee *et al.*, 256×256	0.7658	0.1713	2.5814 10^{-2}
	256×256	0.7656	0.1680	2.5298 10^{-4}
top left, secondary	source	x	y	Ψ
	Oosterlee *et al.*, 128×128	——	——	——
	128×128	0.0313	0.5234	2.8672 10^{-6}
	Oosterlee *et al.*, 256×256	——	——	——
	256×256	0.0273	0.5273	2.9238 10^{-6}

Table 2.9: Comparison of vortex properties for the L-shaped driven cavity flow, $Re\,100$.

top right vortex	source	x	y	Ψ
	Oosterlee *et al.*, 128×128	0.6983	0.7464	-8.3419 10^{-2}
	128×128	0.6953	0.7500	-8.3992 10^{-2}
	Oosterlee *et al.*, 256×256	0.6947	0.7488	-8.5392 10^{-2}
	256×256	0.6953	0.7500	-8.4969 10^{-2}
	Oosterlee *et al.*, 512×512	0.6938	0.7509	-8.5425 10^{-2}
bottom right vortex	source	x	y	Ψ
	Oosterlee *et al.*, 128×128	0.6855	0.3009	5.8084 10^{-3}
	128×128	0.6875	0.3047	6.0725 10^{-3}
	Oosterlee *et al.*, 256×256	0.6877	0.3069	6.2503 10^{-3}
	256×256	0.6875	0.3047	6.2295 10^{-3}
	Oosterlee *et al.*, 512×512	0.6868	0.3089	6.2712 10^{-3}
top left, secondary	source	x	y	Ψ
	Oosterlee *et al.*, 128×128	0.1825	0.7525	6.7005 10^{-3}
	128×128	0.1797	0.7500	6.0725 10^{-3}
	Oosterlee *et al.*, 256×256	0.1819	0.7505	6.2021 10^{-3}
	256×256	0.1836	0.7500	6.2295 10^{-3}
	Oosterlee *et al.*, 512×512	0.1822	0.7515	6.4022 10^{-3}
top left, tertiary	source	x	y	Ψ
	Oosterlee *et al.*, 128×128	——	——	——
	128×128	0.0156	0.5078	-2.0703 10^{-7}
	Oosterlee *et al.*, 256×256	——	——	——
	256×256	0.0156	0.5117	-2.3633 10^{-7}
	Oosterlee *et al.*, 512×512	——	——	——
bottom left, tertiary	source	x	y	Ψ
	Oosterlee *et al.*, 128×128	——	——	——
	128×128	0.5156	0.0156	-2.7734 10^{-7}
	Oosterlee *et al.*, 256×256	——	——	——
	256×256	0.5195	0.0156	-2.6953 10^{-7}
	Oosterlee *et al.*, 513×513	——	——	——
bottom right, tertiary	source	x	y	Ψ
	Oosterlee *et al.*, 128×128	——	——	——
	128×128	0.9844	0.0156	-1.4063 10^{-7}
	Oosterlee *et al.*, 256×256	——	——	——
	256×256	0.9844	0.0156	-1.3477 10^{-7}
	Oosterlee *et al.*, 513×513	——	——	——

Table 2.10: Comparison of vortex properties for the L-shaped driven cavity flow, $Re\,1000$.

Early on, I computed a spectral elements solution to the L-shaped cavity at Re 1000 with Nekton, a commercial software package, and compared it with my simulation at the transient stage of flow development. Figure (2.14) shows the grid used for Nekton. Note that each quadrilateral is gridded using polynomial basis functions, so the finite element grid is much finer than it would appear from the diagram. Unfortunately, only copious hard copy remains of those runs, so plots at the standard comparison places (u along $y = .75$ and v along $x = .25$) have been scanned in for visual comparison with my results, Figures (2.15) and (2.16).

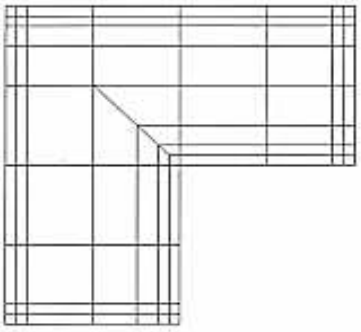

Figure 2.14: Nekton grid for L-shaped driven cavity flow.

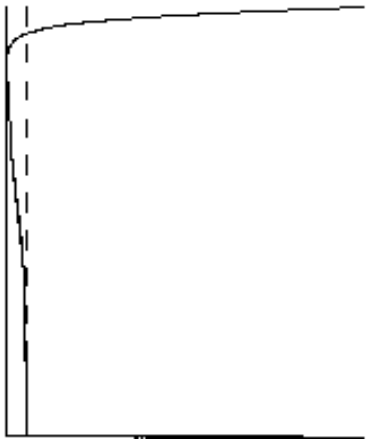

Nekton

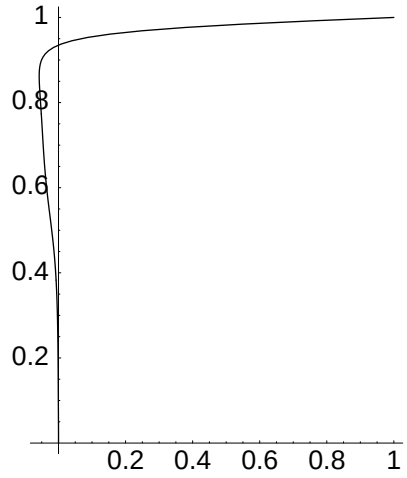

256×256

Figure 2.15: Comparison of u component of transient solution along the vertical line $x = .25$, plotted (u, y) for L-shaped driven cavity flow at $Re\,1000$.

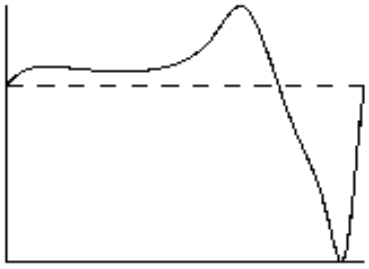

Nekton

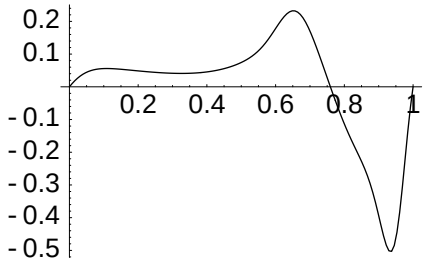

256×256

Figure 2.16: Comparison of v component of transient solution along the horizontal line $y = .75$, plotted (x, v) for L-shaped driven cavity flow at $Re\,1000$.

2.11.5 Backfacing step

The flow past a backfacing step is another well-documented subject of numerical study. Recently there was some controversy over the stability of two-dimensional flow at Reynolds number 800 [48]. That paper found unsteady flow at this value of Re using the spectral element method. This finding was supported by several studies using unsteady finite volume methods [49],[50], but conflicted with previous results which found the flow steady [51]. This prompted an exhaustive exploration of the backfacing step flow at $Re\,800$ by Gresho *et al.* [52] which compared four independent methods and four independent codes, all at adequate grid resolution, and all which find the flow steady at $Re\,800$. At least two more papers used the spectral element method to confirm steady flow at 800 [53],[54]. The criterion for reaching steady state in Gresho's paper is that the change per time step in relative L^1 norm for the velocity vector field be of $O(10^{-7})$. I have used a similar but more stringent criteria of requiring the relative L^2 norm of each velocity component to be less than 10^{-7}. Another important benchmark for this problem is found in Gartling's work [51].

While the problem is that of a step, it is customary to use a rectangular computational domain. The step is modeled by specifying Poiseuille flow on the upper half of the left edge and no-slip boundary conditions on the lower half. Top and bottom are no-slip as well. The domain needs to be large enough so that Poiseuille flow is obtained at the outflow on the right edge. I used a domain of width n and length $30n$ (Figure (2.17)) for $n = 64$ and $n = 128$. My code reached a steady state using mixed upwinding for the convection terms. Figure (2.18) shows the stream function contours for the steady state for $n = 128$. Figure (2.19) shows the vorticity contours. Red contours indicate negative values, blue positive, and black dots mark the vortex locations. The flow at the outlet is not shown (it would look just like Figure (2.8)), but is in excellent agreement with the expected

Poiseuille velocity profile. In previous flow problems, I have used a simple pointwise algorithm for locating minima by checking the neighbors was adequate, but for this flow, it generated two minima very near one another. I found that if I used *Mathematica* to interpolate the stream function field and used the two found minima as initial guesses to *Mathematica*'s "FindMinimum[ ]" module, both guesses led to a common minimum to at least four decimal places. The interpolated extrema for the lower vortex are reported in the comparisons of vortex locations which follow in Table (2.11). Eddy length for both upper and lower eddies as well as separation and reattachment locations are reported in Table (2.12). The separation points were found by locating the zeros of vorticity at the horizontal walls.

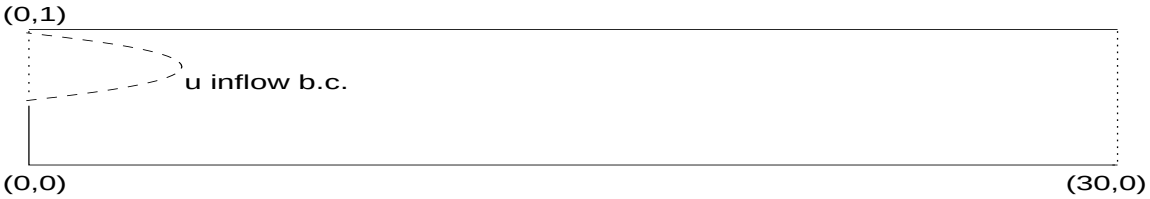

Figure 2.17: Computational domain (not to scale) for flow past a back-facing step.

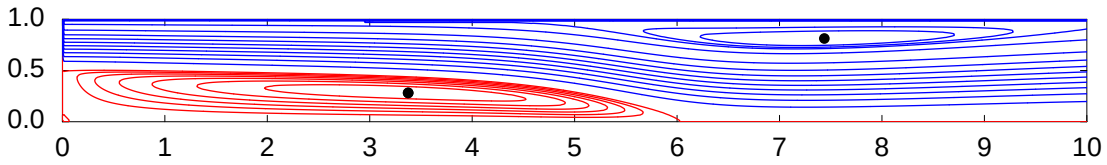

Figure 2.18: Stream function contours for the steady flow past a back-facing step at $Re\,800$ with grid $n = 128$ (partial flow field).

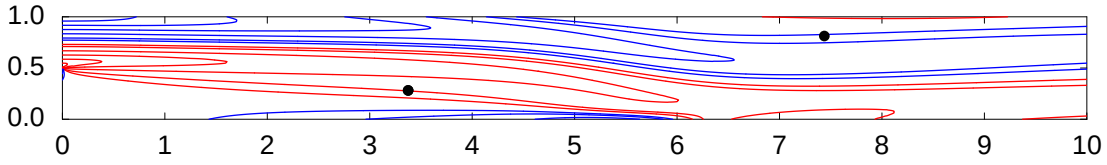

Figure 2.19: Vorticity contours for the steady flow past a back-facing step at $Re\,800$ with grid $n = 128$ (partial flow field).

bottom vortex	source	x	y	Ψ
	Gresho *et al.*	3.375	0.2968	-0.034195
	Gartling	3.350	0.300	-0.0342
	$n = 64$	3.3753	0.2874	-0.033898
	$n = 128$	3.3933	0.2916	-0.034169
top vortex	source	x	y	Ψ
	Gresho *et al.*	7.4375	0.8125	0.506609
	Gartling	7.400	0.800	0.5064
	$n = 64$	7.4688	0.8125	0.506568
	$n = 128$	7.4453	0.8125	0.506389

Table 2.11: Comparison of vortex properties for the flow past a back-facing step, $Re\,800$.

source	lower eddy length	upper eddy start	upper eddy stop	upper eddy length
Gresho *et al.*	6.0817	4.8388	10.4648	5.62597
Gartling	6.10	4.85	10.48	5.63
$n = 64$	6.05240	4.81011	10.45730	5.64722
$n = 128$	6.07566	4.83227	10.48210	5.64988

Table 2.12: Comparison of eddy properties for the flow past a back-facing step, $Re\,800$.

2.11.6 Flow past a square cylinder

Two-dimensional open (as opposed to channel) flows past a bluff body share a common flow development as a function of Reynolds number. The body is often referred to as a cylinder since the problem can be viewed as a two-dimensional projection of a three-dimensional cylinder extruded from the bluff body. The physics involved in this process may be described as follows:

> As a fluid particle flows toward the leading edge of a cylinder, the pressure in the fluid particle rises from the free stream pressure to the stagnation pressure. The high fluid pressure near the leading edge impels flow about the cylinder as boundary layers develop about both sides. However, the high pressure is not sufficient to force the flow about the back of the cylinder at high Reynolds numbers. Near the widest section of the cylinder, the boundary layers separate from each side of the cylinder surface and form two shear layers that trail aft in the flow and bound the wake. Since the innermost portion of the shear layers, which is in contact with the cylinder, moves much more slowly than the outermost portion of the shear layers, which is in contact with the free flow, the shear layers roll into the near wake, where they fold on each other and coalesce into discrete swirling vortices (Perry *et al.*, 1982; Williamson and Roshko, 1988). A regular pattern of vortices, called a *vortex street*, trails aft in the wake [56].

In fact, for Reynolds numbers above unity, the flow separates, and a pair of steady symmetric vortices forms behind the body. The recirculation region grows linearly with Re, but eventually the flow becomes unstable to small disturbances, and the time-periodic vortex street develops. This critical Re is dependent on the shape of the body and is ≈ 50 for the square cylinder. The sharp corners of the square

cylinder ensure that the points at which the flow separates from the body are fixed for a range of Reynolds numbers. Separation occurs at the rear corners for $Re \leq 100$, and at the upstream corners for $Re = 175$. For Re numbers between 100 and 175, the likelihood of separation fore or aft is weighted by its proximity to these Reynolds numbers [6]. While numerical studies can be done in two dimensions for higher Reynolds numbers, the results cannot be corroborated by experiment since Karniadakis and Triantafyllou [55] have shown that the secondary instability mechanism is three-dimensional. Sohankar *et al.* [6] have numerically investigated the transition from 2-D flow to 3-D. Their 3-D simulations indicated stable 2-D laminar shedding at $Re\,150$ but found 3-D effects at $Re\,200$ associated with a spanwise wavelength of approximately five diameters.

The frequency f of the periodic wake flow is incorporated into a dimensionless quantity S, the Strouhal number, defined by $f = \frac{S\,U}{D}$ where U is the free stream flow velocity and D is the cylinder diameter. Typically $U = D = 1$, so the Strouhal number is just the frequency in units of Hertz (cycles per second). There are many factors which can influence numerical results for any flow problem. The Strouhal number is the de facto standard for characterizing wake flows in the periodic shedding regime, but this is complicated by the sensitivity of this quantitative measure to numerical method, boundary conditions, blockage (relative size of bluff body in relationship to the domain size), spatial extent fore and aft of the body, and grid resolution [57]. As mentioned in the DNS chapter 2, I have parameterized the physical domain in alignment with Sohankar's findings with the notable exception of the boundary conditions on the horizontal edges. For benchmarking of the square cylinder flow, I did a numerical simulation at $Re\,100$ with free-slip boundary conditions on those edges to match Sohankar's simulations, and computed a Strouhal number of 0.144, in good agreement with his published value of 0.146 in a grid refinement study [57]. However, when the horizontal edges are set to the

freestream value, my simulations yield a Strouhal number of 0.153, so I expect that this boundary condition will bias all of my Strouhal results to the high side of Sohankar's values. The work of Davis and Moore [58] also used freestream boundary conditions. Their results indicate a Strouhal number of about 0.153 (figure 4 of that publication) for their highest resolution simulation which support this conjecture. Robichaux *et al.* [60] likewise used freestream boundary conditions in a two-dimensional spectral multidomain simulation. They report a Strouhal number of 0.154, a value corroborated by Franke *et al.* [61]. Finally, a more recent publication [59], though using the free-slip boundary conditions, reports a Strouhal number of 0.150 for $Re\,100$, indicative of the difficulty in rigorously pinning down this measure.

Obtaining the Strouhal number from the numerical data is a nontrivial task. I routinely track time series at twenty six points in the wake at the centerline and lines through the top and bottom edges of the square. For each time series, I calculate the frequency in three ways:

- the inverse of the period which has been calculated by correlation in the DNS code prior to the POD,
- Fourier transform with *Mathematica*-interpolated intermediate points such that the dominant frequency does not change when the number of bins used for the transform doubles,
- least squares estimation for the dominant frequency which assumes a "sinusoid plus constant" model [62].

The least squares estimation generates a function $R(w)$ which attains its maximum value when $w =$ the dominant frequency. Assuming discrete data $x_i = x(t_i), i = 0, \cdots, n$ (n even) of the (a priori) functional form

$x(t) = \mu + A\cos(\omega t) + B\sin(\omega t)$ where μ, α, β and ω are unknown:

$$\begin{aligned}
\tilde{\mu} &= (\sum_{i=0}^{n-1} x_i)/n\,, \\
\tilde{A}(\omega) &= 2(\sum_{i=0}^{n-1}(x_i - \mu)\cos(\omega t))/n\,, \\
\tilde{B}(\omega) &= 2(\sum_{i=0}^{n-1}(x_i - \mu)\sin(\omega t))/n\,, \\
\tilde{R}(\omega)^2 &= \tilde{A}(\omega)^2 + \tilde{B}(\omega)^2\,.
\end{aligned}$$

The best value for ω maximizes $\tilde{R}(\omega)^2$. Using an initial guess for ω defined by the inverse of the DNS-calculated period, a refined value for the frequency is then determined with *Mathematica*'s "FindMinimum[ ]" function applied to $-\tilde{R}(\omega)^2$. I get 100% agreement at all history points for *all* of these measures for the square cylinder simulations done for Reynolds numbers 55 to 100.

3 Proper Orthogonal Decomposition: Method and Application

Finding the optimal basis for a linear decomposition of a data set is relevant to many fields in mathematics and science. The Karhunen-Loève decomposition was initially proposed (independently) by Karhunen [15] in 1946 and Loève [16] in 1955, The method is known by different names depending on the field of study [17]. Principal component analysis, Proper Orthogonal Decomposition, empirical eigenfunction decomposition, and singular value decomposition are a few of the alternate names for equivalent procedures. This procedure has found application in the fields of random variables, image processing, signal analysis, data compression, process identification and control in chemical engineering, and oceanography as well as fluid mechanics [1]. The goal of identifying the major patterns or coherent structures in fluid flow is a perfect application for the Proper Orthogonal Decomposition (POD). As we shall see, this procedure extracts a hierarchical set of both temporal and spatial eigenfunctions ranked by their contribution to the total flow dynamics.

3.1 Background

There are many ways to choose an orthonormal set of basis functions for the purpose of a space/time decomposition of a spatial time series such as the simulation sampled data. The 2-d Fourier transform is one such option. However, the representation would be much more efficient if the basis functions were determined from the statistical properties of the data itself, rather than being forced upon the data a priori. The Karhunen-Loève (KL) method, which is the foundation for the Principal Orthogonal Decomposition, does just that, and earns the reputation of being the best approximation to the data. "Best" in this context means that for any given number of basis functions it has a smaller mean square

error than a comparable representation using any other set of basis functions.

The simple idea behind this method is the fact that a real symmetric nonsingular matrix $\mathbf{C}$ can be diagonalized by a special orthonormal matrix $\mathbf{W}$ such that $\mathbf{W}^T\mathbf{C}\mathbf{W} = \mathbf{D}$ where $\mathbf{D}$ is a diagonal matrix. The columns of $\mathbf{W}$ are the normalized eigenvectors of $\mathbf{C}$ and the diagonal entries of $\mathbf{D}$ are the eigenvalues of $\mathbf{C}$. Moreover, the eigenvectors form an orthogonal basis, hence are uncorrelated, thereby maximizing the information content in each and minimizing redundancy. The covariance matrix of a data set is the real symmetric matrix used for the KL procedure.

3.2 Procedure

One can look at the application of this method in two ways: find the eigenstructure of the spatial covariance matrix or of the temporal covariance matrix. The eigenvalues are equivalent and there is a simple relationship between the eigenvectors of both covariance matrices, but the magnitude of the two problems is not necessarily equivalent. It is usually more tractable to use the temporal covariance matrix (of dimension $M \times M$, where M is the number of snapshots) because it is usually the case that there are many more grid points than snapshots. The i^{th} eigenvector corresponds to the coefficients for a linear combination of snapshots to form the i^{th} principal spatial orthogonal component. If there is redundancy in the data, the number of significant eigenvalues will be less than M, and only those corresponding eigenvectors are used, producing less than M principal components.

3.3 Justification

Given a computational domain with a spatial discretization of

$$(x_i, y_j)\,,\ i = 1, \ldots, n_x,\ j = 1, \ldots, n_y,\ ,$$

and a temporal discretization $t_i, i = 1, \ldots, M$, let u and v be the x and y velocities, respectively.

$$\begin{aligned}
\text{Let } \mathbf{x} &= \left((x_1, y_1)\,(x_2, y_1) \cdots (x_{n_x}, y_1)\,(x_1, y_2) \cdots (x_{n_x}, y_2) \cdots (x_{n_x}, y_{n_y})\right)^T, && (3.1)\\
\mathbf{U}_i &= \left(u(\mathbf{x}, t_i)\, v(\mathbf{x}, t_i)\right)^T \in \mathbb{R}^N, i = 1, M\,, && (3.2)\\
\mathbf{V}_i &= \mathbf{U}_i - \langle \mathbf{U}_i \rangle\,, && (3.3)\\
\mathbf{V} &= (\mathbf{V}_1\, \mathbf{V}_2 \cdots \mathbf{V}_M)\,. && (3.4)\\
\text{Then } \mathbf{S} &= \mathbf{V}\,\mathbf{V}^T \in \mathbb{R}^{N \times N}\,, \text{where } n_x * n_y = \frac{N}{2}\,. && (3.5)
\end{aligned}$$

$\mathbf{S}$ is a real symmetric positive semidefinite matrix, so it can be diagonalized, and its eigenvectors correspond to the spatial eigenfunctions.

However, note that $\mathbf{V}^T\,\mathbf{V} \in \mathbb{R}^{M \times M}$ is also a real symmetric positive semidefinite matrix, and typically $M \ll N$. It would be a huge computational advantage to solve the eigenstructure of this matrix as opposed to $\mathbf{V}\,\mathbf{V}^T$, and it will be shown that this approach will provide the needed information.

Suppose $\lambda_i, \boldsymbol{\theta}_i$, $i = 1, \cdots, M$ are the eigenvalues and eigenvectors, respectively, of $\mathbf{V}^T\,\mathbf{V}$. Then $\mathbf{V}^T\,\mathbf{V}\,\boldsymbol{\theta}_i = \lambda_i \boldsymbol{\theta}_i \Rightarrow (\mathbf{V}\,\mathbf{V}^T)\,(\mathbf{V}\,\boldsymbol{\theta}_i) = \lambda_i\,(\mathbf{V}\,\boldsymbol{\theta}_i)$. Note that the eigenvalues of $\mathbf{V}\,\mathbf{V}^T$ and $\mathbf{V}^T\,\mathbf{V}$ are the same, λ_i.

Normalize $\boldsymbol{\theta}_i$ and let $\boldsymbol{\theta} = (\boldsymbol{\theta}_1\, \boldsymbol{\theta}_2 \cdots \boldsymbol{\theta}_M)$. Define $\boldsymbol{\Phi} = \mathbf{V}\,\boldsymbol{\theta}$.

$$\text{Let } \mathbf{D} = \begin{pmatrix} \lambda_1 & 0 & \cdots & 0 \\ 0 & \lambda_2 & \cdots & 0 \\ \vdots & \vdots & \vdots & \vdots \\ 0 & 0 & \cdots & \lambda_M \end{pmatrix},$$

so $\mathbf{V}^T\,\mathbf{V}\,\boldsymbol{\theta} = \mathbf{D}\,\boldsymbol{\theta}$. Then $\boldsymbol{\Phi}^T\,\boldsymbol{\Phi} = \boldsymbol{\theta}^T\,\mathbf{V}^T\,\mathbf{V}\,\boldsymbol{\theta} = \mathbf{D}$. Thus, the column vectors of $\boldsymbol{\Phi} = \boldsymbol{\Phi}_i$ are orthogonal and $\|\boldsymbol{\Phi}_i\|^2 = \lambda_i$. $\boldsymbol{\Phi} = \mathbf{V}\,\boldsymbol{\theta}$ implies that each $\boldsymbol{\Phi}_i$ can be

expressed as a linear combination of $\mathbf{V}_i$ (so in particular, $\mathbf{\Phi}_i$ are divergence-free if $\mathbf{V}_i$ are). $\mathbf{\Phi} = \mathbf{V}\,\boldsymbol{\theta}$ further implies that $\mathbf{V} = \mathbf{\Phi}\,\boldsymbol{\theta}^T$ so each $\mathbf{V}_i$ is a linear combination of vectors $\mathbf{\Phi}_i$ with coefficients given by the columns of $\boldsymbol{\theta}^T$, *i.e.*, the rows of $\boldsymbol{\theta}$.

Therefore,

$$\mathbf{V}_i = \sum_{j=1}^{M} \theta_{ij}\,\mathbf{\Phi}_j\,, \tag{3.6}$$

$$\text{normalizing } \mathbf{\Phi}_j, \qquad = \sum_{j=1}^{M} \sqrt{\lambda_j}\,\theta_{ij}\,\mathbf{\Phi}_j\,, \tag{3.7}$$

where $\boldsymbol{\theta}_i$ are the normalized temporal eigenfunctions and $\mathbf{\Phi}_i$ are the normalized spatial eigenfunctions.

It is a fact that the matrix $\mathbf{V}\,\mathbf{V}^T$ has N eigenvalues while matrix $\mathbf{V}^T\,\mathbf{V}$ has only M eigenvalues, $M \ll N$. Has information been lost by solving the dual problem? The intuitive answer is "no" because only M data vectors were used to calculate $\mathbf{V}$, and this is indeed the case. This can be proved by looking at the singular value decomposition of $\mathbf{V}$ and $\mathbf{V}^T$ (*e.g.* [63]). Let $\mathbf{W}$ and $\mathbf{Z}$ be unitary matrices such that

$$\mathbf{W}^T\,\mathbf{V}\,\mathbf{Z} = \begin{pmatrix} \mathbf{\Sigma} & 0 \\ 0 & 0 \end{pmatrix} \in \mathbb{R}^{N\times M}\,, \tag{3.8}$$

where $\sigma_i, i = 1, n$ are the (unique) singular values of $\mathbf{V}$ and

$$\mathbf{\Sigma} = \mathbf{I}\,\left(\sigma_1\sigma_2\,\cdots\,\sigma_n\right)^T \in \mathbb{R}^{n\times n}\ .$$

Taking the transpose of each side,

$$\mathbf{Z}^T\,\mathbf{V}^T\,\mathbf{W} = \begin{pmatrix} \mathbf{\Sigma} & 0 \\ 0 & 0 \end{pmatrix} \in \mathbb{R}^{M\times N}\,. \tag{3.9}$$

multiplying matrices (3.8) and (3.9),

$$\Rightarrow \quad \mathbf{W}^T \mathbf{V} \mathbf{V}^T \mathbf{W} = \begin{pmatrix} \mathbf{\Sigma}^2 & 0 \\ 0 & 0 \end{pmatrix} \in \mathbb{R}^{N \times N}, \tag{3.10}$$

$$\text{and} \quad \mathbf{Z}^T \mathbf{V}^T \mathbf{V} \mathbf{Z} = \begin{pmatrix} \mathbf{\Sigma}^2 & 0 \\ 0 & 0 \end{pmatrix} \in \mathbb{R}^{M \times M}, \tag{3.11}$$

i.e., the nonzero eigenvalues of $\mathbf{V}\mathbf{V}^T$ and $\mathbf{V}^T\mathbf{V}$ are the same. This method of calculating the POD is known in the literature as the "snapshot" method [64].

3.4 Properties

To summarize some of the important properties of the POD, given a data set $\mathbf{u}(\mathbf{x}, t)$, spatial basis functions $\mathbf{B}_i(\mathbf{x})$ and corresponding temporal functions $a_i(t), i = 1, N$:

- The POD choice $a_i = y_i$ and $\mathbf{B}_i = \mathbf{\Phi}_i$ minimizes the reconstruction error $\langle \|\mathbf{u}(\mathbf{x}, t) - \sum_{i=1}^{M} a_i(t)\mathbf{B}(\mathbf{x})\|^2 \rangle$ for any level of truncation $M \leq N$; more precisely, the error is smaller than the square root of the $(M+1)^{st}$ eigenvalue [4].

- If $\mathbf{C}$ is the covariance matrix derived from $\mathbf{U}(\mathbf{x}, t)$ with eigenvalues $\lambda_i, i = 1, N$, then $\sum_{j=1}^{M} \lambda_i = \text{Trace}(\mathbf{C})$ represents the average, unsteady energy in the data set and is invariant under the KL decomposition.

- λ_i is the relative energy associated with principal component i so for a given number of modes, the POD maximizes the captured energy.

- The transformation is invertible, which means that each original snapshot can be written as a linear combination of the POD components.

- In particular, if the solution vectors are divergence-free, then so are the POD components.

The spatial fields $\mathbf{\Phi}_i$ may also be interpreted as a quantitative representation of the coherent structures in the flow. The eigenvalue of each field indicates the importance of that component to the average unsteady energy of the flow. For non-turbulent flows, most of the eigenvalues are close to zero, so one can obtain a significantly simpler representation of the flow, as well as a space/time decoupling.

3.5 Technical note: implementation details

The DNS is run at a fixed time step, and flow field "snapshots" of velocity components **u** and **v** are stored to disk at regular intervals for a total of $M+1$ snapshots. The time step and sampling interval are chosen such that the first and last snapshots are nominally the same, *i.e.*, full periods of data are collected. The mean is computed and subtracted from the snapshots. The mean and mean-free snapshots are then sampled to a uniform grid of size $nx+1 \times ny+1$. This constitutes the input to the KL method. The KL code computes the covariance matrix as $\frac{1}{M}\sum_{i=1}^{nx+1}\sum_{j=1}^{ny+1}(u_{ij}^2+v_{ij}^2)$. The factor $\frac{1}{M}$ is included so that the eigenvalues represent the average kinetic energy in the data ensemble and are independent of M. My software is written in the "C" programming language, but the workhorse is a Fortran module "RS" from Argonne National Laboratory that computes the complete eigenstructure of a real symmetric matrix. I normalize the eigenvectors such that they too are independent of the number of snapshots used. $\|\boldsymbol{\theta}_k\|^2 = \frac{1}{M}\sum_{i=1}^{M}\theta_{ki}^2$. The spatial eigenfunctions can be normalized similarly. Letting u and v represent the u and v components of $\mathbf{\Phi}_k$: $\|\mathbf{\Phi}_k\|^2 = \sum_{i=1}^{nx+1}\sum_{j=1}^{ny+1}(u_{ij}^2+v_{ij}^2)$. This is fine in theory, but jumping ahead a bit, problems arise. A goal is to derive a parameterized system of ODEs that are amenable to parameter continuation with the well-established and respected software package, AUTO [65]. The system of

ODEs has the form:

$$\frac{dy_k}{dt} = a_k + \sum_{i=1}^{N} b_{ki} y_i + \sum_{i=1}^{N} \sum_{j=1}^{N} c_{kij} y_i y_j \tag{3.12}$$

Suppose we uniformly change the scaling of the $\mathbf{y}$, e.g., $y_k = \alpha\, Y_k$. Then the system of ODEs for $\mathbf{Y}$ is:

$$\frac{dY_k}{dt} = \frac{a_k}{\alpha} + \sum_{i=1}^{N} b_{ki} Y_i + \sum_{i=1}^{N} \sum_{j=1}^{N} \alpha\, c_{kij} Y_i Y_j \tag{3.13}$$

AUTO is sensitive to the value of α. I was unable to obtain convergence even with extremely small step sizes for some values of α. However, it is a simple matter to scale the spatial eigenfunctions by $\frac{1}{\sqrt{nx\, ny}}$ and the temporal eigenfunctions by $\sqrt{nx\, ny}$ and avoid problems with AUTO.

There are other issues that arise in the application of the POD when one wants to compare eigenfunctions derived at different Reynolds numbers for a given flow problem. The eigenvectors of the covariance matrix are only uniquely determined up to sign. A change in sign in temporal eigenfunction $\boldsymbol{\theta}_i$ will propagate to the spatial eigenfunction $\boldsymbol{\Phi}_i$. This situation can be detected by a negative correlation coefficient between the corresponding spatial eigenfunctions or a 180 degree phase shift in the corresponding temporal eigenfunctions. The latter can be difficult to observe in practice, however, since the temporal eigenfunctions need not be in phase. Visual inspection of the stream function plots from the spatial eigenfunctions with discrimination of negative and positive values can also be very helpful.

As we shall see, the eigenfunctions are logically paired, and pairs of eigenvalues can be quite close in value. Sometimes the ordering at one Reynolds number will differ from that at another Reynolds number due to an ambiguity in the hierarchy. This situation can also be detected by the spatial correlation coefficient. For instance, if spatial eigenfunctions one and two are highly correlated with the

corresponding eigenfunctions at a different Reynolds number, but the correlation of three and four, respectively, is extremely poor, one might suspect that swapping eigenfunctions three and four at one of the Reynolds number could be required. Note that swapping must also occur for the corresponding temporal eigenfunctions and the eigenvalues.

3.6 Application to the driven cavity flow

3.6.1 Data collection and analysis

Direct numerical simulation (DNS) data was uniformly sampled for three periods at Reynolds numbers 8500, 9000, 9500, 9600, 9700, 9800, and 9900. At Re 10000 the flow is quasi-periodic. Two cycles of data were collected, where a cycle is defined as the approximate repeat time. A cycle in this case is approximately thirteen times the period at the lower Reynolds numbers. Figure (3.1) summarizes the DNS data through the kinetic energy time series, computed as $0.5 \triangle x \triangle y \sum_{i=1}^{nx} \sum_{j=1}^{ny} (u_{ij}^2 + v_{ij}^2)$. These plots shows the periodic nature of the flow through Re 9900, the quasi-periodic flow at Re 10000, and the linear dependence of total kinetic energy with Reynolds number. In the following discussion of POD results, the factor $0.5 \triangle x \triangle y$ is needed to convert the eigenvalues into kinetic energy as defined above.

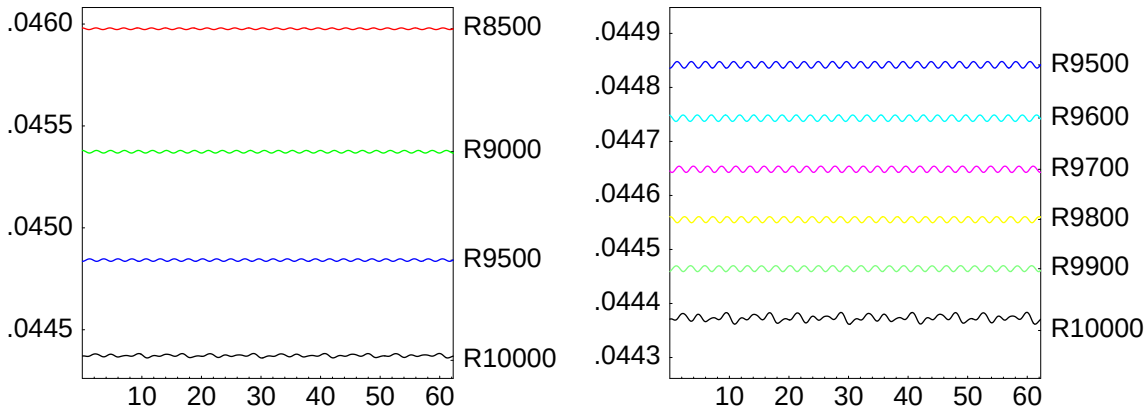

$Re 8500 - 10000$ $Re 9500 - 10000$, rescaled y to show detail.

Figure 3.1: Kinetic energy time series from DNS data.

The wealth of data collected near Re 10000 was done to try to establish the point where the flow bifurcates from periodic to quasi-periodic for comparison with the dynamical system results presented in Chapter 5. The mean flow was computed and subtracted from the sampled data. The data was then resampled from the staggered grid to a uniform grid[6].

3.6.2 Interpretation

Fifty snapshots per period for three periods was collected for ingest into the POD for the periodic flows and 650 snapshots per cycle for two cycles for the quasi-periodic flow. The choice to maintain uniformity in the number of snapshots across Reynolds number for the POD means that the variation of period with Reynolds number is not represented in the temporal eigenfunctions. In snapshot time, all the periodic flows have a period of 50. We shall see the utility of this decision in Chapter 5. For the periodic flows, the temporal eigenfunctions correspond largely to the primary frequency and its harmonics. For the quasi-periodic flow, this is no longer the case, although the first two temporal eigenfunctions inherit the frequency peak of its periodic counterparts. Figure (3.2) illustrates the first and third temporal eigenfunctions for Re $8500, 9000, 9500, 9900$ and 10000. For the periodic flows, they are virtually identical. The even eigenfunctions are simply phaseshifts of the odd ones because the dynamics really correspond to a system of 2^{nd} order ODEs to capture the rotational motion in the driven cavity. In fact, even at Re $9900, 96\%$ of the energy is accounted for by the first pair of modes, and at Re 10000 those *same* modes still capture 89% of the

[6]Code was also developed for doing the POD on a staggered grid, thereby generating spatial eigenfunctions on a staggered grid. This was done to see if more accuracy would be achieved in the dynamical system coefficients by doing the numerical differentiation on a staggered grid. This did not turn out to be the case (second order methods were employed in both scenarios). In addition, I think the covariance matrix is more authentic when done with the resampled data. For example, a zero boundary condition is implemented on a staggered grid by requiring the average to be zero, but this would make a positive contribution to the covariance matrix.

energy of the motion. The gross features of the flow at this range of Reynolds numbers are modeled well by a linear oscillator, as noted in Podvin *et. al* [70] for the differentially heated cavity in the same dynamical regime. The Fourier spectrum is a convenient way to compare the temporal signatures since they are usually not in phase. The periodic data has been repeated to achieve the same data length as needed for the quasi-periodic data, 1300 points corresponding to two full cycles of the quasi-periodic flow and 26 full periods of the periodic flows. At Re 10000, the very first temporal eigenfunction reveals a new frequency as the secondary mode, occurring at wavenumber 16, not a harmonic of the primary wavenumber at 26. To get a better picture of the frequency spectrum at Re 10000, it is helpful to look at the Fourier spectrum of the sum of the temporal eigenfunctions weighted by the square root of the corresponding eigenvalue (which is its magnitude). From this information, presented in Figure (3.3), it is evident that the fundamental frequencies occur at modes 26 and 16. All other representatives in the Fourier spectrum can be expressed as linear combinations of these two wavenumbers. Adjusting for time T (DNS simulation time for this time period is $\langle \#\ steps \rangle \times \Delta t \times$ (2 cycles) $= 39001 * .0008 * 2$), the corresponding frequencies ($2\,\pi$ wavenumber$/T$) are ≈ 2.6 and ≈ 1.6. Cazemier's [8] DNS simulations at Re 10000 exhibited frequencies of ≈ 2.7 and ≈ 1.7, in good agreement with these results. Those runs were done at higher spatial and temporal accuracy. I have done DNS runs at Re 10000 on a 512×512 grid to verify that the quasi-periodicity is grid-independent. Comprehensive results on the Fourier spectrum of time series taken at points along the cavity diagonals (Chapter 2, page 31) yield a primary frequency at 2.74 and a secondary frequency of 1.73, an even better match to Cazemier's results. DNS runs at 512 x 512 for Re 8500 also corroborated the Hopf bifurcation frequency of ≈ 2.7.

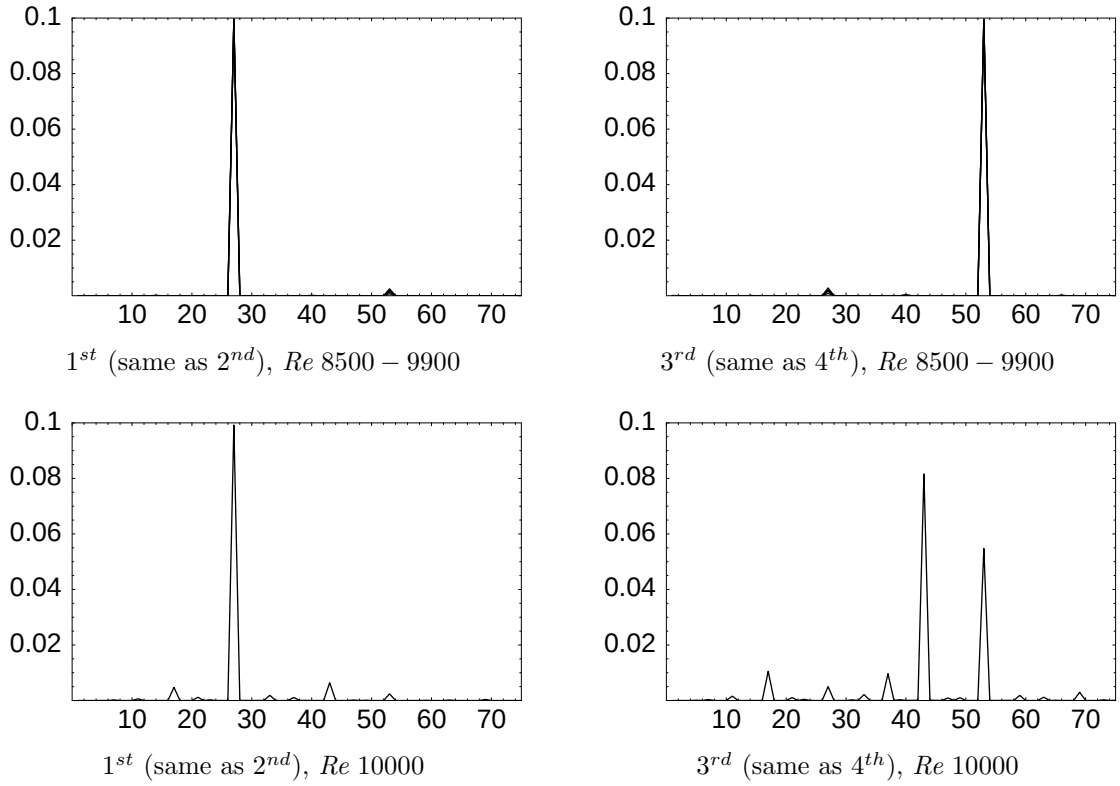

Figure 3.2: Fourier spectrum of significant temporal eigenfunctions for the driven cavity flow, Re $8500 - 10000$, bin # of 1300 on x axis.

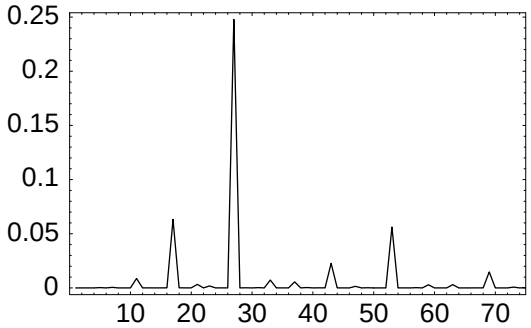

Figure 3.3: Fourier spectrum of the sum of the significant temporal eigenfunctions at Re10000 weighted by the square root of the corresponding eigenvalues

Figure (3.4) shows the variation of period with Reynolds number for the range 8500 - 9900. This information has not been captured in the temporal eigenfunctions (by choice), but nevertheless will be incorporated into the low-dimensional model to come. It is useful to note the clear linear relationship which will play a role later on.

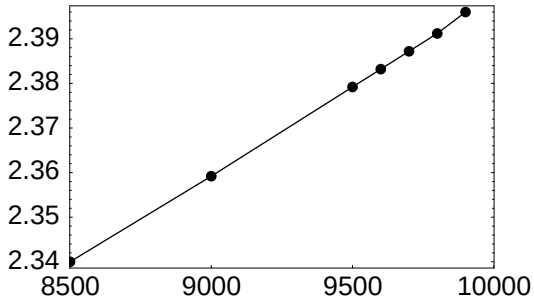

Figure 3.4: Variation of period with Reynolds number for the driven cavity flow (dots mark the DNS data).

Projections onto pairs of the temporal eigenfunctions (Figures (3.5) and (3.6)) illustrate how the pairs of eigenfunctions constitute a periodic cycle. For Re 9000 the first pair complete a closed curve in 50 snapshots. At Re 10000, it takes 13 orbits to reach closure, but the path closely resembles that at Re 9000. The story is entirely different for eigenfunctions 3 and 4. They constitute the first harmonic for Re 9000 and make 2 loops in 50 snapshots before returning to the starting value. In contrast, the temporal behavior at Re 10000 captured by eigenfunctions 3 and 4 is quite complex as it features two independent frequencies from a strongly bimodal spectrum.

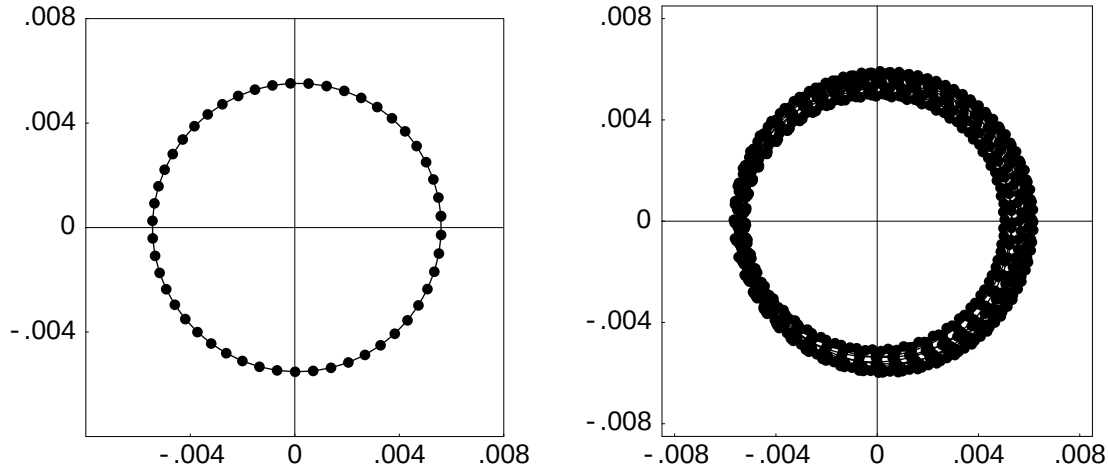

Figure 3.5: Projection on eigenvectors 1 & 2 for Re 9000 (left) and Re 10000 (right) $((\theta_1(t), \theta_2(t)))$.

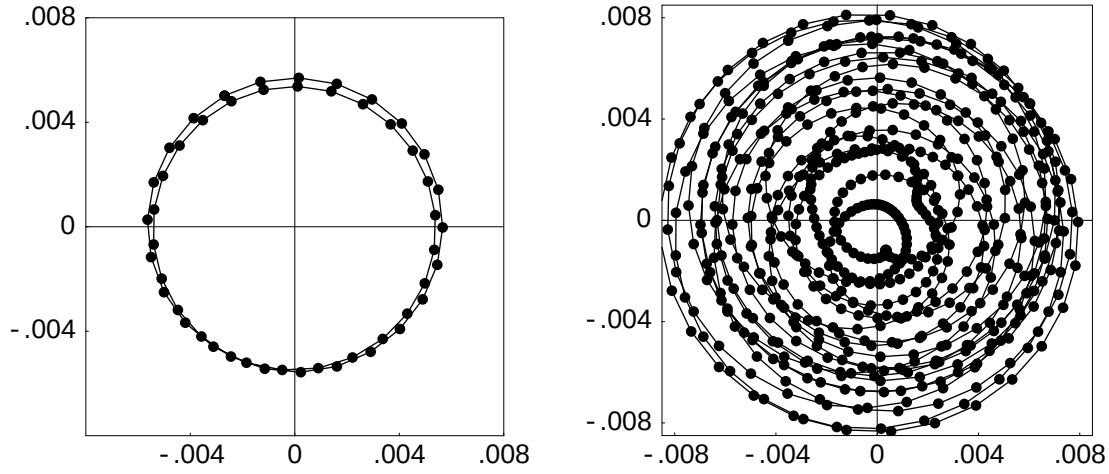

Figure 3.6: Projection on eigenvectors 3 & 4 for Re 9000 (left) and Re 10000 (right) $((\theta_3(t), \theta_4(t)))$.

The eigenvalues show the distribution of energy. Figure (3.7) shows how the total amount of unsteady energy changes with Reynolds number. This is computed from the POD data as the sum of the eigenvalues. The line connects the POD values and the dots show the average unsteady kinetic energy from the DNS runs, which when scaled by $0.5 \triangle x \triangle y$ are consistent with the POD energy results. The Reynolds number where the unsteady energy is zero corresponds to the critical Re where the flow bifurcates from a steady to a periodic flow, known as a Hopf bifurcation. The linear trend of the data makes sense for a Hopf bifurcation and will be discussed in the next chapter on dynamical systems. Figure (3.8) plots the energy in the mean flow versus Reynolds number. This pair of figures shows dramatically just how small the energy content of the unsteady motion is, and perhaps explains why the driven cavity flow was considered to be steady even at Re 10000 for so long.

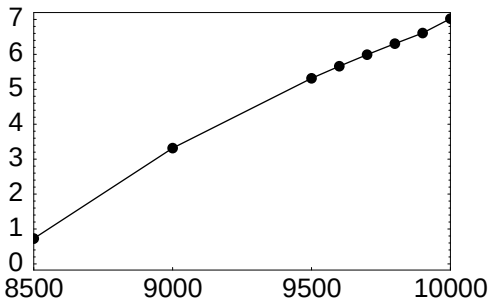

Figure 3.7: average unsteady "kinetic energy"

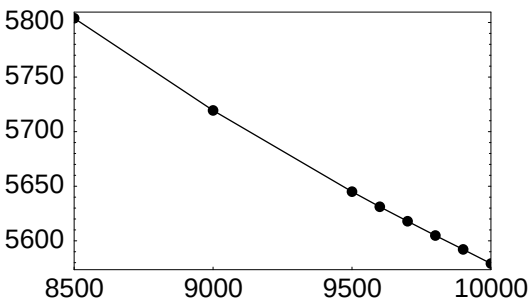

Figure 3.8: mean "kinetic energy"

Figure (3.9) plots the fractional portion of the total unsteady energy in each of the first six POD modes, and illustrates how the distribution of energy changes with increasing Reynolds number.

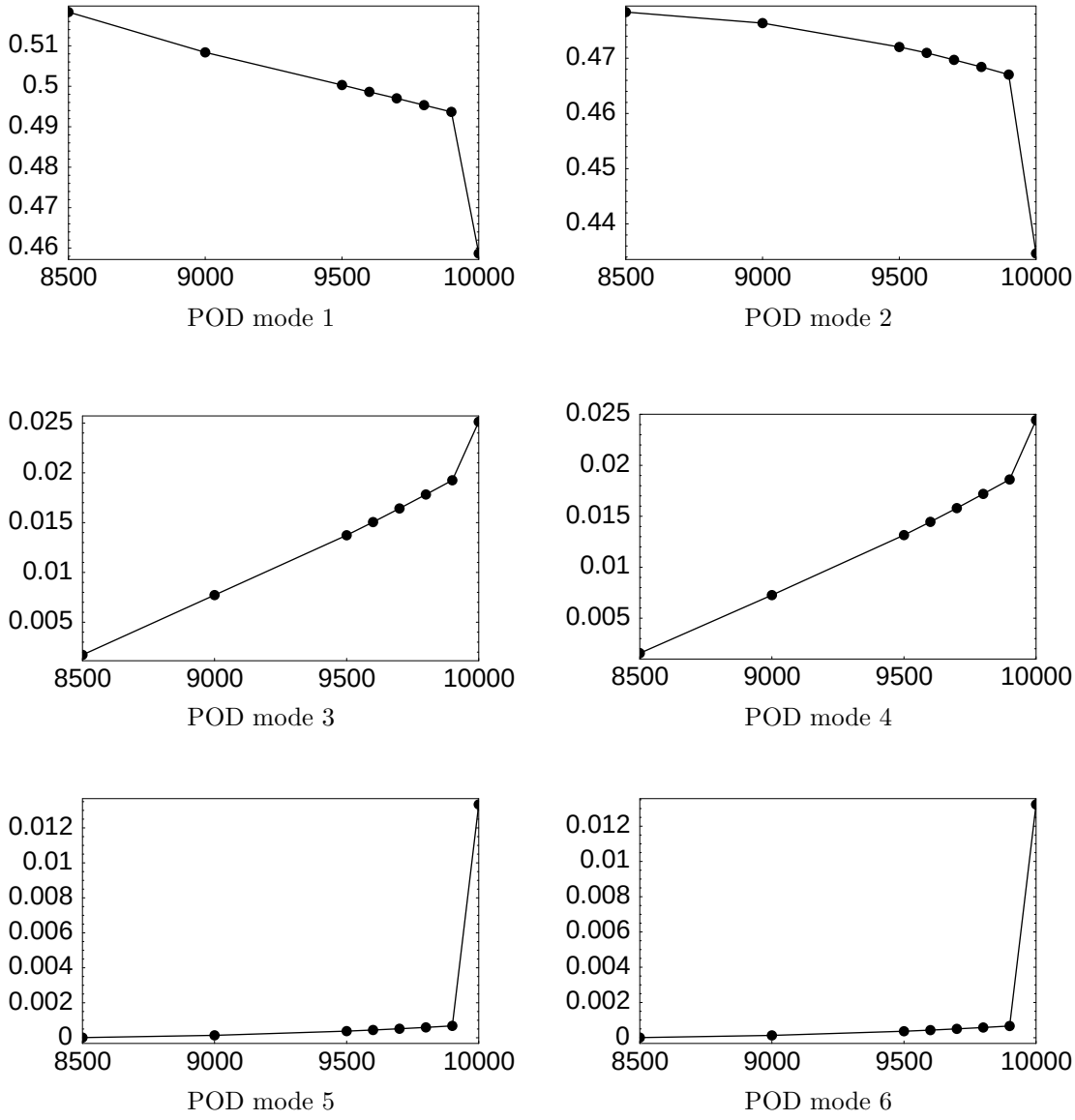

Figure 3.9: Fractional portion of energy per POD mode versus Reynolds number

There is a clear linear transfer of the allotment of energy from the primary modes to the higher order modes up to the point where the flow characteristics change dramatically ($Re\,10000$). This observation will be helpful in characterizing the changes that occur in the dynamical systems as the Reynolds number increases.

The spatial eigenfunctions $\mathbf{\Phi}_i$, including the mean as $\mathbf{\Phi}_0$[7] , share the same similarities as the temporal eigenfunctions: for the *Re* range of $8500 - 9900$, they have common structure, and for *Re* 10000, the first two spatial modes are quite similar to the primary modes of the periodic flow. This structure is best seen by visualizing the stream function from the component fields in the spatial eigenfunctions, so similarity measures have been applied to the stream function of the eigenfunctions rather than the eigenfunctions themselves. The similarity of the spatial fields has been quantized by calculating the percent error incurred by approximating one field by another, and by computing the cross-correlation coefficient, *ccorr*.

Let $\mathbf{\Psi}_i$ and $\mathbf{\Psi}_j$ be two spatial fields representing the stream function for spatial eigenfunctions $\mathbf{\Phi}_i$ and $\mathbf{\Phi}_j$ respectively, and $\|.\|$ is the L^2 norm.

$$\%error = \frac{\|\mathbf{\Psi}_i - \mathbf{\Psi}_j\|}{\|\mathbf{\Psi}_j\|}, \tag{3.14}$$

$$ccorr = \frac{\langle \mathbf{\Psi}_i, \mathbf{\Psi}_j \rangle}{\|\mathbf{\Psi}_i\| \, \|\mathbf{\Psi}_j\|}. \tag{3.15}$$

Note that the magnitude of the cross-correlation coefficient is always less than one unless one field is a constant multiple of the other. This is only a consideration for the mean since the spatial eigenfunctions are normalized.

Figure (3.10) shows the very close similarity of the structure of the mean fields. The norm of the mean fields varies linearly from 0.297591 at *Re* 8500 to 0.291773 at *Re* 10000, as the kinetic energy is diverted from steady to unsteady motion. It is a small change, and is dwarfed in comparison with the structural changes in the remaining POD modes. Still, this fact could be used to improve reconstruction of the flow at a new Reynolds number from a given set of POD basis functions derived at another Reynolds number. Figures (3.11) and (3.12) illustrate the similarity of

[7]When the POD is performed on a data set which has not had the mean subtracted out, the leading POD does largely correspond to the mean field.

POD modes 1 and 3 for the range of Re considered. The scaling is not the same as in Figure (3.10) because the similarity is not nearly as pronounced as it is for the mean fields. The results using POD mode 2 and POD mode 4 are extremely close to those for POD mode 1 and POD mode 3, respectively, and are not shown. Results for Re 10000 are included for POD mode 3 but the spatial structure is radically different for the higher spatial eigenfunctions at this Reynolds number, as expected by the change from periodic to quasi-periodic flow, so the correlation and error are off the scales. The fact that the error functions are locally linear indicates that the best compromise for approximating the PODs within a range Re_i to Re_j is found by the PODs at $\frac{Re_i+Re_j}{2}$. These facts will be important later when we look at the corresponding dynamical systems.

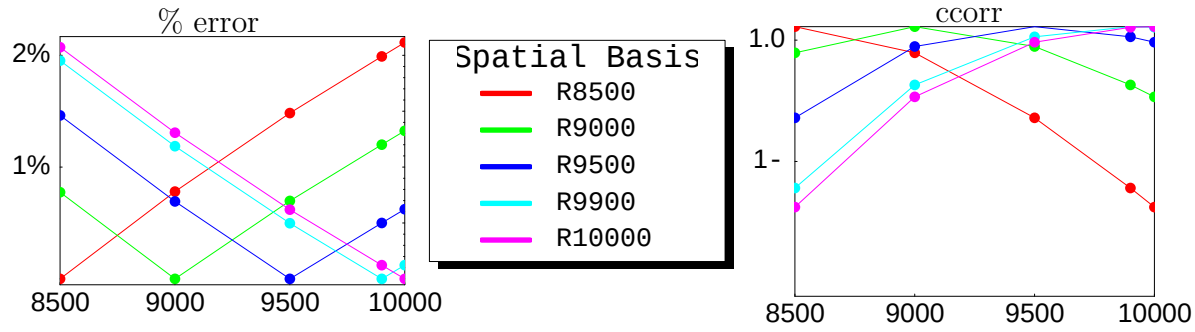

Figure 3.10: Similarity of stream function of mean field ($1^- = .99999$). Left, % error; right, correlation.

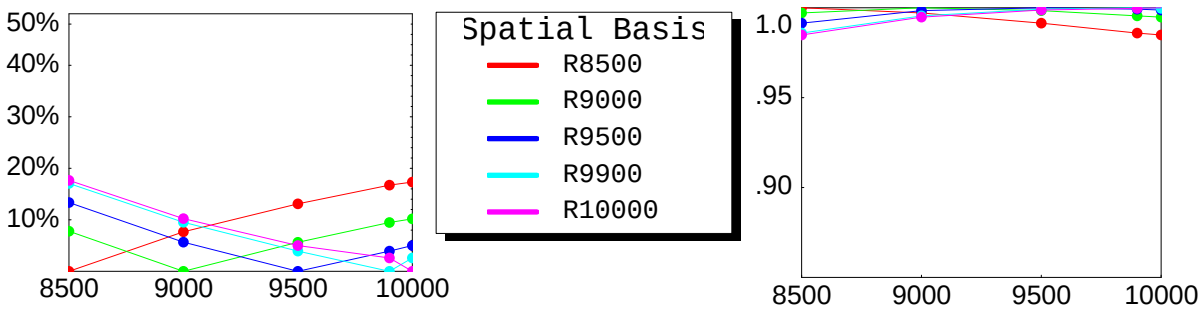

Figure 3.11: Similarity of stream function of POD spatial mode 1 (≈ 2). Left, % error; right, correlation.

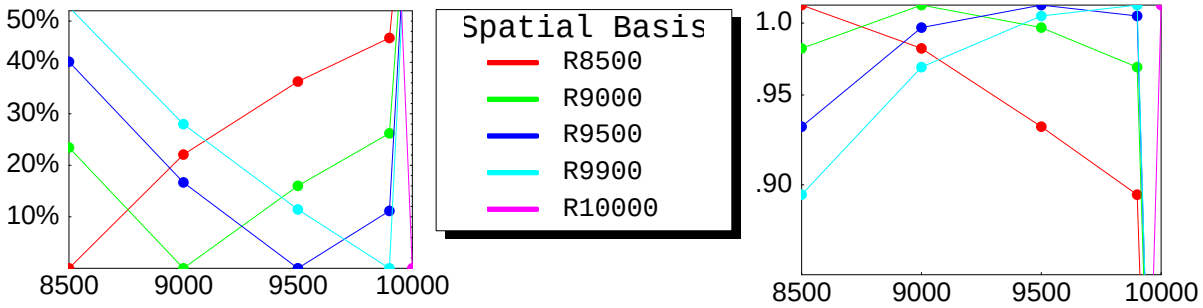

Figure 3.12: Similarity of stream function of POD spatial mode 3 (≈ 4). Left, % error; right, correlation.

While it would appear that the error in approximating a spatial mode at one Reynolds number by that at another is quite high, despite the high correlation, this is not really the case due to the much higher weighting of POD modes 1 & 2, 99.7% at $Re8500$, decreasing linearly to 96.1% at $Re9900$. It is more realistic to look at the errors in reconstruction of the flow using the 4 most significant spatial eigenfunctions. Figure (3.13) shows the percent error incurred when approximating the unsteady flow at one Reynolds number using the spatial basis functions derived at another Reynolds number (left) and the percent error of the total flow using the new spatial basis but the true mean flow.

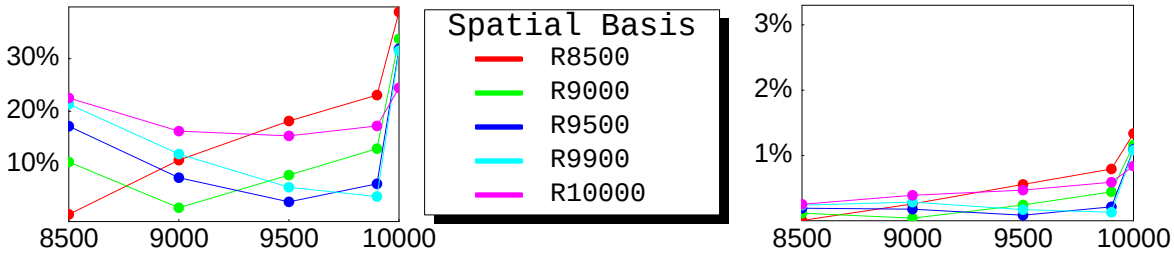

Figure 3.13: % error made when reconstructing the unsteady (left) and total (right) flow using 4 spatial basis functions derived at various Reynolds numbers.

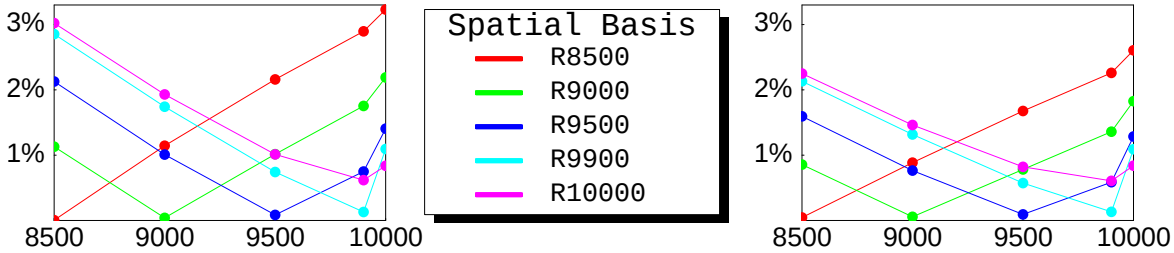

Figure 3.14: % error made when reconstructing the total flow us ing mean and 4 spatial basis functions derived at various Reynolds numbers (left), adjusted me an (right).

Figure (3.14) contrasts the percent error made when using the mean flow as well as the spatial basis functions at another Reynolds number (left), with a minor correction to the mean to compensate for the linear trend in the energy of the mean flow. This scaling of the mean flow has been useful in the past [5] in extending the range of viability of the dynamical system derived at a specific Reynolds number, and there is some improvement in the reconstruction error. Jumping ahead to the

definition of the dynamical system coefficients on page 117, this scaling would modify the constant coefficients a_k and A_k and the linear coefficients that are Re-independent, b_{ki}. Alternatively, this dissertation seeks to quantify energy transfer through the eigenvalues of the POD for this purpose, although the mean scaling technique will be done as well for comparison in Chapter 5.

The stream function plots for typical spatial eigenfunctions are presented in Figures (3.15), (3.17), and (3.19) for the mean, first, and third spatial modes (second and fourth are just rotations of these) for the periodic flow regime. Blue indicates positive values and red, negative. In contrast, the mean, first, and third modes are shown in Figures (3.16), (3.18), and (3.20) for the quasi-periodic flow. The structural similarity of the mean and primary mode can be seen. Vortex locations are located by searching for maxima and minima of the stream function,[8] and are indicated by a black dot in the plots. The new frequency that occurs with the advent of quasi-periodic flow is coincident with a new spatial structure in the flow.

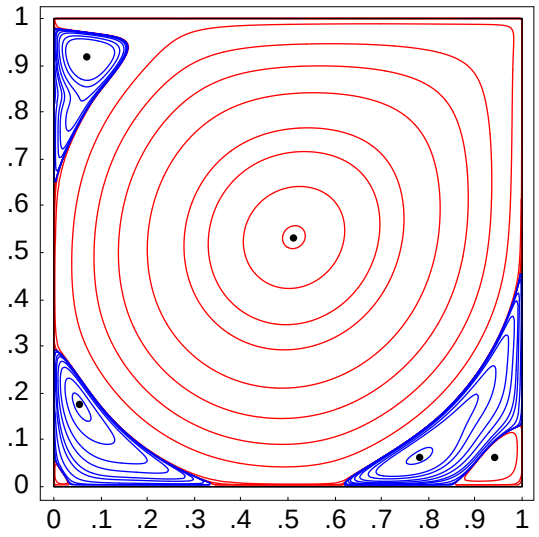

Figure 3.15: mean flow @ Re9000

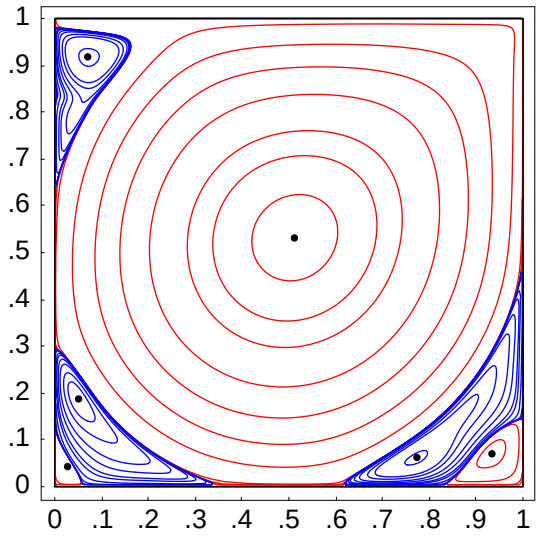

Figure 3.16: mean flow @ Re10000

Stream function contours, red = -, blue = +.

[8] At extrema of f(x,y), the x and y derivatives vanish. For the stream function, this means u and v are zero, which is one way of identifying a vortex.

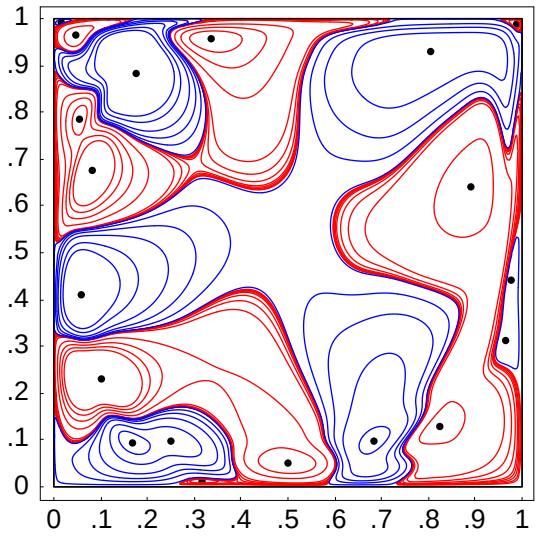

Figure 3.17: Spatial mode 1 @ $Re9000$

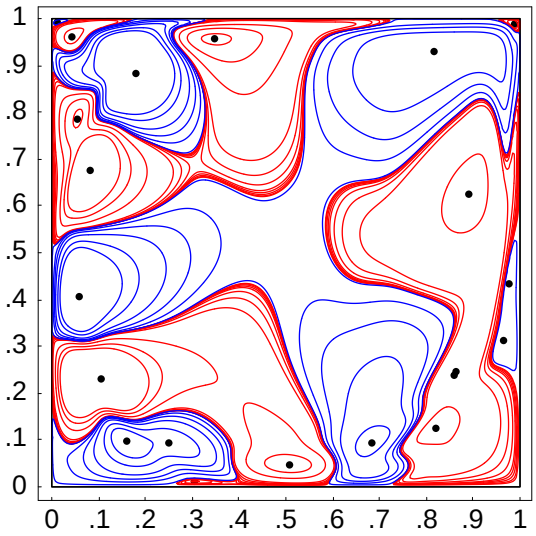

Figure 3.18: Spatial mode 1 @ $Re10000$

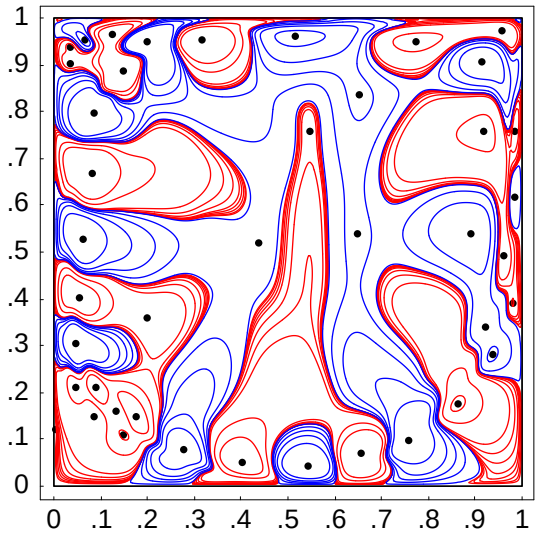

Figure 3.19: Spatial mode 3 @ $Re9000$

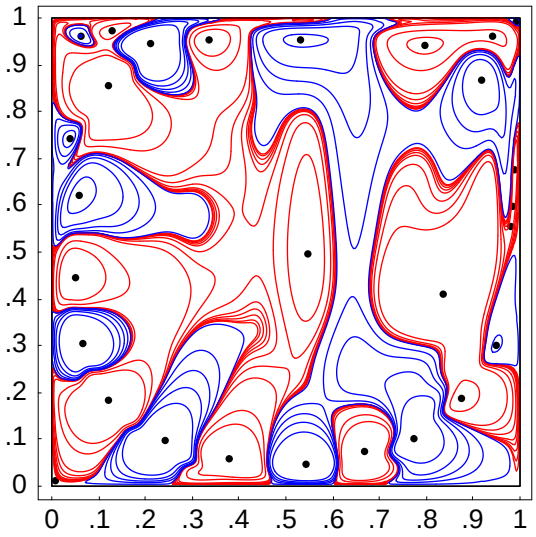

Figure 3.20: Spatial mode 3 @ $Re10000$

Stream function contours, red = -, blue = +.

The vorticity plots of the spatial eigenfunctions are interesting, as well, and are presented in the same format as the stream function plots: Figures (3.21), (3.23), and (3.25) for the mean, first, and third spatial modes (second and fourth are just rotations of these) for the periodic flow regime. Blue indicates positive values and red, negative which for vorticity mean clockwise and counter-clockwise rotation, respectively. The mean, first, and third modes for the quasi-periodic flow are shown in Figures (3.22), (3.24), and (3.26). Stream function contours are at $-1.0 \times 10^{-10}, -1.0 \times 10^{-7}, -1.0 \times 10^{-5}, -1.0 \times 10^{-4}, -.01, -.03, -.05, -.07, -.09, -.1, -.11, -.115, -.1175, 1.0 \times 10^{-}8, 1.0 \times 10^{-7}, 1.0 \times 10^{-6}, 1.0 \times 10^{-5}, 5.0 \times 10^{-5}, 1.0 \times 10^{-4}, 2.5 \times 10^{-4}, 5.0 \times 10^{-4}, 1.0 \times 10^{-3}, 1.5 \times 10^{-3}, 3.0 \times 10^{-3}$. Vorticity contours are at $-5, -4, -3, -2, -1, -.5, -.25, -.1, 0.00020, .001, .1, .25, .5, 1, 2, 3.$

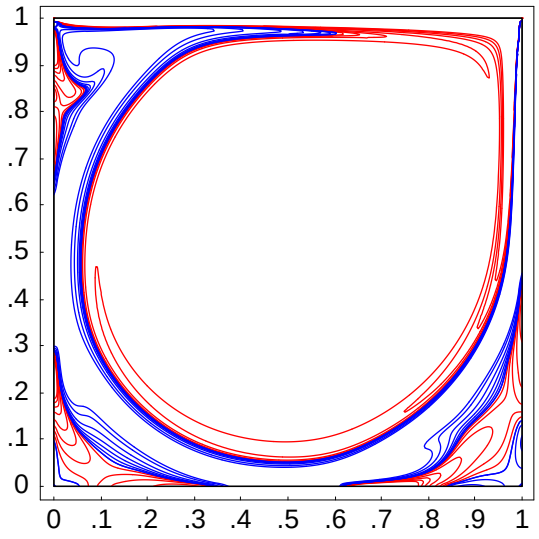

Figure 3.21: Mean flow @ $Re9000$

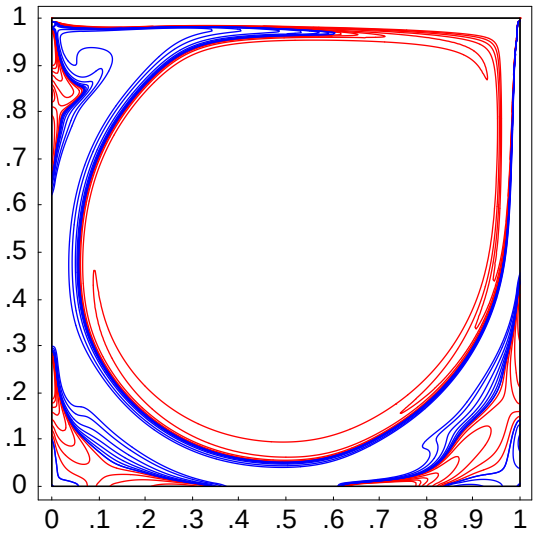

Figure 3.22: Mean flow @ $Re10000$

Vorticity contours, red = -, blue = +.

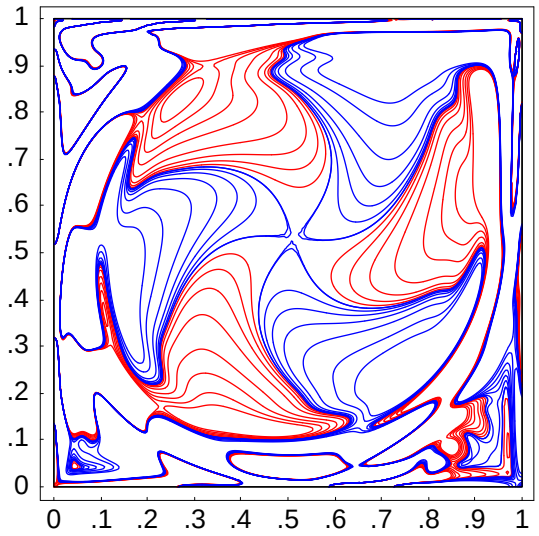

Figure 3.23: Spatial mode 1 @ $Re9000$

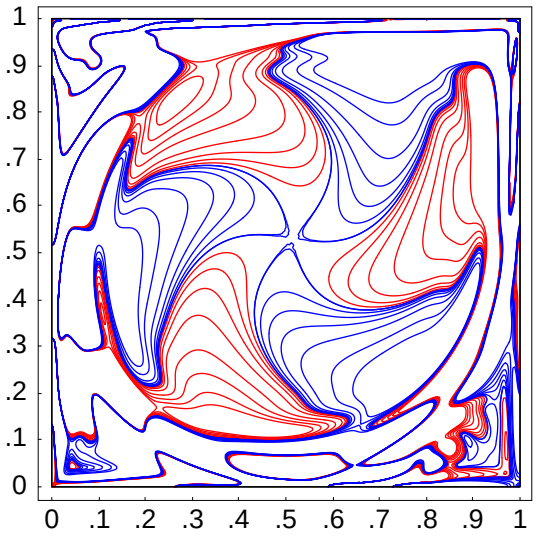

Figure 3.24: Spatial mode 1 @ $Re10000$

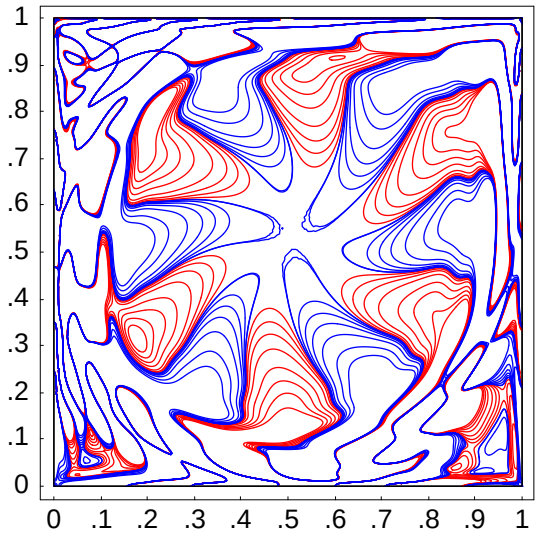

Figure 3.25: Spatial mode 3 @ $Re9000$

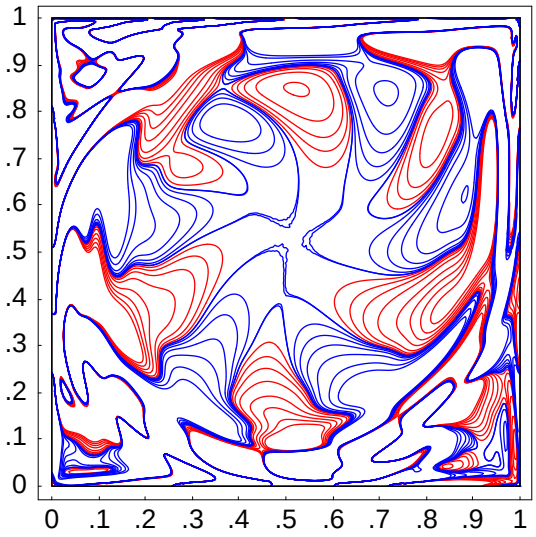

Figure 3.26: Spatial mode 3 @ $Re10000$

Vorticity contours, red = -, blue = +.

3.7 Application to the square cylinder wake flow

3.7.1 Data collection and analysis

DNS data was sampled at 50 snapshots per period for three periods at Reynolds numbers 55, 70, 80, 90, and 100. The kinetic energy was monitored as well as the wake frequency (through history points). The literature places the onset of unsteady behavior at about $Re\,50$ which is consistent with the observed periodic behavior at $Re\,55$. Analysis of the history points in the wake yield a Strouhal number of 0.123, compared with the only available comparison value of 0.120 in a paper by Sohankar *et al.* [57] which used different boundary conditions on the horizontal domain edges. Figure (3.27) of the DNS kinetic energy illustrates several aspects of the flow. Each plotted curve represents the kinetic energy variation for 3 full periods. The kinetic energy mirrors the periodic behavior but at twice the wake frequency. Time is plotted on the x-axis, and graphically shows the marked decrease in period (hence increase in frequency) from $Re\,55$ to $Re\,70$.

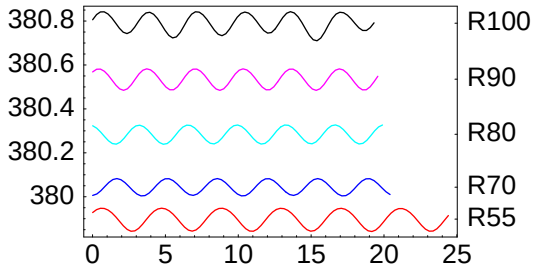

Figure 3.27: Kinetic energy time series for flow past a square cylinder over 3 full periods.

3.7.2 Interpretation

After the the rapid changes associated with the initial onset of periodicity, the flow exhibits moderate change between $Re\,70$ and 100. Figure (3.28) plots the increase in Strouhal number s and Figure (3.29) shows the decrease in the mean recirculation length z. Both Figures are in qualitative agreement with the graphs in Robichaux's

paper, Figures (3) and (5) [60], although numerical values were not published for direct comparison. Sohankar [6] also notes that the shedding frequency "exhibits an approximate linear increase with the Reynolds number when non-dimensionalized by the viscous time scale" in the laminar shedding regime between the primary and secondary instabilities. The scaled shedding frequency is known as the Roshko number and for the unit square cylinder flow is simply Re times the Strouhal number. Figure (3.30) plots the Roshko number vs Reynolds number, and the linear relationship is evident. Another relationship can be discerned from this data as well: the inverse of the mean recirculation length scaled by the Reynolds number also shows a linear increase with Reynolds number. This is demonstrated in Figure (3.31) which plots Re/(mean recirculation length) vs Re. Dots denote the DNS data. As

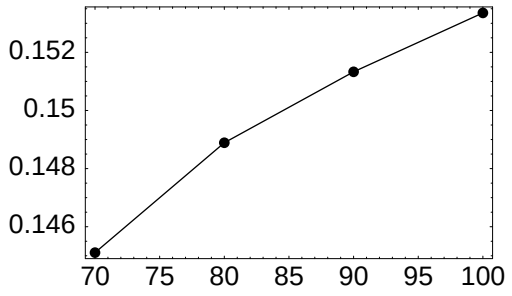

Figure 3.28: Strouhal number, square cylinder.

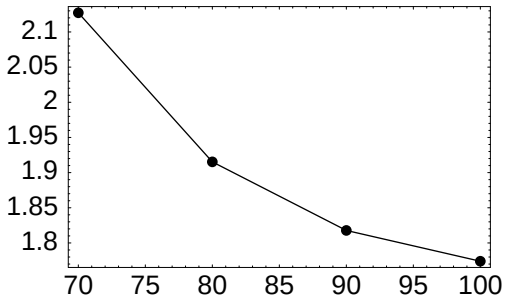

Figure 3.29: Mean recirculation length, square cylinder.

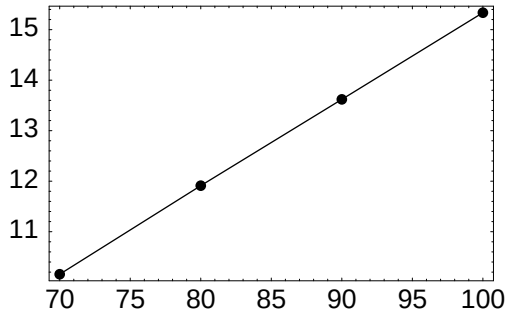

Figure 3.30: Roshko number, square cylinder.

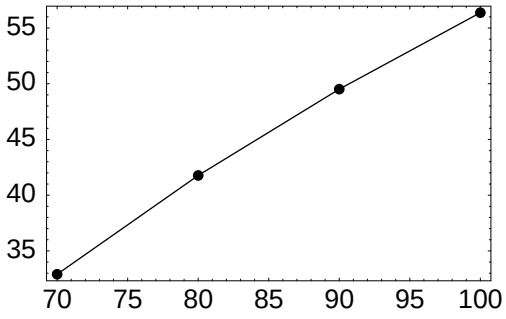

Figure 3.31: Re/Mean recirculation length, square cylinder.

with the driven cavity flow, the variation of period with Reynolds number is not captured in the POD since on the snapshot time scale, the periodicity is fixed at 50.

The temporal eigenfunctions (in pairs) correspond to the primary frequency and harmonics. The first pair of modes accounts for 96% of the energy for the flows under consideration. In contrast to the closed driven cavity flow, the percentage of energy per mode is relatively constant in the Re range, and the change in amplitude is due to the increase in kinetic energy. Figures (3.32) and (3.33) show that the kinetic energy is increasing in both the mean and the unsteady flow components.[9]

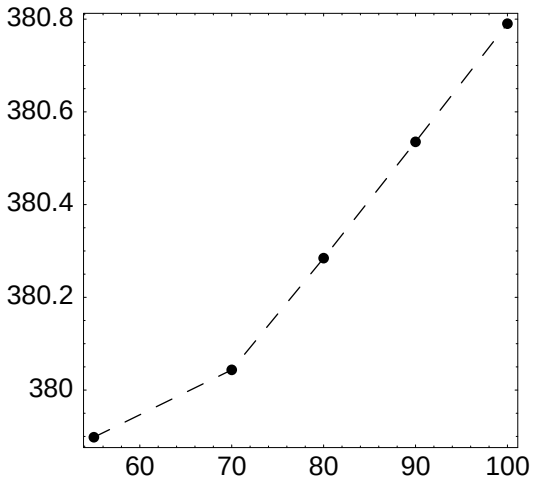

Figure 3.32: Mean kinetic energy for the square cylinder.

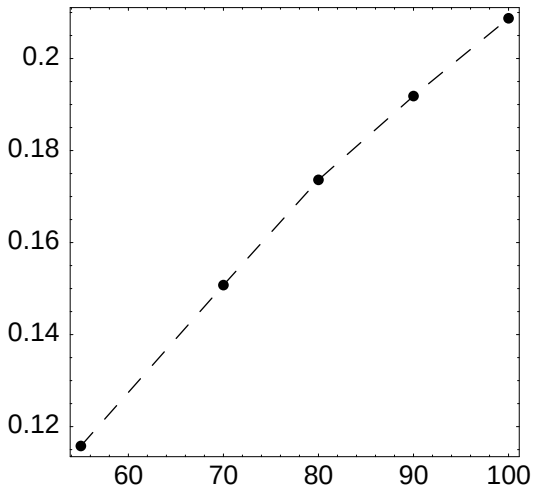

Figure 3.33: Unsteady kinetic energy for the square cylinder.

The first four modes account for over 98% of the unsteady energy and the first six capture over 99%. Figure (3.34) show the variation of the first 6 eigenvalues with Reynolds number, and Figure (3.35) shows the normalized values.

[9]Scaling is different between the DNS and the POD, so the sum of the eigenvalues has been converted to DNS units by dividing by (area $\times$ $2/\triangle x$) = 47360.

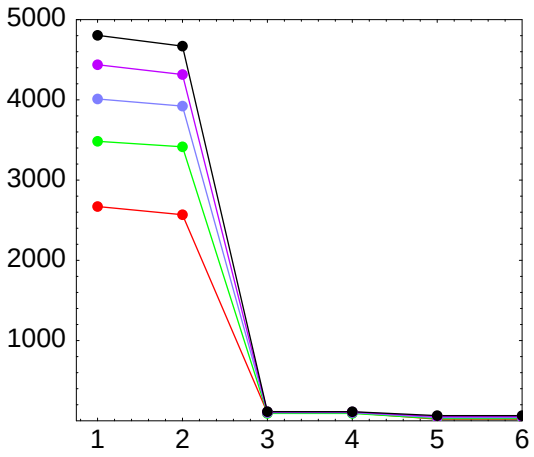

Figure 3.34: Eigenvalues for the square cylinder (bottom to top: R55,R70,R80,R90,R100).

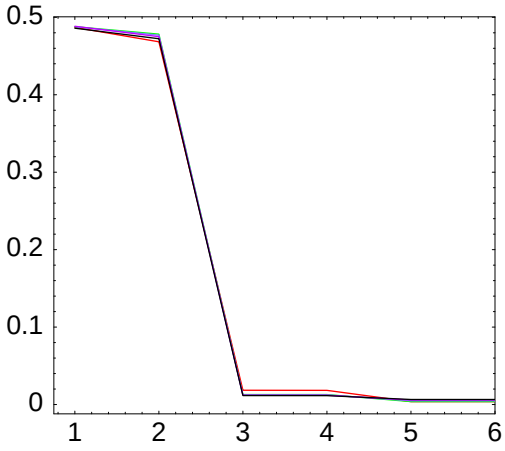

Figure 3.35: Normalized eigenvalues for the square cylinder.

In contrast to the driven cavity flow, there is a large variation in the spatial eigenfunctions. An instantaneous view of the flow is given in Figure (3.36) that clearly shows the vortex-shedding phenomena. The extremes of the Reynolds number range considered here are both presented for the mean and spatial modes 1, 3, and 5. For both stream function and vorticity density plots, red indicates negative values and blue positive values. The magnitude of values is illustrated by the color intensity: white = 0. The scaling has been fixed so proper comparison can be made between Reynolds numbers where applicable. Scaling is linear except for the vorticity of the POD modes, where a nonlinear scaling enhances the level of detail. Extrema of the stream function are indicated on spatial mode 1.

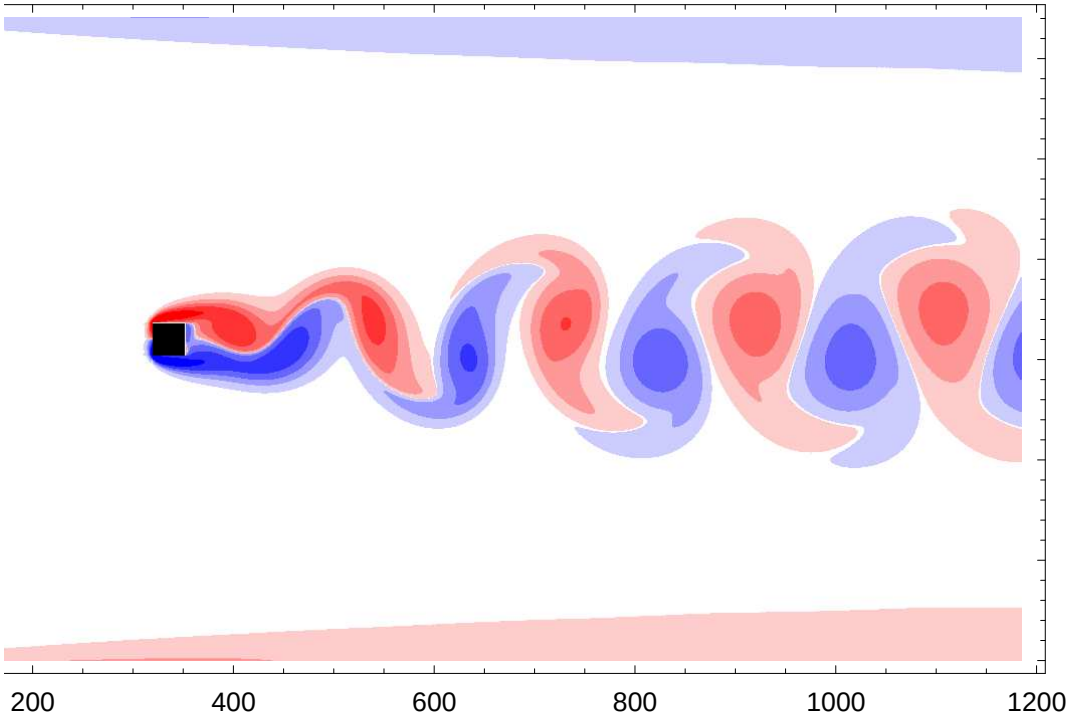

Figure 3.36: Vorticity of instantaneous flow filed at Re 100, nonlinearly scaled -8 to 8.

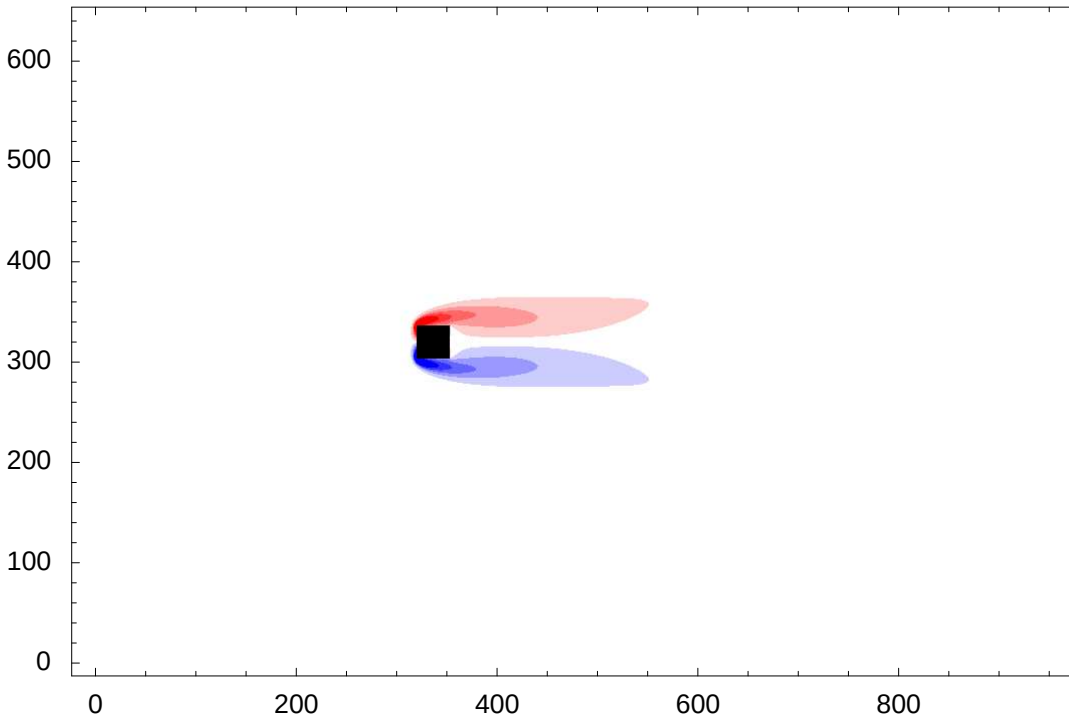

Figure 3.37: Vorticity for mean, Re 55, linearly scaled -8 to 8.

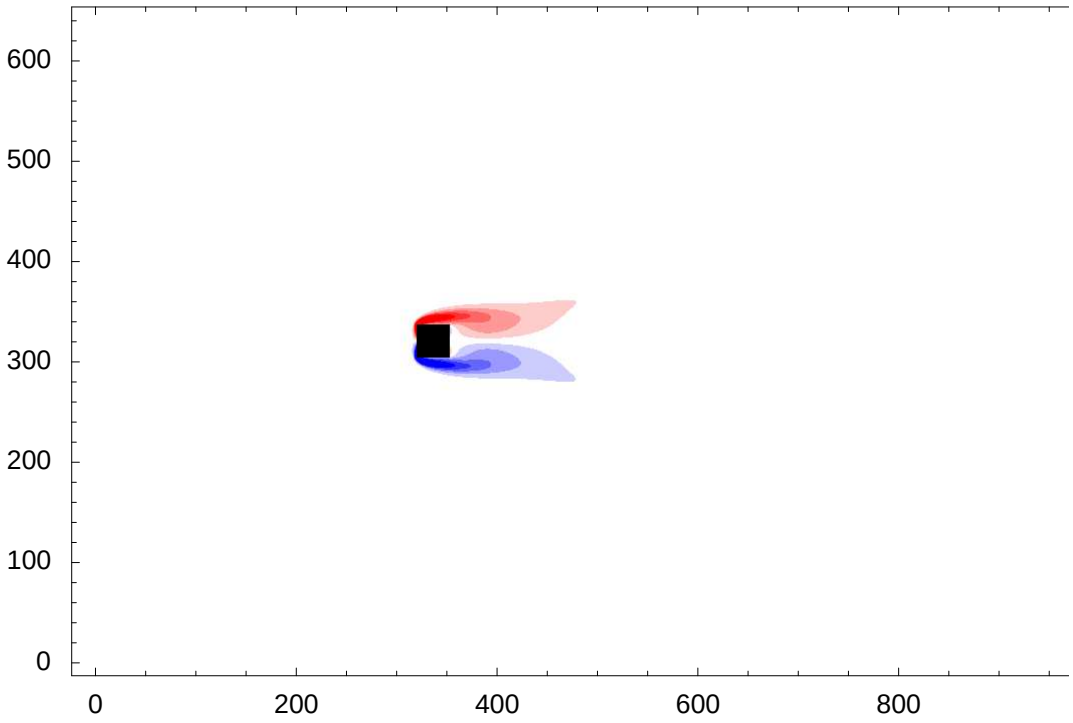

Figure 3.38: Vorticity for mean, Re 100, linearly scaled -8 to 8.

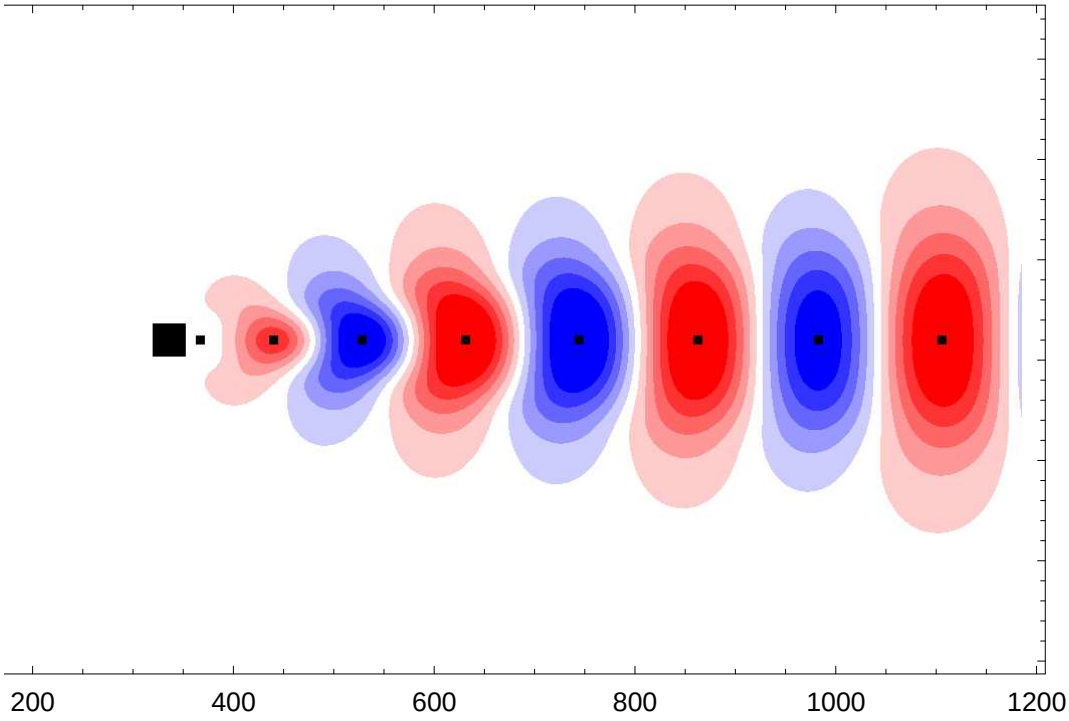

Figure 3.39: Stream function for POD 1, Re 55, linearly scaled -4 to 4.

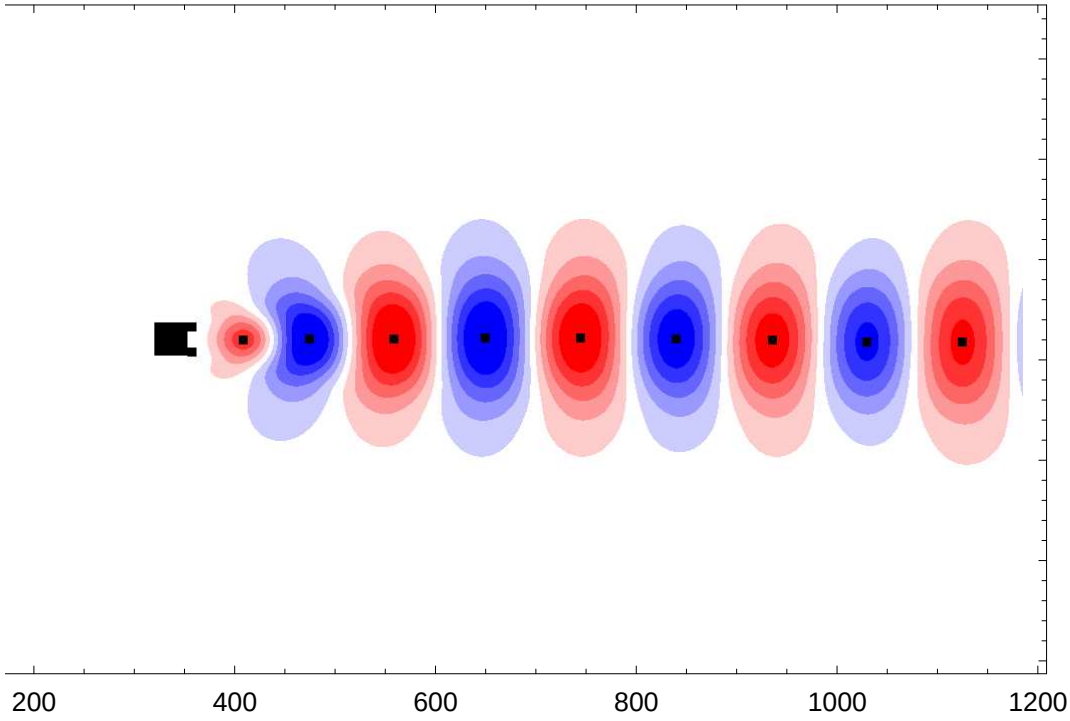

Figure 3.40: Stream function for POD 1, Re 100, linearly scaled -4 to 4.

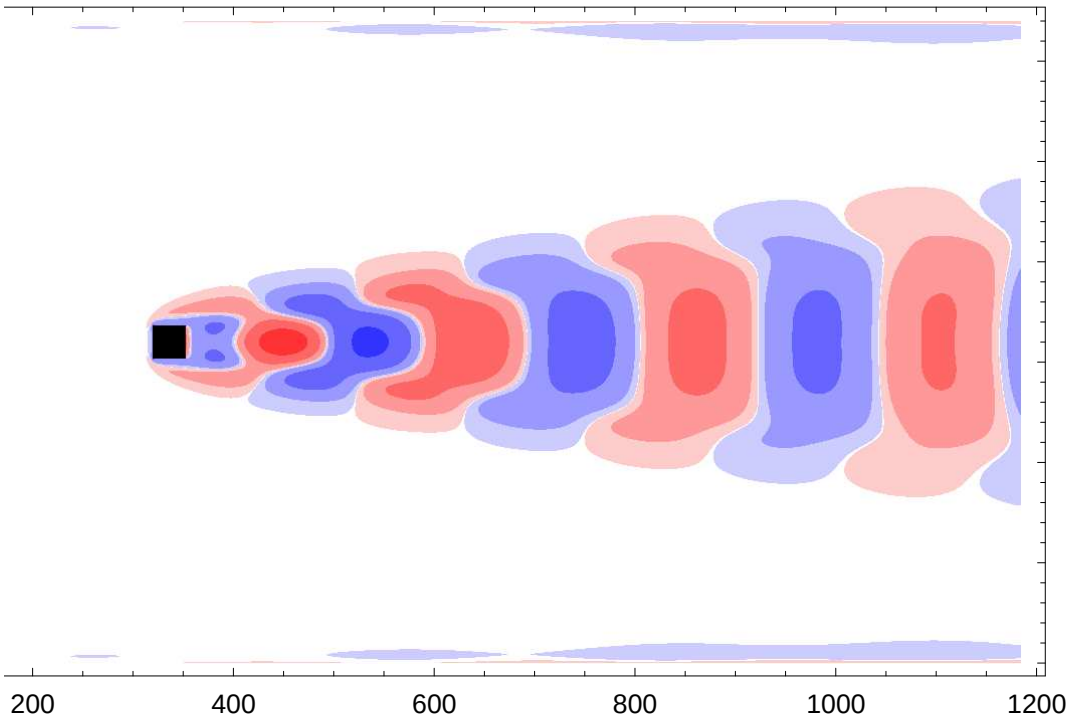

Figure 3.41: Vorticity for POD 1, Re 55, nonlinearly scaled -60 to 60.

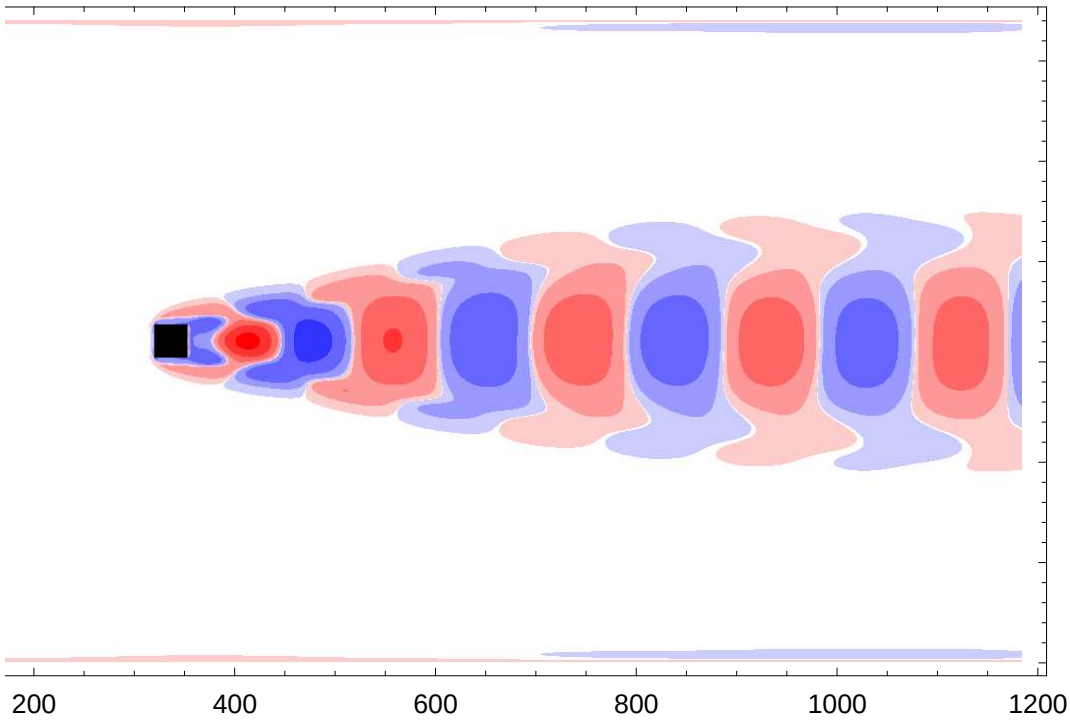

Figure 3.42: Vorticity for POD 1, Re 100, nonlinearly scaled -60 to 60.

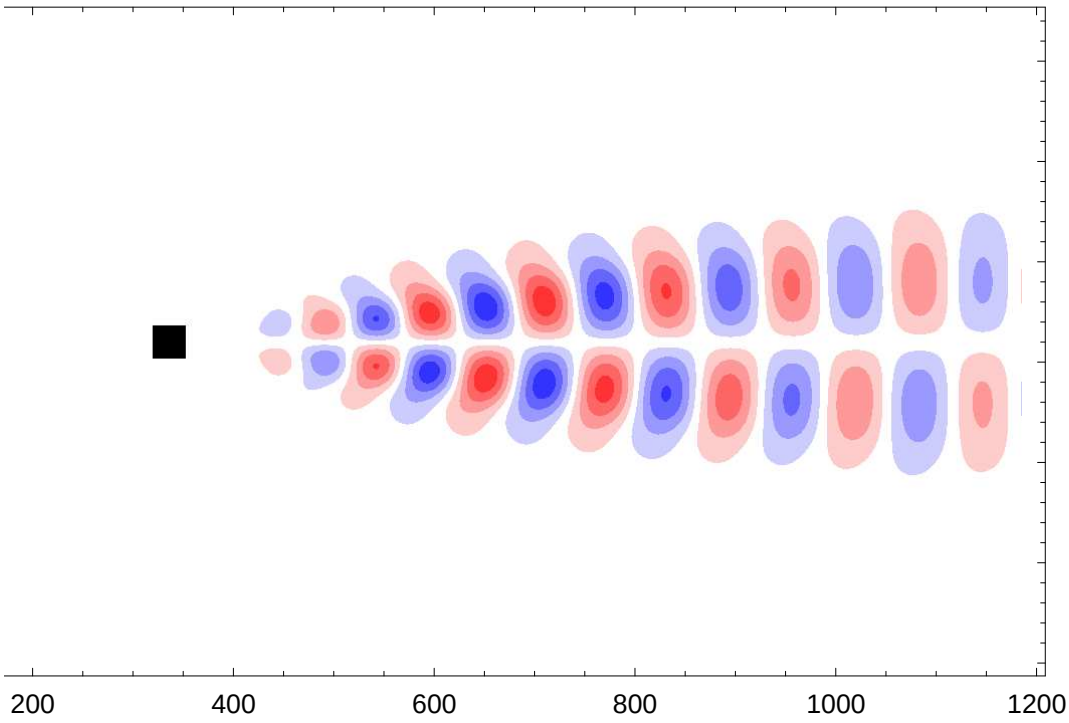

Figure 3.43: Stream function for POD 3, Re 55, linearly scaled -4 to 4.

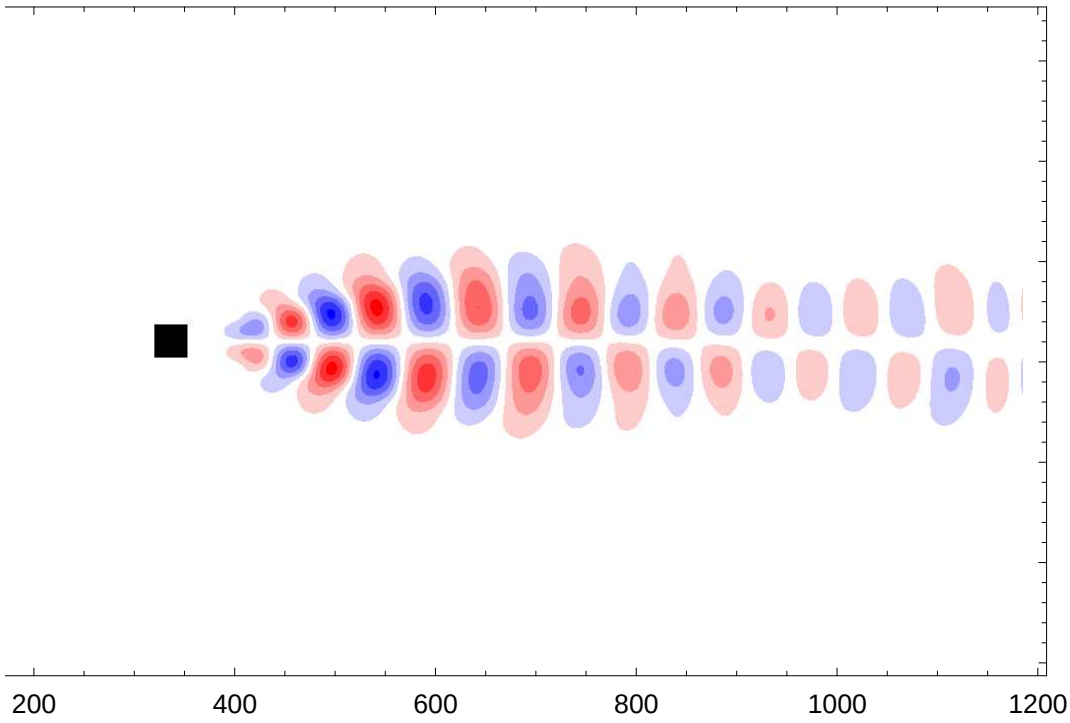

Figure 3.44: Stream function for POD 3, Re 100, linearly scaled -4 to 4.

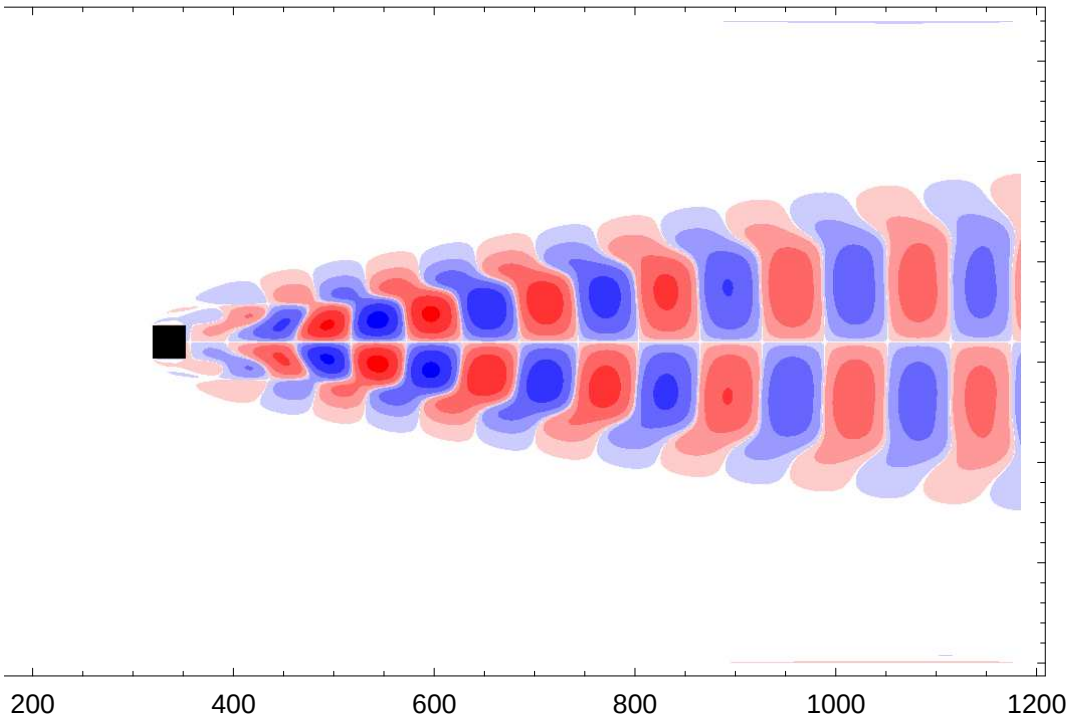

Figure 3.45: Vorticity for POD 3, Re 55, nonlinearly scaled -60 to 60.

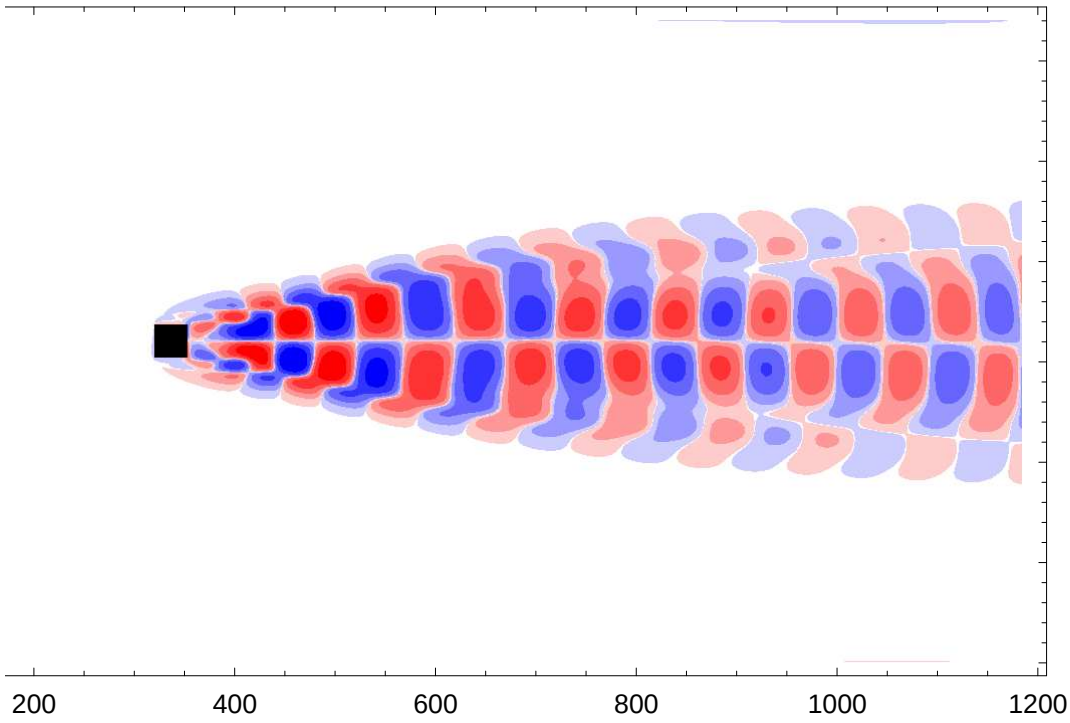

Figure 3.46: Vorticity for POD 3, Re 100, nonlinearly scaled -60 to 60.

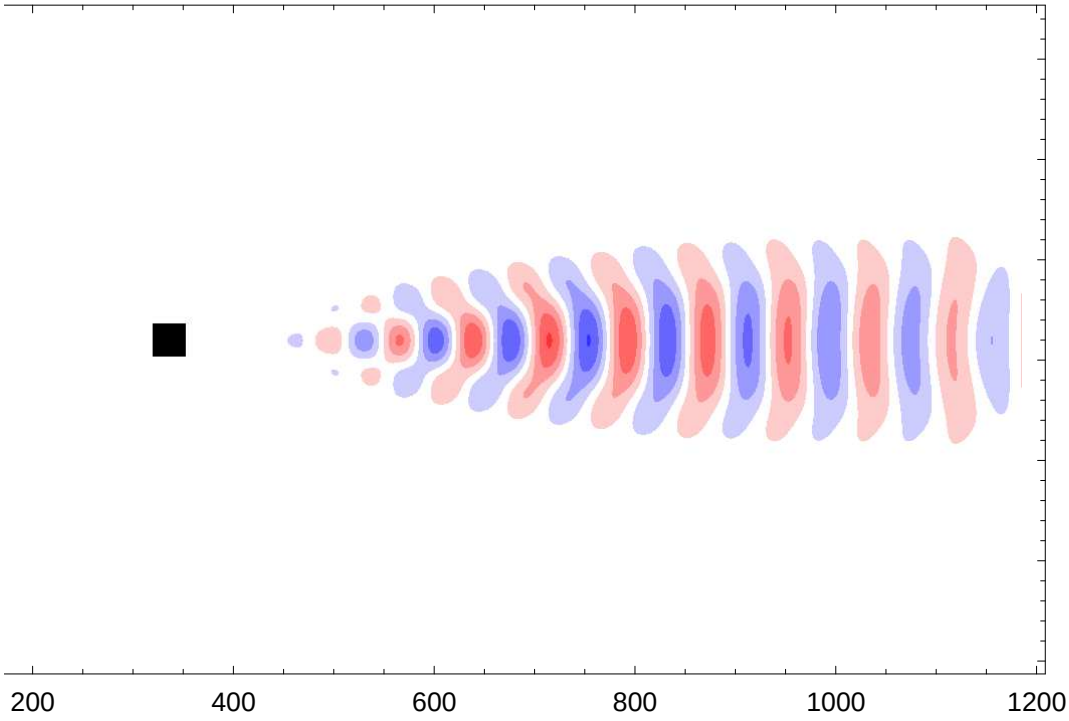

Figure 3.47: Stream function for POD 5, Re 55, linearly scaled -4 to 4.

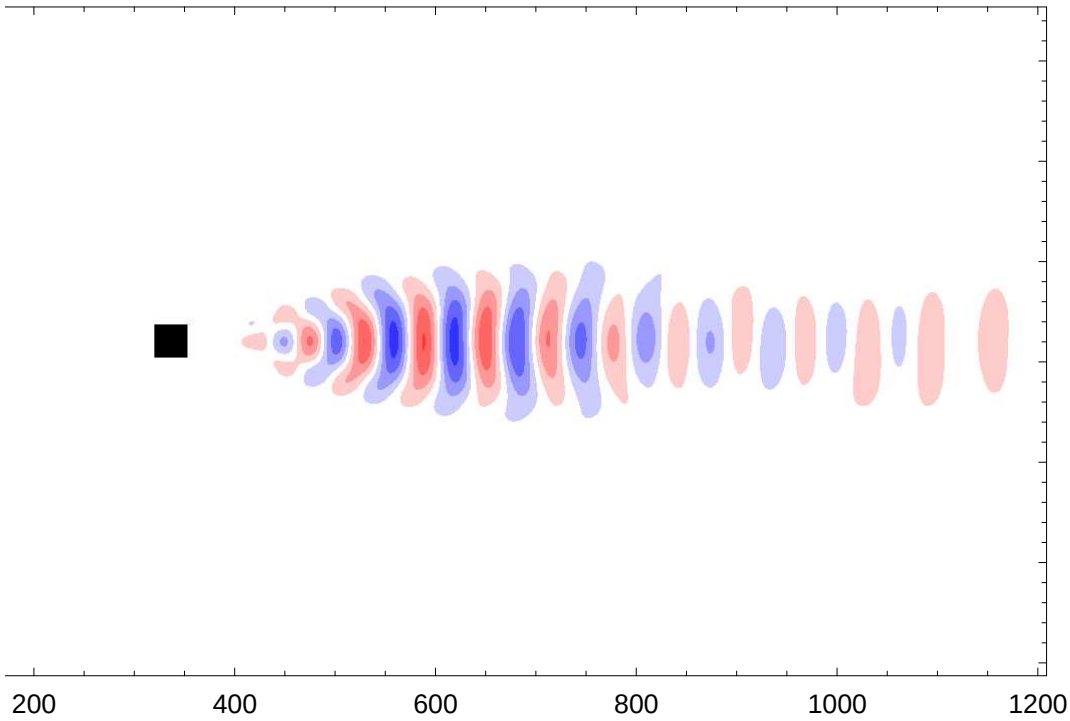

Figure 3.48: Stream function for POD 5, Re 100, linearly scaled -4 to 4.

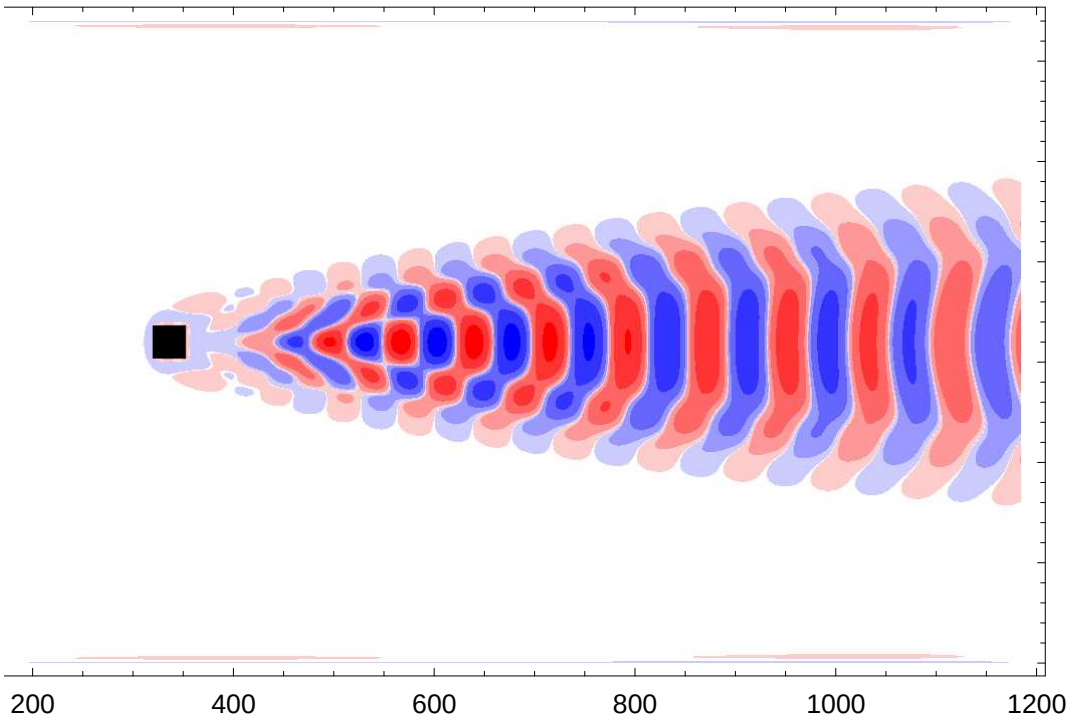

Figure 3.49: Vorticity for POD 5, Re 55, nonlinearly scaled -60 to 60.

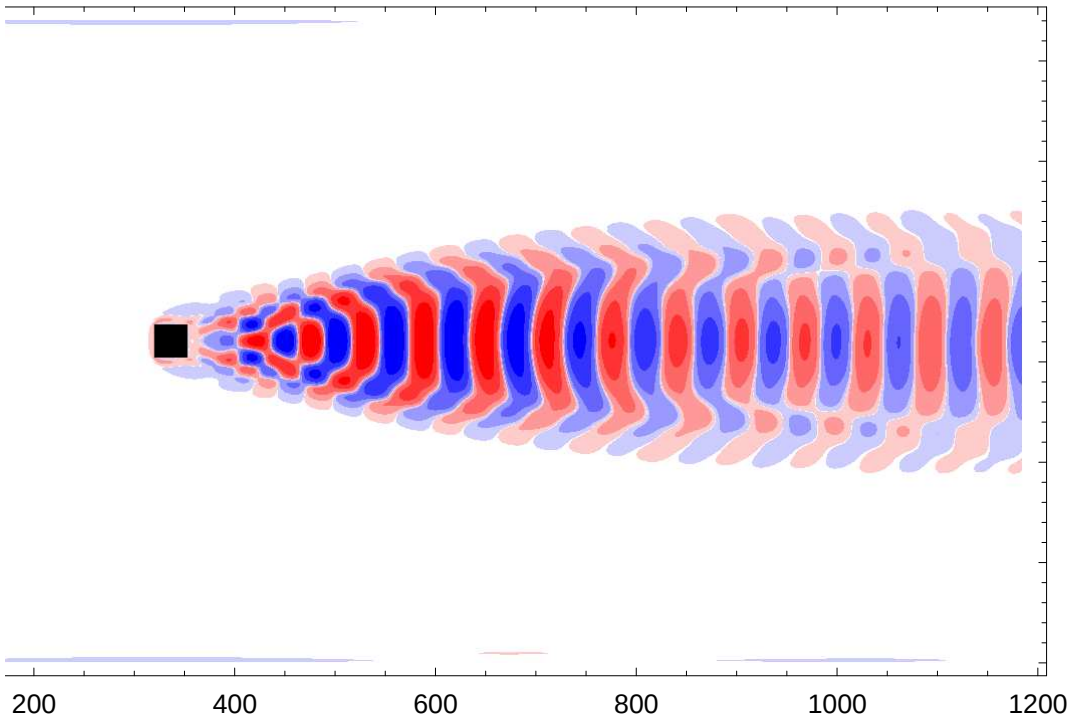

Figure 3.50: Vorticity for POD 5, Re 100, nonlinearly scaled -60 to 60.

Just as the temporal frequency changes radically between $Re\,55$ and $Re\,70$, so does the spatial frequency. However, we have seen in Figure (3.28) that the change is not nearly as extreme in the range $Re\,70 - 100$, so Figures (3.51) - (3.53) examine the similarity measures defined earlier for the driven cavity applied to the square cylinder mean and spatial modes 1 & 3 for this limited range of Reynolds numbers.

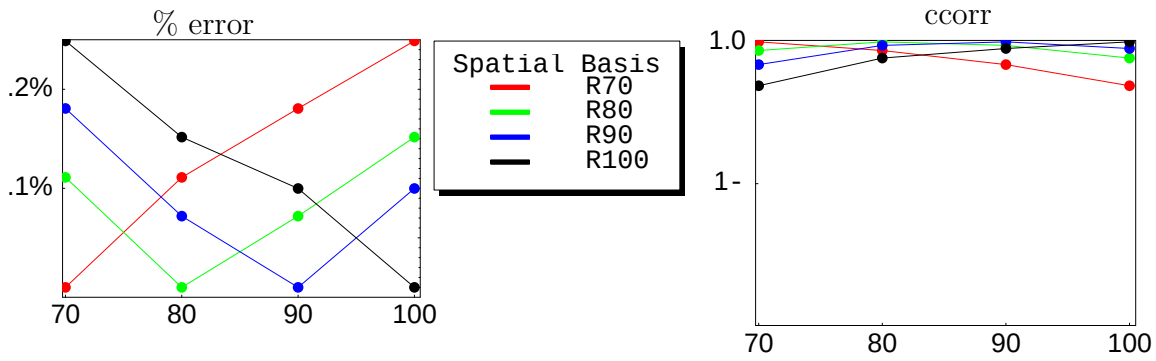

Figure 3.51: Similarity of stream function of mean field ($1^- = .99999$). Left, % error; right, correlation.

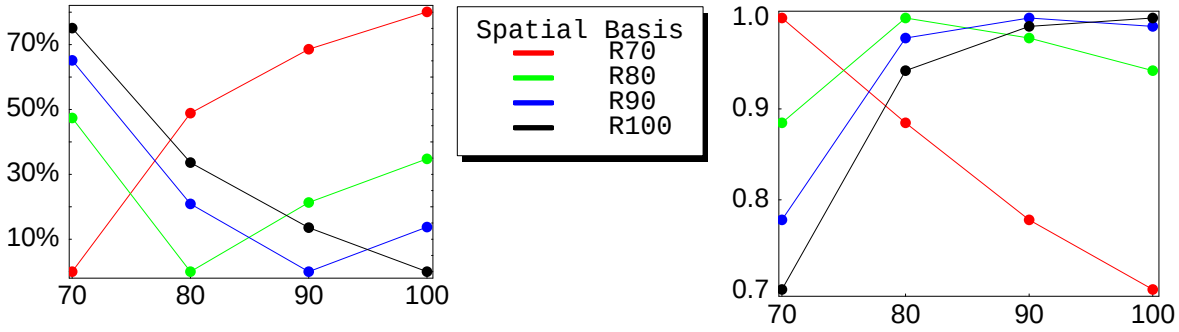

Figure 3.52: Similarity of stream function of POD spatial mode 1 (≈ 2). Left, % error; right, correlation.

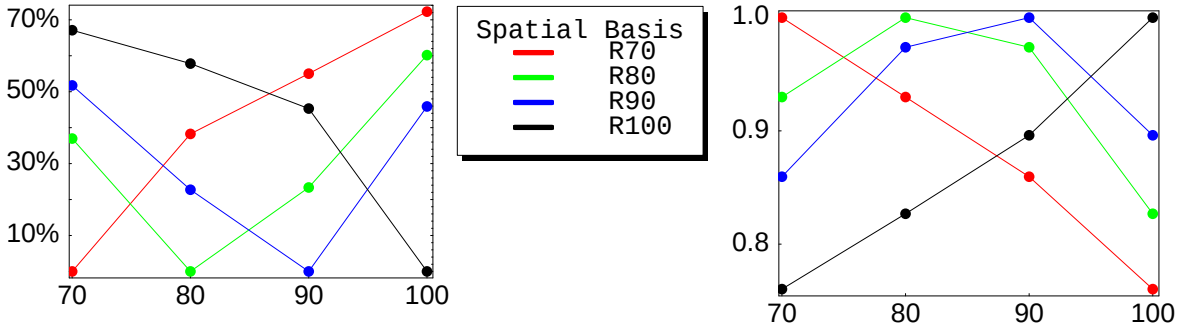

Figure 3.53: Similarity of stream function of POD spatial mode 3 (≈ 4). Left, % error; right, correlation.

The mean flow changes relatively little; the structural change corresponds to the shrinking of the recirculation eddies and the diminishing mean recirculation length. However, the spatial modes still differ quite a bit even in this limited range. In contrast with the driven cavity spatial results, mode 1 (& 2) do not show a markedly better match over mode 3 (& 4) across Reynolds numbers.

Next, consider the errors in reconstruction of the flow using the six most significant spatial eigenfunctions, for example, which capture over 99% of the unsteady energy. Figure (3.54) shows the percent error incurred when approximating the unsteady flow at one Reynolds number using the spatial basis functions derived at another Reynolds number (left) and the percent error of the total flow using the new spatial basis including the new mean flow. The truncated spatial basis does a great job of recovering the snapshots at the Reynolds number of computation. However, the basis at one Reynolds number does a poor job of reproducing the flow at a different Reynolds number. This is not unexpected, given the spatial frequency changes of the spatial eigenfunctions with Reynolds number, This is in stark contrast to the equivalent figure, Figure (3.13), for the driven cavity flow.

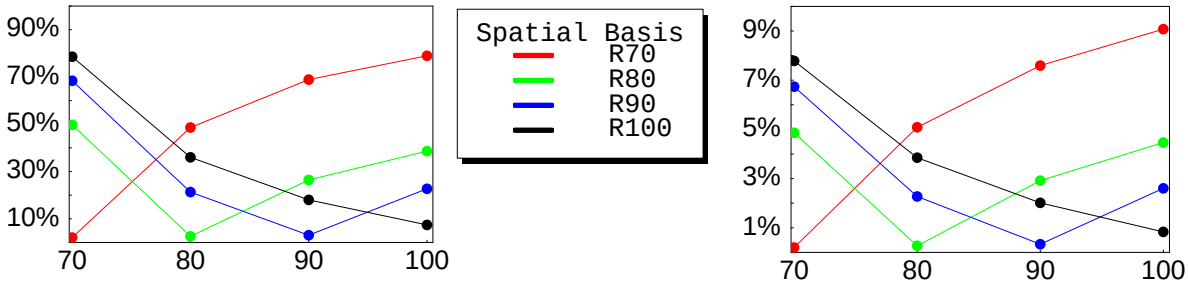

Figure 3.54: % error made when reconstructing the unsteady (left) and total (right) flow using 6 spatial basis functions & mean derived at various Reynolds numbers.

4 Dynamical systems

Application of the Proper Orthogonal Decomposition (POD) to the sampled flow field results in a hierarchical set of temporal and spatial basis functions, ranked by contribution to the unsteady kinetic energy of the fluid flow. The flow field can be approximated by a linear combination of the spatial basis functions. Significant data reduction can be achieved when the energy content is concentrated in the leading modes, as is the case with non-turbulent flow. Substitution of this linear combination for $\mathbf{u}$ in the Navier-Stokes equations followed by Galerkin projection on the spatial basis functions results in a system of ordinary differential equations for the temporal fluctuation of $\mathbf{u}$. A nominal criterion for truncation was suggested by Sirovich [64] as the capture of 99% of the energy. In terms of eigenvalues λ_n of the POD, this is equivalent to finding the smallest M such that $\sum_{n=1}^{M} \lambda_n / \sum_{n=1}^{N} \lambda_n > .99$, where N is the total number of basis functions. An alternative method, the Scree Test, was suggested by Cattell [67]. This method plots the (ordered) eigenvalues, and looks for a point where the plot abruptly levels out. In practice, the number of terms needed depends on both the specific problem and the goal. In next chapter, Chapter 5, we will see how the truncation level affects the ability of the dynamical system to reproduce the correct bifurcation scenario. Chapter 6 addressed this issue on the basis of reconstruction accuracy. This chapter focuses on the mechanics of deriving the dynamical system at a given truncation level.

4.1 Formation of the low-order model

From the POD, we have the representation of the solution to the Navier-Stokes equation as:

$$\mathbf{u}(t, \mathbf{x}) = \mathbf{u}_m + \sum_{i=1}^{M} y_i(t) \mathbf{\Phi}_i(\mathbf{x}) \ . \tag{4.1}$$

where $\mathbf{u}_m$ is the mean flow field and M is the number of significant eigenfunctions y_i[10] and $\mathbf{\Phi}_i$.

Replacing $\mathbf{u}$ in the Navier-Stokes equations by this representation yields:

$$\begin{aligned}
\frac{\partial \mathbf{u}}{\partial t} &= -(\mathbf{u}\cdot\nabla)\mathbf{u} - \nabla p + \frac{1}{Re}\nabla^2\mathbf{u}\,, && (4.2)\\
\sum_{i=1}^{M}\frac{dy_i}{dt}\mathbf{\Phi}_i &= -\Big((\mathbf{u}_m + \sum_{i=1}^{M} y_i\mathbf{\Phi}_i)\cdot\nabla)(\mathbf{u}_m + \sum_{i=1}^{M} y_i\mathbf{\Phi}_i\Big) \\
&\quad -\nabla p + \frac{1}{Re}\nabla^2(\mathbf{u}_m + \sum_{i=1}^{M} y_i\mathbf{\Phi}_i)\,, && (4.3)\\
&= -(\mathbf{u}_m\cdot\nabla)\mathbf{u}_m - \sum_{i=1}^{M} y_i(\mathbf{\Phi}_i\cdot\nabla)\mathbf{u}_m \\
&\quad -\sum_{i=1}^{M} y_i(\mathbf{u}_m\cdot\nabla)\mathbf{\Phi}_i - \sum_{i=1}^{M}\sum_{j=1}^{M} y_i y_j(\mathbf{\Phi}_i\cdot\nabla)\mathbf{\Phi}_j \\
&\quad -\nabla p + \frac{1}{Re}\nabla^2(\mathbf{u}_m + \sum_{i=1}^{M} y_i\mathbf{\Phi}_i)\,. && (4.4)
\end{aligned}$$

The Galerkin projection onto the orthonormal spatial basis functions $\mathbf{\Phi}_k$ yields:

$$\begin{aligned}
\frac{dy_k}{dt} &= -\langle\mathbf{\Phi}_k, (\mathbf{u}_m\cdot\nabla)\mathbf{u}_m\rangle - \langle\mathbf{\Phi}_k, \sum_{i=1}^{M} y_i(\mathbf{\Phi}_i\cdot\nabla)\mathbf{u}_m\rangle \\
&\quad -\langle\mathbf{\Phi}_k, \sum_{i=1}^{M} y_i(\mathbf{u}_m\cdot\nabla)\mathbf{\Phi}_i\rangle - \langle\mathbf{\Phi}_k, \sum_{i=1}^{M}\sum_{j=1}^{M} y_i y_j(\mathbf{\Phi}_i\cdot\nabla)\mathbf{\Phi}_j\rangle \\
&\quad -\langle\mathbf{\Phi}_k, \nabla p\rangle + \langle\mathbf{\Phi}_k, \frac{1}{Re}\nabla^2(\mathbf{u}_m + \sum_{i=1}^{M} y_i\mathbf{\Phi}_i)\rangle\,. && (4.5)
\end{aligned}$$

The pressure term can be integrated by parts to yield:

$$-\langle\mathbf{\Phi}_k, \nabla p\rangle = -\langle\nabla\cdot\mathbf{\Phi}_k, p\rangle - \int_\Gamma \mathbf{\Phi}_k p\,. \qquad (4.6)$$

The spatial basis functions $\mathbf{\Phi}_k$ are divergence-free as mentioned in the Chapter 3

[10] strictly speaking, y_i is not a temporal eigenfunction since in this representation, it is not normalized

section, so the first term vanishes. The $\mathbf{\Phi}_k$ vanish on the cavity boundaries since the flow there is constant, hence equal to the mean flow. Thus, the boundary integration term is zero as well. For the flow past the square cylinder, the $\mathbf{\Phi}_k$ are likewise zero on all except the outflow boundary. At outflow, however, the pressure is zero, so again there is no contribution from the boundary term [5].

Using the orthonormality of the $\mathbf{\Phi}_k$:

$$\begin{aligned}
\frac{dy_k}{dt} &= -\langle \mathbf{\Phi}_k, (\mathbf{u}_m \cdot \nabla)\mathbf{u}_m \rangle - \sum_{i=1}^{N} \langle \mathbf{\Phi}_k, (\mathbf{\Phi}_i \cdot \nabla)\mathbf{u}_m \rangle y_i \\
&\quad - \sum_{i=1}^{N} \langle \mathbf{\Phi}_k, (\mathbf{u}_m \cdot \nabla)\mathbf{\Phi}_i \rangle y_i - \sum_{i=1}^{N}\sum_{j=1}^{N} \langle \mathbf{\Phi}_k, (\mathbf{\Phi}_i \cdot \nabla)\mathbf{\Phi}_j \rangle y_i y_j \\
&\quad + \frac{1}{Re}\langle \mathbf{\Phi}_k, \nabla^2 \mathbf{u}_m \rangle + \frac{1}{Re}\sum_{i=1}^{N} \langle \mathbf{\Phi}_k, \nabla^2 \mathbf{\Phi}_i \rangle y_i \ , \qquad (4.7) \\
&= a_k + \sum_{i=1}^{N} b_{ki} y_i + \sum_{i=1}^{N}\sum_{j=1}^{N} c_{kij} y_i y_j \ , \qquad (4.8)
\end{aligned}$$

where

$$\begin{aligned}
a_k &= -\langle \mathbf{\Phi}_k, (\mathbf{u}_m \cdot \nabla)\mathbf{u}_m \rangle + \frac{1}{Re}\langle \mathbf{\Phi}_k, \nabla^2 \mathbf{u}_m \rangle \ , \qquad (4.9) \\
b_{ki} &= -\langle \mathbf{\Phi}_k, (\mathbf{\Phi}_i \cdot \nabla)\mathbf{u}_m \rangle - \langle \mathbf{\Phi}_k, (\mathbf{u}_m \cdot \nabla)\mathbf{\Phi}_i \rangle + \frac{1}{Re}\langle \mathbf{\Phi}_k, \nabla^2 \mathbf{\Phi}_i \rangle \ , \qquad (4.10) \\
c_{kij} &= -\langle \mathbf{\Phi}_k, (\mathbf{\Phi}_i \cdot \nabla)\mathbf{\Phi}_j \rangle \ . \qquad (4.11)
\end{aligned}$$

From a practical consideration, it is beneficial to use integration by parts to reduce the terms involving second order derivatives to functions of first order derivatives because it is necessary to compute first order derivatives for all other terms. As

with the pressure term, the boundary terms vanish:

$$a_k = -\langle \mathbf{\Phi}_k, (\mathbf{u}_m \cdot \nabla)\mathbf{u}_m \rangle - \frac{1}{Re}\langle \nabla\mathbf{\Phi}_k, \nabla\mathbf{u}_m \rangle \ , \tag{4.12}$$

$$b_{ki} = -\langle \mathbf{\Phi}_k, (\mathbf{\Phi}_i \cdot \nabla)\mathbf{u}_m \rangle - \langle \mathbf{\Phi}_k, (\mathbf{u}_m \cdot \nabla)\mathbf{\Phi}_i \rangle - \frac{1}{Re}\langle \nabla\mathbf{\Phi}_k, \nabla\mathbf{\Phi}_i \rangle \ , \tag{4.13}$$

$$c_{kij} = -\langle \mathbf{\Phi}_k, (\mathbf{\Phi}_i \cdot \nabla)\mathbf{\Phi}_j \rangle \ . \tag{4.14}$$

4.2 Long-term dynamics

The actual computation of these coefficients entails numerically computing first order derivatives of the mean flow field and the eigenfunctions, and many inner products. This is far from a perfect process: "There may be a significant margin of error in the coefficients, especially those involving derivatives [1]." This in turn is a significant problem, because the long term stability of the system of Equation (4.8) is at stake. We need the asymptotic behavior of these equations to accurately reflect the DNS solution, or it will be useless in a parameter continuation scenario. As a simple example, Figure (4.1) shows a comparison of the evolution of Equation (4.8) versus the actual temporal modes for the driven cavity flow at *Re* 8500 where the flow is periodic and the first two POD modes capture over 99% of the energy. Short term tracking is not terrible, but long term evolution of Equation (4.8), shown in Figure (4.2), is not acceptable. If this system of differential equations was analyzed with a parameter continuation algorithm in Reynolds number, a steady flow would be predicted at *Re* 8500, not a periodic solution.

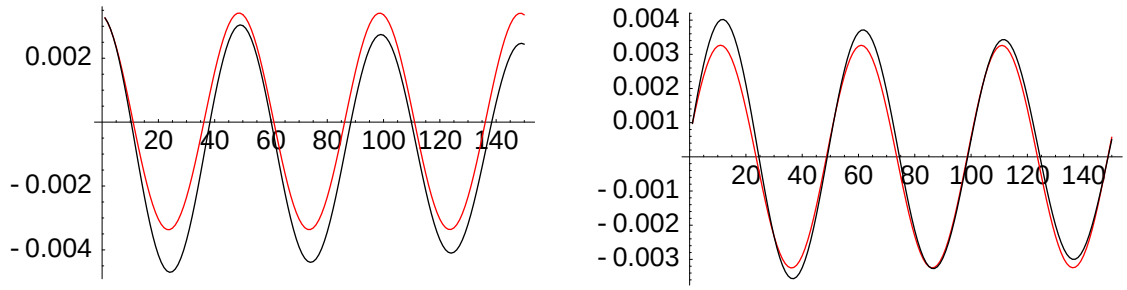

Figure 4.1: 2 mode low dimensional model (left: mode 1; right: mode 2) for driven cavity flow at *Re* 8500; red = exact from POD, black = evolved.

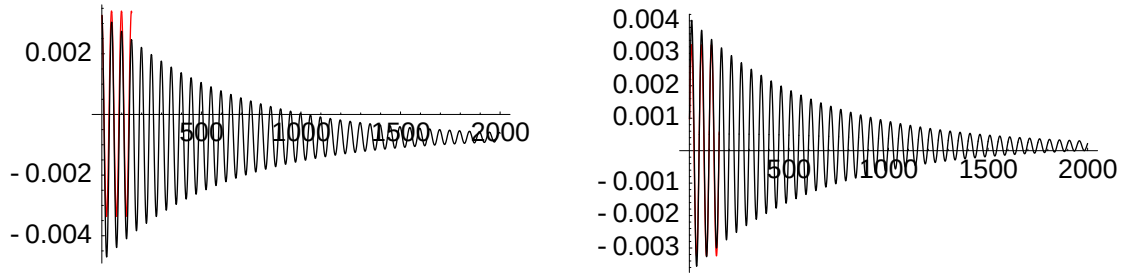

Figure 4.2: Asymptotic behavior of 2 mode low dimensional model (left: mode 1; right: mode 2) for driven cavity flow at *Re* 8500; red = exact from POD, black = evolved.

Various methods have been proposed for closure or stabilization of the dynamical system under the assumption that the main problem lies with the truncation of the system. One method of stabilizing the dynamical system is nonlinear Galerkin projection [69] which was introduced specifically to address the problem of long-term integration of evolution differential equations. Given a truncated dynamical system of order M, this method seeks to incorporate the effect of the neglected higher modes on the premise that they are in fact important for asymptotic behavior. An example of this method was presented in Bangia *et al.* [81]. They treat the first M modes as master modes which govern the dynamics of the flow, and the higher modes as slave modes. The equations for the slave modes are not differential equations, but algebraic equations dependent on the master modes. However, this method proves inadequate for some reduced flow systems [72].

The Heisenberg model augments each ordinary differential equation (ODE) in Equation (4.8) with a linear term $\mu\, y_k$ where μ is a free parameter that is not

determined a priori, but is tuned for stabilizing the integration. The idea behind this method is compensation for the loss of dissipation incurred by neglecting the higher order modes [70].

Another strategy for dealing with non-chaotic flows is to include transient behavior to get statistical variance about the attractor (*e.g.*, [5],[71]). However, while this may stabilize the scheme, the limit cycle amplitude obtained may be different from that obtained from the full simulation, which was the case in [5].

Cazemier [8] also proposed a dissipative closure model which would (possibly) add a linear damping term to the dynamical system. The coefficient of the new term is determined from the requirement that the energy of the new dynamical system be conserved. Using the notation of Equation (4.8), the new term is $d_k\, y_k$ and $\sum_{i=1}^{M}\sum_{j=1}^{M} -c_{kij}\langle y_k(t_m)y_i(t_m)y_j(t_m)\rangle_N - (b_{kk}+d_k)\lambda_k = 0$ where λ_k is the k^{th} eigenvalue from the POD and the triple product is a temporal average. However, this factor does not always behave in the desired manner, so its inclusion is on an ad hoc basis.

A recently introduced stabilization scheme [72] is based on the Spectral Vanishing Viscosity (SVV) idea of Tadmor [73]. This approach adds a small amount of dissipation, decreasing with mode number, to high-frequency components of the POD. SVV is implemented by a convolution viscosity kernel parameterized by a viscosity amplitude $\epsilon = \frac{\alpha}{N}$ where N is the truncation level of the POD-based dynamical system, and a cut-off mode $M < N$ which determines the modes for added viscosity. The free parameters need to be determined for the specific flow problem at hand. Results are given for the periodic flow past a 2-d circular cylinder in [72]. However, as the authors state: "correcting the long-term behavior of the POD model does not imply that the model can correctly capture the correct bifurcation dynamics of the flow", as they demonstrate at $Re\,500$.

The irony lies in the fact that we know the solution to the system of differential

Equation (4.8) very well from the POD procedure. For instance, the driven cavity flow at $Re\,8500$ was uniformly sampled after all transients had ceased, and the POD temporal eigenfunctions are periodic as expected. Therefore, it seems reasonable to assume that the failure of the dynamical system to reproduce the temporal eigenfunctions lies with numerical inaccuracies, not a deficiency of the basis functions. Why not use the known solution of Equation (4.8) to adjust the coefficients so that the dynamical system can evolve the correct solution at the Reynolds number of simulation?

4.3 The Intrinsic Stabilization scheme

This method will be called *intrinsic stabilization* to emphasize that the information required for its implementation is inherent in the problem. The algorithm begins by initializing the ODEs with the true solution at time zero at whatever truncation level M is desired. For each time step thereafter, time-step the dynamical system (I used fourth order Runge-Kutta), compute and save the error made, and reset the time-stepped solution from the known solution. Evolve the system for the time period covered by the POD analysis. Let z_k be the computed solution, y_k be the exact solution, and err_k be the derived error function for mode k. Then,

$$\frac{dy_k}{dt} = \frac{dz_k}{dt} + err_k(t)\ . \tag{4.15}$$

If the error function could be characterized functionally, then the dynamical system could be adjusted to more closely approximate the ideal system whose solution is the exact y_k.

After looking at the error functions for the simple periodic driven cavity flow, it was evident that there was a strong correlation with the temporal functions y_k themselves, as can be seen in Figures (4.3) and (4.4) for the first pair of temporal

modes.

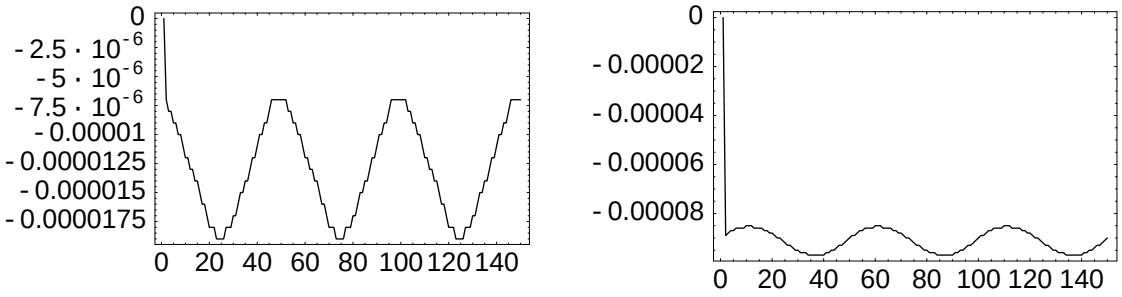

Figure 4.3: 1^{st} (left) and 2^{nd} (right) error functions err_1 and err_2 for driven cavity flow at Re 8500.

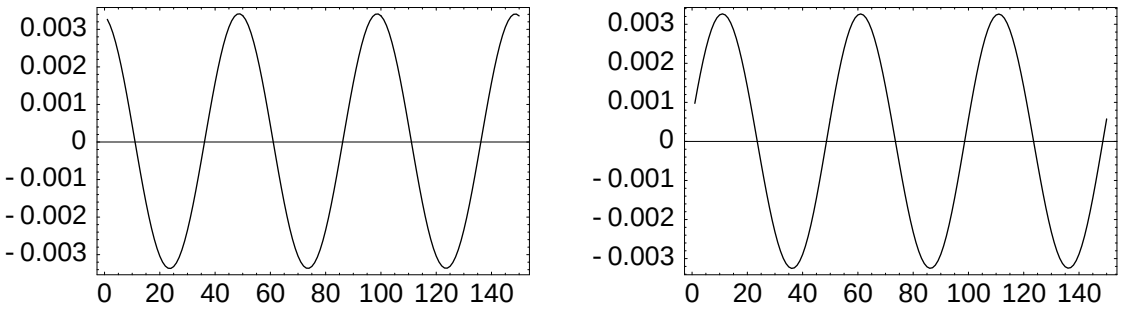

Figure 4.4: 1^{st} (left) and 2^{nd} (right) temporal functions y_1 and y_2 for driven cavity flow at Re 8500.

Since these functions form an orthogonal basis, it makes sense to project the error function onto this basis. The mean of z_k is not necessarily zero (as it should be), so this produces a constant term in the correction.[11]

$$\alpha_k = \frac{(\sum_{i=1}^{N} err_k(t_i))}{N} , \tag{4.16}$$

$$\beta_{ki} = \frac{\langle err_k - \alpha_k, y_i \rangle}{\langle y_i, y_i \rangle} , \tag{4.17}$$

$$err_k \approx \alpha_k + \sum_{i=1}^{M} \beta_{ki} y_i . \tag{4.18}$$

The advantage of this formulation is its ease of incorporation into the dynamical

[11]In practice, $err_k(t)$ needs a few time steps to settle, as can be seen in Figure (4.3), so the correction factors are based on data from the 2^{nd} period.

system:

$$\frac{dy_k}{dt} \approx (a_k + \alpha_k) + \sum_{i=1}^{M}(b_{ki} + \beta_{ki})y_i + \sum_{i=1}^{M}\sum_{j=1}^{M} c_{kij}y_i y_j \tag{4.19}$$

Figure (4.5) shows the effect of intrinsic stabilization for the driven cavity flow at Re 8500, and Figure (4.6) illustrates its asymptotic behavior.

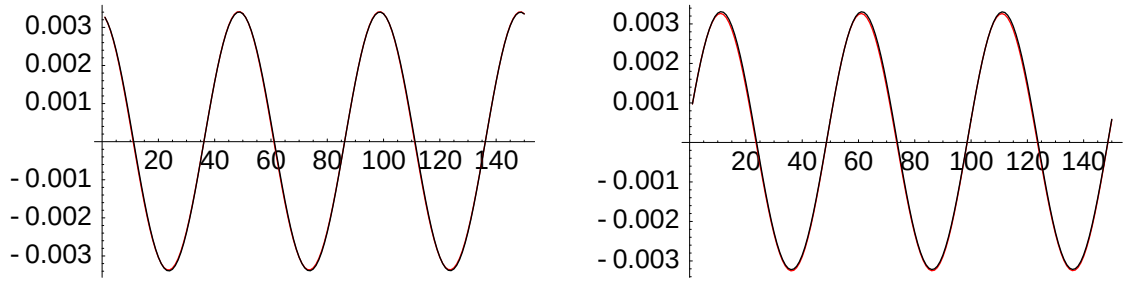

Figure 4.5: 2 mode low-dimensional intrinsically stabilized model (left: mode 1; right: mode 2) for driven cavity flow at Re 8500; red = exact from POD, black = evolved.

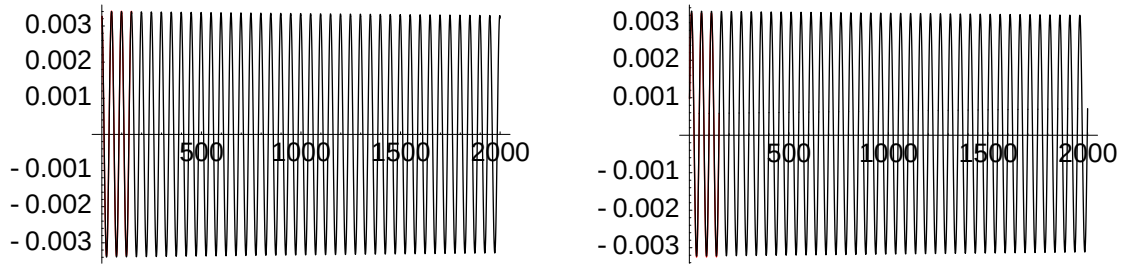

Figure 4.6: Asymptotic behavior of 2 mode low-dimensional (left: mode 1; right: mode 2) intrinsically stabilized model for driven cavity flow at Re 8500; red = exact from POD, black = evolved.

The short term tracking for the flow past the square cylinder is quite good without any special treatment, as shown in Figure (4.7), but again the asymptotic behavior (Figure 4.8) could sabotage a parameter continuation effort. Intrinsic stabilization corrects this, as illustrated in Figures (4.9) and (4.10). Moreover, the correct limit cycle behavior is obtained by this method.

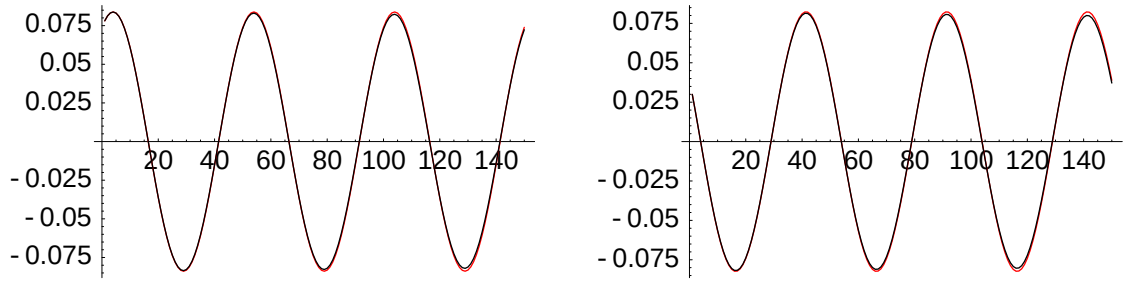

Figure 4.7: 2 mode low-dimensional model (left: mode 1; right: mode 2) for square cylinder wake flow at Re 55; red = exact from POD, black = evolved.

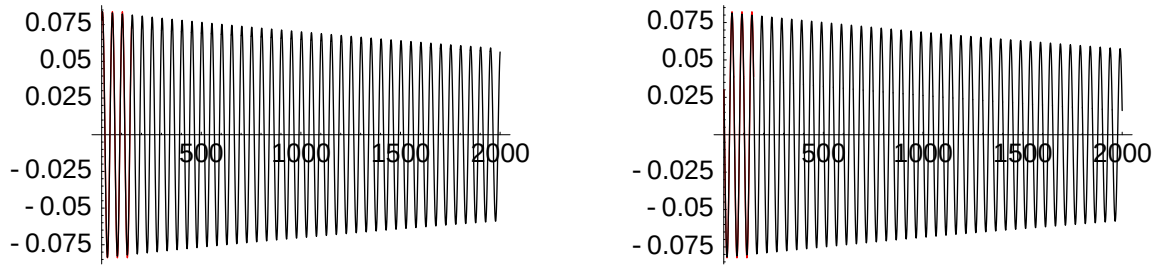

Figure 4.8: Asymptotic behavior of 2 mode low-dimensional model (left: mode 1; right: mode 2) for square cylinder wake flow at Re 55; red = exact from POD, black = evolved.

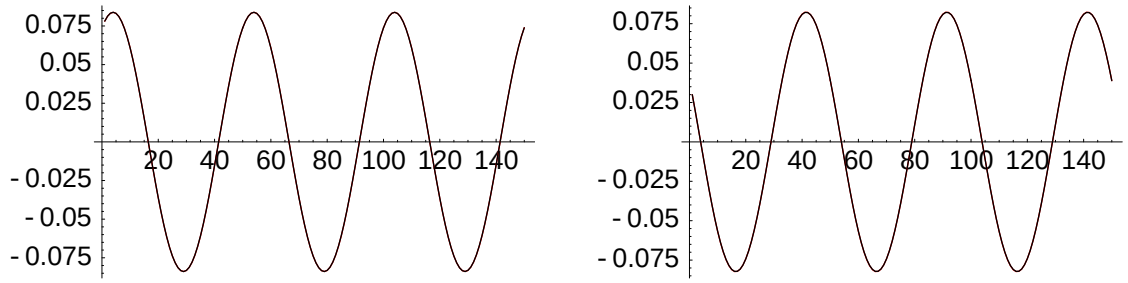

Figure 4.9: 2 mode low-dimensional intrinsically stabilized model (left: mode 1; right: mode 2) for square cylinder wake flow at Re 55; red = exact from POD, black = evolved.

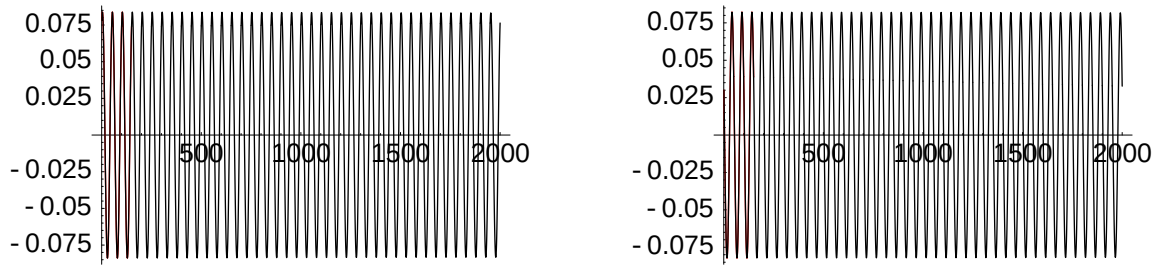

Figure 4.10: Asymptotic behavior of 2 mode-low dimensional intrinsically stabilized model (left: mode 1; right: mode 2) for square cylinder wake flow at Re 55; red = exact from POD, black = evolved.

Sirisup *et al.* [72] point out that a dynamical system may appear to be accurate for a certain number of shedding cycles, and then diverge. For flow past a circular cylinder at $Re\,100$, a six-mode model with no stabilization exhibits divergence after 40 shedding cycles and a ten-mode model diverges after 500 shedding cycles. Figures (4.11) - (4.14) show the envelopes for the four-mode intrinsically stabilized model for flow past a square cylinder at $Re\,90$ for 1000 shedding cycles, clearly showing that divergence is not a problem using this stabilization method, even for the extremely low-dimensional system of four modes which captures only 98.75% of the energy.

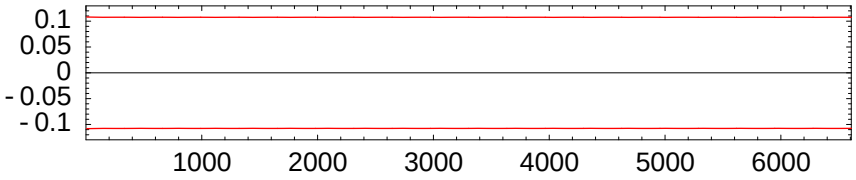

Figure 4.11: Envelope of first temporal mode.

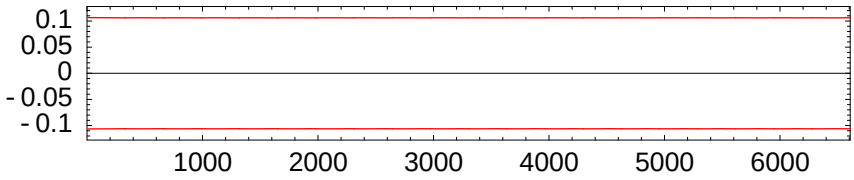

Figure 4.12: Envelope of second temporal mode.

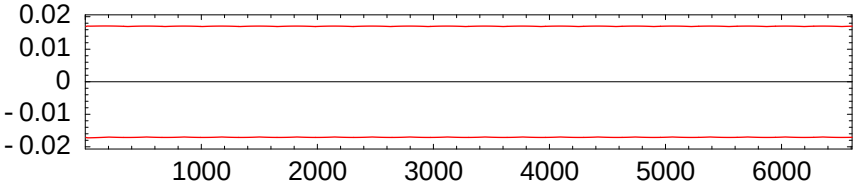

Figure 4.13: Envelope of third temporal mode.

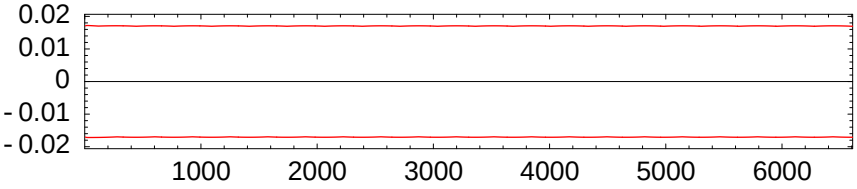

Figure 4.14: Envelope of fourth temporal mode.

Time history of envelopes of temporal modes for a four-mode intrinsically stabilized dynamical system of flow past a square cylinder at $Re\,90$ for 1000 shedding cycles. One shedding cycle is 6.6.

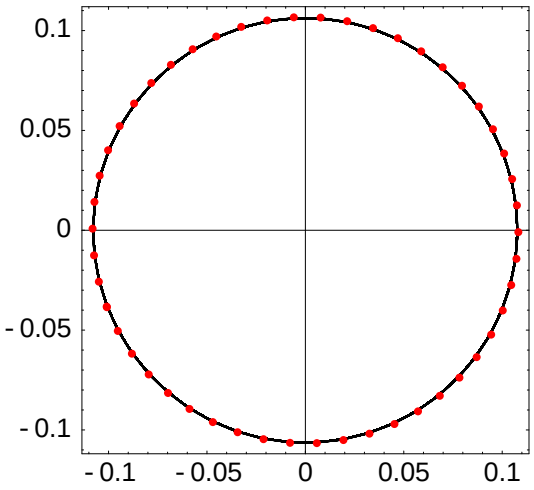

Figure 4.15: Phase portrait of modes 1 & 2.

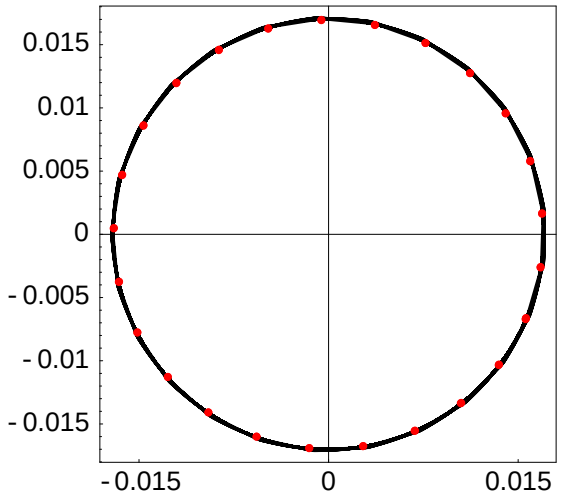

Figure 4.16: Phase portrait of modes 3 & 4.

Four-mode intrinsically stabilized dynamical system of flow past a square cylinder at Re 90 for 1000 shedding cycles in black; red dots mark one cycle of corresponding temporal modes from POD.

Figures (4.17) - (4.32) show a more dramatic example of the success of this procedure for the driven cavity flow for short term tracking at Re 10000 where the flow is quasi-periodic. The modes are plotted over nominally two full cycles, the time period covered by the snapshots ingested by the POD. A cycle is approximately $T = 31.2$. The sixteen-mode low dimensional model for this flow illustrates the ability of the intrinsic stabilization method to recover modes containing very little energy; mode 16 in Figure (4.32) accounts for only 0.04% of the energy. The need for the stabilization procedure to compensate for divergence from zero mean is evident in modes 13 - 16. Another strong advantage of intrinsic stabilization over the SVV method is the fact that all modes of the model are recovered quite well. With the SVV method, after the cut-off mode inaccuracies are introduced which worsen with increasing modes although the amplitude of even those modes is bounded, an improvement over no stabilization at all [72].

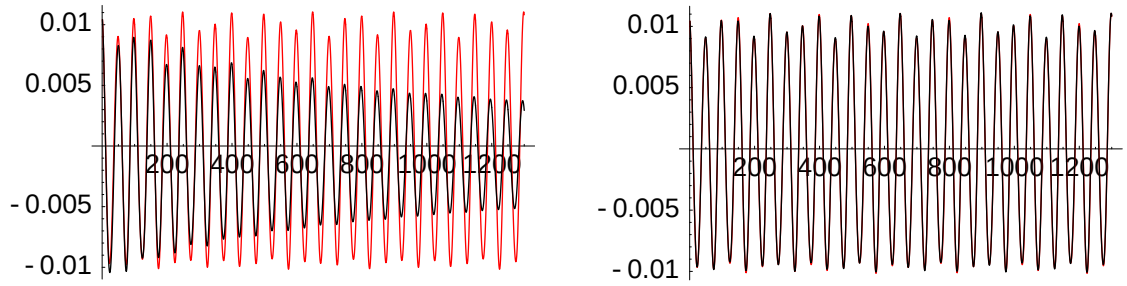

Figure 4.17: Mode 1 of 16 mode model for driven cavity flow at Re 10000; red = exact from POD, black = evolved, left = "raw" coefficients, right = intrinsically stabilized.

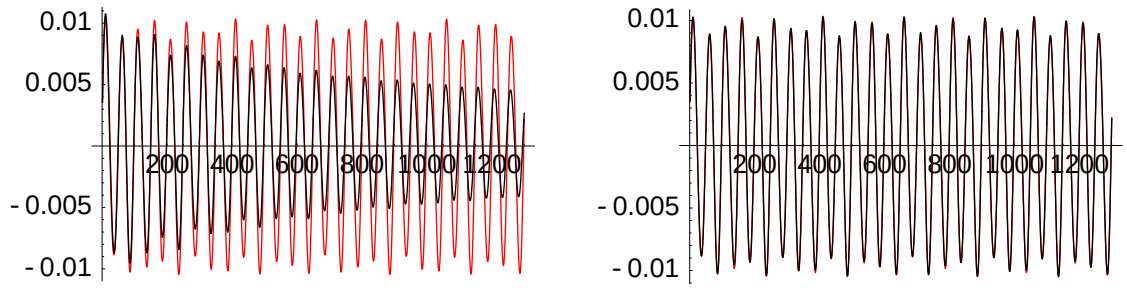

Figure 4.18: Mode 2 of 16 mode model for driven cavity flow at Re 10000; red = exact from POD, black = evolved, left = "raw" coefficients, right = intrinsically stabilized.

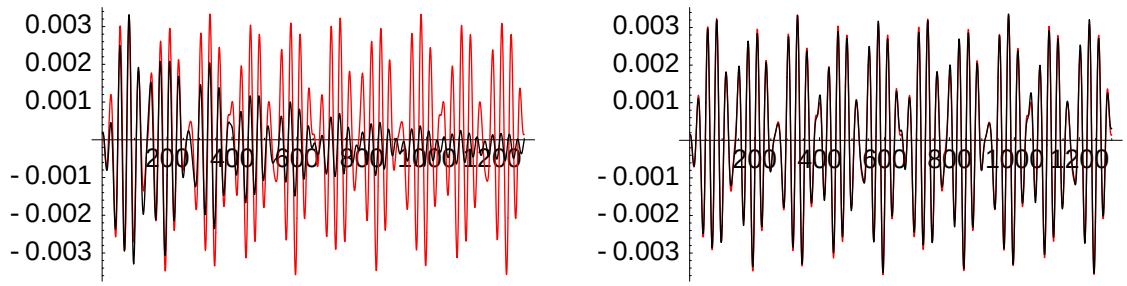

Figure 4.19: Mode 3 of 16 mode model for driven cavity flow at Re 10000; red = exact from POD, black = evolved, left = "raw" coefficients, right = intrinsically stabilized.

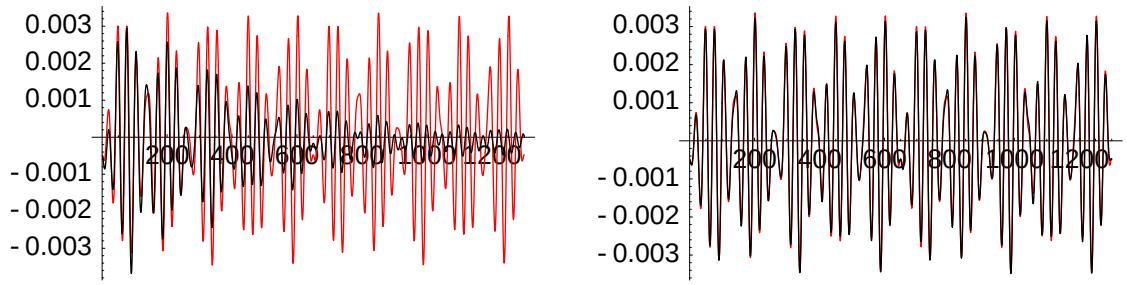

Figure 4.20: Mode 4 of 16 mode model for driven cavity flow at Re 10000; red = exact from POD, black = evolved, left = "raw" coefficients, right = intrinsically stabilized.

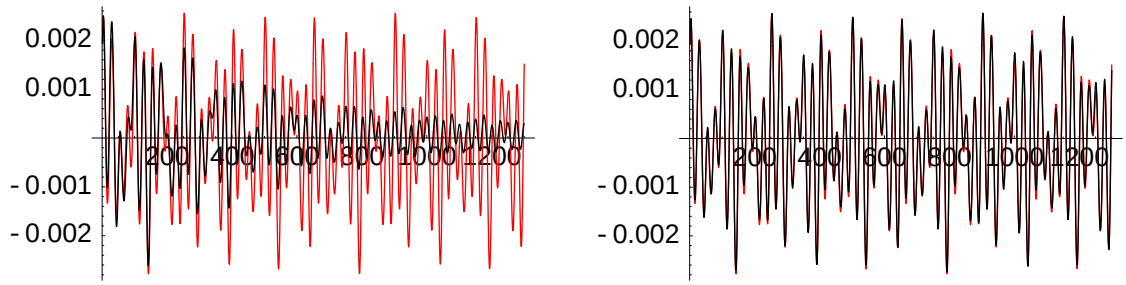

Figure 4.21: Mode 5 of 16 mode model for driven cavity flow at *Re* 10000; red = exact from POD, black = evolved, left = "raw" coefficients, right = intrinsically stabilized.

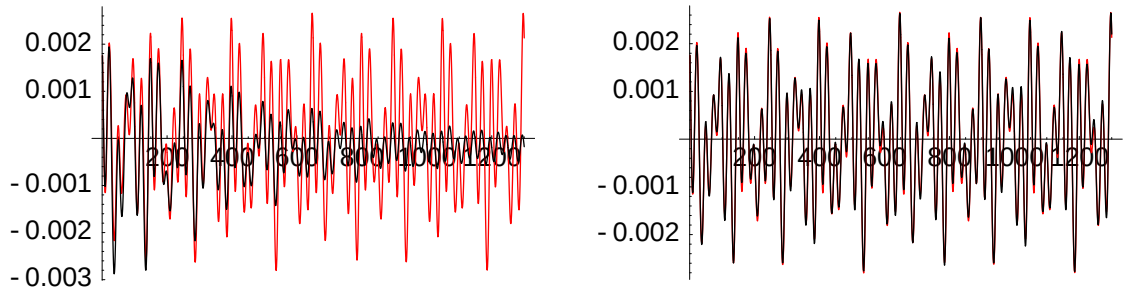

Figure 4.22: Mode 6 of 16 mode model for driven cavity flow at *Re* 10000; red = exact from POD, black = evolved, left = "raw" coefficients, right = intrinsically stabilized.

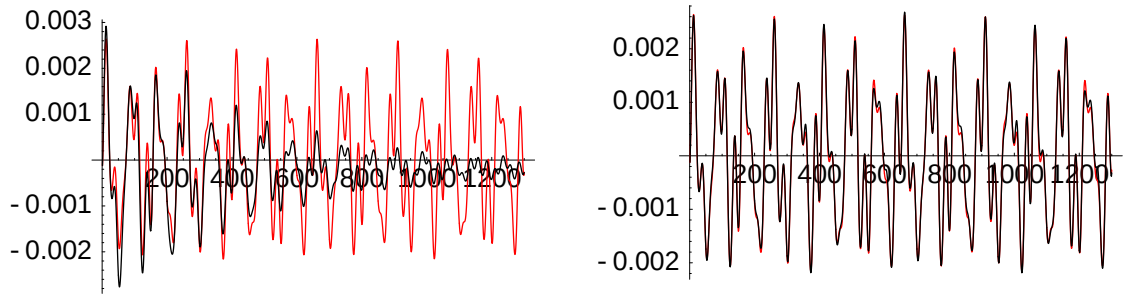

Figure 4.23: Mode 7 of 16 mode model for driven cavity flow at *Re* 10000; red = exact from POD, black = evolved, left = "raw" coefficients, right = intrinsically stabilized.

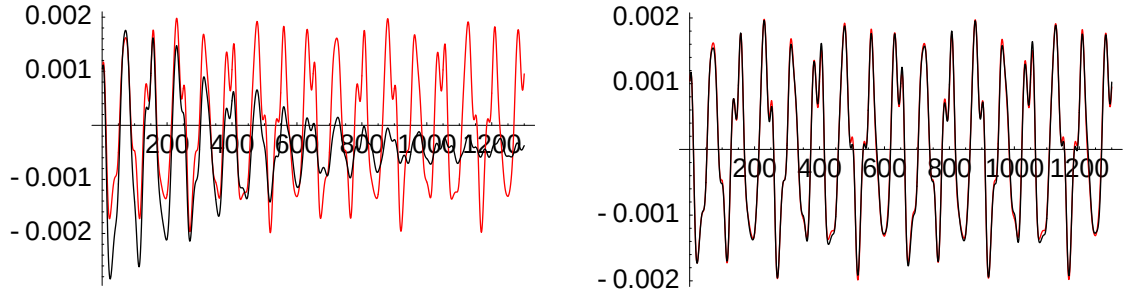

Figure 4.24: Mode 8 of 16 mode model for driven cavity flow at *Re* 10000; red = exact from POD, black = evolved, left = "raw" coefficients, right = intrinsically stabilized.

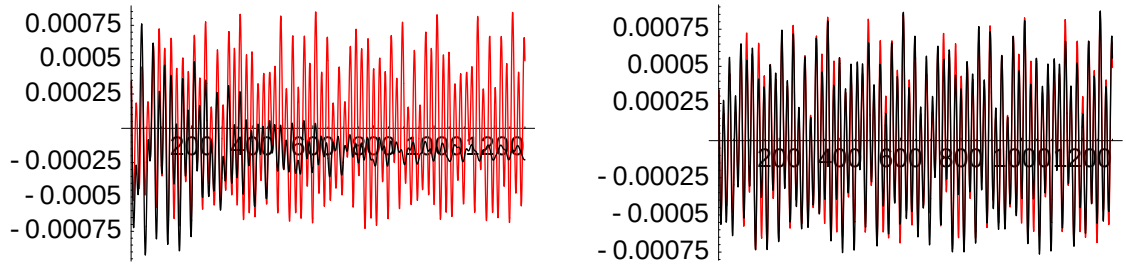

Figure 4.25: Mode 9 of 16 mode model for driven cavity flow at Re 10000; red = exact from POD, black = evolved, left = "raw" coefficients, right = intrinsically stabilized.

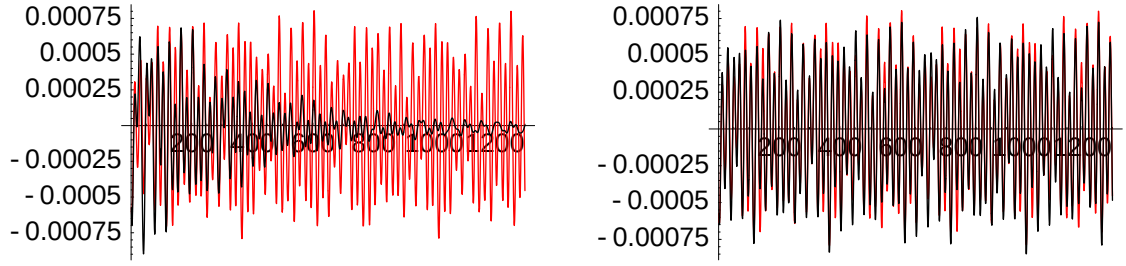

Figure 4.26: Mode 10 of 16 mode model for driven cavity flow at Re 10000; red = exact from POD, black = evolved, left = "raw" coefficients, right = intrinsically stabilized.

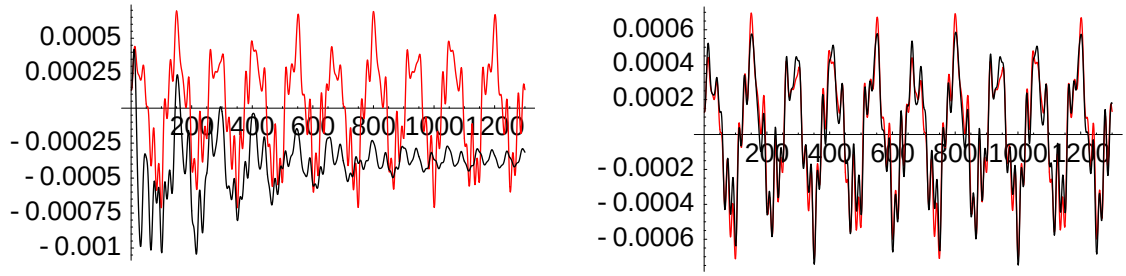

Figure 4.27: Mode 11 of 16 mode model for driven cavity flow at Re 10000; red = exact from POD, black = evolved, left = "raw" coefficients, right = intrinsically stabilized.

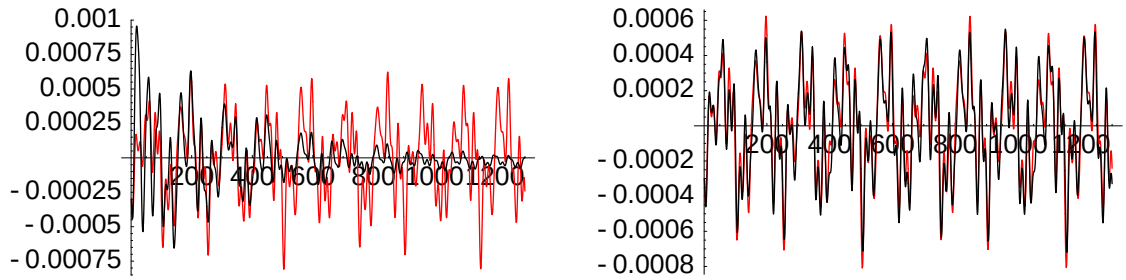

Figure 4.28: Mode 12 of 16 mode model for driven cavity flow at Re 10000; red = exact from POD, black = evolved, left = "raw" coefficients, right = intrinsically stabilized.

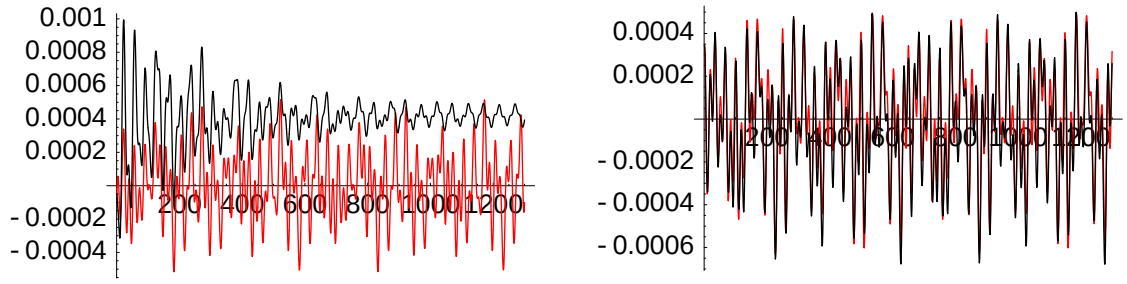

Figure 4.29: Mode 13 of 16 mode model for driven cavity flow at Re 10000; red = exact from POD, black = evolved, left = "raw" coefficients, right = intrinsically stabilized.

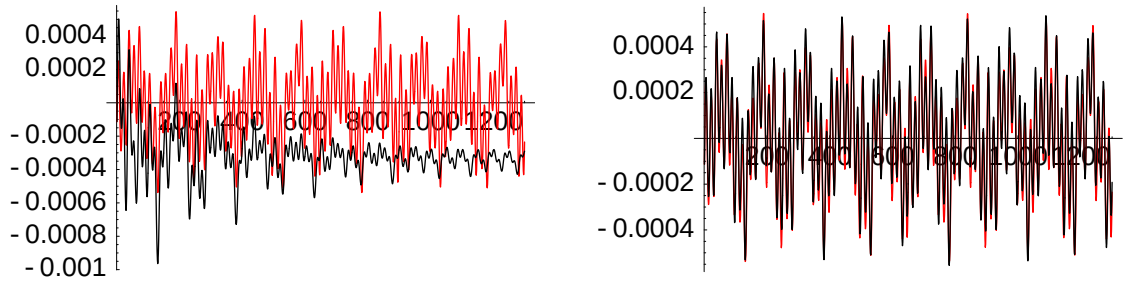

Figure 4.30: Mode 14 of 16 mode model for driven cavity flow at Re 10000; red = exact from POD, black = evolved, left = "raw" coefficients, right = intrinsically stabilized.

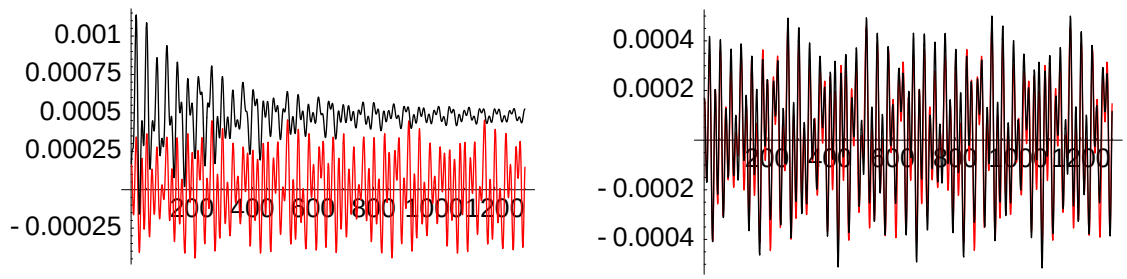

Figure 4.31: Mode 15 of 16 mode model for driven cavity flow at Re 10000; red = exact from POD, black = evolved, left = "raw" coefficients, right = intrinsically stabilized.

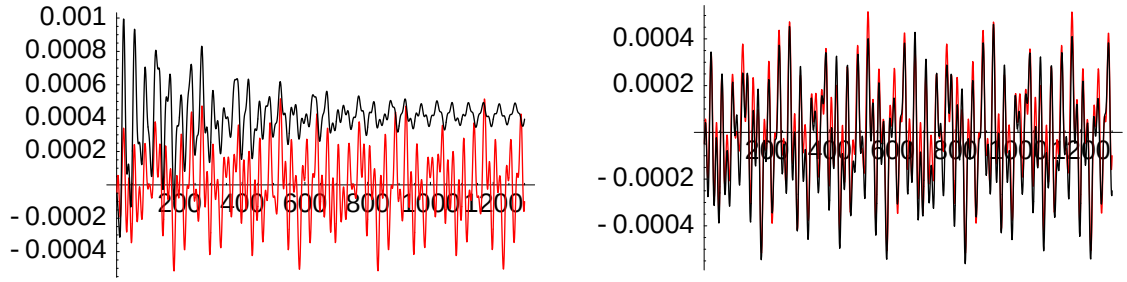

Figure 4.32: Mode 16 of 16 mode model for driven cavity flow at Re 10000; red = exact from POD, black = evolved, left = "raw" coefficients, right = intrinsically stabilized.

The long term tracking issue raised for the four-mode model for the square cylinder is addressed for the quasi-periodic flow of the driven cavity in Figures (4.33) - (4.48) which show the envelopes for the sixteen-mode intrinsically stabilized model for 1000 shedding cycles. We see again that divergence is not a problem using this stabilization method, even for the extremely low-energy higher modes.

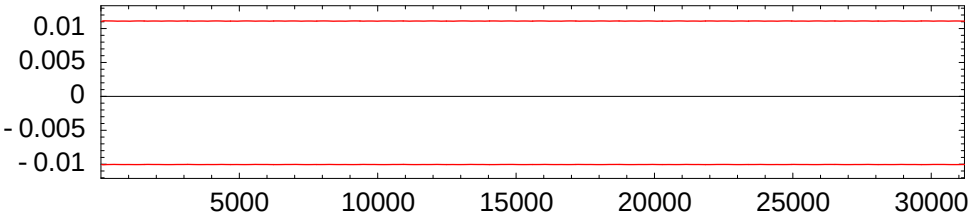

Figure 4.33: Envelope of first temporal mode.

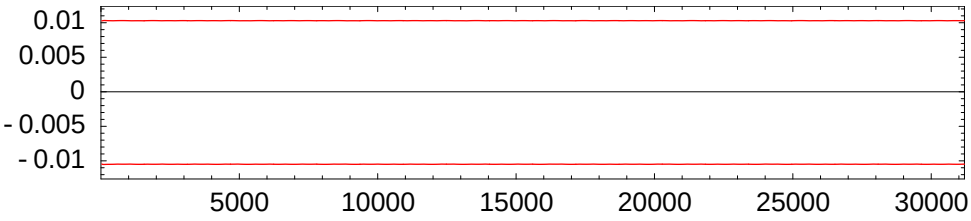

Figure 4.34: Envelope of second temporal mode.

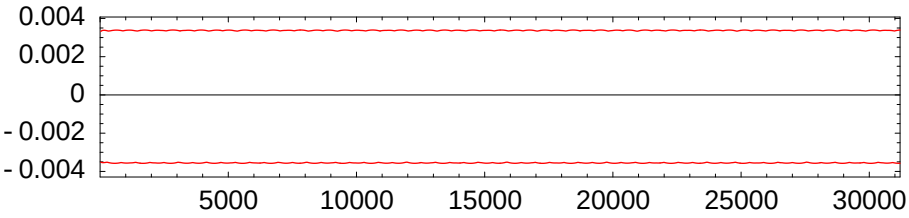

Figure 4.35: Envelope of third temporal mode.

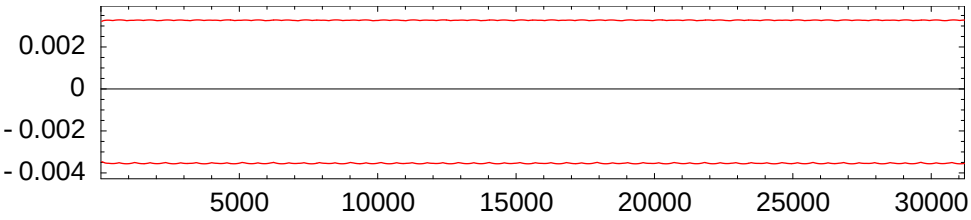

Figure 4.36: Envelope of fourth temporal mode.

Time history of envelopes of temporal modes for a four-mode intrinsically stabilized dynamical system of the quasi-periodic driven cavity flow at Re 10000 for 1000 shedding cycles. One shedding cycle is ≈ 31.2.

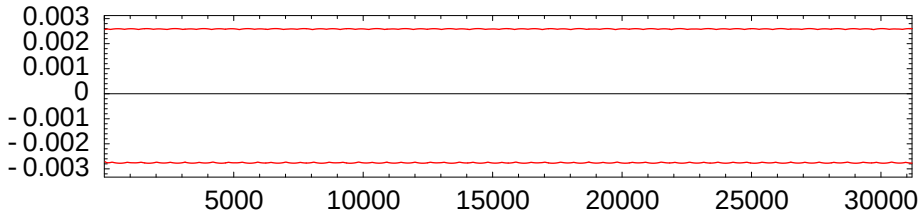

Figure 4.37: Envelope of temporal mode 5.

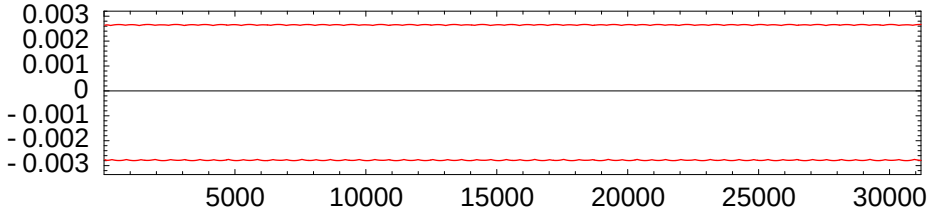

Figure 4.38: Envelope of temporal mode 6.

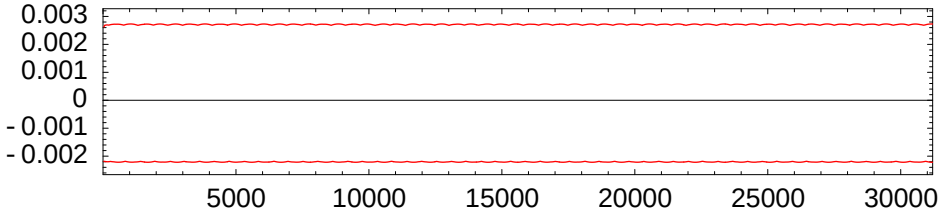

Figure 4.39: Envelope of temporal mode 7.

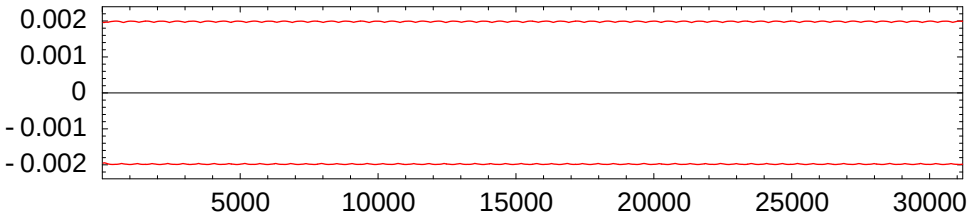

Figure 4.40: Envelope of temporal mode 8.

Time history of envelopes of temporal modes for a four-mode intrinsically stabilized dynamical system of the quasi-periodic driven cavity flow at Re 10000 for 1000 shedding cycles. One shedding cycle is ≈ 31.2.

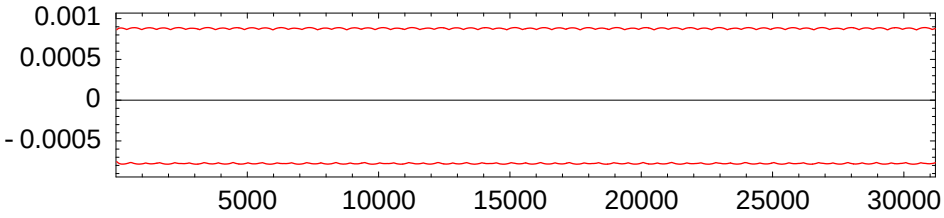

Figure 4.41: Envelope of temporal mode 9.

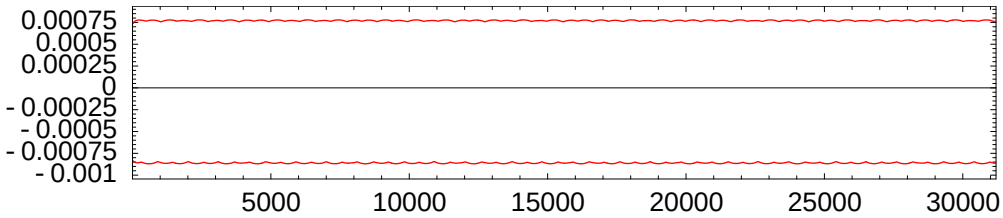

Figure 4.42: Envelope of temporal mode 10.

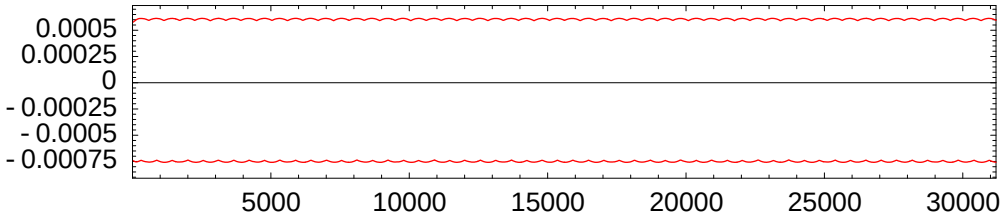

Figure 4.43: Envelope of temporal mode 11.

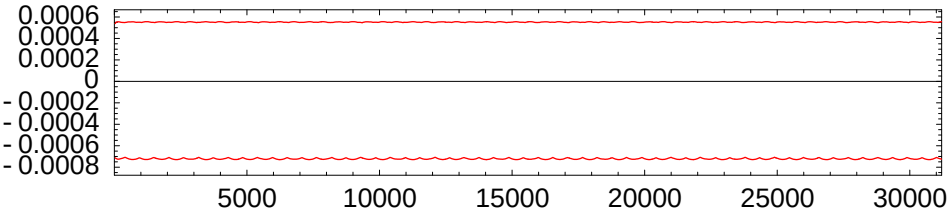

Figure 4.44: Envelope of temporal mode 12.

Time history of envelopes of temporal modes for a four-mode intrinsically stabilized dynamical system of the quasi-periodic driven cavity flow at Re 10000 for 1000 shedding cycles. One shedding cycle is ≈ 31.2.

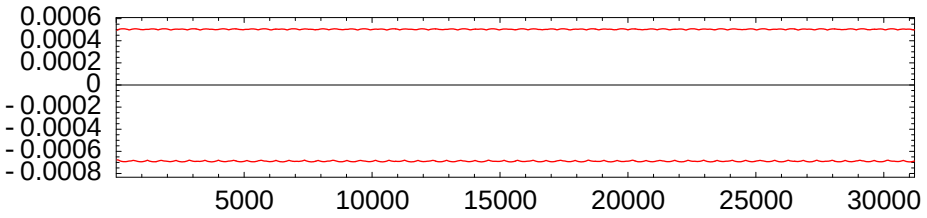

Figure 4.45: Envelope of temporal mode 13.

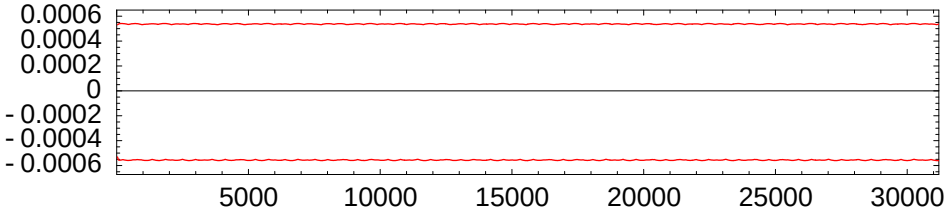

Figure 4.46: Envelope of temporal mode 14.

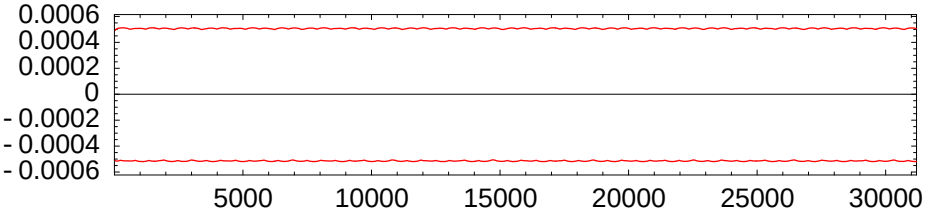

Figure 4.47: Envelope of temporal mode 15.

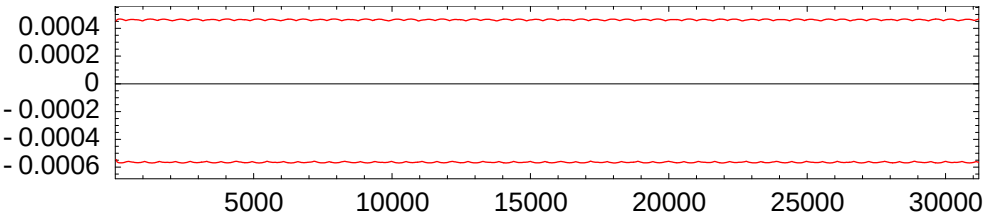

Figure 4.48: Envelope of temporal mode 16.

Time history of envelopes of temporal modes for a four-mode intrinsically stabilized dynamical system of the quasi-periodic driven cavity flow at Re 10000 for 1000 shedding cycles. One shedding cycle is ≈ 31.2.

Finally, phase portraits of pair of temporal modes are plotted in Figures (4.49) - (4.56) for 1000 cycles. "Cycle" is used loosely, since the modes do not exactly repeat, as evidenced by the seemingly solid black region which is the accumulation of paths traversed during this time period. The red dots mark two cycles of the temporal modes derived from the POD.

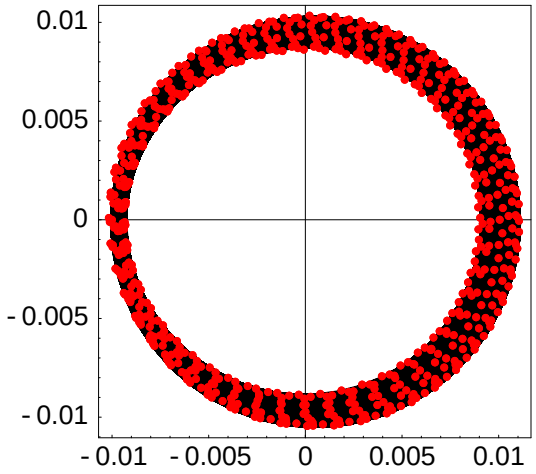

Figure 4.49: Phase portrait of modes 1 & 2.

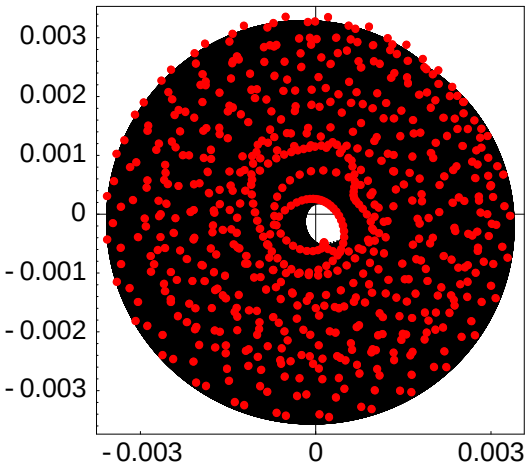

Figure 4.50: Phase portrait of modes 3 & 4.

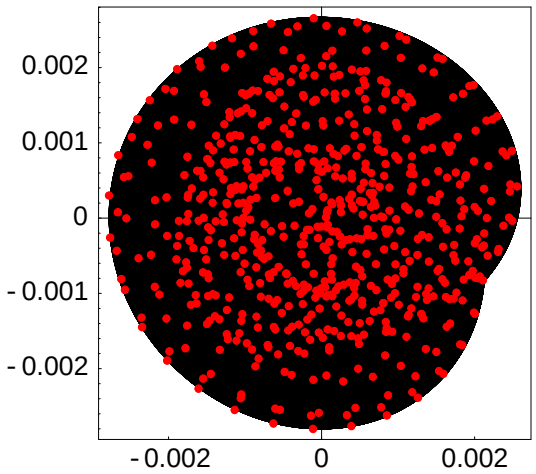

Figure 4.51: Phase portrait of modes 5 & 6.

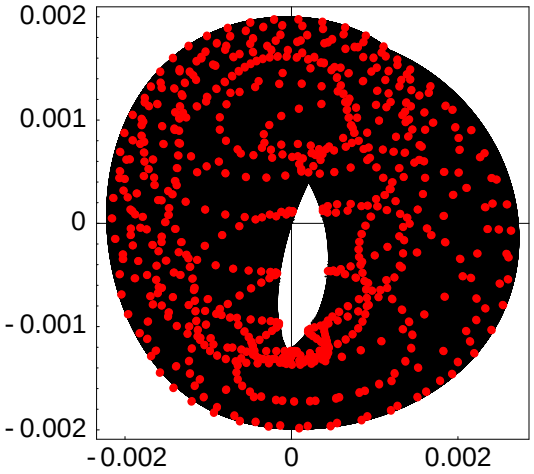

Figure 4.52: Phase portrait of modes 7 & 8.

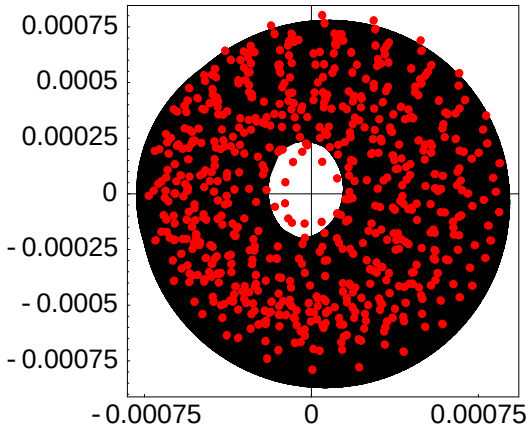

Figure 4.53: Phase portrait of modes 9 & 10.

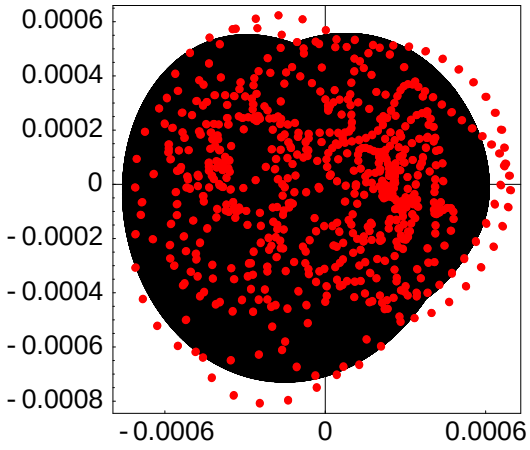

Figure 4.54: Phase portrait of modes 11 & 12.

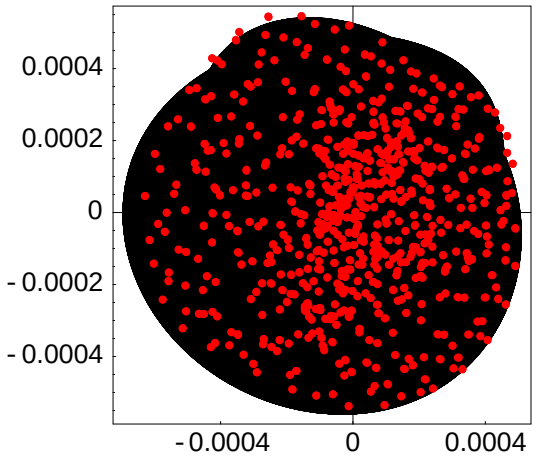

Figure 4.55: Phase portrait of modes 13 & 14.

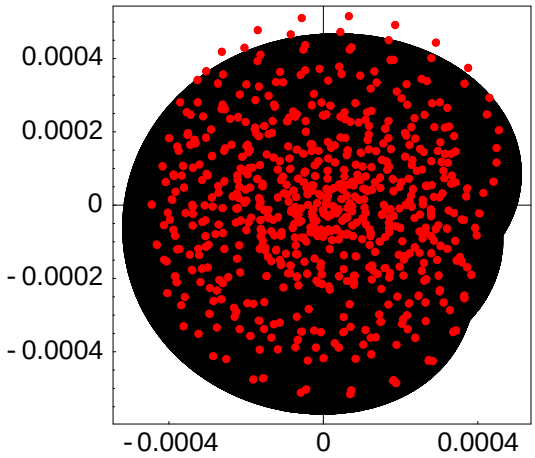

Figure 4.56: Phase portrait of modes 15 & 16.

Four-mode intrinsically stabilized dynamical system of the quasi-periodic driven cavity flow at Re 10000 for 1000 shedding cycles in black; red dots mark two cycles of corresponding temporal modes from POD.

5 Parameter continuation

A main objective in obtaining a dynamical system is to extend the validity of the dynamical system over a range of Reynolds numbers for the prediction of flow dynamics at unmodeled Reynolds numbers.

Specifically for fluid flow problems in the non-turbulent regime, we hope to identify transitions from steady to periodic behavior (Hopf bifurcation), and possibly a second bifurcation due to instability of the periodic flow via a torus or period-doubling bifurcation. We have seen how the dynamical system coefficients are computed at a particular Reynolds number. For parameter continuation to be successful, the dynamical system must predict the correct temporal behavior at Reynolds numbers other than the value used to generate the system. Projection onto the Navier-Stokes equations parameterizes the dynamical system by Re in a natural way (Equations (4.12) - (4.14)).

This chapter first describes parameter continuation techniques. Then these methods are applied to the dynamical system obtained via Equations (4.12) - (4.14) for the driven cavity flow (section 5.2) and the square cylinder flow (section 5.3). This proves to be inadequate for correct flow prediction both in amplitude and frequency, however. Section 5.4 details how to fix these shortcomings by parameterizing the dynamical system coefficients themselves with Reynolds number. The success of this strategy is illustrated for the driven cavity flow (section 5.5) and the square cylinder flow (section 5.6) . While coefficient parameterization does not help in the quasi-periodic flow at Re 10000, straightforward parameter continuation does reproduce qualitatively correct flow behavior for a range of Reynolds numbers and agrees with the DNS results at 10000. The caveat here is that the *stabilized* dynamical system was used. It should be noted that the stabilized system was used in every example in this chapter.

5.1 Single parameter continuation methods

Our system of ODEs can be written as:

$$\frac{d\mathbf{y}}{dt} = \mathbf{F}(\mathbf{y}, Re) \qquad \mathbf{y} \in \Re^M, Re \in \mathbb{R} \; . \tag{5.1}$$

We are interested in exploring solutions to this system as a function of Reynolds number using initial data and $\mathbf{F}$ for a specific Re. The Doedel's AUTO 97: Continuation and Bifurcation Software for Ordinary Differential Equations [65] has been used for this purpose, but a brief description of the algorithms involved follows.

The first step is to look for steady solutions of equation (5.1) starting at an initial value of $Re = Re_0$. Assuming the Jacobian $\mathbf{F_y}$ is nonsingular, this is not a problem. Call the starting solution $\mathbf{y}_0$. The goal is to find the branch of solutions starting from $(\mathbf{Y}, Re_0)$ as Re increases. Newton's method (solve $\mathbf{F}(\mathbf{y}, Re_0 + \Delta Re)$ with starting guess $\mathbf{y}_0$) is guaranteed to work if ΔRe is small enough by the Implicit Function Theorem, but it will fail near a fold point. The pseudo-arclength continuation method [74] is preferable because it is more robust and can detect folds (cusps or turning points) in the solution branch. Given a steady solution $(\mathbf{y}_0, Re_0)$ of (5.1) and the direction vector of the solution branch $(\frac{\mathbf{y}_0}{ds}, \frac{dRe_0}{ds})$ where s is any parameterization of the solution arc $(\mathbf{y}(s), Re(s))$, pseudo-arclength continuation consists of solving the following equations for $(\mathbf{y}_1, Re_1)$ [75]:

$$\mathbf{F}(\mathbf{y}_1, Re_1) = 0 \; , \tag{5.2}$$

$$(\mathbf{y}_1 - \mathbf{y}_0)^T \frac{d\mathbf{y}_0}{ds} + (Re_1 - Re_0) \frac{dRe_0}{ds} - \Delta s = 0 \; . \tag{5.3}$$

Define:

$$\mathbf{x} = (\mathbf{y}, Re)\,, \tag{5.4}$$

$$\mathbf{G}(\mathbf{x}) = \begin{pmatrix} \mathbf{F}(\mathbf{x}) \\ (\mathbf{x}-\mathbf{x}_0)^T \frac{d\mathbf{x}_0}{ds} - s \end{pmatrix}\,. \tag{5.5}$$

The eigenvalues of the pseudo-arclength Jacobian, $\mathbf{G}_\mathbf{x}$, are used to track the stability of the steady solutions: the real parts of the eigenvalues must be less than or equal to zero for stability. During continuation, the determinant of this Jacobian is monitored. A change in sign indicates a bifurcation at $\mathbf{x}_0$. When the Jacobian has a pair of pure imaginary eigenvalues $\pm\alpha\, i$, a Hopf bifurcation may arise with period $2\pi/\alpha$. After confirmation that a point is indeed the starting point for a branch of periodic solutions, an extended system can be defined for pseudo- arclength continuation along the branch. A periodic solution γ defines a Poincaré map T which tracks crossings of an $M-1$ dimensional disk transverse to γ at $\mathbf{y}_0$ on γ. $\mathbf{y}_0$ is a fixed point of T, and the stability of the solution γ can be determined by looking at the eigenvalues of the $(M-1)\times(M-1)$ Jacobian matrix of T. These eigenvalues are known as the Floquet multipliers of the periodic orbit γ. Monitoring these multipliers is necessary to identify bifurcations from the periodic branch. If a Floquet multiplier decreases through -1, then a period-doubling bifurcation may develop. If a pair of complex conjugate multipliers $q, \bar{q}$ have a modulus which increase though one, there may be a torus bifurcation signaling a branch of quasi-periodic solutions whose fundamental frequencies are $2\pi/P$ and $Im(\ln\, q)/P$ where P is the period of the solution and $q = e^{i\theta}$, each evaluated at the bifurcation point. [77]

The AUTO parameter continuation software "automates" all of these tasks. A subroutine needs to be generated to compute the specific function $\mathbf{F}$ for the problem of interest. Computation is then directed via text input files which define AUTO's

runtime constants. For evolution equations, the subroutine defines initial conditions and the computation of the right hand side of the system of ODEs at each time step. The text input files define the parameter range for that run. A run may be continued from either a special point, *e.g.*, a Hopf bifurcation point, identified in a previous run, or from a user-defined labeled point from a previous run. This feature permits the user to direct computation to the dynamical regions of interest. While the Jacobian $\mathbf{F_y}$ is mentioned above in the parameter continuation algorithm, in fact its specification is an option in AUTO. The user may specify it in a subroutine. If not, AUTO uses differencing to estimate it. There are size restrictions in the include file, *auto.h* on the effective problem dimension $NDIM$ and several other AUTO constants. If your problem exceeds the default, the file may be edited, followed by recompilation of AUTO. Computation time depends strongly on the hardware used, the type of computation, the setting of AUTO parameters such as tolerances and step sizes, and the problem dimension. Given all these variables, it is difficult to give a guideline in general, but Figure (5.1) shows the time dependency on the problem dimension. For these results, all AUTO parameters were held constant except for the number of modes used (equal to the number of ordinary differential equations in the dynamical system). The problem is computing the steady branch, and then continuing the periodic branch from the Hopf bifurcation for Re 10000. For this case, the time required[12] varies (approximately) as the cube of the problem dimension.

[12]Elapsed (wall clock) time from Linux *time -v* command.

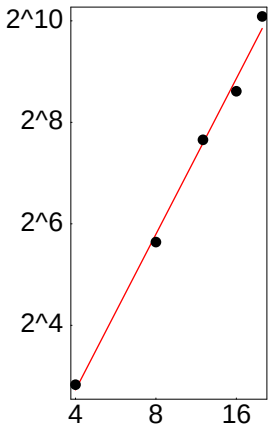

Figure 5.1: Sample timing for AUTO parameter continuation plotted as $\log_2(n)$ versus $\log_2(time)$. The slope of the least squares fitted line (red) is approximately 3, indicating a cubic growth of time with problem dimension.

5.2 Straightforward parameter continuation for the driven cavity flow

For the driven cavity flow, the dynamical system coefficients were computed at Re 8500 by Equations (4.12) - (4.14) This entails using the spatial eigenfunctions and mean flow at Re 8500, but leaving Re as a parameter. Four modes were used, and $M = 4$ unless otherwise specified. The optimal number for M will be addressed at the end of this chapter. AUTO was used to compute the steady branch. It located a Hopf bifurcation at Re 8446 which is consistent with both the DNS and POD total kinetic energy prediction. AUTO was able to continue the branch of periodic solutions from the Hopf bifurcation. Figures (5.2) and (5.3) compare the AUTO-computed solutions with the DNS results. The steady branch loses stability at the bifurcation point, as indicated by the dashed line in this and later diagrams. As expected, the coefficients at Re 8500 do an excellent job at 8500, but do not change as Re increases, hence cannot predict the orbit well at higher Reynolds numbers. This deficiency will be corrected in section 5.5.

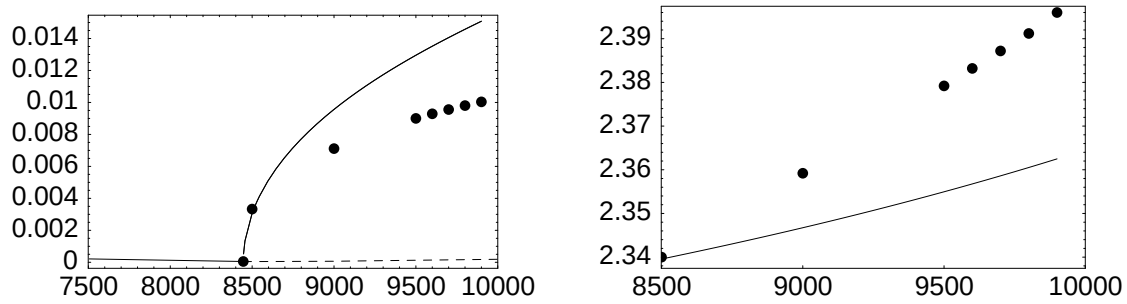

L_2 norm of solution

Period of solution

Figure 5.2: AUTO parameter continuation using basis functions at *Re* 8500 (solid line), DNS results (dots).

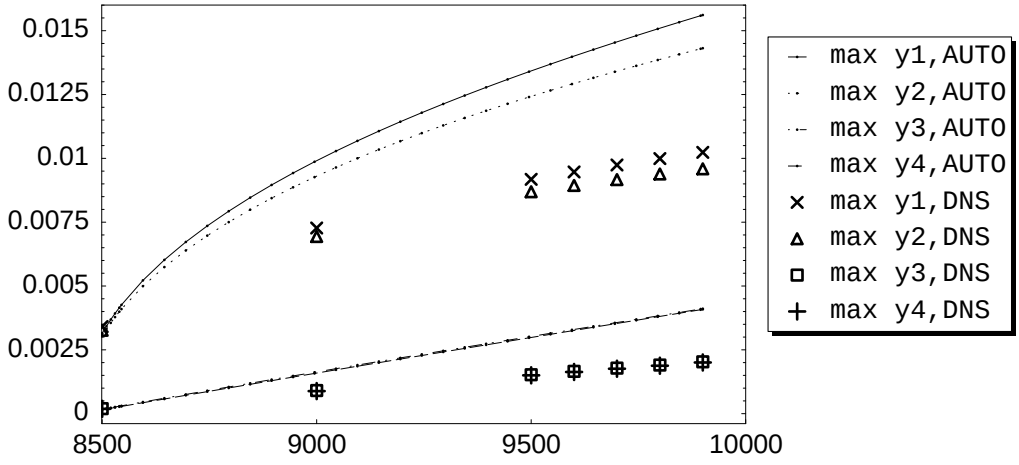

Figure 5.3: Maximum value of first 4 modes of solution: AUTO parameter continuation using basis functions at *Re* 8500 (solid line) compared with DNS results (see legend).

Next, we look at compensation for the loss of energy in the mean flow by modifying the linear and Re-independent coefficients in the dynamical system, as mentioned in Chapter 3, page 66. There is modest improvement in the amplitude prediction and good improvement in the period (Figures (5.4) and (5.5)). However, as we shall see in section 5.5, it is possible to do much better than this.

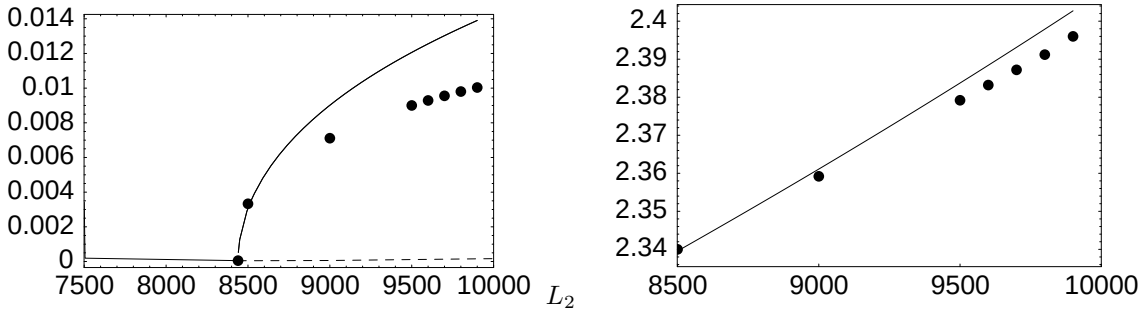

Figure 5.4: AUTO parameter continuation using basis functions at Re 8500 (solid line) with a mean correction compared with DNS results (dots).

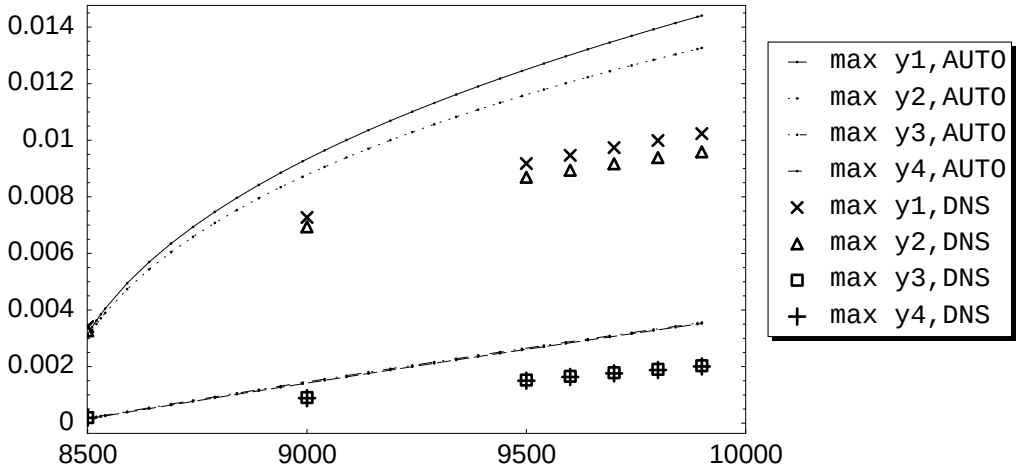

Figure 5.5: Maximum value of first 4 modes of solution: AUTO parameter continuation using basis functions at Re 8500 (solid line) with a mean correction compared with DNS results (see legend).

5.3 Straightforward parameter continuation for the square cylinder wake flow

As with the driven cavity, first see how well parameter continuation works by simply using the 4-dimensional dynamical system derived at $Re\,55$ (Figures (5.6) and 5.7). AUTO found a Hopf bifurcation at $\approx Re\,46$, which is a bit on the low side. The literature predicts the onset of vortex shedding between $Re\,50$ and $Re\,55$.[79], [78]. Overall, the amplitude predictions are poor, and the period extrapolation is worse. However, recall that we are going to fix this in section 5.6.

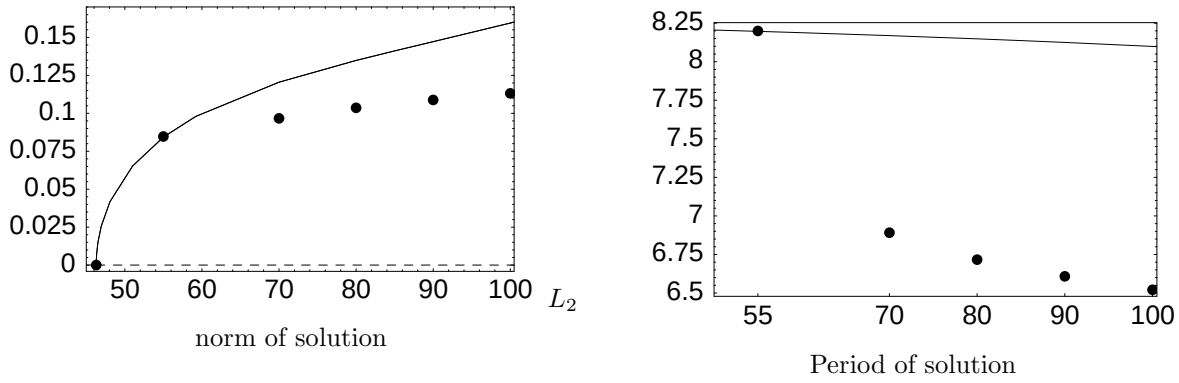

Figure 5.6: AUTO parameter continuation using basis functions at *Re* 55 (solid line), DNS results (dots).

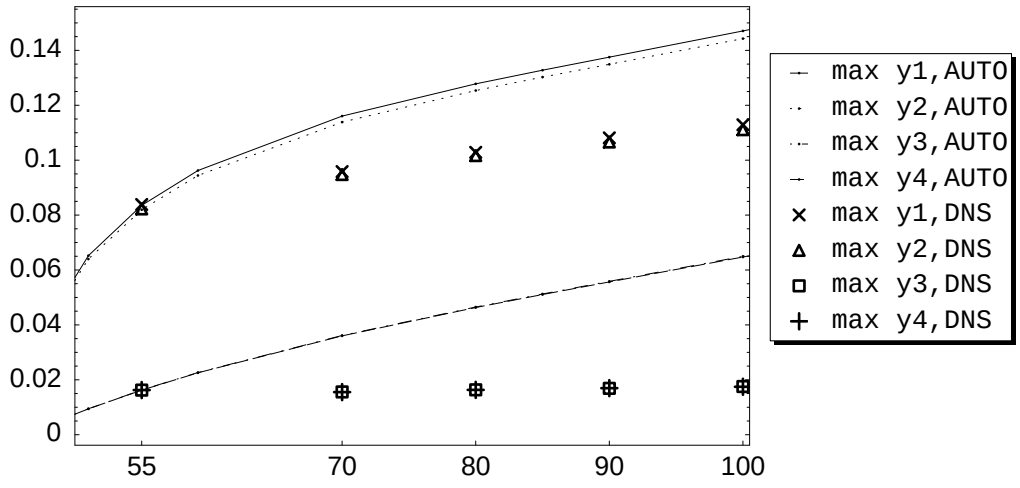

Figure 5.7: Maximum value of first 4 modes of solution: AUTO parameter continuation using basis functions at *Re* 55 (solid line) compared with DNS results (see legend).

5.4 Coefficient parameterization of the dynamical system

As we have seen in the previous sections, simply varying Re in a dynamical system with constant coefficients computed at a reference Reynolds number is not satisfactory for the dynamical systems derived from the driven cavity flow and the square cylinder wake flow. This is not really surprising, since the coefficients of the dynamical system depend upon the flow dynamics encapsulated in the eigenfunctions, and the dynamics change with Reynolds number. In this section, we show how to quantify the changes that occur in these coefficients, and then show how to parameterize them so that parameter continuation in Reynolds number can succeed.

Writing the dynamical system in terms of the normalized temporal eigenfunctions θ_k as well as the normalized spatial eigenfunction $\mathbf{\Phi}_k$ with eigenvalues λ_k yields:

$$\frac{d(\sqrt{\lambda_k}\,\theta_k)}{dt} = a_k + \sum_{i=1}^{N} b_{ki}\sqrt{\lambda_i}\,\theta_i + \sum_{i=1}^{N}\sum_{j=1}^{N} c_{kij}\sqrt{\lambda_i}\,\theta_i\sqrt{\lambda_j}\,\theta_j \;, \tag{5.6}$$

$$\Rightarrow \frac{d\theta_k}{dt} = \frac{a_k}{\sqrt{\lambda_k}} + \sum_{i=1}^{N} b_{ki}\frac{\sqrt{\lambda_i}}{\sqrt{\lambda_k}}\phi_i + \sum_{i=1}^{N}\sum_{j=1}^{N} c_{kij}\frac{\sqrt{\lambda_i}\,\sqrt{\lambda_j}}{\sqrt{\lambda_k}}\theta_i\,\theta_j \;. \tag{5.7}$$

For the driven cavity flow up to Re 9900 and the computed wake flow, the temporal eigenfunctions are quite similar because the input to the POD was normalized by period. In other words, on the snapshot time scale, the periodicity is the same for each flow. This implies that the change in coefficients is entirely due to the changes in eigenvalues at different Reynolds number.

We have seen empirical evidence in Chapter 3 to support linear scaling of the total kinetic energy and the percentage of kinetic energy belonging to each mode. The eigenvalues can be recovered as a product of these terms. This suggests modeling the eigenvalues as a product of the best linear fit to the total kinetic

energy and the percent energy per mode as a function of Reynolds number.

The linear scaling of the total kinetic energy has a theoretical basis as well. At a Hopf bifurcation occurring at $Re_{critical}$, the amplitude of the burgeoning disturbance grows as the square root of $Re - Re_{critical}$, *i.e.*, the square of the amplitude has linear growth [66]. The temporal signature is given by $\mathbf{y}$, and since the components of $\mathbf{y}$ are orthogonal,

$$\begin{aligned} \|\mathbf{y}\|^2 &= \sum_{k=1}^{M} \|y_k\|^2 \ , & (5.8) \\ &= \sum_{k=1}^{M} \lambda_k \ , & (5.9) \\ &= \text{total kinetic energy} \ . & (5.10) \end{aligned}$$

This suggests a way of adjusting the dynamical system coefficients to capture the transfer of energy between modes as a function of Reynolds number.

Rewriting the ODE system from Equation (4.8), for the temporal eigenfunctions with explicit Re dependence:

$$\frac{d\theta_k}{dt} = \frac{a_k}{\sqrt{\lambda_k}} + \frac{1}{Re}\frac{A_k}{\sqrt{\lambda_k}} + \sum_{i=1}^{M} b_{ki}\frac{\sqrt{\lambda_i}}{\sqrt{\lambda_k}}\theta_i + \sum_{i=1}^{M}\frac{B_{ki}}{Re}\frac{\sqrt{\lambda_i}}{\sqrt{\lambda_k}}\theta_i + \sum_{i=1}^{M}\sum_{j=1}^{M} c_{kij}\frac{\sqrt{\lambda_i}\sqrt{\lambda_j}}{\sqrt{\lambda_k}}\theta_i\,\theta_j \ , \tag{5.11}$$

where

$$\begin{aligned} a_k &= -\langle \mathbf{\Phi}_k, (\mathbf{u}_m \cdot \nabla)\mathbf{u}_m \rangle \ , \\ A_k &= -\langle \nabla\mathbf{\Phi}_k, \nabla\mathbf{u}_m \rangle \ , \\ b_{ki} &= -\langle \mathbf{\Phi}_k, (\mathbf{\Phi}_i \cdot \nabla)\mathbf{u}_m \rangle - \langle \mathbf{\Phi}_k, (\mathbf{u}_m \cdot \nabla)\mathbf{\Phi}_i \rangle \ , \\ B_{ki} &= -\langle \nabla\mathbf{\Phi}_k, \nabla\mathbf{\Phi}_i \rangle \ , \\ c_{kij} &= -\langle \mathbf{\Phi}_k, (\mathbf{\Phi}_i \cdot \nabla)\mathbf{\Phi}_j \rangle \ . \end{aligned}$$

Making the first order approximation that the coefficients in equation (5.11) derived at $Re = R_1$ and $Re = R_2$ are the same (since θ_k at $R_1 \approx \theta_k$ at R_2), the coefficients for R_2 can be derived from the coefficients at R_1 given the eigenvalues at R_1. For example,

$$a_k(R_2) = a_k(R_1) * \frac{\sqrt{\lambda_k(R_2)}}{\sqrt{\lambda_k(R_1)}} ,$$
$$A_k(R_2) = A_k(R_1) * \frac{R_2 * \sqrt{\lambda_k(R_2)}}{R_1 * \sqrt{\lambda_k(R_1)}} ,$$

where the notation $\langle\cdot\rangle_k(R_*)$ denotes a dependence on $Re = R_*$. Assuming the equality of eigenfunctions at differing Reynolds numbers is a major simplification and will be tested on the driven cavity flow and the square cylinder wake flow, although the premise is valid for any flow near a Hopf bifurcation.

5.5 Coefficient parameterizion for the driven cavity flow

To first test the validity of this premise, *Mathematica* was used to fit a quadratic curve to the top four eigenvalues known from the KL decomposition for the at Re 8500 , 9000 , 9500 , 9600 , 9700 , 9800, and 9900 for the driven cavity flow. Figures (5.8) and (5.9) show the results of AUTO parameter continuation using the modified coefficients. Now we see improved prediction of the amplitude change with Reynolds number, but the period extrapolation is terrible – the reason and cure for this will be discussed next.

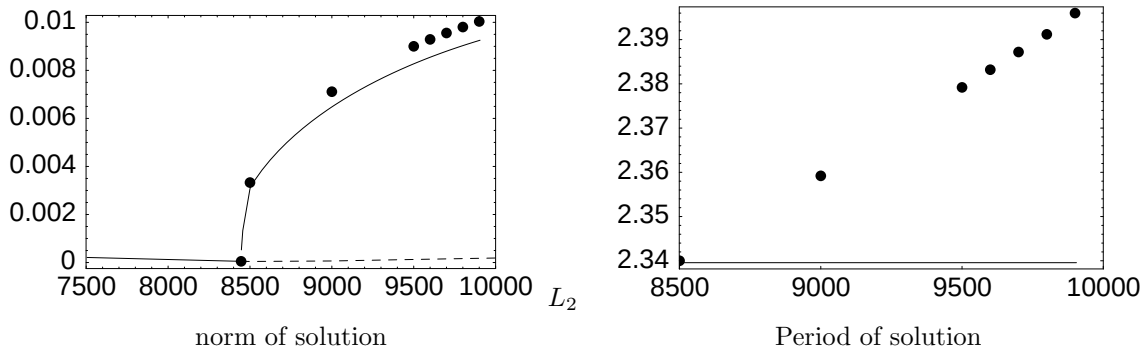

norm of solution Period of solution

Figure 5.8: AUTO parameter continuation using basis functions at *Re* 8500 (solid line) with eigenvalue scaling using best fit for eigenvalues compared with DNS results (dots).

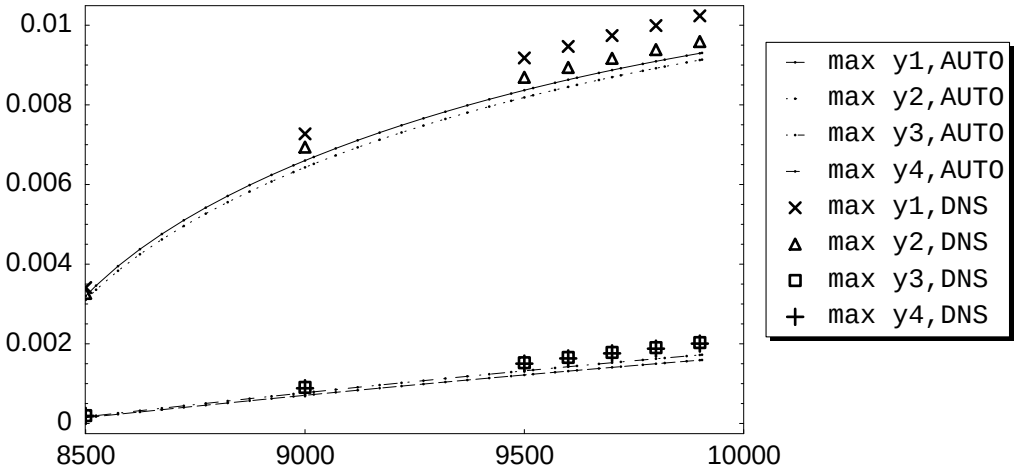

Figure 5.9: Maximum value of first 4 modes of solution: AUTO parameter continuation using basis functions at *Re* 8500 (solid line) with eigenvalue scaling using best fit for eigenvalues compared with DNS results (see legend).

As mentioned before, on the snapshot time scale used in this work, the period is fixed. This is why AUTO can't track the change in period that should occur with Reynolds number. However, this normalization was the key to the recognition of the eigenvalue scaling for amplitude change. Fortunately, amplitude and period effects on the dynamical system coefficients decouple quite nicely. Equations (5.12) - (5.14) illustrate how a change in time scale affects an ordinary differential equation:

$$\frac{dy}{dt} = F(y)\,, \tag{5.12}$$

$$\tau = \omega t\,, \tag{5.13}$$

$$\Rightarrow \frac{dy}{d\tau} = \frac{F(y)}{\omega}\,. \tag{5.14}$$

We see that a change in time scale is equivalent to introducing a factor times each coefficient on the right hand side. Incidentally, this also explains why parameter continuation of the dynamical system in Equation (4.8) with coefficients only parameterized by Reynolds number from the Galerkin projection (as in Equations (4.12) - (4.14)) is ineffectual at recovering the correct periodicity.

A linear fit to the period, as suggested by Figure(3.4), was used to introduce a factor $\frac{pref}{p(R)}$ where $pref$ is the period at $Re\,8500$ and R is the current Reynolds number in the parameter continuation. This factor is applied to all the coefficients to correct for the known change in time scale from a normalized period. This factor is independent of the amplitude scaling, and must be incorporated if the correct period is to be recovered. Since the eigenvalue scaling can't begin until the Reynolds number is 8500, the unscaled dynamical system at 8500 was used while AUTO computed the steady branch and found the Hopf bifurcation. A short continuation was then done to 8500, then the eigenvalue scaling and temporal factor were applied. Figures (5.10) and (5.11) show a vast improvement in the prediction

of the period of the solution at higher Reynolds numbers, so now we expect better amplitude prediction, particularly since we assume very good knowledge of the eigenvalues throughout the range.

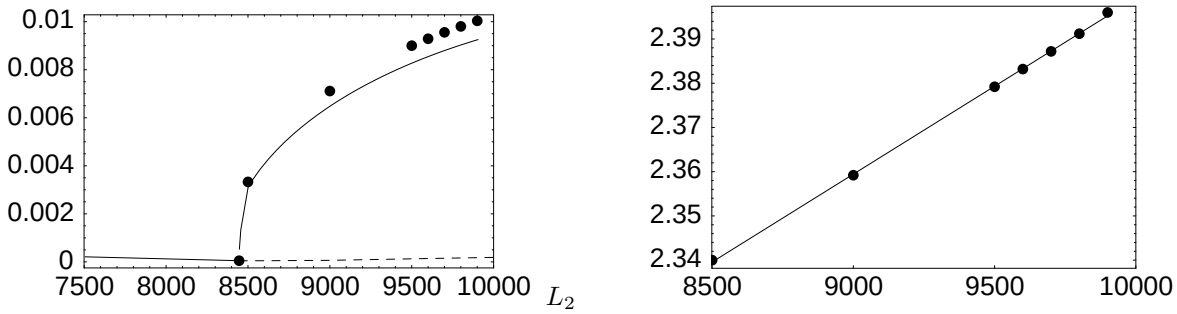

Figure 5.10: AUTO parameter continuation using basis functions at *Re* 8500 (solid line) with eigenvalue scaling using best fit for eigenvalues and period-modeling compared with DNS results (dots).

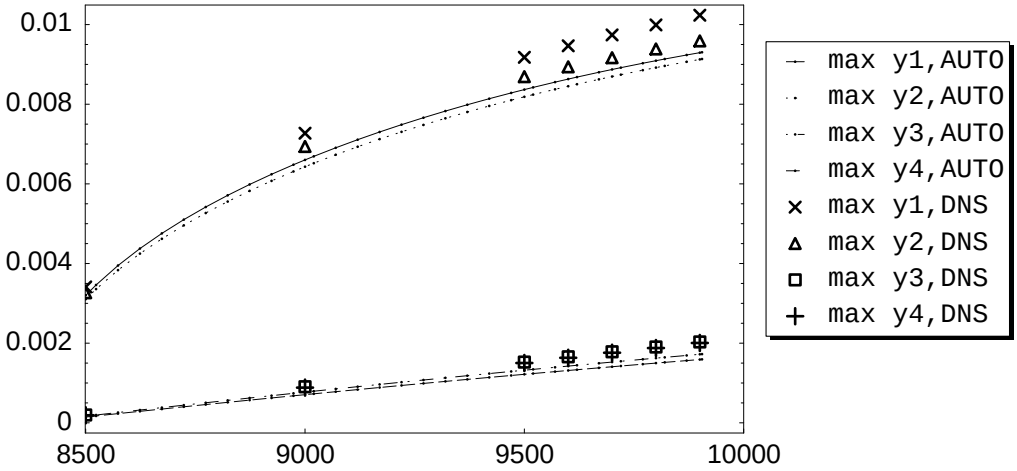

Figure 5.11: Maximum value of first 4 modes of solution: AUTO parameter continuation using basis functions at *Re* 8500 (solid line) with eigenvalue scaling using best fit for eigenvalues and period-modeling compared with DNS results (see legend).

The temporal eigenfunctions include more harmonics as the Reynolds number increases, so using reference functions in the middle of the dynamic range is a good compromise. To demonstrate this, Re 9000 was used as the reference. Again, the Re 8500 dynamical system was used to locate the Hopf bifurcation and march up to 8500. Figures (5.12) and (5.13) indeed show improvement.

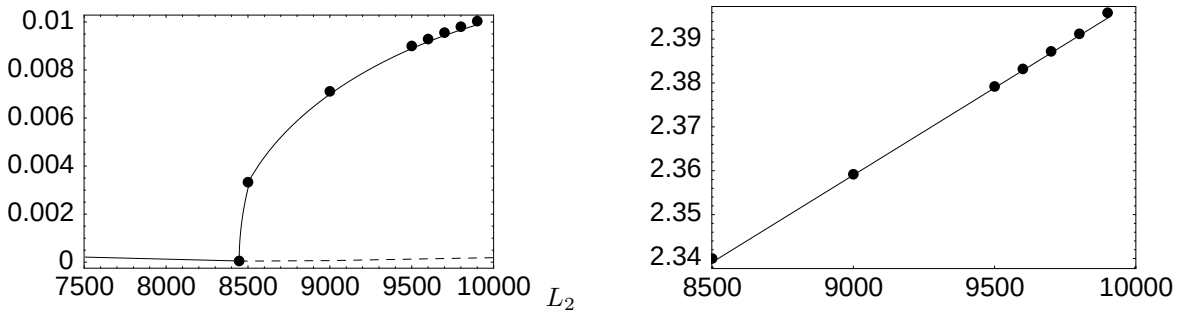

Figure 5.12: AUTO parameter continuation using basis functions at Re 9000 (solid line) with eigenvalue scaling using best fit for eigenvalues and period-modeling compared with DNS results (dots).

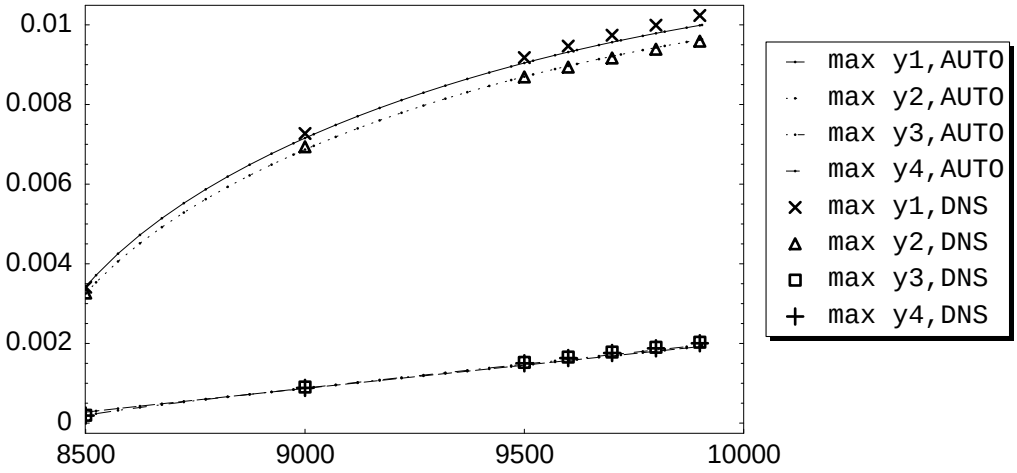

Figure 5.13: Maximum value of first 4 modes of solution: AUTO parameter continuation using basis functions at Re 9000 (solid line) with eigenvalue scaling using best fit for eigenvalues and period-modeling compared with DNS results (see legend).

For the previous cases, a good model of the eigenvalues was used. A more practical scenario was tested, assuming only knowledge of the flow at Re 8500 and Re 9500. A linear fit to the normalized eigenvalues and the total energy at these Reynolds numbers was made since Chapter 3 provided empirical evidence that this was a reasonable strategy. The eigenvalues were estimated by their modeled percentage $\times$ the modeled total energy. Figures (5.14) and (5.15) illustrate that this fairly drastic downsizing of a priori knowledge yields surprising good results.

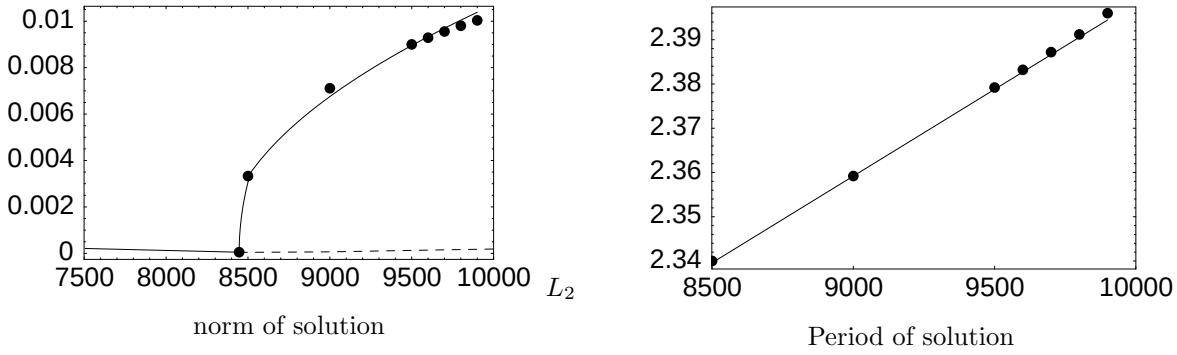

Figure 5.14: AUTO parameter continuation using POD data from Re 8500 and Re 9500 (solid line) with eigenvalue scaling, modeled eigenvalues and period-modeling compared with DNS results (see legend).

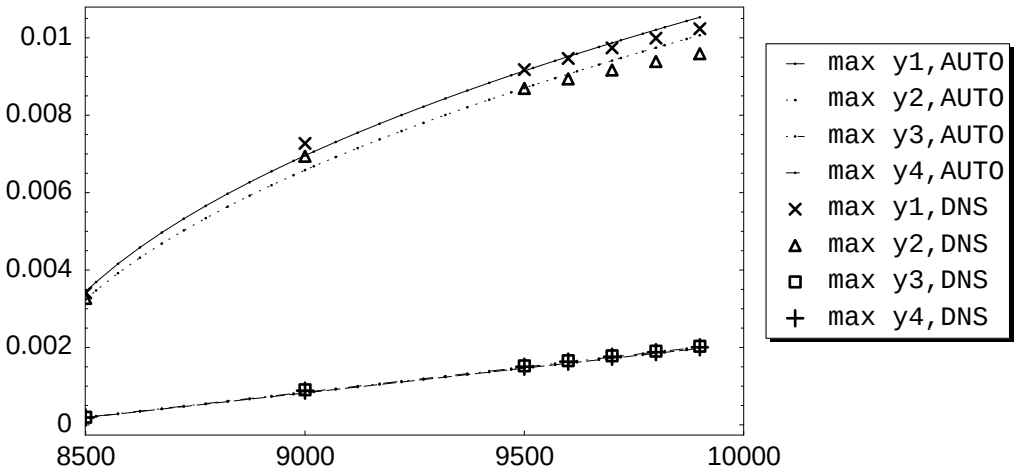

Figure 5.15: Maximum value of first 4 modes of solution: AUTO parameter continuation using POD data from Re 8500 and Re 9500 (solid line) with eigenvalue scaling, modeled eigenvalues and period-modeling compared with DNS results (see legend).

5.6 Coefficient parameterizion for the square cylinder wake flow

The temporal eigenfunctions for the *Re* range of 50 to 100 are again quite similar given the normalization of periodicity. Using the explicit parameterization by eigenvalues, equation (5.11), and the best fit to the eigenvalues allows AUTO to properly scale the amplitude of the solution as the Reynolds number changes, as shown in Figures (5.16) and (5.17).

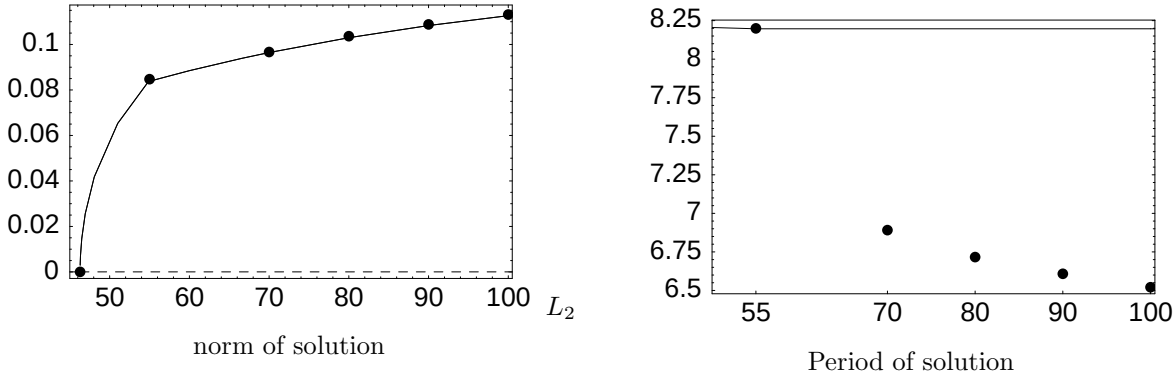

Figure 5.16: AUTO parameter continuation using basis functions at *Re* 55 (solid line) using best fit for eigenvalues compared with DNS results (dots).

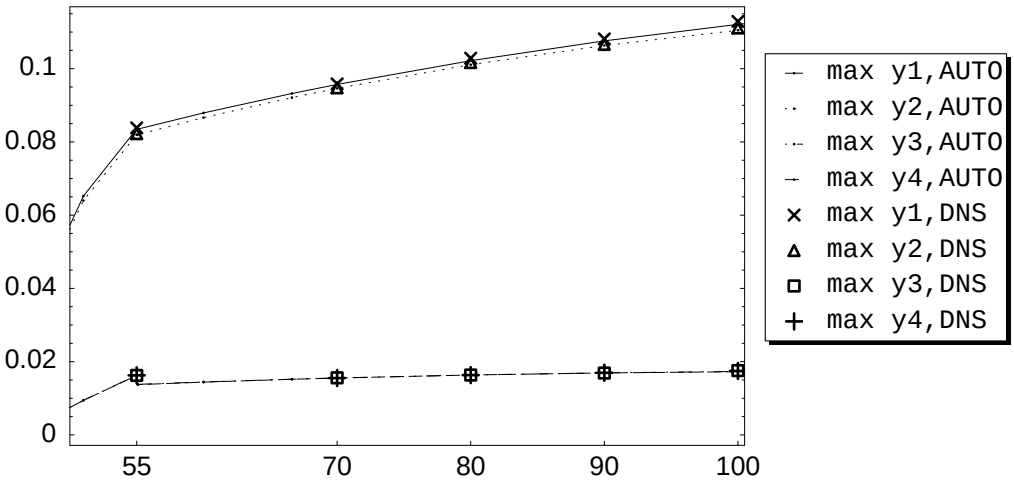

Figure 5.17: Maximum value of first 4 modes of solution: AUTO parameter continuation using basis functions at *Re* 55 (solid line) using best fit for eigenvalues compared with DNS results (see legend),

As mentioned in the driven cavity discussion, AUTO can't automatically track the period since the period was in essence normalized in the computation of the dynamical system coefficients. For the driven cavity, this modification was trivial since the period varies in an unequivocal linear manner for the Reynolds number range considered. This is definitely not the case for bluff body wake flows. A best fit from the DNS data for the period was computed to add a period correction factor to the dynamical system, and the results are shown in Figures (5.18) and (5.19). Alternatively, an experimentally-based parameterization of the period could be derived from the equation $S \times Re = -3.7 + 0.18 \times Re$ [6] where S is the Strouhal number, so its inverse is the period.

The final modeling effort capitalizes on the fact that the normalized eigenvalues are essentially constant and the unsteady kinetic energy is approximately linear in this Reynolds number range. Figures (5.20) and (5.21) show good agreement for amplitude change which only depend upon eigenstructure for $Re\,55$ and $Re\,100$.

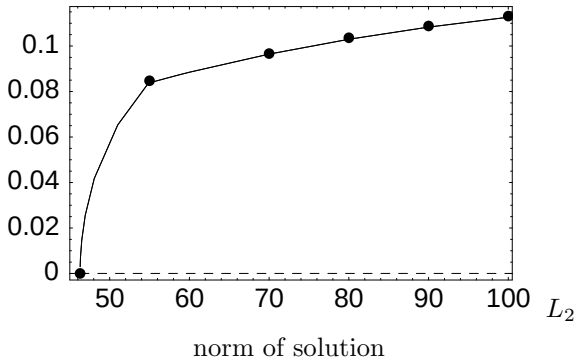

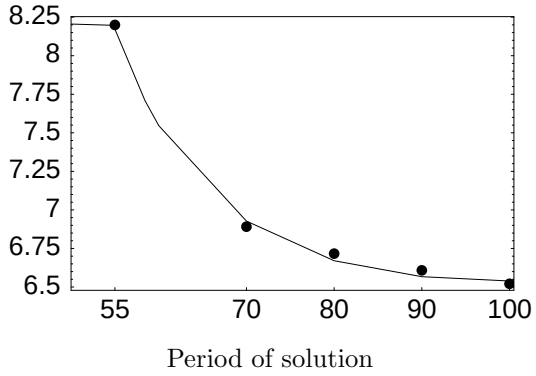

Figure 5.18: AUTO parameter continuation using basis functions at *Re* 55 (solid line) using best fit for eigenvalues and curve fit to parameterize the period compared with DNS results (dots).

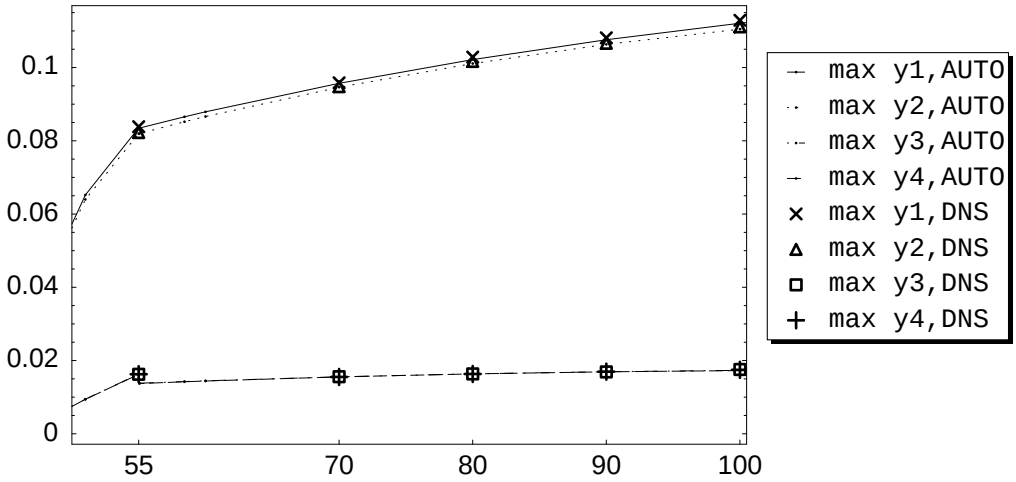

Figure 5.19: Maximum value of first 4 modes of solution: AUTO parameter continuation using basis functions at *Re* 55 (solid line), using best fit for eigenvalues and curve fit to parameterize the period compared with DNS results (see legend).

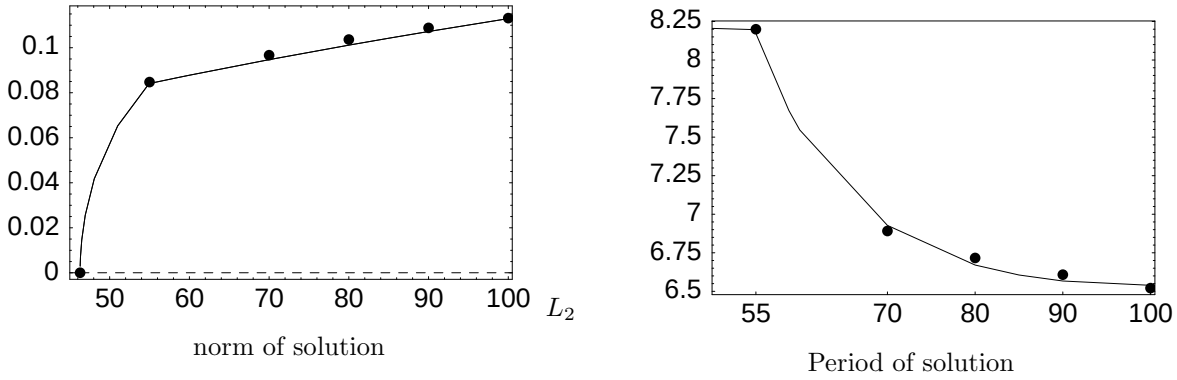

Figure 5.20: AUTO parameter continuation using basis functions at Re 55 (solid line) using constant normalized eigenvalues, and POD data from Re 100 for a linear fit to total unsteady kinetic energy and modeled period compared with DNS results (dots).

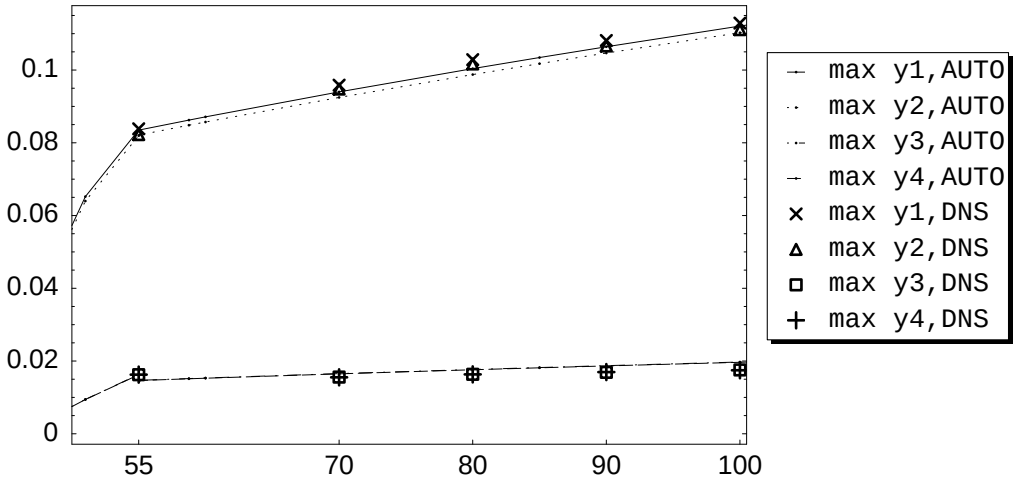

Figure 5.21: Maximum value of first 4 modes of solution: AUTO parameter continuation using basis functions at Re 55 (solid line) using constant normalized eigenvalues, and POD data from Re 100 for alinear fit to total unsteady kinetic energy and modeled period compared with DNS results (see legend).

5.7 Quasi-periodic driven cavity flow at $Re\,10000$

The complexity of the flow increases greatly at $Re\,10000$. The dynamical system at that Reynolds number was computed and analyzed with AUTO. Sixteen modes were used to capture 99.9% of the energy. AUTO predicted the qualitative nature of the history of the flow, but not the specifics since the previous methods of eigenvalue scaling are not applicable across a bifurcation. For instance, AUTO found a Hopf bifurcation at $Re\,9320$ while the flow becomes periodic prior to $Re\,8500$. The kinetic energy in the primary pair of modes is much lower at $Re\,10000$ so the dynamical system cannot accurately pinpoint the correct transition point. However, AUTO does find a realistic location for the torus bifurcation responsible for the quasi-periodic nature of the flow at $Re\,10000$, at $Re\,9906$. This is in excellent agreement with the DNS data which is still periodic at $Re\,9900$. Figure (5.22) summarizes the flow transitions.

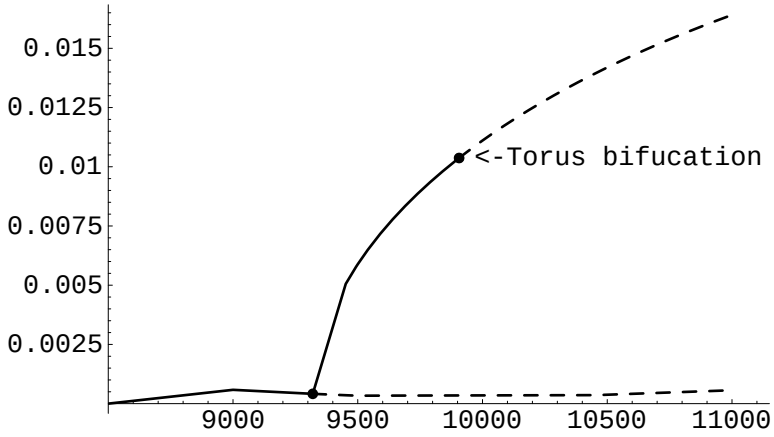

Figure 5.22: L^2 norm of solution derived from AUTO parameter continuation using 16 basis functions at $Re\,10000$.

After the torus bifurcation, the periodic branch becomes unstable, as indicated again by the dashed line. The frequencies predicted by AUTO at the torus bifurcation are $2\pi/P$ and $Im(\ln q)/P$ where $P = 49.97813$ and $q = -.7513615 + .6598912i$ in AUTO units. Correcting for time, $P_{DNS} = P * \Delta t * sampling\,rate = 2.4$. Thus the primary frequency expected is

2.61799, which agrees well with the primary frequency found in the Fourier spectrum of the first temporal eigenfunction, $f_1 = 2.61793$. The brand new frequency was computed as:

$$\begin{aligned} f_{AUTO} &= (\pi - \arcsin(.6598912))/P\,, \\ p_{AUTO} &= \frac{2\pi}{f_{AUTO}}\,, \\ p_{DNS} &= p_{AUTO} * \delta t * sampling\,rate\,, \\ f_{DNS} &= \frac{2\pi}{p_{DNS}}\,, \\ f_{DNS} &= 1.02781\,. \end{aligned}$$

The frequency 1.61103 which is dominant in the Fourier spectrum is the difference between the frequency originating with the Hopf bifurcation and this frequency.

Bifurcation diagrams were constructed using 4, 8, 12, and 16 modes. The bifurcation points found using 16 POD modes are robust in the sense that a Hopf bifurcation on the steady branch and a torus bifurcation of the periodic branch persist using as few as 4 modes. In all cases, the location of the Hopf bifurcation is inaccurate because the dynamical system was derived from the data at $Re\,10000$, but the frequency is fairly accurate. The Reynolds number of the torus bifurcation is too high with 4 and 8 modes, and too low with 12 modes, but again there is reasonable agreement in the predicted frequency.

5.8 Technical note: choosing a truncation level for the dynamical system

A nominal criterion for truncation was suggested by Sirovich [64] as the capture of 99% of the energy. In terms of eigenvalues λ_n of the POD, this is equivalent to finding the smallest M such that $\sum_{n=1}^{M} \lambda_n / \sum_{n=1}^{N} \lambda_n > .99$, where N is the total number of basis functions. For the periodic flows considered here, driven cavity and

square cylinder wake, four modes have been both necessary and sufficient for the goal of extrapolation through parameter continuation. This guideline is satisfied for the four mode model for the driven cavity periodic regime where the minimum captured energy occurs at $Re\,9900$ and is still 99.9%. However, for the square cylinder wake flow, four modes only capture 98% at $Re\,100$, although the criterion is satisfied for $Re \leq 90$. Sufficiency is proven by the results in this chapter. But are four modes necessary?

Figure (5.23) shows parameter continuation using a two-dimensional dynamical system [13] with constant coefficients derived at $Re\,8500$ for the driven cavity flow. The gross qualitative behavior is correct; a Hopf bifurcation is detected at $Re\,8510$, which is just past the predicted location based on the full numerical simulation. However, the amplitude growth is two orders of magnitude too large, and the periodicity is too large as well.

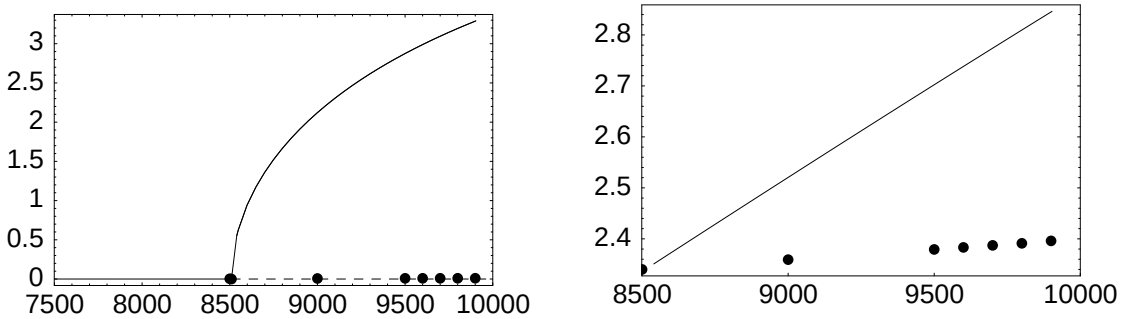

Figure 5.23: AUTO parameter continuation using only two basis functions at $Re\,8500$ (solid line) compared with DNS results (dots).

With only one pair of modes, there cannot be an energy cascade as the Reynolds number increases, which eliminates the possibility of parameterizing the dynamical system coefficients. Thus, four modes is also a necessary constraint for quantitatively correct parameter continuation.

[13] The *stabilized* dynamical system was used for all results in this section.

6 Spatial extrapolation

The Proper Orthogonal Decomposition (POD) method projected to a dynamical system addresses parameter continuation in the temporal domain. However, that is only half the problem, since the goal is to obtain low-dimensional models that describe the temporal and spatial nature of the original fluid flow. Historically, this problem has not been specifically addressed, as noted by Wallace [21]: "Current tools used in nonlinear dynamics for temporal systems are clearly inadequate for these [open] flows; they do not account for spatial development or spatial coupling." However, the spatial basis set has been augmented in a variety of ways:

- Deane *et al.* parameterized the mean and propagated that parameter through the dynamical system coefficients [5],
- more commonly, include data from transient flow or other Reynolds numbers in the POD so that the spatial eigenfunctions can span a broader range (at the cost of optimality at any Reynolds number) *e.g*, [80],[10],
- or by including specific spatial eigenfunctions in addition to the ones derived from the POD prior to projecting to the dynamical system, *e.g.*, [81], [82].

In each of the above scenarios, the temporal eigenfunctions are obtained by projection onto the spatial eigenfunctions in the usual way: given a vector $\mathbf{u}$ and a set of orthogonal basis vectors $\mathbf{\Phi}_i, i = 1, \ldots, n$, the problem of expressing $\mathbf{u}$ as a linear combination of a set of these basis vectors , $\sum_{i=1}^{n} \alpha_i \mathbf{\Phi}_i$, is optimized by setting $\alpha_i = \langle \mathbf{u}, \mathbf{\Phi}_i \rangle$. The goal in these efforts was to improve the range of the dynamical system by expanding the spatial content used in deriving the dynamical system coefficients, however, not the creation of a spatial model.

In contrast, this work explores the spatial changes through the eigenfunctions in pursuit of predicting the spatial content at neighboring Reynolds numbers. The

earlier concepts are useful in this context as well, however, as another way of verifying the adequacy of a proposed set of spatial eigenfunctions at a given Reynolds number: compare the temporal coefficients derived from the POD procedure with those obtained by projecting the snapshots onto the spatial basis functions.

6.1 Driven cavity flow, spatial modes

In section 3.6 (Figures (3.10) - (3.12)) similarity measures of the spatial modes for the driven cavity indicated strong resemblance of modes across Reynolds numbers, particularly for the mean flow. The errors made increase linearly with Re, so field interpolation for the PODs representing unsteady flow seems like a reasonable tactic to try to improve the spatial representation. Two and three point schemes have been tested. The two point method simply linearly interpolates the fields from those at $Re\,8500$ and $Re\,9500$. The three point method adds $Re\,9000$ information for a quadratic fit to the data. Both methods are a weighted average of flow fields, so the results are still divergence-free. Figures (6.1) - (6.3) show the similarity measures for the interpolated fields as well as for the POD fields used in their construction as a means to measure of the improvement. Reconstruction error is shown in Figure (6.4). The effort here was to model the flow in the periodic regime. After the torus bifurcation, the first pair of spatial eigenfunctions are quite similar in spatial structure, but the remaining basis functions are radically different. Follow on work on flow at higher Reynolds numbers must be done to investigate the persistence of these new eigenfunctions.

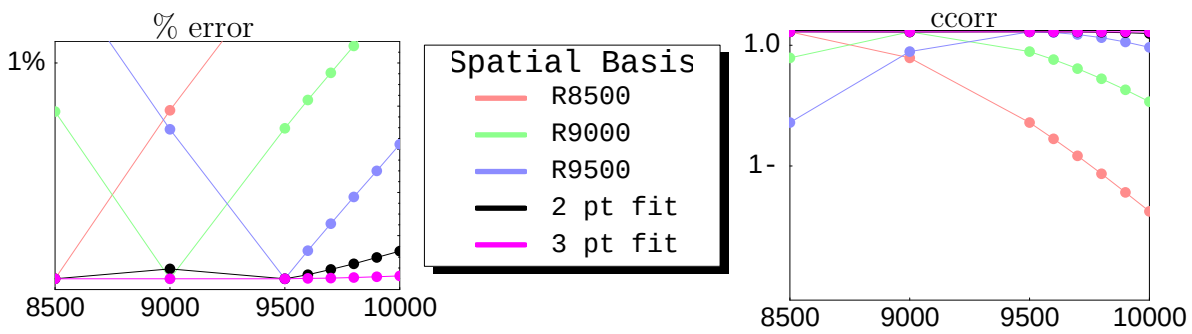

Figure 6.1: Similarity of stream function of mean field. Left, % error; right, correlation.

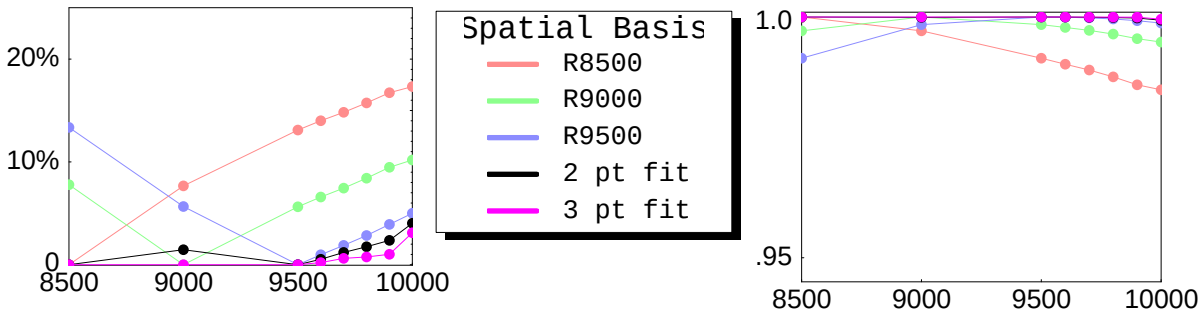

Figure 6.2: Similarity of stream function of POD spatial mode 1 ($\approx$ 2). Left, % error; right, correlation.

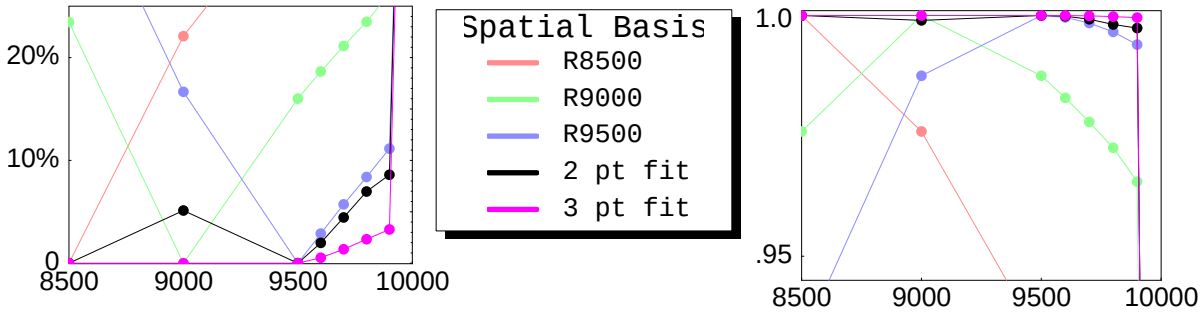

Figure 6.3: Similarity of stream function of POD spatial mode 3 ($\approx$ 4). Left, % error; right, correlation.

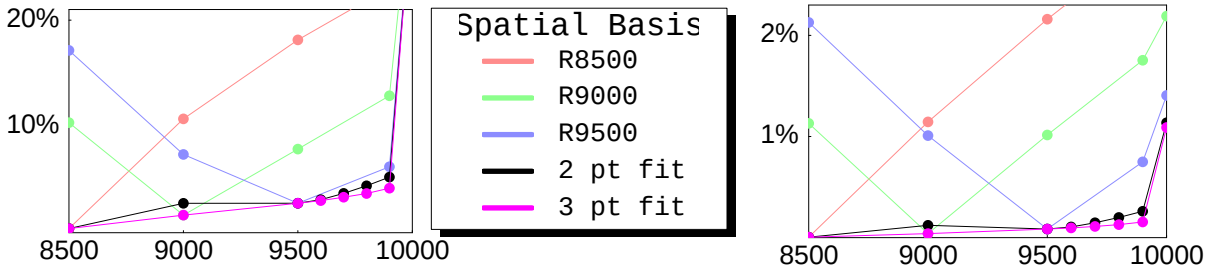

Figure 6.4: % error made when reconstructing the unsteady flow (left) and total flow (right) using 4 spatial basis functions derived at $Re\,8500, 9000, or 9500$ or weighted average of those bases.

Projection of the snapshot data at $Re = R$ onto the POD spatial eigenfunctions derived at a different Reynolds number and comparison with the true temporal functions at $Re = R$ is shown next as a comparison measure. First, the recovery of the primary temporal function at Re 10000 is evaluated by projection on PODs from Re 8500, Re 9000, Re 9500, and the two and three point interpolated basis functions. This represents the most challenging case for the first temporal function, but as can be seen in Figure (6.5), it isn't a difficult job at all given the very high level of similarity in the primary pair of spatial eigenfunctions. Re 9900 is used to test the recovery of the third temporal function since one can't reasonably expect to recover this mode for Re 10000 given the new frequency component that becomes dominant after the torus bifurcation. Figure (6.6) shows that the interpolated basis does an excellent job in this comparison as well.

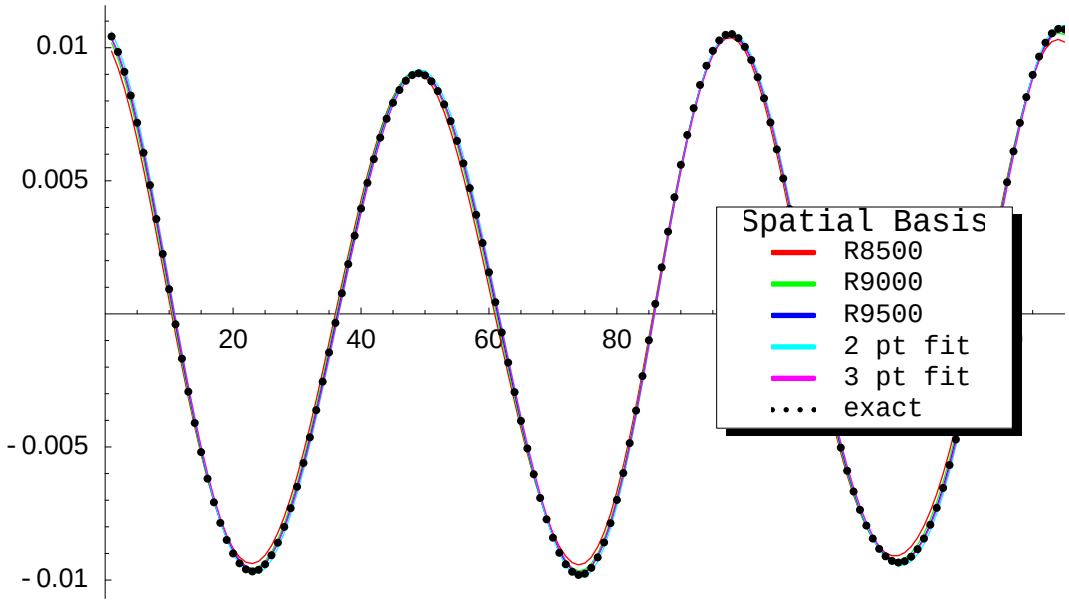

Figure 6.5: Recovery of first temporal eigenfunction at Re 10000 by projection of the snapshots onto the first four spatial eigenfunctions from different bases.

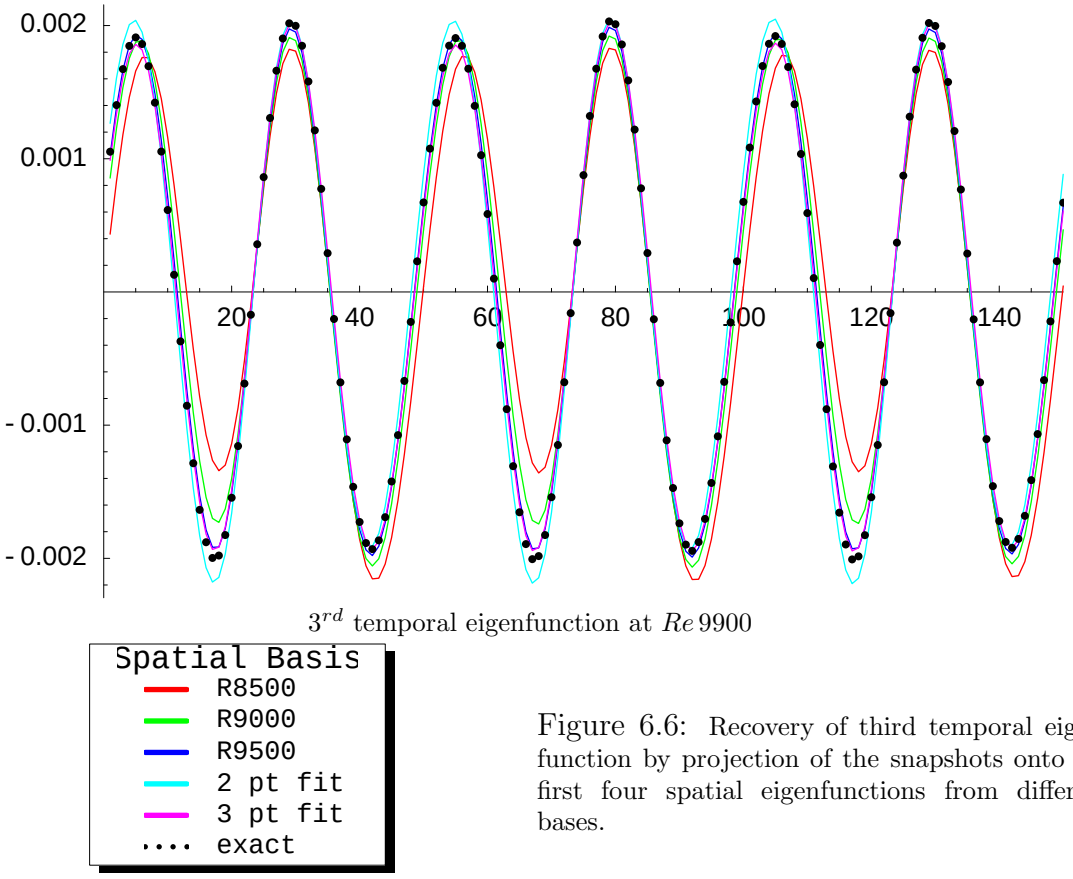

Figure 6.6: Recovery of third temporal eigenfunction by projection of the snapshots onto the first four spatial eigenfunctions from different bases.

6.2 Square cylinder flow, spatial modes

In section 3.7, similarity measures of the spatial modes for the square cylinder flow were not promising other than for the mean flow, and indicated large changes in modes across Reynolds numbers (Figures (3.51) - (3.53)). This is the huge difference between closed flows, such as the driven cavity flow, and open flows like the wake flow. Geometry doe not force a similarity in spatial structure. Numerous possibilities for a spatial model are possible; to list a few:

- Point-wise interpolation/extrapolation (as implemented for the driven cavity),
- Locate dominant flow features in the spatial eigenfunctions (*e.g.* vortical structure) and parameterize a smooth mapping over a range of Reynolds numbers,
- The recent work of Ahlborn, Seto and Noack [83] details a phenomenological wake model that might be useful in characterizing the wake structure.

Investigating the first technique, we will attempt field interpolation as with the driven cavity flow to try to improve the spatial representation. Two 2-point methods have been tested. The first method simply linearly interpolates the fields from those at $Re\,70$ and $Re\,100$ in Reynolds number. However, the spatial changes mirror the Strouhal number changes, or equivalently the change in period, and this is known to be nonlinear in Reynolds number. To try to use that information, the second 2-point method uses the period as a weighting factor in the linear interpolation. Both methods are just a weighted average of flow fields, so the results are divergence-free. Figures (6.7) - (6.9) show the similarity measures for the interpolated fields as well as for the POD fields used in their construction as a means to measure of the improvement. While these simple measures are successful in improving spatial similarity for the mean flow and primary spatial eigenfunctions at $Re\,80$ and $Re\,90$, they are not as successful for higher modes.

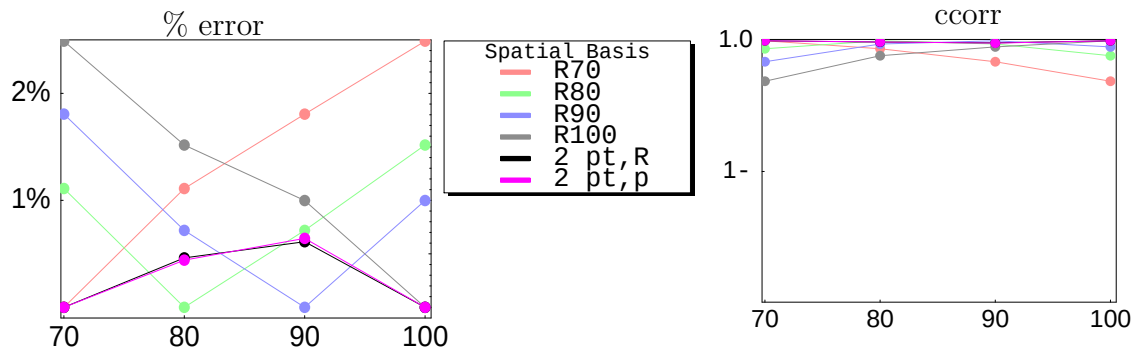

Figure 6.7: Similarity of stream function of mean field. Left, % error; right, correlation. ("1^- = .99999")

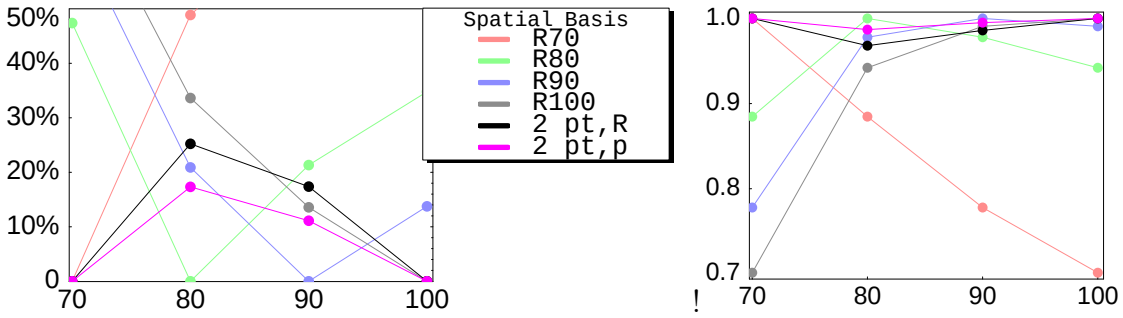

Figure 6.8: Similarity of stream function of POD spatial mode 1 ($\approx$ 2). Left, % error; right, correlation.

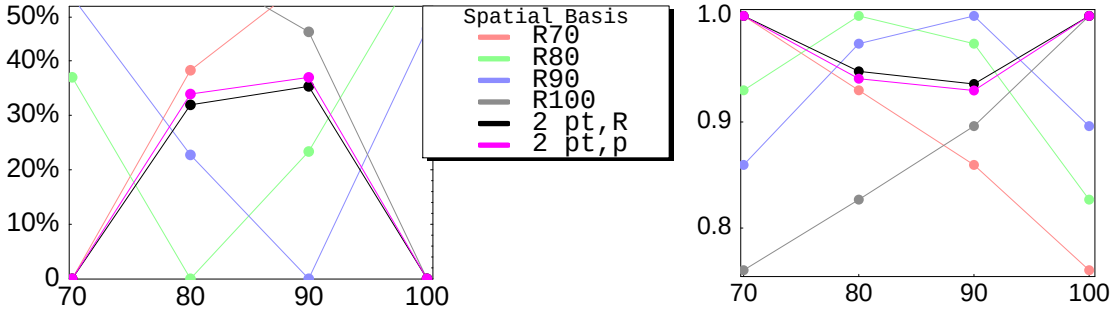

Figure 6.9: Similarity of stream function of POD spatial mode 3 ($\approx$ 4). Left, % error; right, correlation.

A comparison of the mean recirculation length, indicated by a change in sign in u along the x-axis in the mean flow field, is shown in Figure (6.10). The black line shows the mean recirculation length from the DNS data, green shows the result from the spatially interpolated field in Reynolds number, and red is from the interpolated field based on period. Use of period to weight the interpolation is particularly effective in retrieving this information.

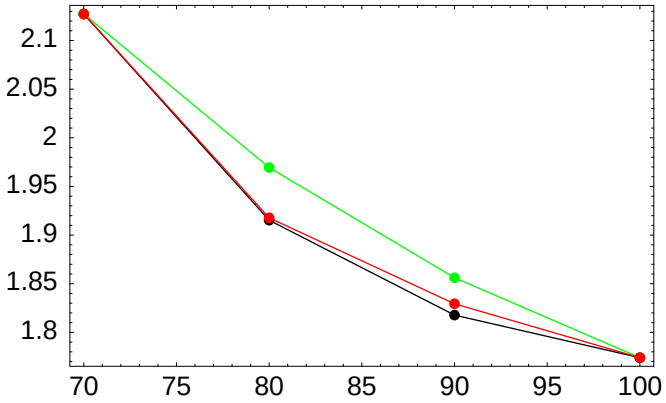

Figure 6.10: Mean recirculation length for square cylinder wake flow versus Reynolds number. Black = DNS, green = 2 point interpolation from $Re\,70$ and $Re\,100$ in Reynolds number and red interpolates using period.

Reconstruction error is shown in Figure (6.11), in contrast to Figure (3.54) without interpolation. Although the similarity measures were not that promising, flow reconstruction results for $Re\,80$ and $Re\,90$ are still markedly improved over using the bases at either $Re\,70$ or $Re\,100$.

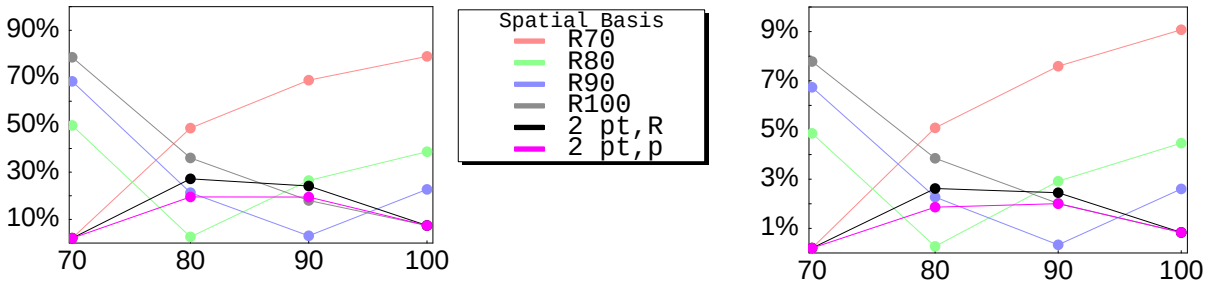

Figure 6.11: % error made when reconstructing the unsteady flow (left) and total flow (right) using 6 spatial basis functions derived at $Re\,70, 80, 90$, or 100 or weighted average of those bases.

6.3 Technical note: minimal number of spatial modes for a low-dimensional spatial model

The eigenvalues λ_i from the POD give a breakdown of the unsteady kinetic energy in the spatial modes. Thus, one can choose the number of modes to include in a low-dimensional model based on recovering a certain percentage of the total energy. But how does the energy recovered impact the reconstruction error?

Let N = the total number of modes, $\mathbf{u}(\mathbf{x}, t_j)$ = the total flow snapshots at t_j, and $\mathbf{u}_m$ = the mean flow field. Then the reconstruction of the unsteady flow is $\mathbf{w}(\mathbf{x}, t_j) = \sum_{i=1}^{M} y_i(t_j)\mathbf{\Phi}_i(\mathbf{x})$ and the percent reconstruction error is defined by:

$$\%error = \langle \|\mathbf{u}(\mathbf{x}, t_j) - \mathbf{u}_m - \mathbf{w}(\mathbf{x}, t_j)\| \rangle / \langle \|\mathbf{w}(\mathbf{x}, t_j)\| \rangle \,, \tag{6.1}$$

averaged over all N snapshots for truncation level M for unsteady flow and

$$\%error = \langle \|\mathbf{u}(\mathbf{x}, t_j) - \mathbf{w}(\mathbf{x}, t_j)\| \rangle / \langle \|\mathbf{u}_m + \mathbf{w}(\mathbf{x}, t_j)\| \rangle \,, \tag{6.2}$$

for total flow reconstruction error. The percent neglected energy for M modes $= 1 - \sum_{i=1}^{M} \lambda_i / \sum_{i=1}^{N} \lambda_i$ for unsteady flow; for total flow, the energy in the mean flow must be added to the unsteady energy. Figures (6.12) - (6.14) summarize the percent error for reconstruction of the unsteady flow as a function of truncation level (left) and the relationship between the percentage of neglected energy and truncation level (right) for the driven cavity flow at Reynolds numbers 8500, 9900, and 10000.

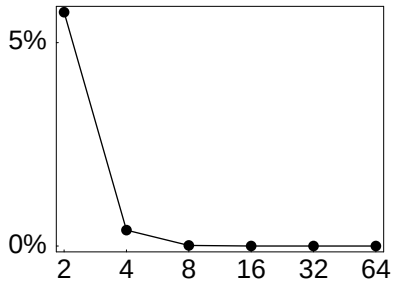

% error vs # modes

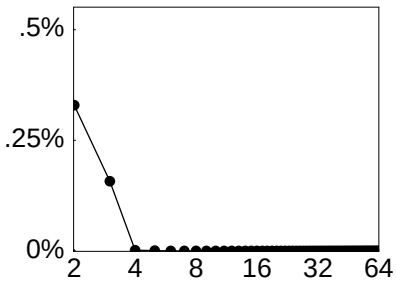

% neglected energy vs # modes

Figure 6.12: Driven cavity flow, Re 8500, unsteady flow reconstruction.

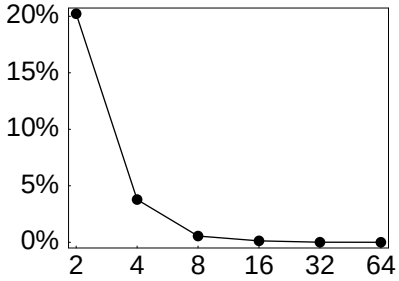

% error vs # modes

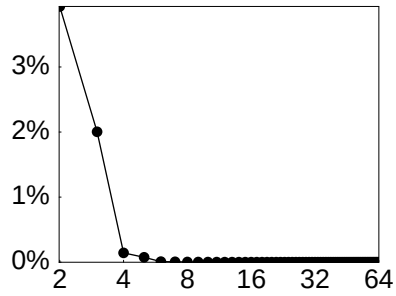

% neglected energy vs # modes

Figure 6.13: Driven cavity flow, Re 9900, unsteady flow reconstruction.

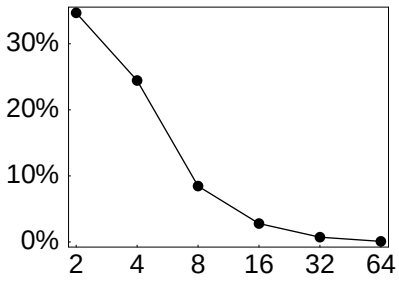

% error vs # modes

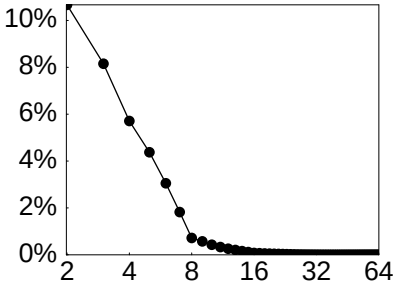

% neglected energy vs # modes

Figure 6.14: Driven cavity flow, Re 10000, unsteady flow reconstruction.

As expected, more modes equals smaller error and less neglected energy. As Reynolds number increases, more modes are needed to attain the same error level and energy level. Not so obvious, however, is the precise relationship between error level and energy level. As Figure (6.15) illustrates, the percent reconstruction error squared is directly proportional to the percent neglected energy. Moreover, this relationship does not seem to depend on Reynolds number; in Figure (6.15), the black line plots the data for Re 10000, green for Re 9900, and red for Re 8500. The rightmost figure zooms in for better visual discrimination in the low energy/error range of the plot.

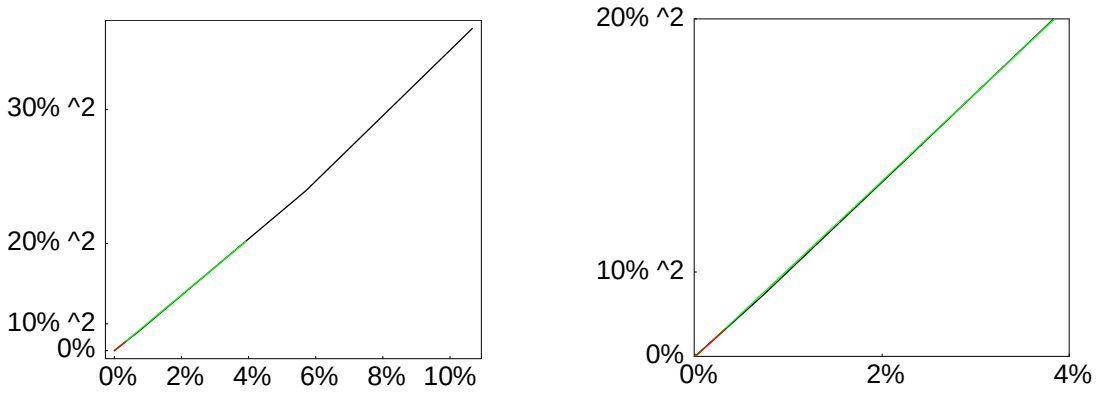

(zoom in on left graphic)

Figure 6.15: Driven cavity flow, % neglected energy squared vs % error for unsteady flow reconstruction. Black = Re 10000, green = Re 9900, red = Re 8500.

Figures (6.16) - (6.18) illustrate the reconstruction error (left) and neglected energy (right) for the total flow as a function of the number of modes. For the driven cavity flow in this range, the energy budget is dominated by the mean flow, so the errors and neglected energy are substantially reduced in comparison with the equivalent figures for the unsteady flow.

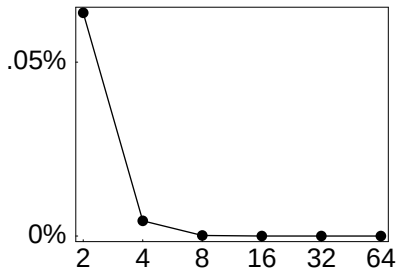

% error vs # modes

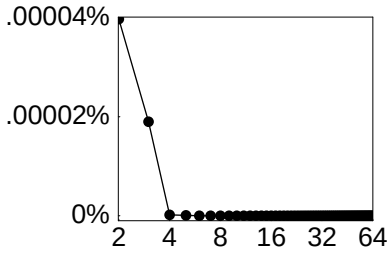

% missing energy vs # modes

Figure 6.16: Driven cavity flow, Re 8500, total flow reconstruction.

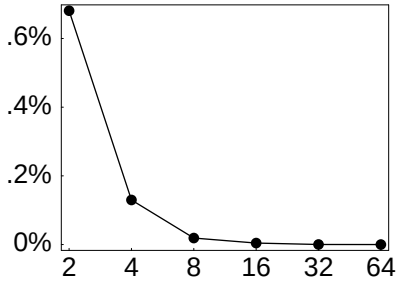

% error vs # modes

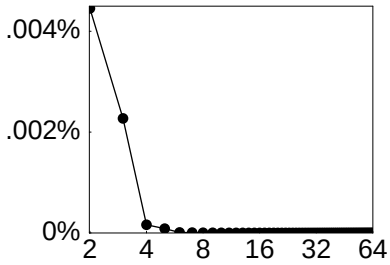

% missing energy vs # modes

Figure 6.17: Driven cavity flow, Re 9900, total flow reconstruction.

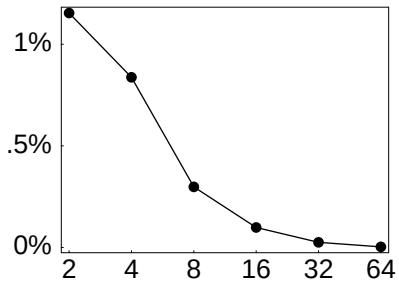

% error vs # modes

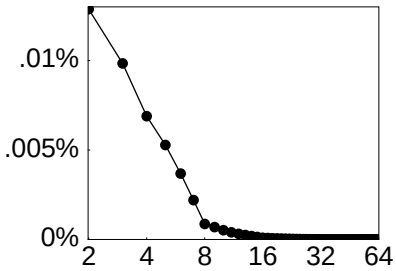

% missing energy vs # modes

Figure 6.18: Driven cavity flow, Re 10000, total flow reconstruction.

A direct relationship still exists between the percent reconstruction error squared and the percent neglected energy for the total flow as illustrated in Figure (6.19) with the same color scheme: Re 10000 in black, Re 9900 in green, and Re 8500 in red. The rightmost figure zooms in on the left.

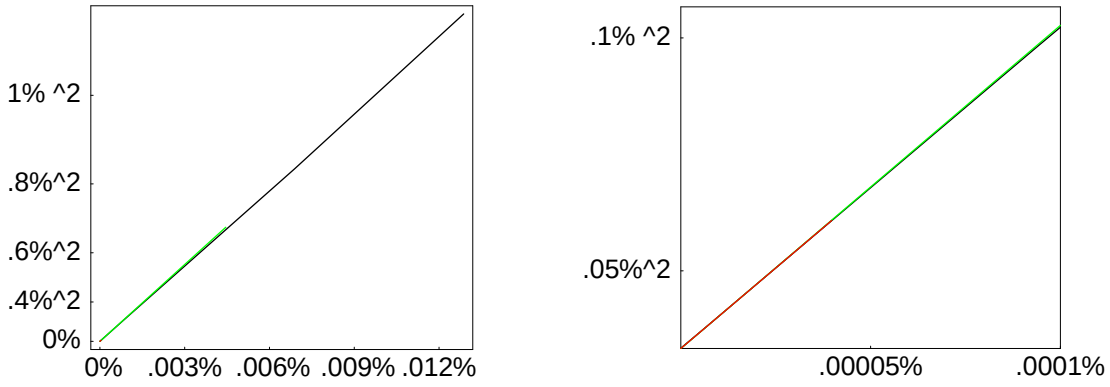

(zoom in on left graphic)

Figure 6.19: Driven cavity flow, % neglected energy vs % error for total flow reconstruction.

Next, consider these measures for the square cylinder wake flow. The extremes of Reynolds numbers were used for comparison, Re 55 and Re 100. Figures (6.20) and (6.21) show the effect of truncation on the percent reconstruction error and the percent neglected energy for the unsteady flow. Figures (6.22) and (6.23) illustrate the same information for the total flow. Finally, Figure (6.24) shows the linear dependence of the percent error squared on the percent neglected energy for the square cylinder wake flow. Again, the relationship does not seem to depend on Reynolds number. Data for Re 100 is plotted in black, Re 55 in red.

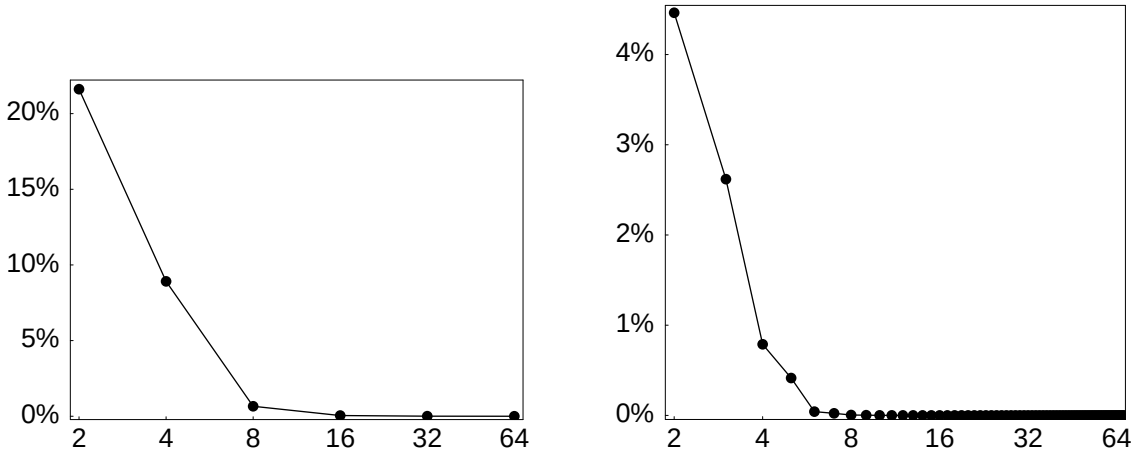

Figure 6.20: Square cylinder wake flow, $Re\,55$, unsteady flow reconstruction.

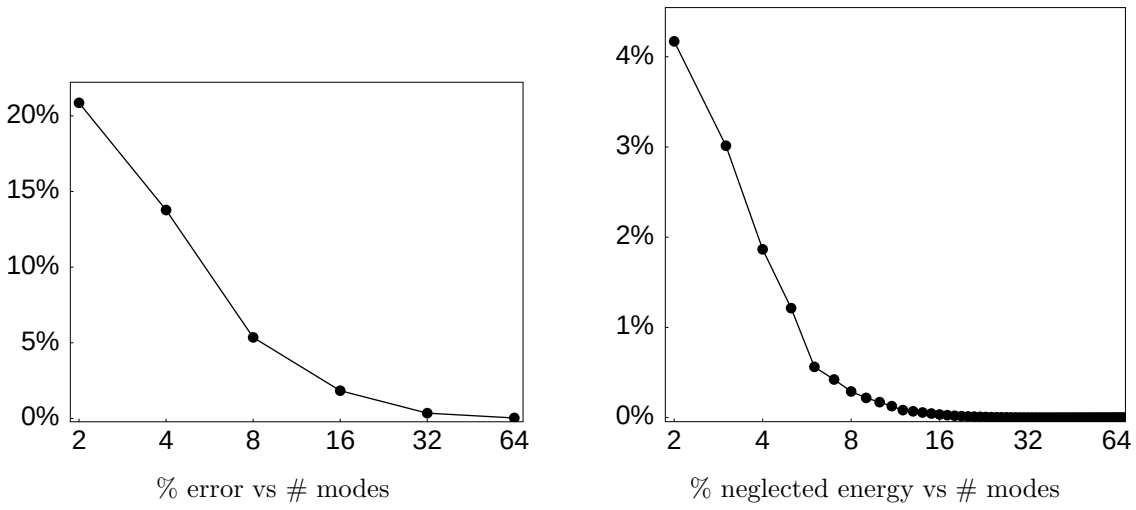

Figure 6.21: Square cylinder wake flow, $Re\,100$, unsteady flow reconstruction.

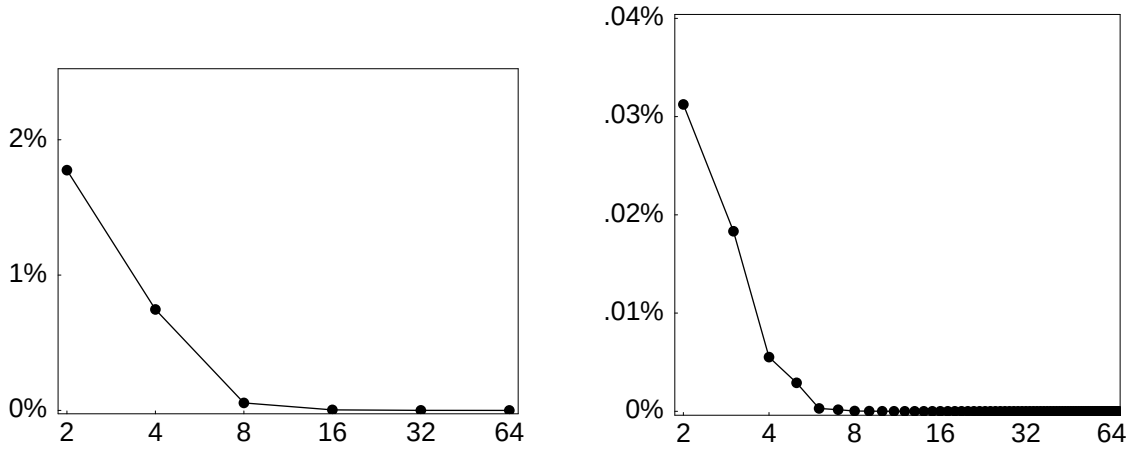

% error vs # modes

% neglected energy vs # modes

Figure 6.22: Square cylinder wake flow, Re 55, total flow reconstruction.

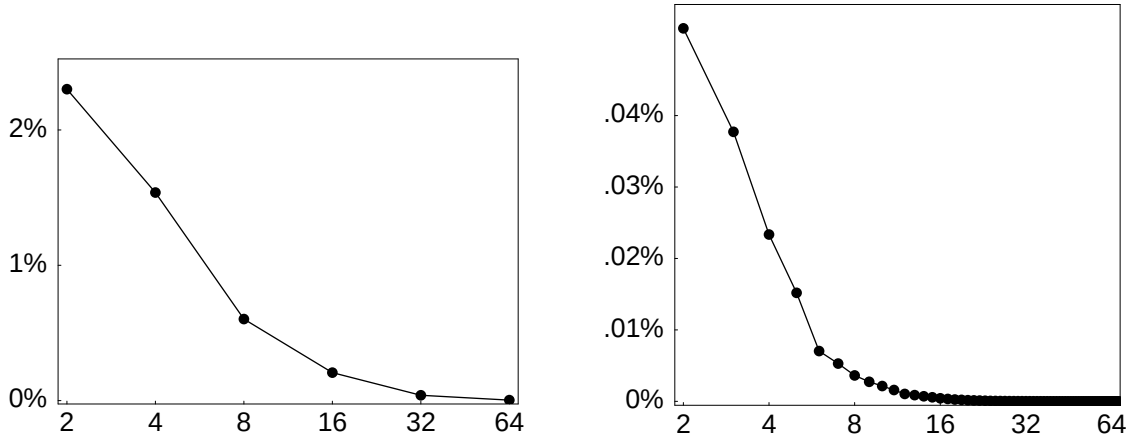

% error vs # modes

% neglected energy vs # modes

Figure 6.23: Square cylinder wake flow, Re 100, total flow reconstruction.

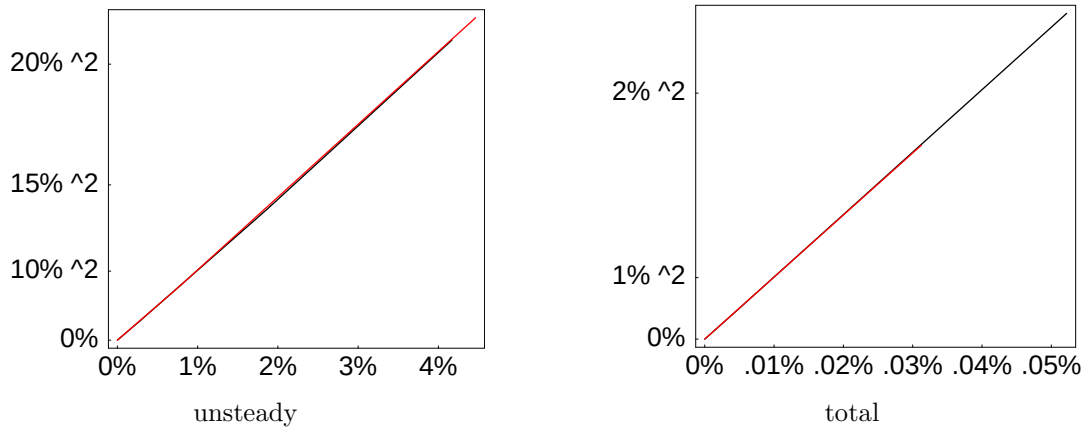

unsteady

total

Figure 6.24: Square cylinder wake flow, % neglected energy squared vs % error for flow reconstruction.

7 Summary and Conclusions

The Proper Orthogonal Decomposition (POD) is a well-established tool for the study of coherent structures in fluid flow and for the construction of low-dimensional temporal models for fluid flow. This dissertation has taken a fresh look at this decomposition, emphasizing the role of both temporal and spatial modes and their inherent relationship. A common viewpoint in the past has been to look at the spatial content as a means to the construction of a dynamical system and to evolve the temporal modes from that dynamical system, but as we have seen, this is not necessary. There is much to be gained from the temporal and spatial eigenfunctions themselves, and evolution of the spatial eigenfunctions is virtually an open field.

This dissertation has made several contributions to the field which are discussed below.

Primary accomplishments:

- a new stabilization method for the POD-based low-dimensional system, coined *intrinsic stabilization*,
- scaling of the dynamical system coefficients for amplitude and period (coefficient parameterization),
- parameter continuation for the square cylinder wake flow using just four modes,
- temporal and spatial low-dimensional model for the driven cavity flow up to Re 10000 using only four modes,
- parameter continuation for the driven cavity flow at Re 10000 that accurately reflects the torus bifurcation and links spatial change to the new frequency.

The new stabilization method is of interest not only because of its demonstrated effectiveness at stabilizing the dynamical system for long-term dynamics, but because of its simplicity in concept and application. It makes use of information already computed: the temporal eigenfunctions and the POD-based dynamical system. The correction terms can be computed for any truncation level, although too severe a truncation would naturally affect the quality of the results. Although the examples presented here dealt with periodic or quasi-periodic data, the principle behind the algorithm is broader, and depends only on a statistically complete data sample. Future work includes application of the stabilization method to data in the turbulent regime.

The appreciation of the bi-orthogonality property of the POD allows one to see the temporal and spatial components of a flow as dual problems that are coupled, yet can be attacked separately. The driven cavity flow and the square cylinder wake flow represent two vastly different types of fluid flow, yet both share a quite similar set of temporal eigenfunctions in the (normalized) periodic regime, as would any periodic flow: the temporal eigenfunctions correspond approximately to the normalized Fourier modes in this case. This is an approximation because the temporal eigenfunctions are not single frequency, but this is by far their dominant component, as seen for the driven cavity flow. The strategy of eigenvalue scaling of the dynamical system results in correct amplitude prediction from parameter continuation because at a Hopf bifurcation the square of the amplitude of the instability grows linearly. Equivalently, the total unsteady kinetic energy grows linearly. This direct link to the POD is the route to implementation of eigenvalue scaling of the dynamical system coefficients and should be successful for any fluid flow in the periodic regime. Future work requires extending the scaling concept beyond the Hopf bifurcation.

A direct result of the first two accomplishments is a robust four-mode model for

the square cylinder wake flow. A six mode model for the circular cylinder was first established by Deane *et al.* [5] in 1991 and is still considered to be the minimum number for an adequate energy cascade) [82]. A four-mode unstabilized dynamical system is also unsatisfactory for the square cylinder as it predicts a torus bifurcation at $Re\,175$ with parameter continuation from $Re\,55$ instead of periodic behavior. The use of intrinsic stabilization permits the square cylinder four-mode model derived in this dissertation to predict periodic flow through parameter continuation well beyond the modeled parameter (at least up to $Re\,200$ for a system derived from $Re\,55$). However, the eigenvalue scaling of the dynamical system is key to obtaining correct amplitude results. The observation that the Reynolds number-dependent frequency can be independently parameterized in the dynamical system is important from the practical side of implementing this energy cascade.

The spatial side is not so easily addressed in general. For the driven cavity, the first pair of spatial eigenfunctions are quite structurally similar up to $Re\,10000$, and all the eigenfunctions are similar within the periodic regime. This simplifies the spatial continuation problem considerably, and the point-wise interpolation techniques applied to the spatial fields in Chapter 6 have proven to be enormously successful. For a limited range of Reynolds numbers, point-wise interpolation works well for the square cylinder as well, but ideally a spatial model should capture the relationship between streamwise wake structure and Strouhal number. A good model for the Strouhal number is critical for the spatial modeling as well as the time-scaling for the temporal dynamical system.

The four-mode temporal and spatial low-dimensional models can be used in combination to predict the flow and thus demonstrate the effectiveness of the the model-building methodology developed in this dissertation. This will be demonstrated for the driven cavity flow and square cylinder wake flow. The models are based only on POD results for flows at two Reynolds numbers bracketing the

Reynolds number of prediction. Comparison of the model prediction with DNS data will be done in two ways:

- the modeled temporal and spatial eigenfunctions will be used to create modeled snapshot data for comparison with the actual snapshots at times corresponding to the 1^{st}, 20^{th} and 40^{th} snapshots (a full period is 50 snapshots),

- the modeled snapshots will be sampled at selected spatial locations (indicated on the mean flow snapshots) for time series comparison with the actual DNS data.

There is a problem with this proposed comparison scheme, however: the temporal eigenfunctions at the reference Reynolds numbers need not be in phase with the time-sampling at other Reynolds numbers. The modeled temporal function can be shifted by using *Mathematica* to create an interpolating polynomial function, and using the "FindMinimum[ ]" module to find the shift which optimizes the correlation between the shifted interpolated function and the true temporal function. It should be noted that this problem only exists for this comparison exercise; the model is just as valid with the phase shift, but at a different sampling scheme than that used for the DNS data. Since the temporal eigenfunctions are very close to sinusoidal components and their harmonics, the shift is incorporated at $f \times \tau$, where f is one for the first pair of modes, two for the second pair, *etc.* and τ is fixed for all modes.

Since the mean flow claims most of the energy in both flows, the snapshots and time series are derived for the unsteady flow as a more rigorous method of comparison. The mean flow fields are illustrated as well, since the overall goal of predicting the total flow requires their interpolation.

7.1 Full low-dimensional model for the driven cavity flow

The phase shift is shown in Figure (7.1) which compares the amplitude-adjusted eigenfunctions at $Re\,8500$ with the temporal functions at $Re\,9000$. Figure (7.2) illustrates the close match between the shifted temporal functions and the true temporal functions.

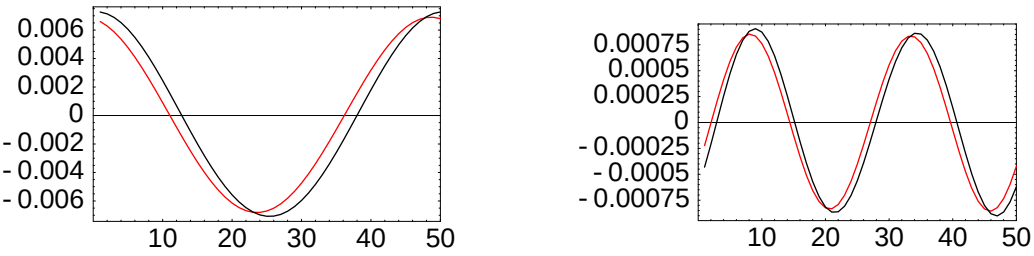

Temporal mode 1. Temporal mode 3.

Figure 7.1: Phase shift between temporal modes of $Re\,8500$ (black) and $Re\,9000$ (red).

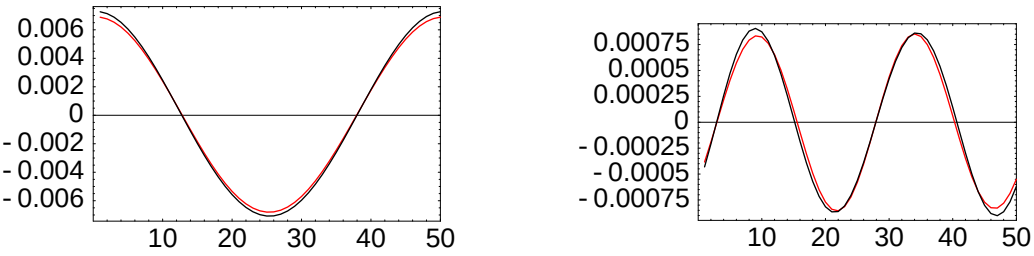

Temporal mode 1. Temporal mode 3.

Figure 7.2: Shifted temporal modes at $Re\,8500$ (black) to approximately match modes $Re\,9000$ (red).

For the driven cavity flow, the first four POD modes from $Re\,8500$ and $Re\,9500$ will be used for the combined model to predict the flow at $Re\,9000$. The spatial eigenfunctions will be used for the linear spatial interpolation (as described in Chapter 6). The eigenvalues at these reference Reynolds numbers permit modeling of the total unsteady kinetic energy and the energy cascade. This information is used to estimate the eigenvalues at $Re\,9000$ for the amplitude modification of the temporal eigenfunctions at $Re\,8500$.

For the snapshot data, stream function contours are at

$-1.0 \times 10^{-10}, -1.0 \times 10^{-7}, -1.0 \times 10^{-5}, -1.0 \times$

$10^{-4}, -.01, -.03, -.05, -.07, -.09, -.1, -.11, -.115, -.1175, 1.0 \times 10^{-}8, 1.0 \times 10^{-7}, 1.0 \times 10^{-6}, 1.0 \times 10^{-5}, 5.0 \times 10^{-5}, 1.0 \times 10^{-4}, 2.5 \times 10^{-4}, 5.0 \times 10^{-4}, 1.0 \times 10^{-3}, 1.5 \times 10^{-3}, 3.0 \times 10^{-3}$. Vorticity contours are at $-5, -4, -3, -2, -1, -.5, -.25, -.1, 0.00020, .001, .1, .25, .5, 1, 2, 3.$

Figures (7.3) and (7.4) compare the modeled and actual mean flow. Black dots mark the locations for the forthcoming time series. Throughout this comparison, all stream function plots use the same contour levels, as do the vorticity plots, so that features may be compared properly between the DNS snapshots on the left, and the modeled snapshots on the right.

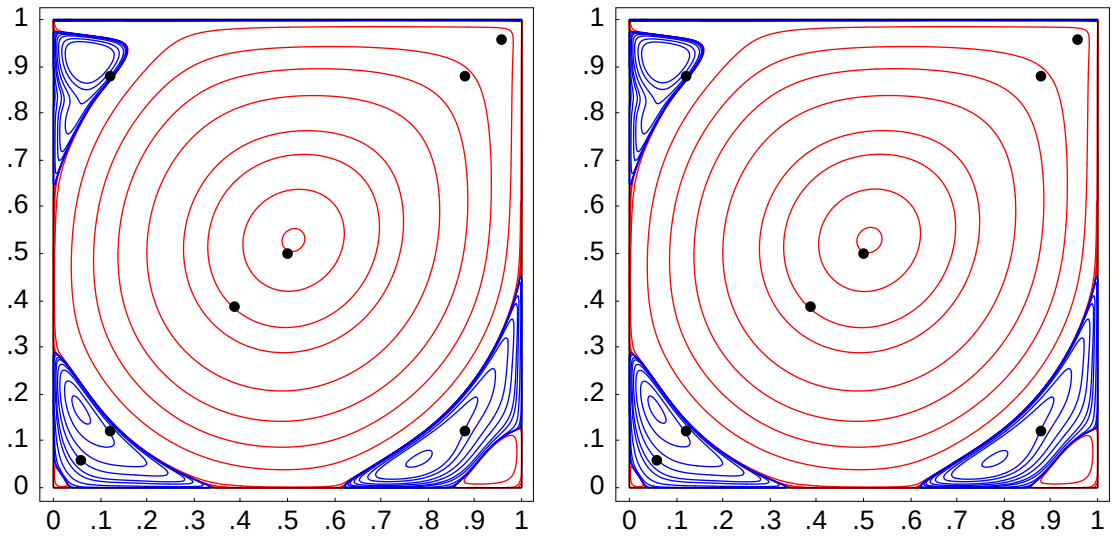

Figure 7.3: Stream function at Re 9000, mean flow: DNS (left) and modeled (right).

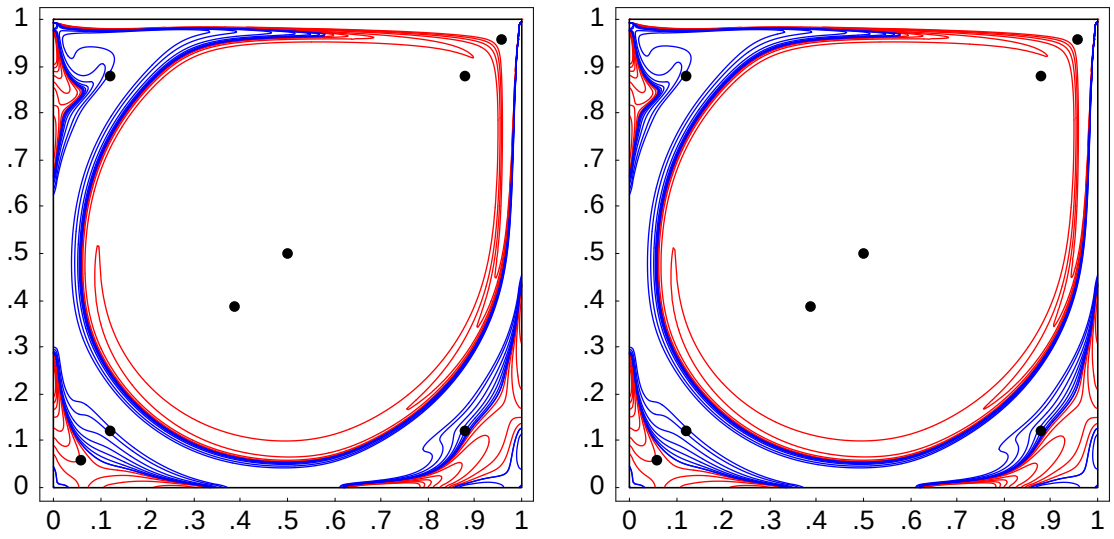

Figure 7.4: Vorticity at Re 9000, mean flow: DNS (left) and modeled (right).

Figures (7.5) and (7.6) compare the stream function and vorticity, respectively, for the first snapshot. The modeled snapshots are computed as a linear combination of the modeled spatial eigenfunctions weighted by the corresponding temporal eigenfunction at the specified snapshot time. [14]

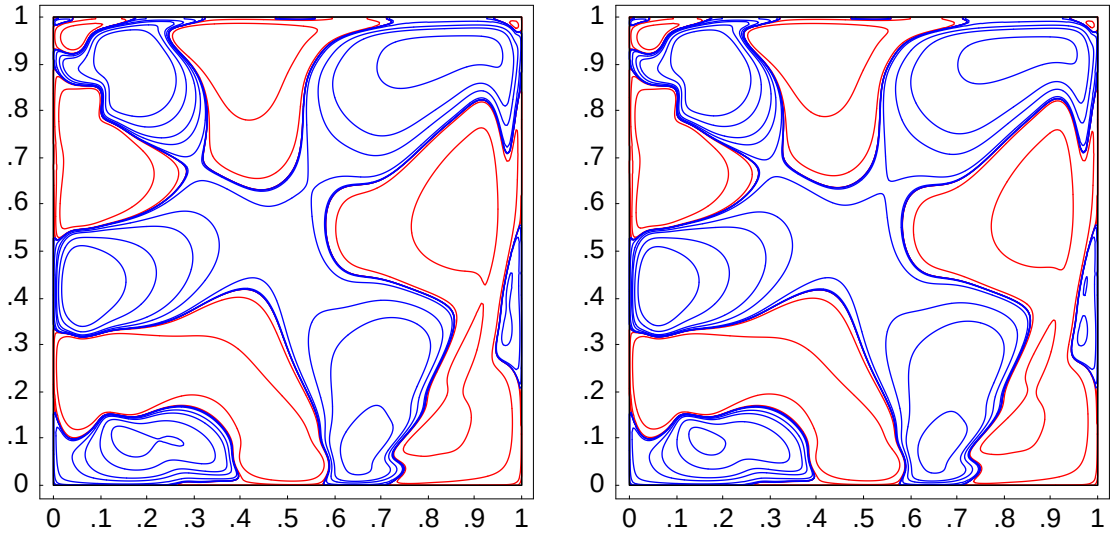

Figure 7.5: Stream function at Re 9000, snapshot 1: DNS (left) and modeled (right).

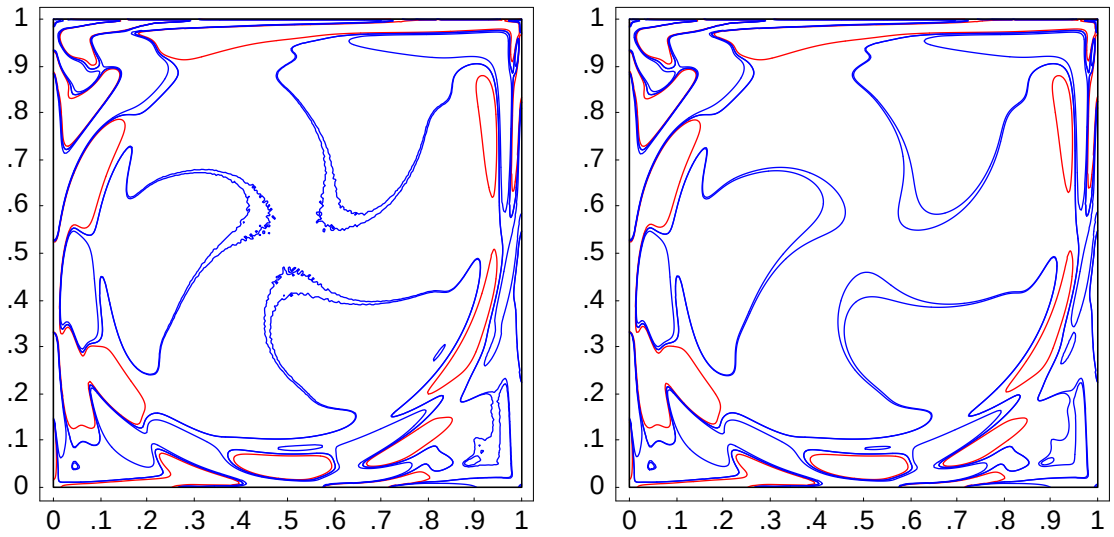

Figure 7.6: Vorticity at Re 9000, snapshot 1: DNS (left) and modeled (right).

[14] There is numerical noise at the vorticity contours near zero in the DNS data, encountered near the primary vortex.

Figures (7.7) and (7.8) compare the stream function and vorticity, respectively, for snapshot 20 of a 50 snapshot cycle.

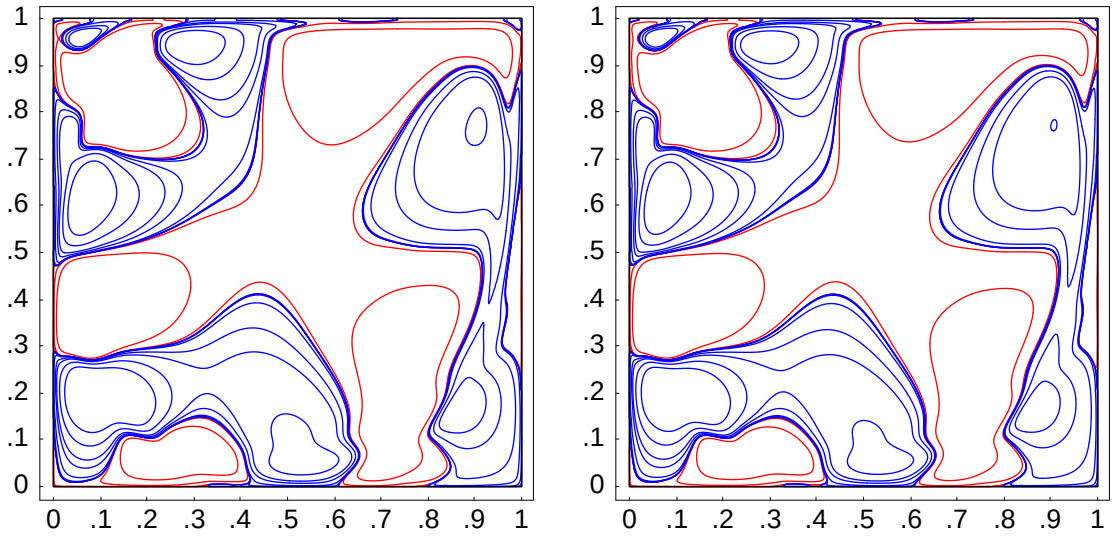

Figure 7.7: Stream function at Re 9000, snapshot 20: DNS (left) and modeled (right).

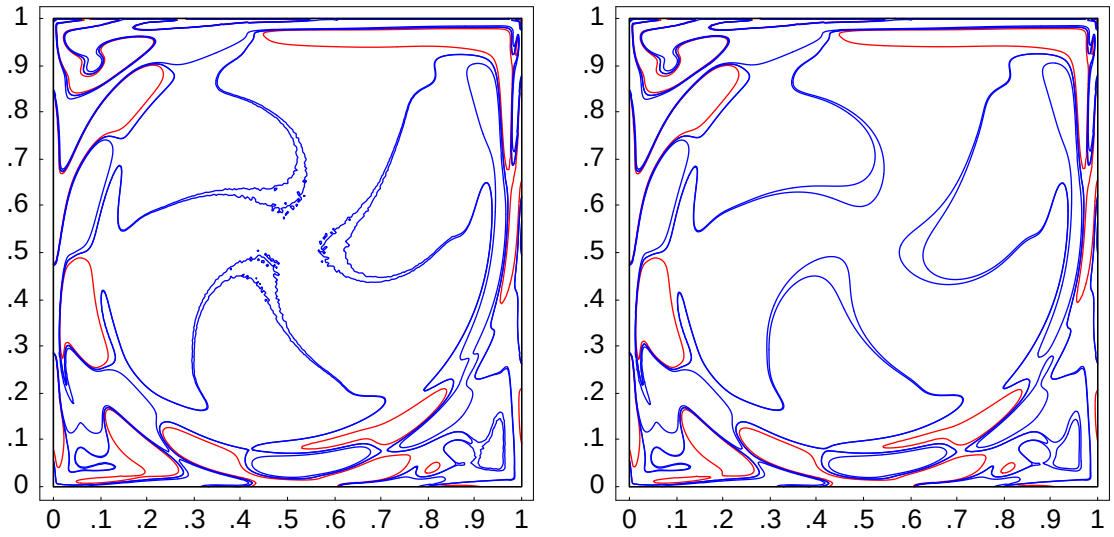

Figure 7.8: Vorticity at Re 9000, snapshot 20: DNS (left) and modeled (right).

Figures (7.9) and (7.10) compare the stream function and vorticity, respectively, for snapshot 40 of a 50 snapshot cycle.

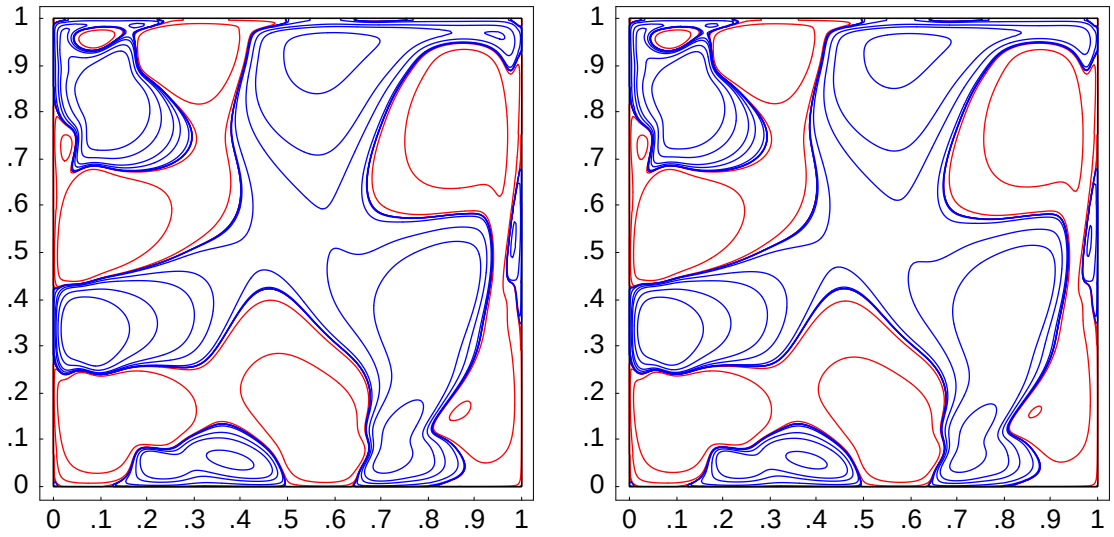

Figure 7.9: Stream function at Re 9000, snapshot 40: DNS (left) and modeled (right).

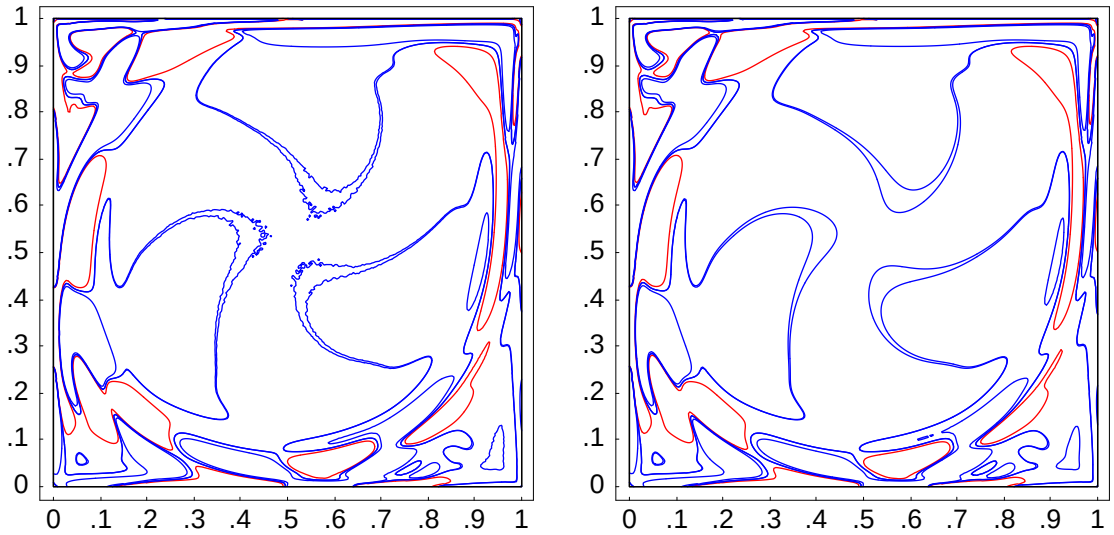

Figure 7.10: Vorticity at Re 9000, snapshot 40: DNS (left) and modeled (right).

The next eight figures, Figures (7.11) - (7.18), compare modeled (red dots) and DNS-sampled (black line) time series in u (left) and v (right) for the driven cavity flow at Re 9000. The spatial locations for the time series are graphically shown in Figures (7.3) and (7.4).

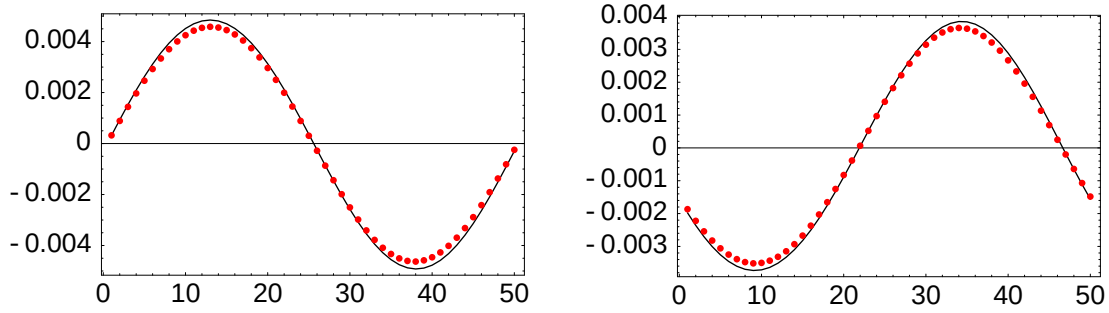

Figure 7.11: Time series in u (left) and v (right) at (.06,.06). Black = Re 9000, red = modeled.

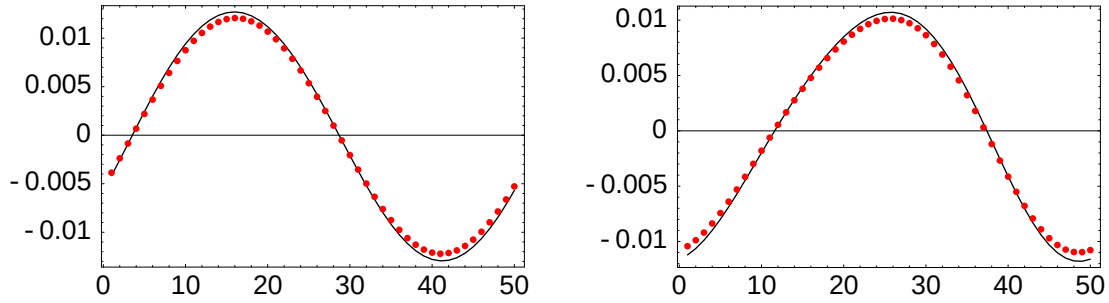

Figure 7.12: Time series in u (left) and v (right) at (.12,.12). Black = Re 9000, red = modeled.

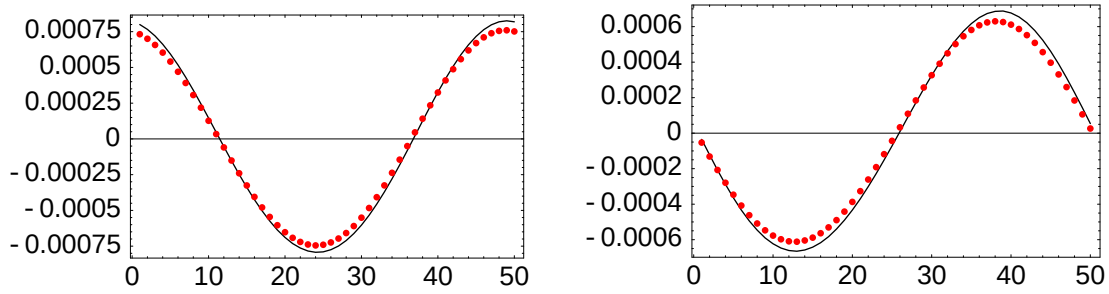

Figure 7.13: Time series in u (left) and v (right) at (.39,.39). Black = Re 9000, red = modeled.

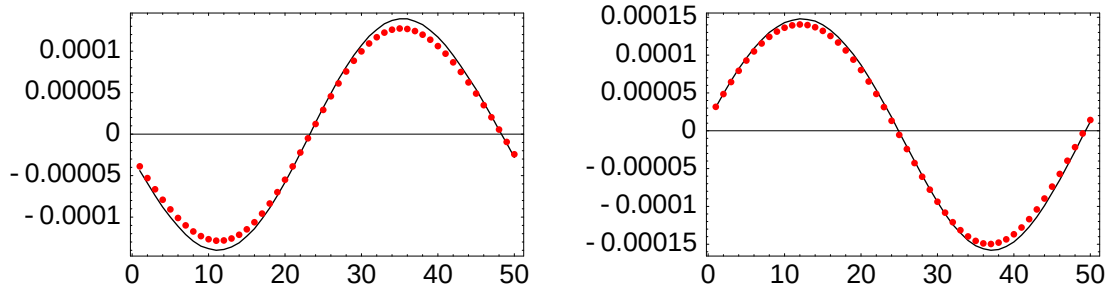

Figure 7.14: Time series in u (left) and v (right) at (.50,.50). Black = Re 9000, red = modeled.

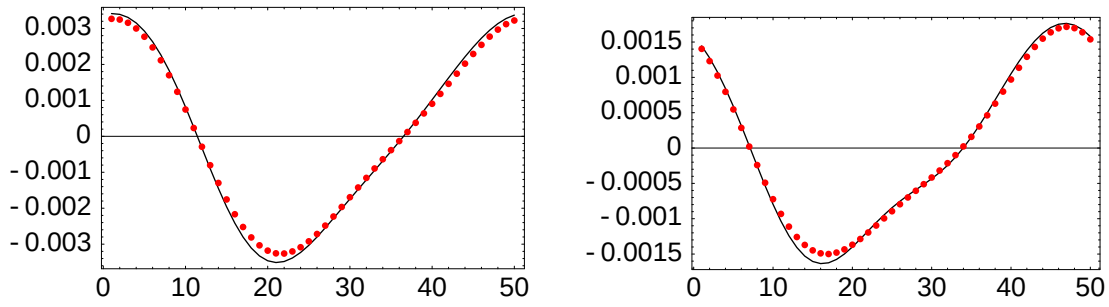

Figure 7.15: Time series in u (left) and v (right) at (.90,.90). Black = Re 9000, red = modeled.

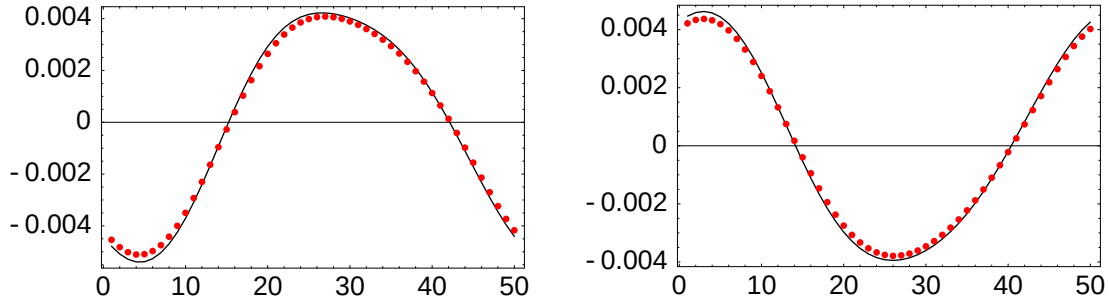

Figure 7.16: Time series in u (left) and v (right) at (.96,.96). Black = Re 9000, red = modeled.

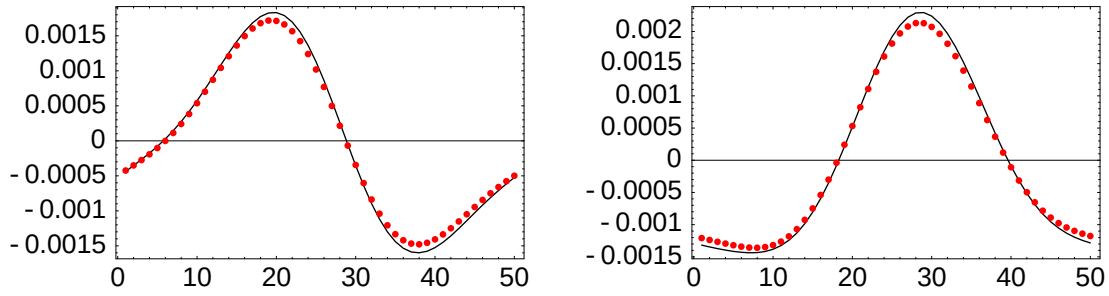

Figure 7.17: Time series in u (left) and v (right) at (.88,.12). Black = Re 9000, red = modeled.

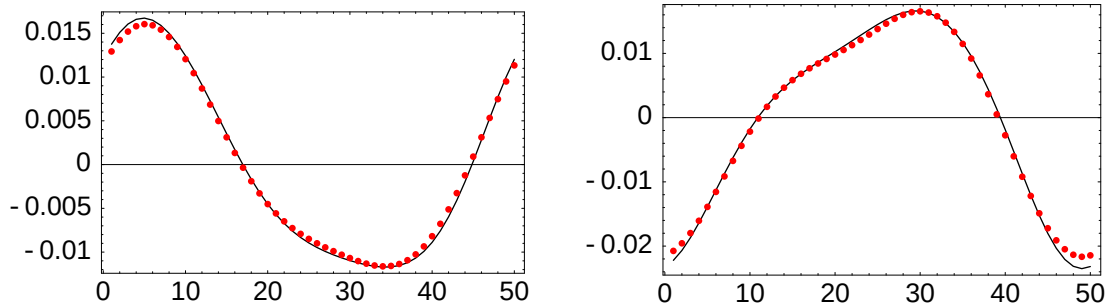

Figure 7.18: Time series in u (left) and v (right) at (.12,.88). Black = Re 9000, red = modeled.

7.2 Full low-dimensional model for the square cylinder wake flow

Next, the square cylinder flow at $Re\,80$ will be reconstructed from the low-dimensional models derived from the four-mode POD at $Re\,70$ and $Re\,90$. The leading four spatial eigenfunctions are used for linear spatial interpolation weighted by period, which was shown in Chapter 6 to be more successful than weighting by Reynolds number. The normalized eigenvalues are estimated by the averages of those at $Re\,70$ and $Re\,90$, and a linear fit for the total unsteady kinetic energy is determined from these reference Reynolds numbers. Figures (7.19) and (7.20) address the necessary phase compensation for direct comparison of modeled data with the DNS data.

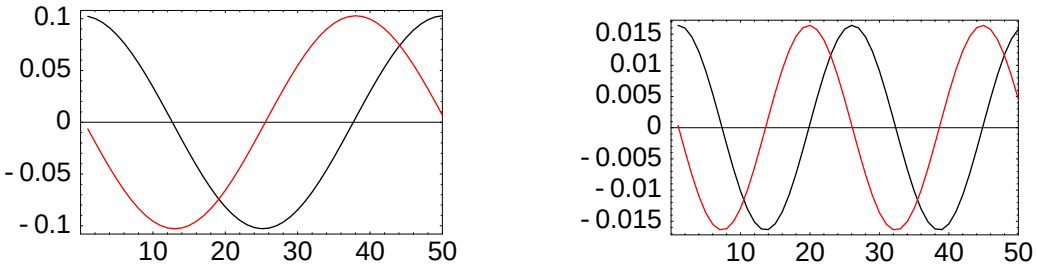

Temporal mode 1. Temporal mode 3.

Figure 7.19: Phase shift between temporal modes of $Re\,90$ (black) and $Re\,80$ (red).

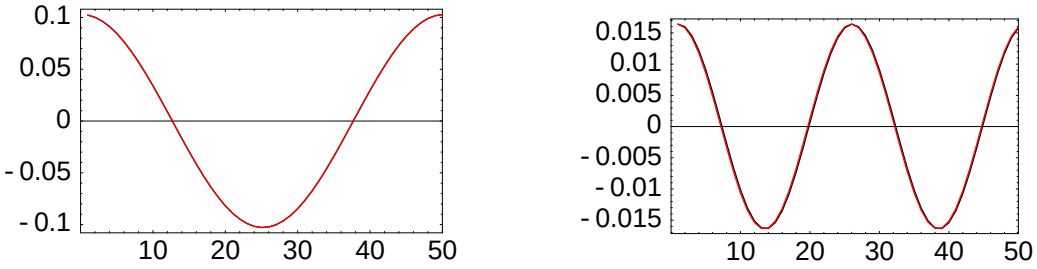

Temporal mode 1. Temporal mode 3.

Figure 7.20: Optimized shift of modeled temporal modes at $Re\,90$ (black) to approximately match phase of modes at $Re\,80$ (red).

Figure (7.21) compares the vorticity for the mean flow of the square cylinder wake. Black dots mark the spatial locations for the time series comparisons to come.

Throughout this comparison, all stream function plots use the same scaling, as do the vorticity plots, so that features may be compared properly between the DNS snapshots on the top, and the modeled snapshots on the bottom of each figure. Figures (7.24) and (7.25) compare the stream function and vorticity, respectively, for snapshot 20 of a 50 snapshot cycle, and Figures (7.26) and (7.27) do likewise for snapshot 40 of a 50 snapshot cycle. Figures (7.28) - (7.35) compare the time series in u, left, and v, right, from the modeled data (red dots) and DNS data (black line). The spatial locations for the time series are graphically shown in Figure (7.21) and sample the entire wake region.

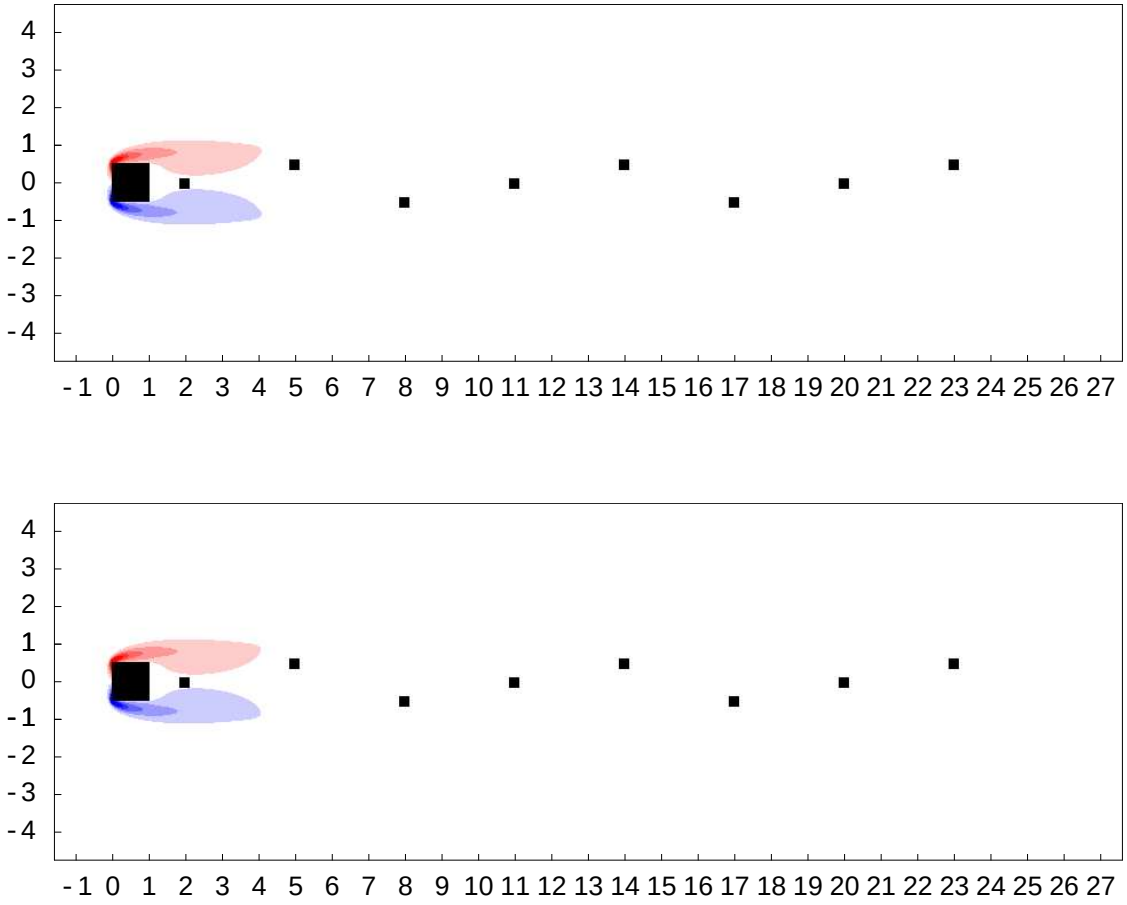

Figure 7.21: Vorticity of mean flow at Re 80: DNS, top and modeled, bottom.

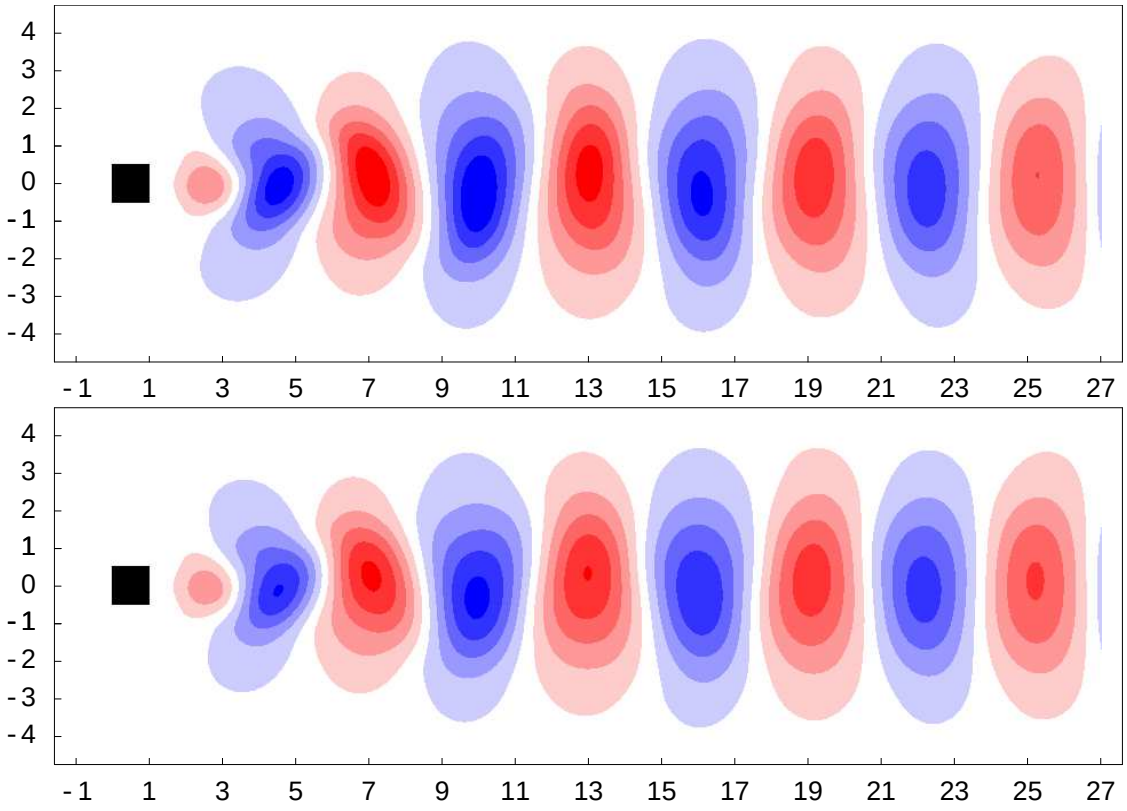

Figure 7.22: Stream function at Re 80, snapshot 1: DNS, top and modeled, bottom.

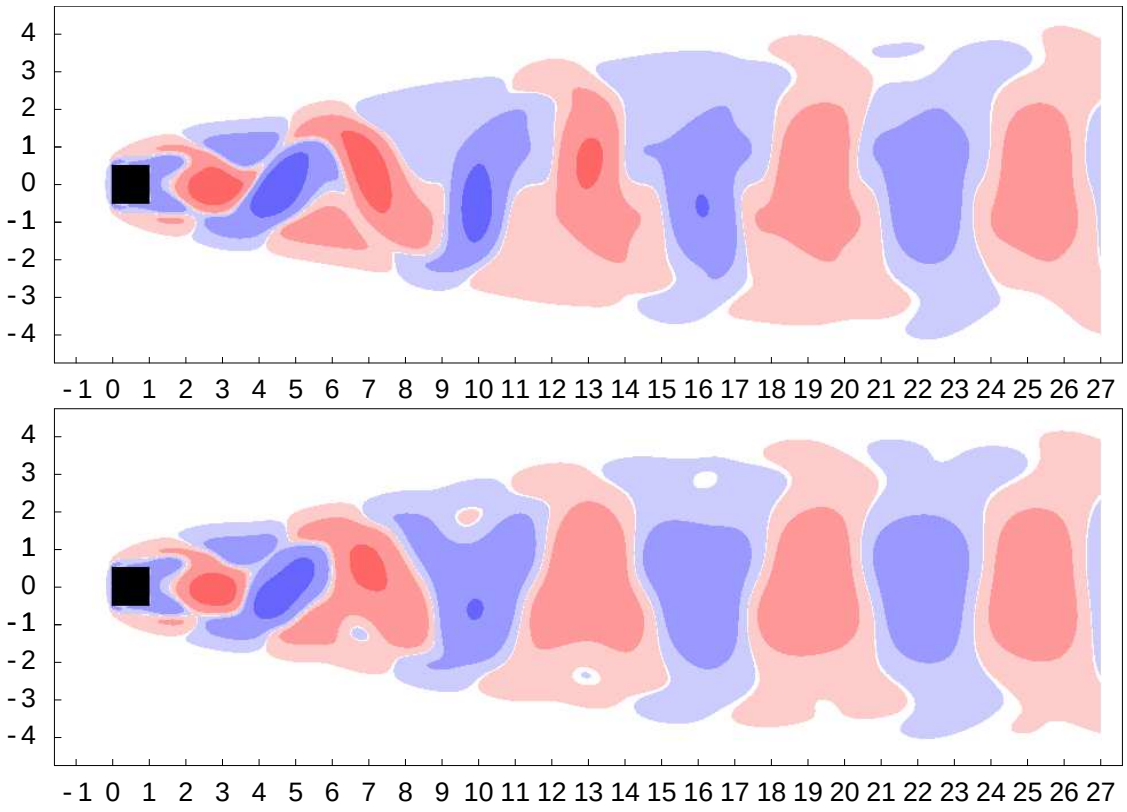

Figure 7.23: Vorticity at Re 80, snapshot 1: DNS, top and modeled, bottom.

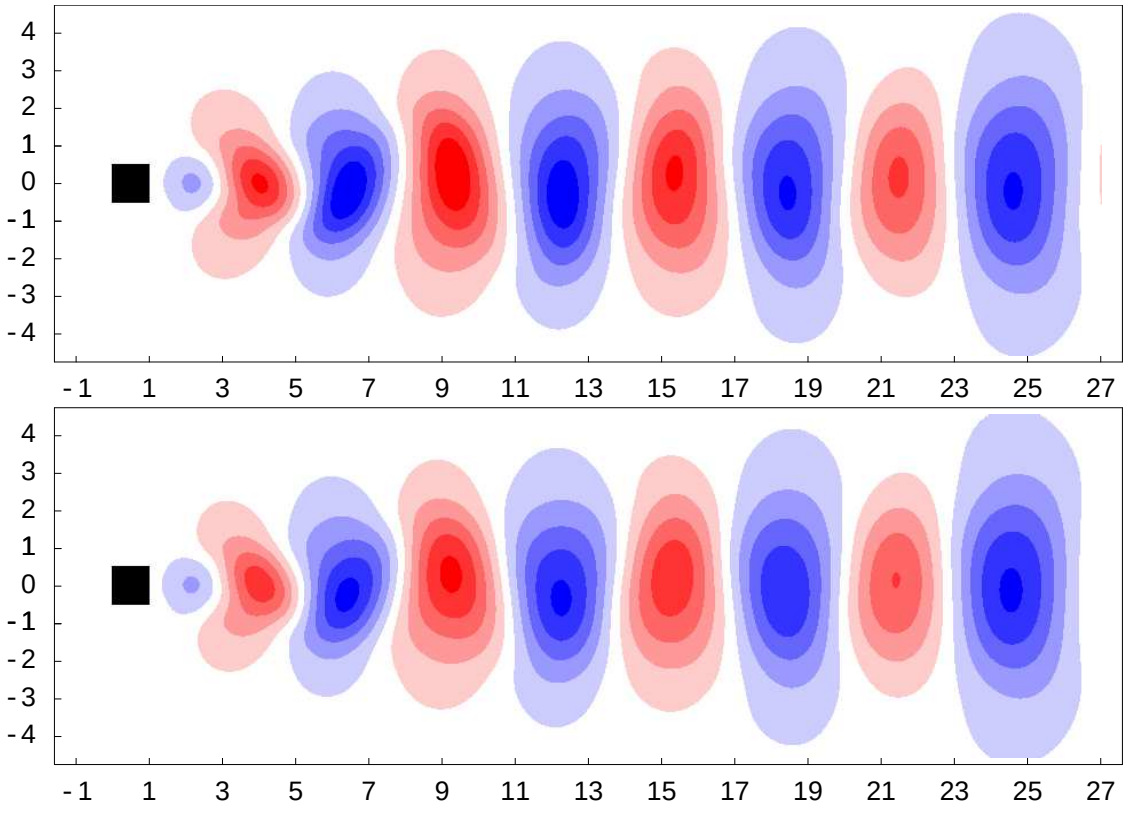

Figure 7.24: Stream function at Re 80, snapshot 20: DNS, top and modeled, bottom.

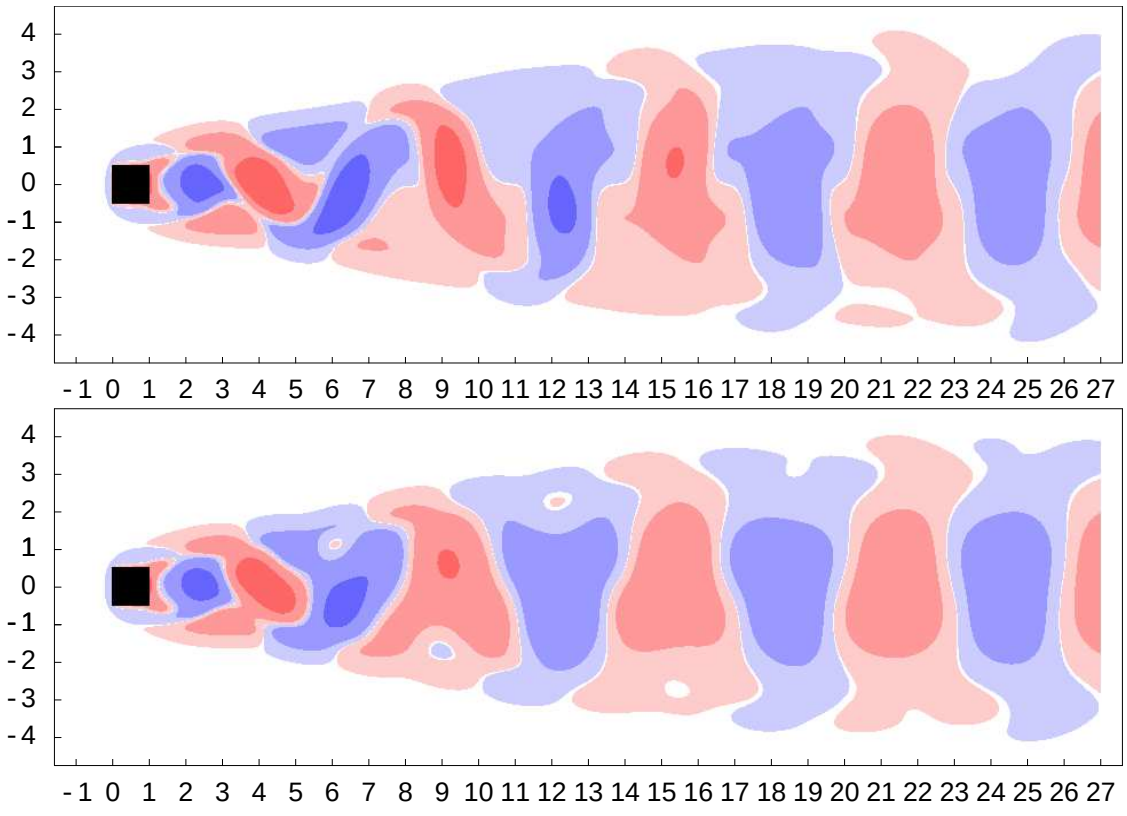

Figure 7.25: Vorticity at Re 80, snapshot 20: DNS, top and modeled, bottom.

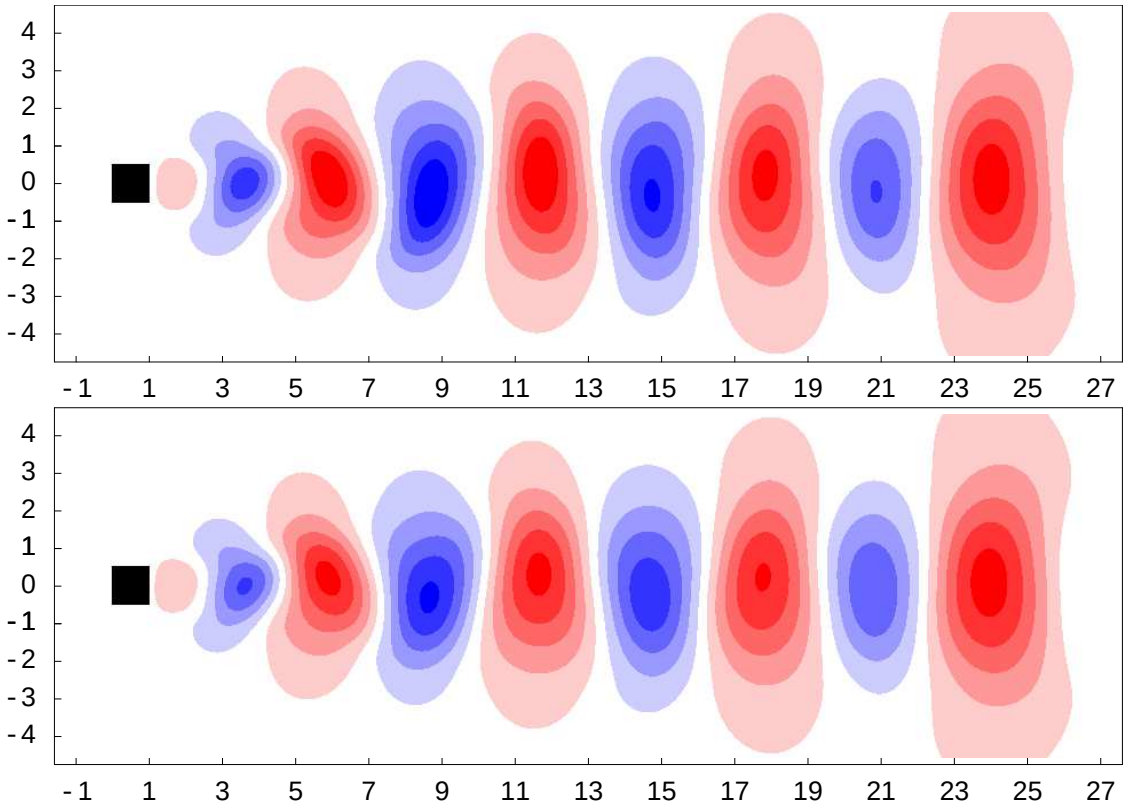

Figure 7.26: Stream function at Re 80, snapshot 40: DNS,top and modeled, bottom.

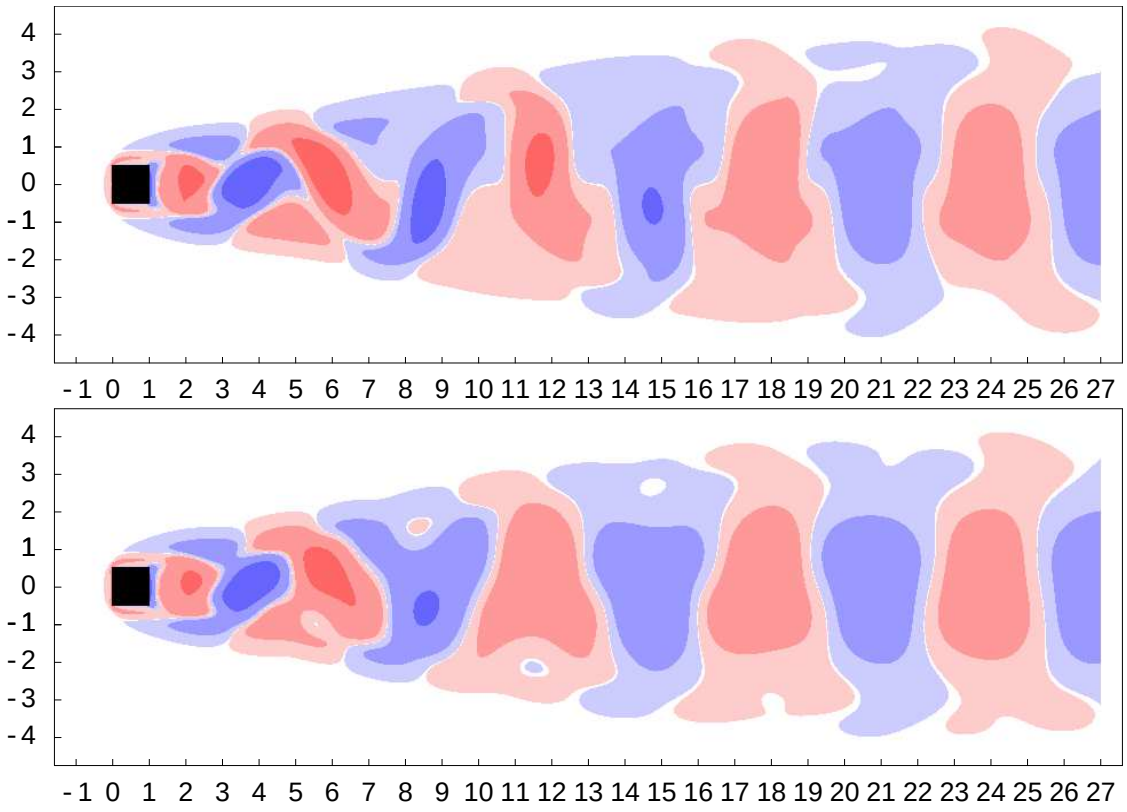

Figure 7.27: Vorticity at Re 80, snapshot 40: DNS, top and modeled, bottom.

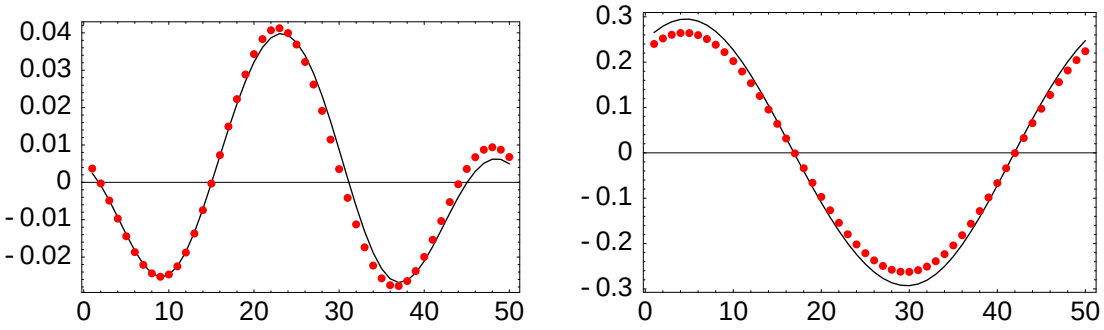

Figure 7.28: Time series in u (left) and v (right) at (2,0). Black = $Re\,80$, red = modeled.

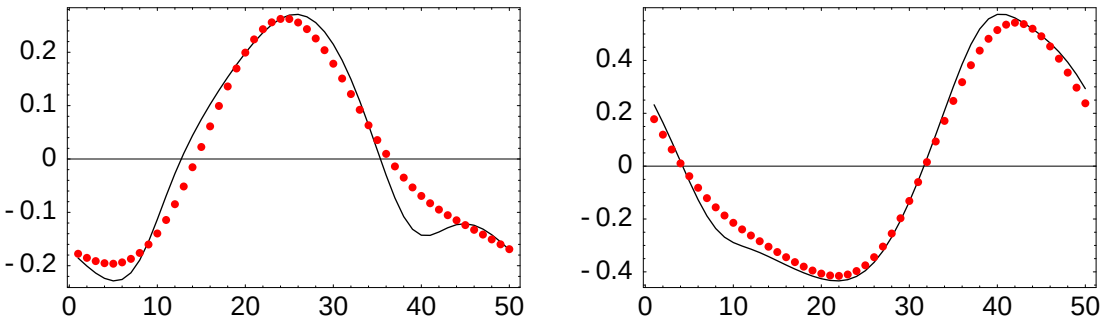

Figure 7.29: Time series in u (left) and v (right) at (5,0.5). Black = $Re\,80$, red = modeled.

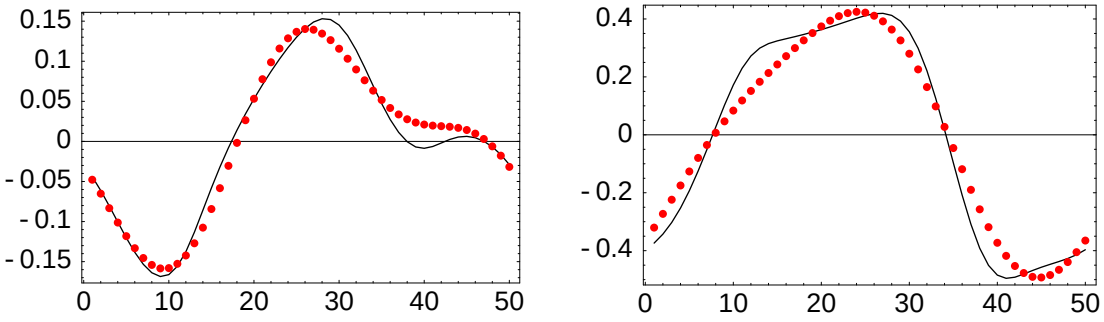

Figure 7.30: Time series in u (left) and v (right) at (8,-0.5). Black = $Re\,80$, red = modeled.

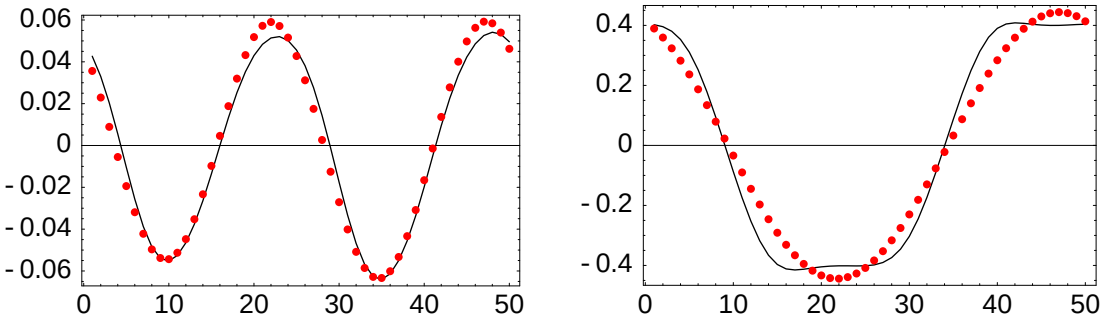

Figure 7.31: Time series in u (left) and v (right) at (11,0). Black = $Re\,80$, red = modeled.

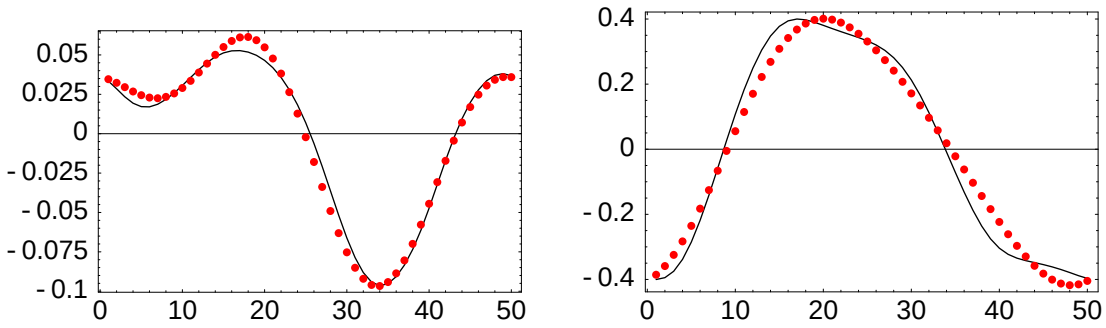

Figure 7.32: Time series in u (left) and v (right) at (14,0.5). Black = $Re\,80$, red = modeled.

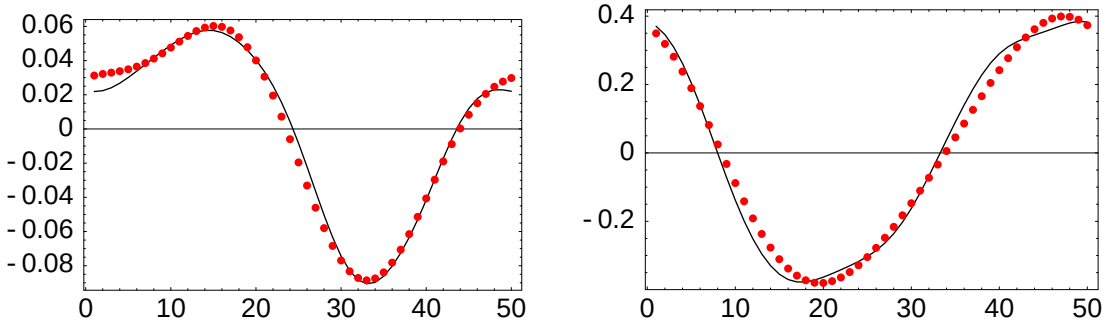

Figure 7.33: Time series in u (left) and v (right) at (17,-0.5). Black = $Re\,80$, red = modeled.

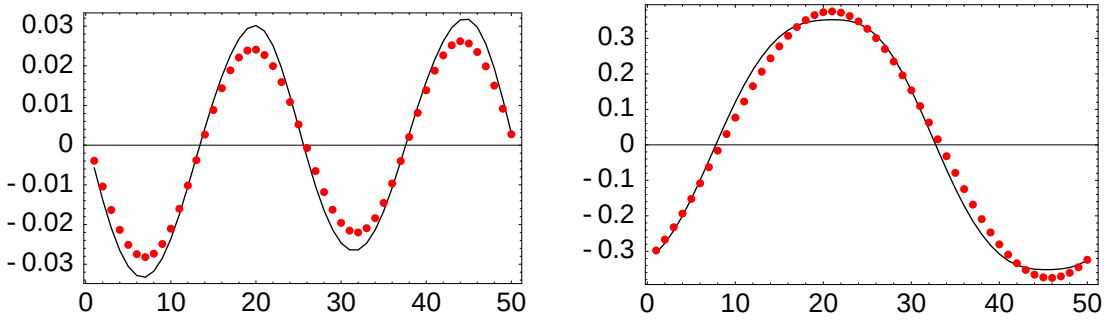

Figure 7.34: Time series in u (left) and v (right) at (20,0). Black = $Re\,80$, red = modeled.

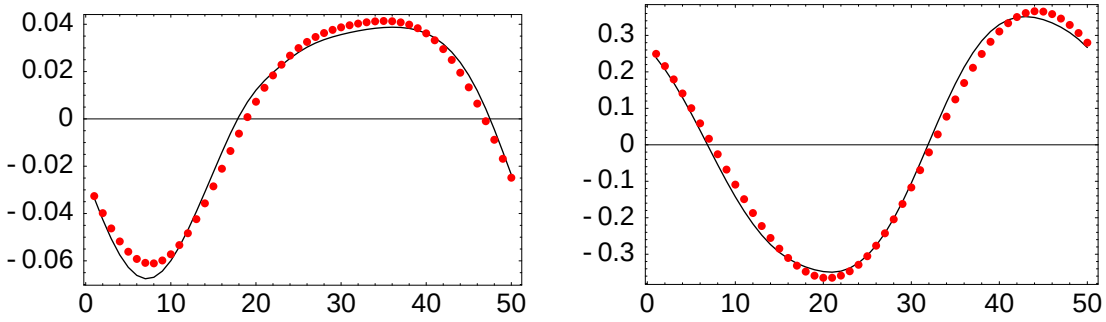

Figure 7.35: Time series in u (left) and v (right) at (23,0.5). Black = $Re\,80$, red = modeled.

Overall, the four-mode reconstruction of the flow at $Re\,9000$ and $Re\,80$ using interpolated data from just two other full simulations ($Re\,8500$ and $Re\,9500$ for the driven cavity and $Re\,70$ and $Re\,90$ for the square cylinder) is remarkably successful. It should be emphasized that these flow predictions are approximations of approximations: even with POD data at the Reynolds number of prediction, flow reconstruction truncated at four modes incurs a 2% error for the unsteady driven cavity flow ($< 1\%$ for total flow) and a 10% error for the unsteady square cylinder wake flow (1% error for total flow).

Secondary accomplishments:

- wrote and time-tested fast Poisson solvers based on **FFTW**,
- coded finite difference software for direct numerical simulation (DNS) of the Navier-Stokes equations with parameterized domain decomposition,
- rigorously benchmarked the DNS code on a wide variety of fluid flows,
- coded proper orthogonal decomposition algorithm with proper scaling for extraction of normalized temporal and spatial eigenfunctions,
- developed and coded software for the Galerkin projection from POD to a dynamical system,
- gained insight into a procedural model for the practical application of these concepts to any fluid flow problem.

While it is true that existing software could have been used for the DNS code, that is not the case for software required for the POD, Galerkin projection, stabilization of the resulting dynamical system, and finally its evolution and/or parameter continuation. I have identified the following special considerations at each stage that may be helpful:

For the DNS, numerical simulations should follow the flow through the transients. For periodic flow, this is easily determined by monitoring the kinetic energy for periodicity. Snapshots of the flow field are then taken at equally spaced intervals. The number of snapshots needed depends on the flow dynamics (periodic through turbulent) for the time duration of the sampling and also for the sampling frequency. For periodic flow, ideally data only needs to be sampled for one period. The intrinsic stabilization method works best with at least two periods from the POD, but this could be achieved by concatenation. The sampling frequency is solely dependent on the temporal frequencies in the data. The Nyquist criteria, sampling frequency must be at least twice the data frequency, is a minimum criterion, and must be calculated to accommodate the harmonics present in a nonlinear periodic flow.

The POD for this dissertation was done from snapshots resampled from a staggered grid to a uniform collocated grid. This is not required; the data for the POD could come from a finite element simulation, for instance, and use weighting factors to properly compute the statistics. However, the next step of Galerkin projection to a dynamical system requires spatial derivatives of the spatial eigenfunctions, so one must know how to do this in whatever coordinate system or methodology used. Since spatial partial derivatives are used in the DNS itself, this could be best accomplished by using parts of the DNS code. The computation of the dynamical system coefficients is straightforward once the spatial eigenfunctions and their spatial partial derivatives in x and y are known. Finally, for periodic flow, the scaling of the dynamical system can be done using the eigenvalues from the POD done at two Reynolds numbers in the range of interest. Given just this information, a subroutine can be compiled with standard AUTO software to evolve the dynamical system and correctly predict the amplitude of oscillation at intermediate Reynolds numbers. The periodicity is not a consequence of these

calculations, however, since the eigenvalue scaling only addresses the change in amplitude. The periodicity can best be accommodated by a parameterization of period by Reynolds number. This can then be incorporated into the AUTO subroutine as a factor applied to each dynamical system coefficient.

While most of the effort has been spent on parameter continuation, the POD has proven effective for analyzing the driven cavity flow at Re 10000 after the torus bifurcation. The appearance of a new frequency can be seen in the DNS data. Figure (7.36) shows a frequency analysis of the flow. The plots are a composite of a point-wise Fourier analysis in u and v at each discretized point. The dominant frequency is plotted. The represented frequencies are the primary frequency $f_1 \approx 2.6$ which originated in the Hopf bifurcation near $Re\,8500$, the new frequency $f_2 \approx 1.6$, and linear combinations of them. In contrast, the Proper Orthogonal Decomposition allows a hierarchical way of dissecting the flow which is far more informative than a Fourier analysis since the POD identifies spatial structures associated with the appearance of the new frequency, specifically in spatial eigenfunction pair 3 and 4 (Figures (3.20) and (3.26)) and will be helpful in understanding the origins of this secondary instability.

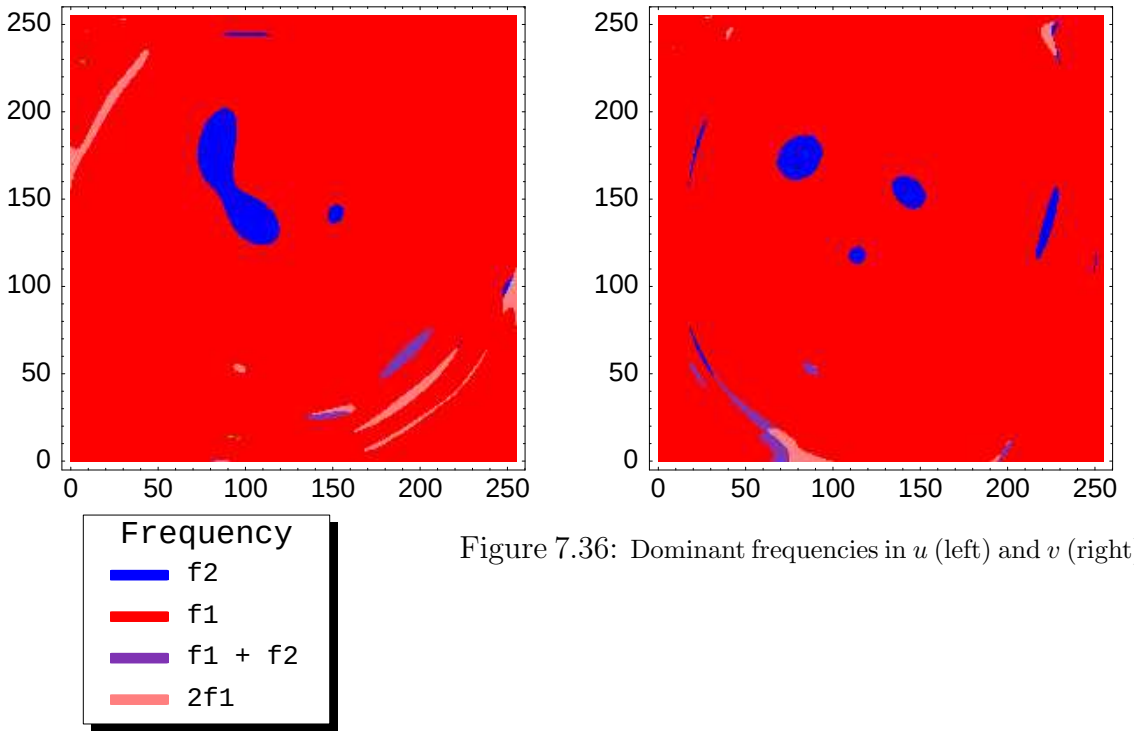

Figure 7.36: Dominant frequencies in u (left) and v (right).

Low-dimensional dynamical systems in the traditional sense of a Galerkin projection of the flow fields onto the spatial eigenfunctions have an undisputed important place in the study of fluid flow. Parameter continuation of the dynamical system for the temporal dynamics works well as a complement to DNS to see how a flow develops and to investigate transitions in flow behavior. A point of view developed through this research, however, is that the temporal and spatial eigenfunctions are equally important, and each yields unique information. This has been used to develop alternative ways to tackle both sides of the problem, *e.g.* the spatial interpolation scheme for the driven cavity flow, which when taken with the temporal parameterized dynamical system comprise a complete low-dimensional model featuring the rich spatial and temporal dynamics of the fluid flow.

A FFTW-based Poisson solver

A.1 Poisson's equation

An efficient solution of Poisson's equation is required in many applications in applied mathematics. In the field of computational fluid dynamics, the solution of the unsteady 2-d incompressible Navier-Stokes equations provides two important examples of solution methods requiring a Poisson solver.

$$\frac{\partial \mathbf{u}}{\partial t} = -\nabla p - (\mathbf{u}\cdot\nabla)\mathbf{u} + \frac{1}{Re}\Delta\mathbf{u}\,, \tag{A.1}$$

$$\nabla\cdot\mathbf{u} = 0\,. \tag{A.2}$$

Each solution method requires a Poisson solver at each time step, and this component is a major portion of the overall computation. One method of solution is the explicit Chorin projection method [11] already discussed in Chapter 2.

$$\frac{\mathbf{u}^\star - \mathbf{u}^n}{\triangle t} = -(\mathbf{u}^n\cdot\nabla)\mathbf{u}^n + \frac{1}{Re}\Delta\mathbf{u}^n\,, \tag{A.3}$$

$$\Delta p^{n+1} = \frac{1}{\triangle t}\nabla\cdot\mathbf{u}^\star\,, \tag{A.4}$$

$$\frac{\mathbf{u}^{n+1} - \mathbf{u}^\star}{\triangle t} = -\nabla p^{n+1}\,. \tag{A.5}$$

The pressure field is determined from Poisson equation (Equation (A.4)).

An alternative method which is strictly limited to 2-d is the vorticity-stream function formulation of the Navier-Stokes equations:

$$\frac{\partial\omega}{\partial t} = \frac{\partial\Psi}{\partial y}\frac{\partial\omega}{\partial x} - \frac{\partial\Psi}{\partial x}\frac{\partial\omega}{\partial y} + \frac{1}{Re}\Delta\omega\,, \tag{A.6}$$

$$\Delta\Psi = \omega\,. \tag{A.7}$$

The equations are derived from the momentum equation (Equation (A.1)) by taking

the curl of both sides, yielding a single equation for vorticity, ω, defined by $\omega = \frac{\partial v}{\partial x} - \frac{\partial u}{\partial y}$ since the x and y components of vorticity vector are zero. The incompressibility constraint is automatically satisfied by introducing the stream function, Ψ, defined by $-\frac{\partial \Psi}{\partial y} = u$ and $\frac{\partial \Psi}{\partial x} = v$. This system of equations may be solved by first updating ω by a time-marching technique, for example a fourth order Runge-Kutta, then solving a Poisson equation for Ψ. For a finite difference solution, both ω and Ψ are defined at the grid points.

Direct solvers for Poisson's equation provide a computationally attractive method for the solution in either situation. In particular, a solver that capitalizes on the economy of the fast Fourier transform is of considerable interest, both from its speed and ease of use. This is certainly not a new concept [31], [34], [35], [36] to cite but a few important works from the abundant literature on the subject. Nevertheless, speed gains over existing methods may still be attained. Recently, a new fast Fourier transform (FFT) software package has been developed that is significantly faster than existing FFT methods: **FFTW** [14]. The drawback of this package (version 2.1.3) for use with Poisson's equation was a lack of the pre- and post-processing necessary to utilize the Fourier transform for the computation of the symmetric transforms (sine, cosine, quarter-wave sine, and quarter-wave cosine). This work seeks to fill this void and provide the required interfaces while maintaining an increase in speed afforded by the underlying very fast Fourier transform code.

A.2 Background: solving Poisson's equation

Consider the 1-d Poisson equation $\Delta u = f$ on the unit interval $[0, 1]$, since the method is easily extended to multiple dimensions. Two grids will be considered: a uniform grid coincident with the Cartesian grid, and a staggered grid where the grid points are offset from the Cartesian grid. For the coincident grid, let

$x_i = ih, \quad i = 0, ..., n, \quad h = \frac{1}{n}$. $x_0 = 0$ and $x_n = 1$. For the staggered grid, let $x_i = (i + \frac{1}{2})h, \quad i = -1, ..., n, \quad h = \frac{1}{n}$. x_{-1} and x_n are ghost points used to express the boundary conditions, and are not used computationally, with the exception of the cosine transform which does require x_n. The second order central difference operator for $\frac{d^2u}{dx^2}$ at x_i is $\frac{u_{i-1}-2u_i+u_{i+1}}{h^2}$. Both Dirichlet and Neumann boundary condition problems will be discussed for coincident and staggered grids. The general technique is the same [38]:

- Homogenize the boundary condition.
- Take the appropriate transform to express the right hand side vector in terms of the (known) eigenvectors.
- Obtain the transform of the solution by dividing each coefficient by the appropriate (known) eigenvalue.
- Take the inverse transform to obtain the solution.

The type of transform depends upon the eigenfunctions of the differential operator, incorporating both boundary conditions and grid. The Dirichlet coincident grid uses the sine transform, the Neumann coincident grid uses the cosine transform, the Dirichlet staggered grid uses the quarter-wave sine transform and its inverse, and the Neumann staggered grid uses the quarter cosine-wave transform and its inverse. The underlying Fourier transform in each case is of length n.

A.3 Dirichlet coincident grid

At x_1, $\frac{u_0-2u_1+u_2}{h^2} = f_1$. If $u_0 = U_0$, the equation can be rewritten as $\frac{-2u_1+u_2}{h^2} = f_1 - \frac{U_0}{h^2}$. The problem at x_{n-1} with $u_n = U_1$ may be similarly rewritten

with the resultant matrix representation:

$$\frac{1}{h^2}\begin{bmatrix} 1 & 0 & 0 & 0 & \cdots & 0 \\ 0 & -2 & 1 & 0 & \cdots & 0 \\ 0 & 1 & -2 & 1 & \cdots & 0 \\ \vdots & \vdots & \vdots & \vdots & \ddots & \vdots \\ 0 & \cdots & 0 & 1 & -2 & 1 \\ 0 & \cdots & 0 & 0 & 1 & -2 \end{bmatrix} \begin{bmatrix} u_0 \\ u_1 \\ u_2 \\ \vdots \\ u_{n-2} \\ u_{n-1} \end{bmatrix} = \begin{bmatrix} \frac{U_0}{h^2} \\ f_1 - \frac{U_0}{h^2} \\ f_2 \\ \vdots \\ f_{n-2} \\ f_{n-1} - \frac{U_1}{h^2} \end{bmatrix}, \tag{A.8}$$

$$\frac{1}{h^2}\,\mathbf{Mu} = \mathbf{f}\,. \tag{A.9}$$

For this case, $\lambda_0 = 1$ and the problem is posed as an $n \times n$ matrix problem because the underlying transform requires a vector of length n, and this is a way of keeping entries in consistent address locations.

The eigenvalues λ_k and eigenvectors $\mathbf{v}_k, k = 1, \ldots, n-1$ of this matrix are (see, for example, Lomax's *Fundamentals of Computational Fluid Dynamics*, Appendix B.[39]):

$$\lambda_k = \frac{-2}{h^2} + \frac{2}{h^2}\cos(\frac{k\pi}{n}) = \frac{-4}{h^2}\sin^2(\frac{k\pi}{2n})\,, \tag{A.10}$$

$$\mathbf{v}_k\,[i] = \sin(\frac{ik\pi}{n}), i = 0, \ldots, n-1\,. \tag{A.11}$$

The expansion of an arbitrary vector in terms of these eigenvectors may be accomplished by taking the sine transform of the vector. Doing so for $\mathbf{u}$ and $\mathbf{f}$ in

Equation (A.9), the original problem may be expressed

$$\mathbf{u} = \sum_{k=1}^{n-1} \mathcal{U}_k \mathbf{v}_k \,, \tag{A.12}$$

$$\mathbf{f} = \sum_{k=1}^{n-1} \mathcal{F}_k \mathbf{v}_k \,, \tag{A.13}$$

$$\mathbf{M} \sum_{k=1}^{n-1} \mathcal{U}_k \mathbf{v}_k = \sum_{k=1}^{n-1} \mathcal{F}_k \mathbf{v}_k \,. \tag{A.14}$$

Upon rearranging terms and using the fact that $\mathbf{M}\,\mathbf{v}_k = \lambda_k\,\mathbf{v}_k, k = 1, \ldots, n-1$ and the orthogonality of the eigenvectors of a real symmetric matrix:

$$\mathcal{U}_k = \frac{\mathcal{F}_k}{\lambda_k}, k = 1, \ldots, n-1 \,. \tag{A.15}$$

The solution at $x_1, \ldots, x_{n-1}$ is obtained by taking the inverse transform, which in this case is again the sine transform. The other 3 cases can be handled in a similar manner. The specifics for each remaining case are summarized in the following sections.

A.4 Neumann coincident grid

Let $\frac{du}{dn}\,|_{x=0} = DU_0$ and $\frac{du}{dn}\,|_{x=1} = DU_1$ where $\mathbf{n}$ is the outward normal.

$$\frac{1}{h^2}\begin{bmatrix} -2 & 2 & 0 & 0 & \cdots & 0 \\ 1 & -2 & 1 & 0 & \cdots & 0 \\ 0 & 1 & -2 & 1 & \cdots & 0 \\ \vdots & \vdots & \vdots & \vdots & \ddots & \vdots \\ 0 & \cdots & 0 & 1 & -2 & 1 \\ 0 & \cdots & 0 & 0 & 2 & -2 \end{bmatrix} \begin{bmatrix} u_0 \\ u_1 \\ u_2 \\ \vdots \\ u_{n-1} \\ u_n \end{bmatrix} = \begin{bmatrix} f_0 - \frac{2DU_0}{h} \\ f_1 \\ f_2 \\ \vdots \\ f_{n-1} \\ f_n - \frac{2DU_1}{h} \end{bmatrix} . \tag{A.16}$$

While the left hand side $n+1$ x $n+1$ matrix $\mathbf{M}$ is not symmetric, it is similar to one: $\mathbf{M} = \mathbf{Z}^{-1}\mathbf{S}\mathbf{Z}$ where:

$$\mathbf{Z} = \begin{bmatrix} 1 & 0 & 0 & 0 & \cdots & 0 & (-1)^{n+1} \\ \frac{1}{2} & \frac{1}{2} & 0 & 0 & \cdots & 0 & (-1)^{n} \\ 0 & \frac{1}{2} & \frac{1}{2} & 0 & \cdots & 0 & (-1)^{n-1} \\ \vdots & \vdots & \vdots & \vdots & \ddots & \vdots & \vdots \\ 0 & 0 & \cdots & \frac{1}{2} & \frac{1}{2} & 0 & (-1)^{4} \\ 0 & 0 & \cdots & 0 & \frac{1}{2} & \frac{1}{2} & (-1)^{3} \\ 0 & 0 & \cdots & 0 & 0 & 1 & (-1)^{2} \end{bmatrix}, \mathbf{S} = \begin{bmatrix} -1 & 1 & 0 & 0 & \cdots & 0 \\ 1 & -2 & 1 & 0 & \cdots & 0 \\ 0 & 1 & -2 & 1 & \cdots & 0 \\ \vdots & \vdots & \vdots & \vdots & \ddots & \vdots \\ 0 & \cdots & 1 & -2 & 1 & 0 \\ 0 & \cdots & 0 & 1 & -1 & 0 \\ 0 & \cdots & 0 & 0 & 0 & -4 \end{bmatrix}. \tag{A.17}$$

The eigenvalues λ_k and eigenvectors $\mathbf{v}_k, k = 0, \ldots, n$ of $\frac{1}{h^2}\mathbf{M}$ are:

$$\lambda_k = \frac{-2}{h^2} + \frac{2}{h^2}\cos(\frac{k\pi}{n}) = \frac{-4}{h^2}\sin^2(\frac{k\pi}{2n}), \tag{A.18}$$

$$\mathbf{v}_k[i] = \cos(\frac{ik\pi}{n}), i = 0, \ldots, n. \tag{A.19}$$

The second order centered finite difference approximation is used to express the boundary data and to homogenize the boundary conditions. The cosine transform will give the expansion in terms of these eigenvectors. The zero eigenvalue indicates the one degree of freedom, up to a constant, of the Neumann problem. This can be resolved by zeroing the leading coefficient of the cosine transform, in effect setting the constant equal to zero.

A.5 Dirichlet staggered grid

Let $u_0 = U_0$ and $u_1 = U_1$.

$$\frac{1}{h^2}\begin{bmatrix} -3 & 1 & 0 & 0 & \cdots & 0 \\ 1 & -2 & 1 & 0 & \cdots & 0 \\ 0 & 1 & -2 & 1 & \cdots & 0 \\ \vdots & \vdots & \vdots & \vdots & \ddots & \vdots \\ 0 & \cdots & 0 & 1 & -2 & 1 \\ 0 & \cdots & 0 & 0 & 1 & -3 \end{bmatrix}\begin{bmatrix} u_{\frac{1}{2}} \\ u_{1+\frac{1}{2}} \\ u_{2+\frac{1}{2}} \\ \vdots \\ u_{n-\frac{3}{2}} \\ u_{n-\frac{1}{2}} \end{bmatrix} = \begin{bmatrix} f_{\frac{1}{2}} - \frac{2U_0}{h^2} \\ f_{1+\frac{1}{2}} \\ f_{2+\frac{1}{2}} \\ \vdots \\ f_{n-\frac{3}{2}} \\ f_{n-\frac{1}{2}} - \frac{2U_1}{h^2} \end{bmatrix}. \tag{A.20}$$

The eigenvalues λ_k and eigenvectors $\mathbf{v}_k, k = 0, \ldots, n-1$ of this matrix are:

$$\lambda_k = \frac{-2}{h^2} + \frac{2}{h^2}\cos(\frac{(k+1)\pi}{n}) = \frac{-4}{h^2}\sin^2(\frac{(k+1)\pi}{2n}), \tag{A.21}$$

$$\mathbf{v}_k[i] = \sin(\frac{(2i+1)(k+1)\pi}{2n}), i = 0, \ldots, n-1. \tag{A.22}$$

The quarter-wave sine transform will give the required expansion in terms of these eigenvectors.

A.6 Neumann staggered grid

Let $\frac{du}{dn}|_{x=0} = DU_0$ and $\frac{du}{dn}|_{x=1} = DU_1$ where $\mathbf{n}$ is the outward normal.

$$\frac{1}{h^2}\begin{bmatrix} -1 & 1 & 0 & 0 & \cdots & 0 \\ 1 & -2 & 1 & 0 & \cdots & 0 \\ 0 & 1 & -2 & 1 & \cdots & 0 \\ \vdots & \vdots & \vdots & \vdots & \ddots & \vdots \\ 0 & \cdots & 0 & 1 & -2 & 1 \\ 0 & \cdots & 0 & 0 & 1 & -1 \end{bmatrix}\begin{bmatrix} u_{\frac{1}{2}} \\ u_{1+\frac{1}{2}} \\ u_{2+\frac{1}{2}} \\ \vdots \\ u_{n-\frac{3}{2}} \\ u_{n-\frac{1}{2}} \end{bmatrix} = \begin{bmatrix} f_{\frac{1}{2}} - \frac{DU_0}{h} \\ f_{1+\frac{1}{2}} \\ f_{2+\frac{1}{2}} \\ \vdots \\ f_{n-\frac{3}{2}} \\ f_{n-\frac{1}{2}} - \frac{DU_1}{h} \end{bmatrix}. \tag{A.23}$$

The eigenvalues λ_k and eigenvectors $\mathbf{v}_k, k = 0, \ldots, n-1$ of this matrix are:

$$\lambda_k = \frac{-2}{h^2} + \frac{2}{h^2}\cos(\frac{k\pi}{n}) = \frac{-4}{h^2}\sin^2(\frac{k\pi}{2n})\,, \tag{A.24}$$

$$\mathbf{v}_k\,[i] = \cos(\frac{(2i+1)k\pi}{2n}), i = 0, \ldots, n-1\,. \tag{A.25}$$

"First" order backward finite difference approximation is used to homogenize the boundary conditions, although on a staggered grid it is actually second order. The quarter-wave cosine transform will give the expansion of the right hand side in terms of these eigenvectors. Again, the zero eigenvalue indicates the one degree of freedom, up to a constant, of the Neumann problem, and is handled by zeroing the coefficient of the quartercosine transform, in effect setting the constant equal to zero.

A.7 Implementation: One dimension

Pre- and post-processing of the input data sequence is needed in order to use the real Fourier transform in the computation of the symmetric transforms. These algorithms have been developed and implemented in **FFTPACK** by Paul Swarztrauber [33], and are put to use here as well. **FFTW** packs the real and imaginary parts of the Fourier transform differently than **FFTPACK**, so suitable adjustments were made in the addressing. Like **FFTPACK**, **FFTW** does not perform any scaling; *e.g.*, a real forward transform followed by a real inverse transform returns the original sequence multiplied by n. This works well for a fast Poisson solver since the FFT scaling can be incorporated into the eigenvalue scaling without incurring an additional speed penalty. **FFTW** has the option of doing transforms in or out of place. The "out of place" option is faster, and is the method used in the **FFTW**-based symmetric transforms, although post-processing puts the final result in place of the input data. **FFTW** has an option for transforming multiple sequences with a single function call, and an interface to this capability has

been provided for the symmetric transforms as well.

A.8 Implementation: Two dimensions

Generalizing the algorithm for solving Poisson's equation in section A.2 to two dimensions requires 2-d symmetric transforms. One approach to computing a 2-d sine transform, for example, is to make two 1-d passes of the data field. First, take the 1-d sine transform of each field row, transpose the field, take the sine transform of each new row, transpose again, and divide each entry by the sum of the appropriate eigenvalues for that row and column in frequency space. There are two options to this approach for a pass: loop on single sine transforms for each row, or use the multiple sequence interface to preprocess all rows, FFT all rows, then postprocess all. The problem with these implementations is that it is very inefficient to make so many passes through the data, since the pre- and post-processing steps already require a pass before and after each FFT and transposing the field requires two more passes. Three distinct alternative strategies have been implemented, and all prove to be faster than the two possible approaches utilizing 1-d passes through the data and matrix transposition. They all avoid the need for taking the transpose as a separate step by either transposing the data during the post-processing step or by picking up the data to be processed and FFT'd from columns instead of rows. The diagram in Figure (A.1) graphically illustrates the data flow. Memory usage is also a consideration for large 2-d problems. Of the alternatives considered, the one called "in place" has the distinction of only requiring two scratch arrays of length n in addition to the n x n data field. All others require an n x n scratch array.

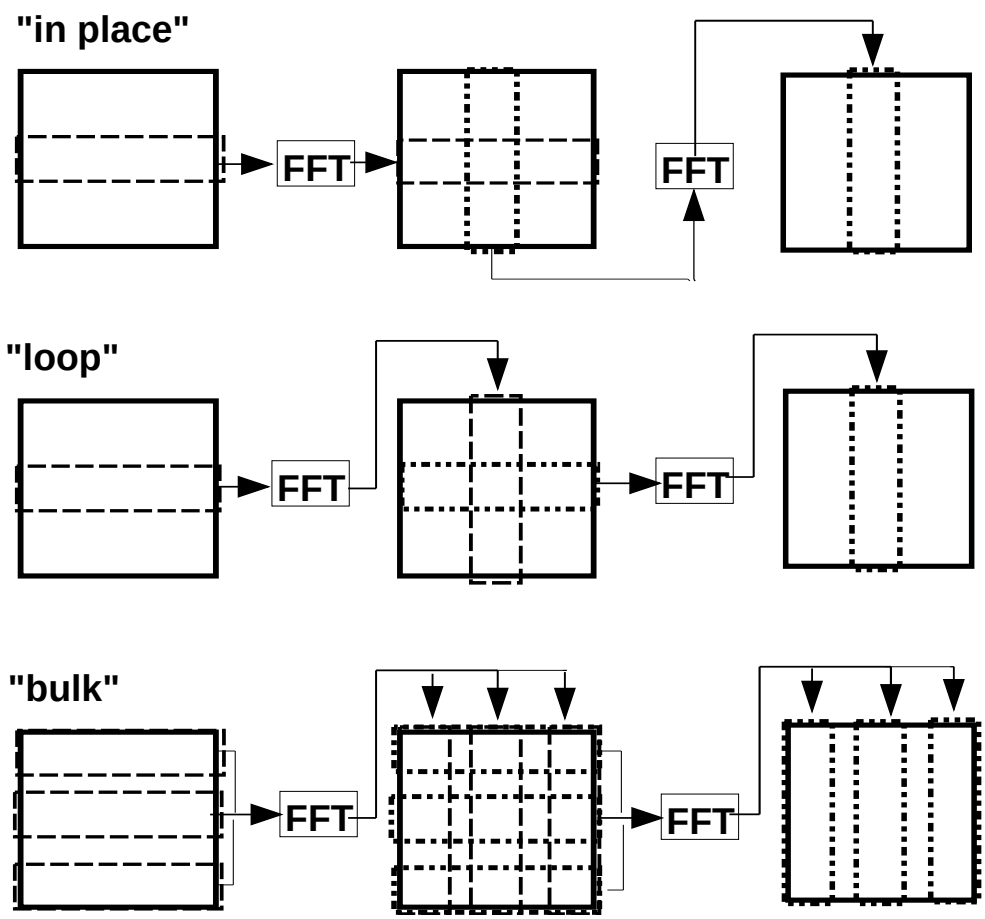

Figure A.1: Data flow diagram for 2-d algorithms: "in place" extracts the 1-d data it needs by row or column and puts it back in its original location in the field, "loop" processes data by rows and stores it in columns, "bulk" is "loop" applied to all rows at a time, so that preprocessing is done to the entire field before performing the FFT, etc.

A.9 Conclusions

FFTW has proven to be an excellent package not only for straight FFTs, but also as a component for the implementation of the symmetric transforms. Timing results confirm that a major speed advantage is gained by using code based on **FFTW** for the solution of Poisson's equation in one and two dimensions. Even in double precision mode, this code has the edge over existing packages run in single precision. This is noteworthy since Poisson's equation is a critical factor in many algorithms in mathematics and the sciences, and its accurate solution is as important as computational efficiency. The inclusion of 2-d specific algorithms for Poisson's equation in two dimensions as opposed to the use of 1-d code and matrix transposition is of special interest since it further increases the speed of computation. The "in place" 2-d transform has the added bonus of requiring less scratch memory than 1-d passes with transposition ($2n$ vs n^2).

To verify that the speed gains achieved at the transform level propagate to the simulation level, a sample problem was run using the two computational methods discussed earlier (vorticity-stream function and Chorin projection method). Each method was run for the driven cavity flow problem on square grids of dimensions ranging from 16×16 to 512×512. Each method was run in two variants: one using **FFTPACK** for the Poisson solver and one using the **FFTW**-based 2-d symmetric transforms, all single precision. The ratio of runtimes for the **FFTPACK** code to the **FFTW**-based code was computed and plotted for each method. Figure (A.2) confirms that overall simulation times are markedly improved by the use of the **FFTW**-based 2-d symmetric transforms and are between $1\frac{1}{2}$ and 2 times smaller.

It should be noted that **FFTW** has several options for use in a parallel processing environment. Comprehensive timing results are follow.

A.10 Timing results

To establish a performance baseline, timing for a real forward and inverse transform pair has been computed for **FFTW**, **FFTPACK**, and **GPFA**[37], an earlier code by C. Temperton, **FFT99**. **VFFTPACK** was not tested since it is a vectorized version of **FFTPACK** and does not perform well on a single processor machine. Of these FFT packages, **FFTW**, **FFTPACK** and **GPFA** do not perform any scaling. Thus, to fairly compare results, these trials have also been performed with an added scaling step. Performance is compared at powers of two and at composite numbers, the same as those used in the benchmark results at **http://FFTW.org**. Since **FFT99** and **GPFA** can only deal with numbers with prime factors of 2, 3, 4, and 5, they couldn't handle most of these numbers, hence were not tested with composite numbers. The other packages have been run in their default mode of single precision, but since it is easy to build both single and double precision versions of **FFTW** without conflict, both precisions have been tested. Of these alternative FFT packages, only **FFTPACK** has implemented the symmetric transforms, so the timing results for the 1-d Poisson solution are somewhat limited. Timing was performed done for the same transform lengths as for the straight FFTs. The number of test cases for the 2-d solution of Poisson's equation is smaller due to memory constraints. It should be noted that initialization is not included in the timing results.

All results were obtained using an AMD-K6 450MHz computer with 528 Mb of memory running Linux RedHat, version 7.1. Results are presented in two ways: comparison of absolute performance and of relative performance. In every graph, the x-axis is labelled with the transform length. Time per transform pair measured in "Mflops", defined by $5Nlog_2N/T$ where T is the time for one forward and one backward FFT measured in microseconds. This is the way speed is scaled for **FFTW** benchmark results on **http://FFTW.org** because $5Nlog_2N$ is an

approximation for the number of operations in an FFT, hence the result is approximately millions of operations per second. The same scaling is used here for the symmetric transforms as well. Thus, absolute performance is displayed with "Mflops" on the y-axis. Note that this measure is inversely proportional to time, so faster results translate to bigger numbers. A second way of looking at the data is to look at the ratio of time required by the alternative methods with **FFTW**. This number is always greater than one since in every case the **FFTW** methods are faster. The results are representative of results obtained on other architectures, which are not presented here for brevity. Figures A.3 through A.6 establish the baseline of **FFTW** performance against other packages on this architecture for a forward and backward transform of a real sequence. Figures A.7 through A.14 show the absolute performance of the symmetric transforms using **FFTW** versus **FFTPACK** for the 1-d Poisson equation. Figures A.15 and A.16 summarize the relative performance of these runs. The only option for the use of **FFTPACK** for the 2-d Poisson's equation is to make 1-d passes and transpose the field in between. This has been timed and compared with both the **FFTW**-based 1-d symmetric transforms used with transposition and with the alternative 2-d strategies in Figures A.17 through A.24. The 2-d specific algorithms always have better performance than the 1-d with transpose methods. The "bulk" methods, those utilizing the multiple FFTs at a time, perform best for smaller data sets and are surpassed by more localized methods as the size of the data increases. The 2-d "in place" method appears to be the overall best choice, both from timing results and memory requirements. Finally, all **FFTW**-based algorithms have been tested for accuracy, and demonstrate second order convergence in the L1, L2, and L∞ norms. Typical log-log plots of error versus transform length for 1-d and 2-d are shown in Figures A.25 and A.26, respectively.

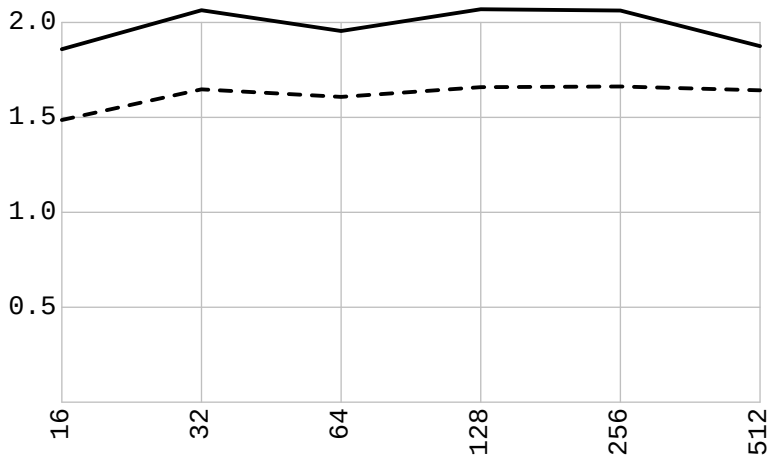

Figure A.2: The ratio of runtimes using **FFTPACK** to runtimes using the **FFTW**-based transforms for the vorticity-stream function method (solid) and the Chorin projection method (dashed) for a 2-d fluid flow. Grid size is on the x axis.

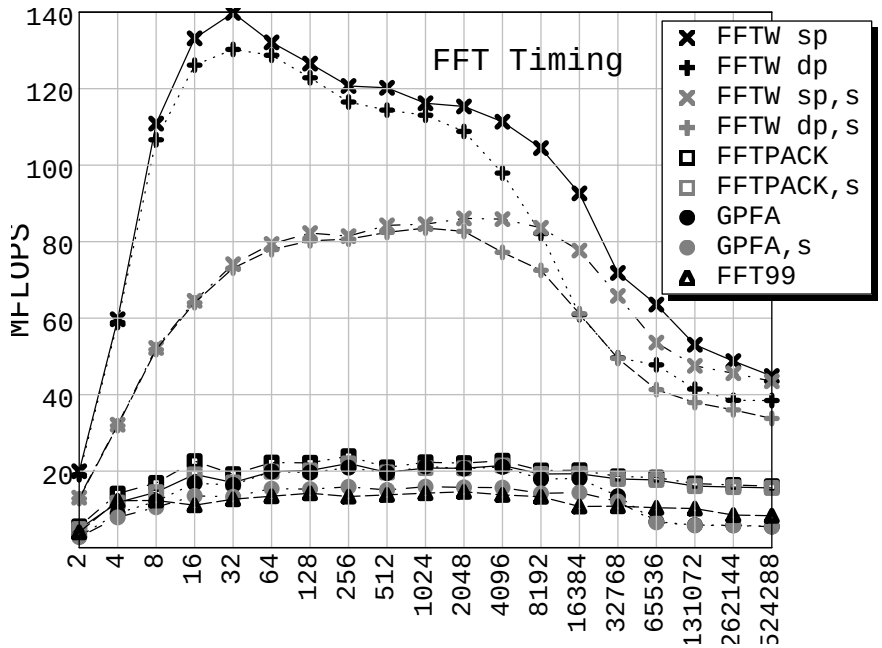

Figure A.3: Comparison of various methods for 1-d FFT, Mflops versus transform length for powers of 2. (Note: sp = single precision, dp = double precision, s = scaled.)

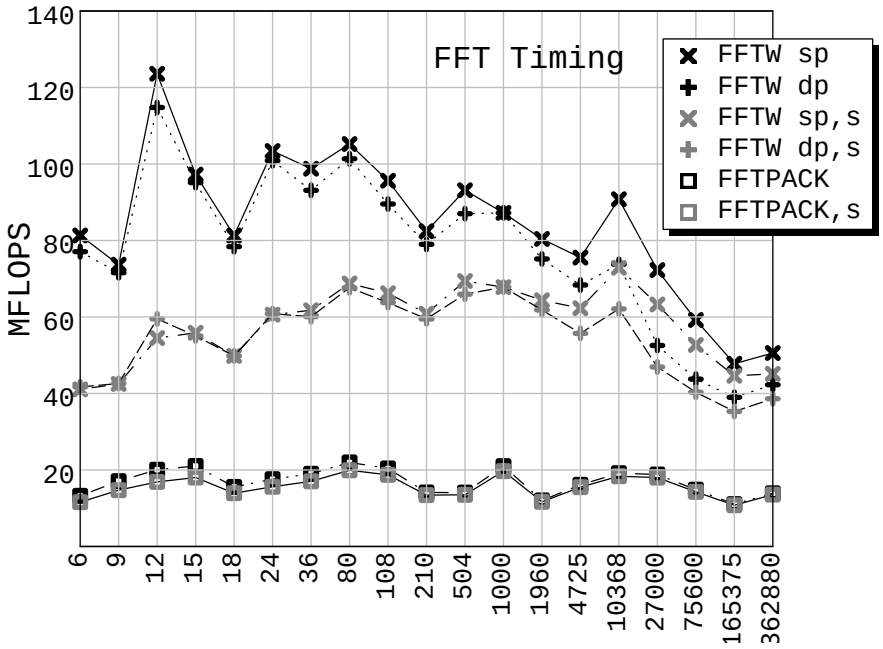

Figure A.4: Comparison of various methods for 1-d FFT, Mflops versus transform length for non-powers of 2. (Note: sp = single precision, dp = double precision, s = scaled.)

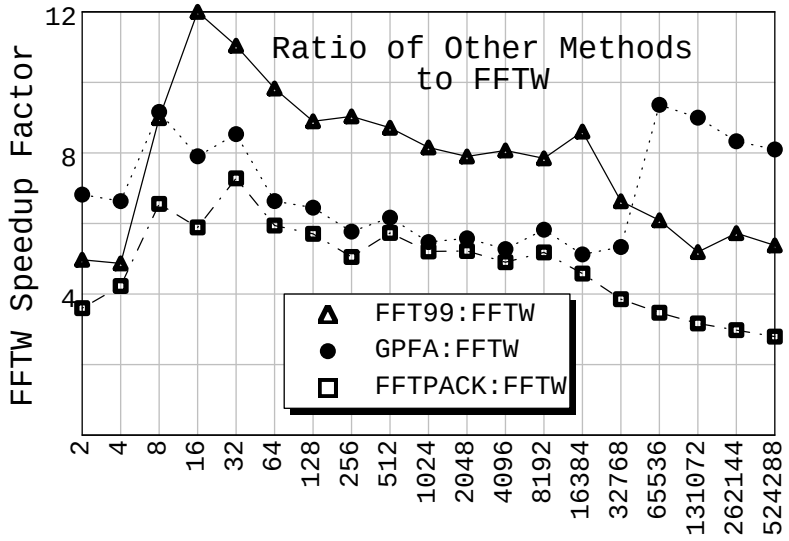

Figure A.5: Ratio of various methods for 1-d FFT to single precision **FFTW** for powers of 2.

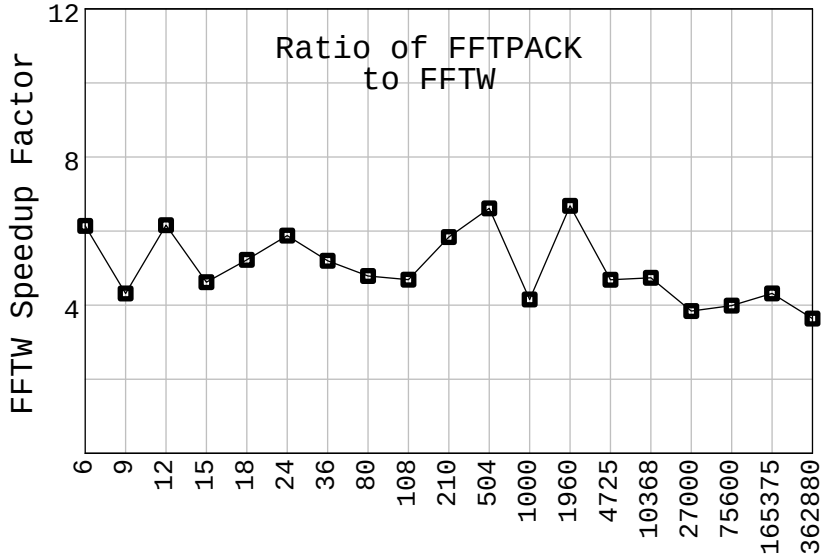

Figure A.6: Ratio of **FFTPACK** for 1-d FFT to single precision FFTW for non-powers of 2.

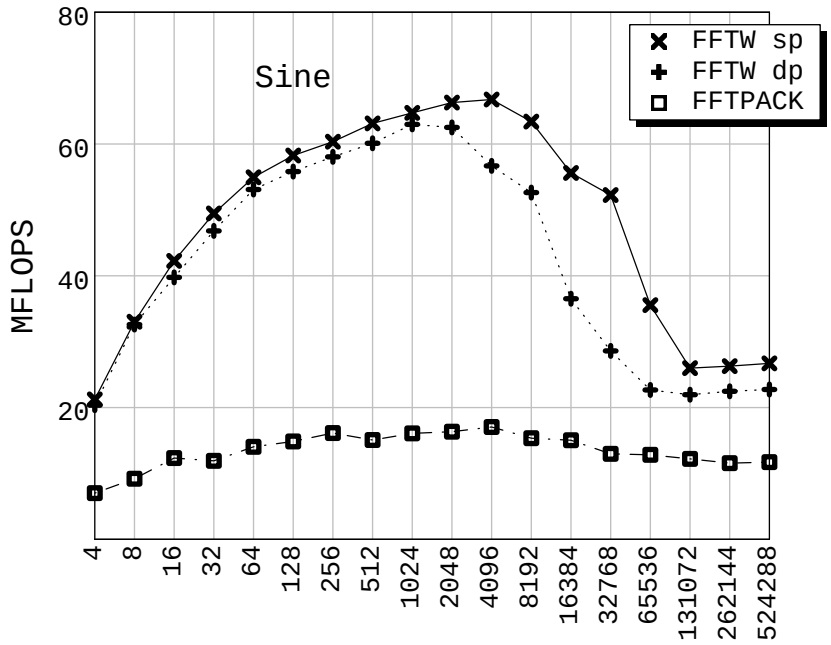

Figure A.7: Comparison of sine transform for powers of 2. (Note: sp = single precision, dp = double precision.)

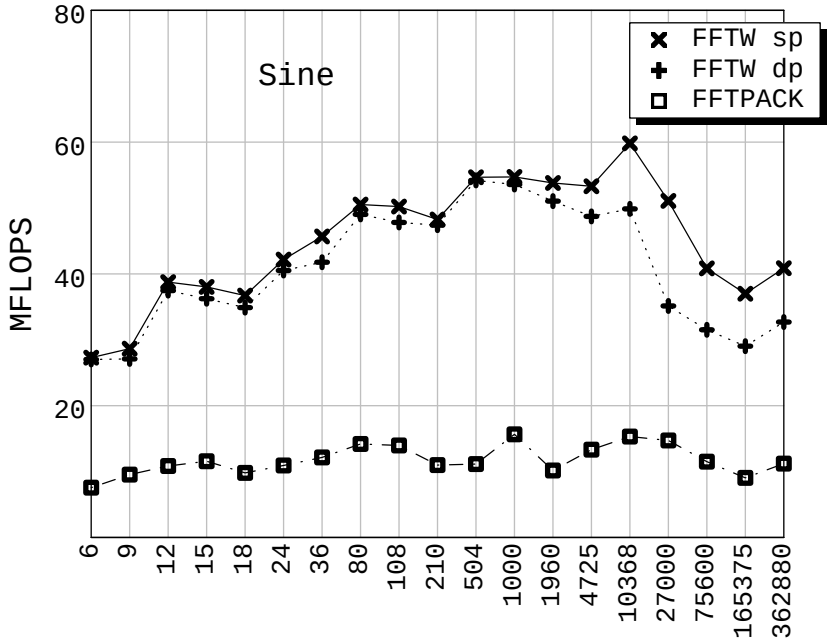

Figure A.8: Comparison of sine transform for non-powers of 2. (Note: sp = single precision, dp = double precision.)

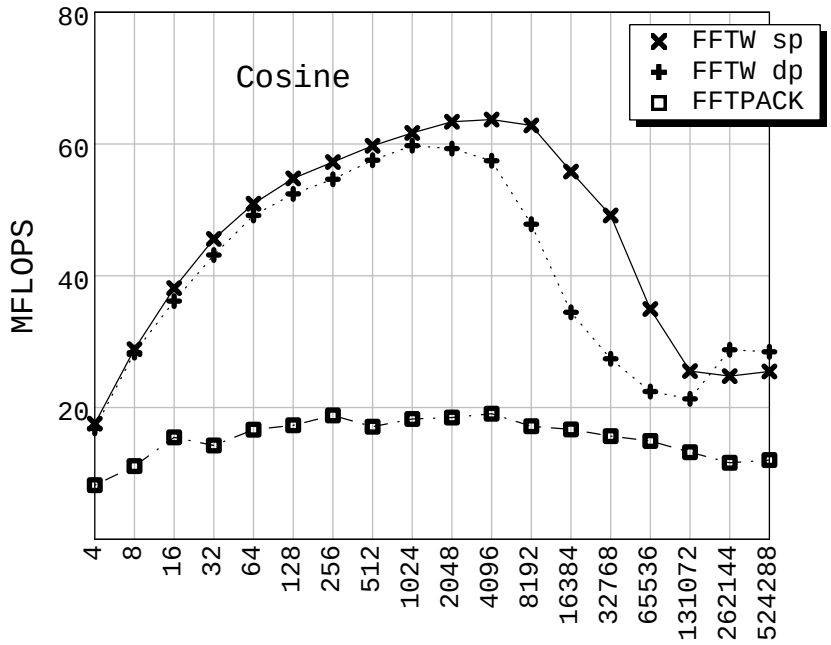

Figure A.9: Comparison of cosine transform for powers of 2. (Note: sp = single precision, dp = double precision.)

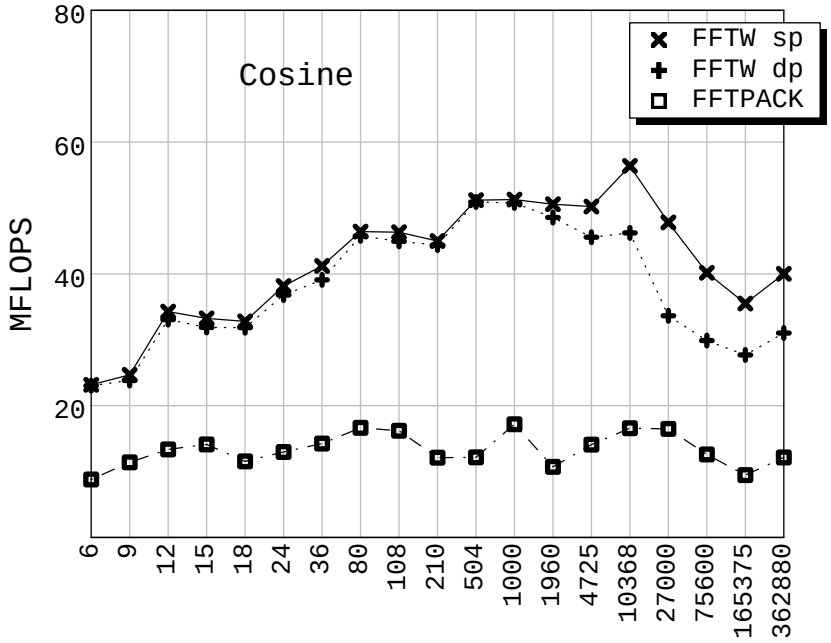

Figure A.10: Comparison of cosine transform for non-powers of 2. (Note: sp = single precision, dp = double precision.)

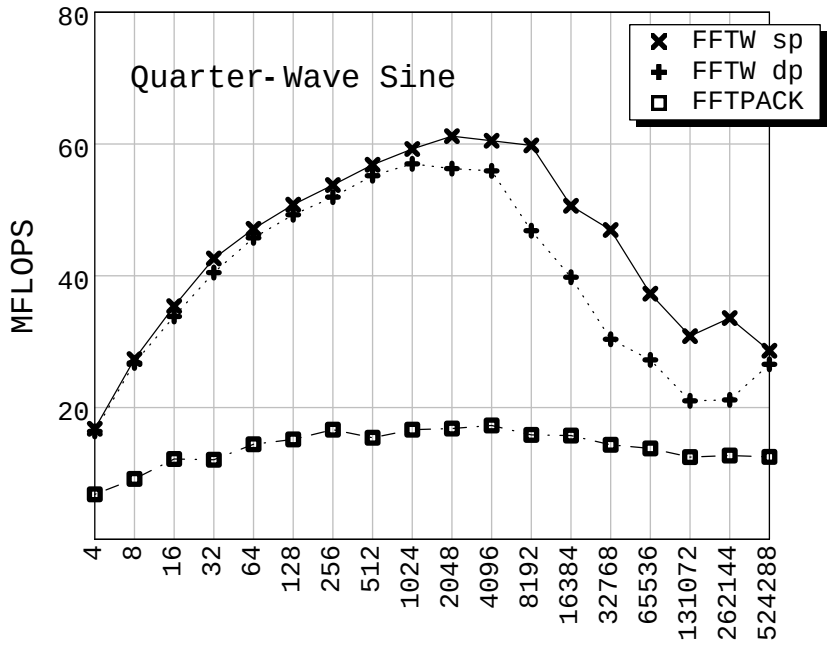

Figure A.11: Comparison of quarter-wave sine transform for powers of 2. (Note: sp = single precision, dp = double precision.)

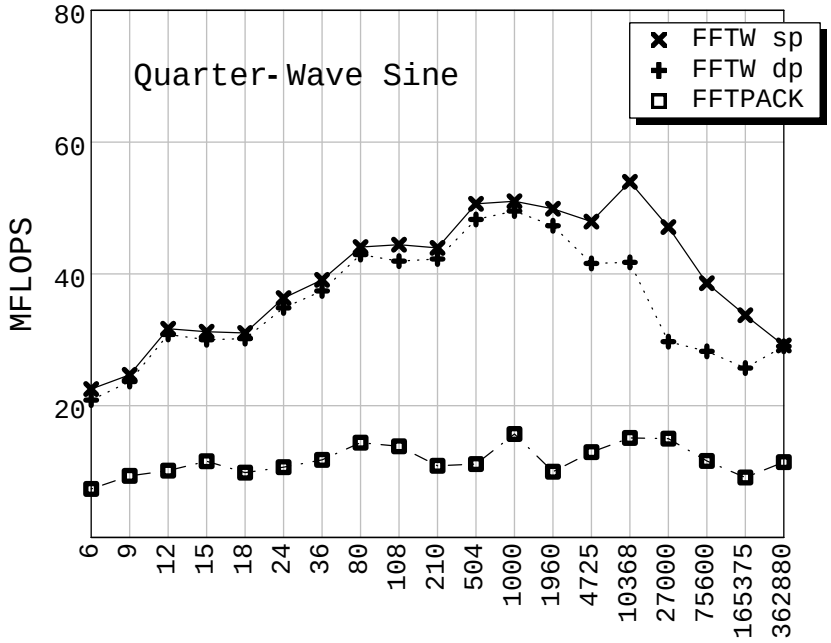

Figure A.12: Comparison of quarter-wave sine transform for non-powers of 2. (Note: sp = single precision, dp = double precision.)

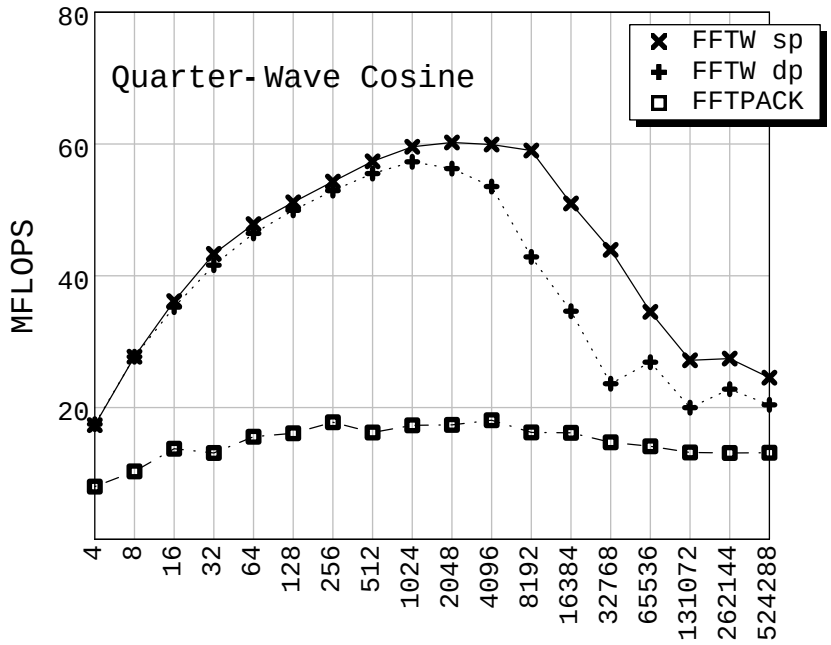

Figure A.13: Comparison of quarter-wave cosine transform for powers of 2. (Note: sp = single precision, dp = double precision.)

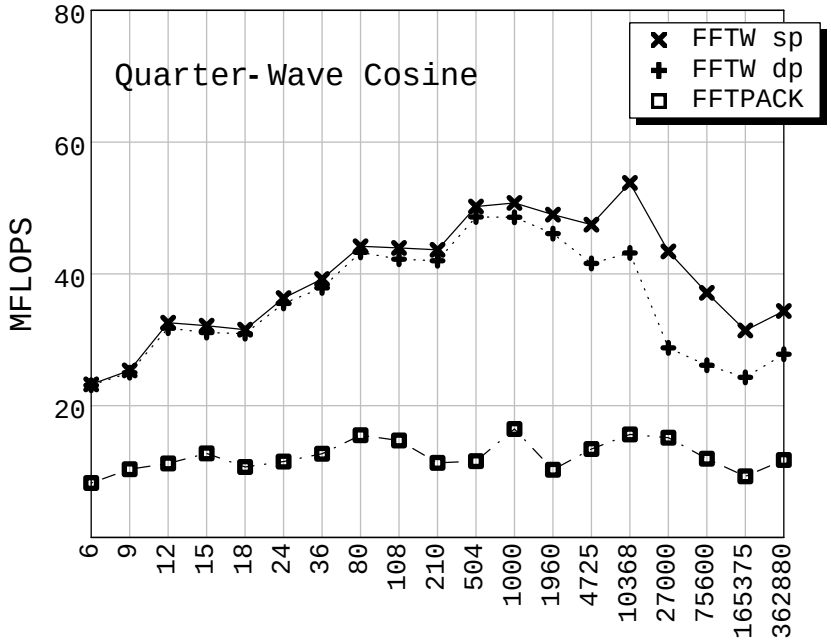

Figure A.14: Comparison of quarter-wave cosine transform for non-powers of 2. (Note: sp = single precision, dp = double precision.)

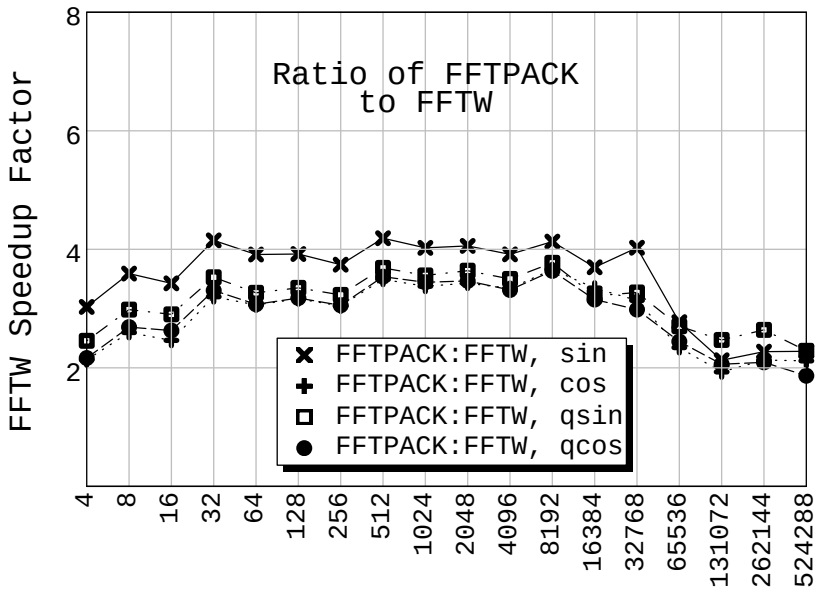

Figure A.15: Ratio of FFTPACK with FFTW-based symmetric transforms for powers of 2.

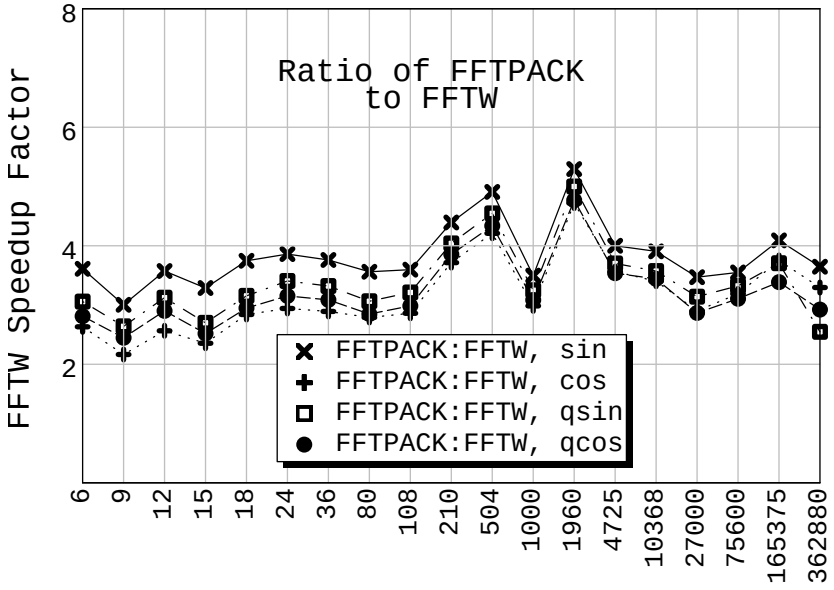

Figure A.16: Ratio of FFTPACK with FFTW-based symmetric transforms for non-powers of 2.

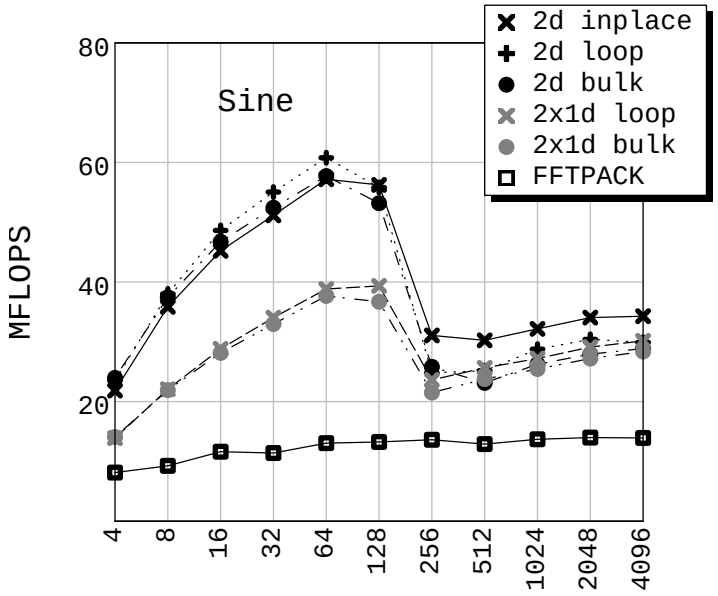

Figure A.17: Comparison of 2-d sine single precision transforms for powers of 2.

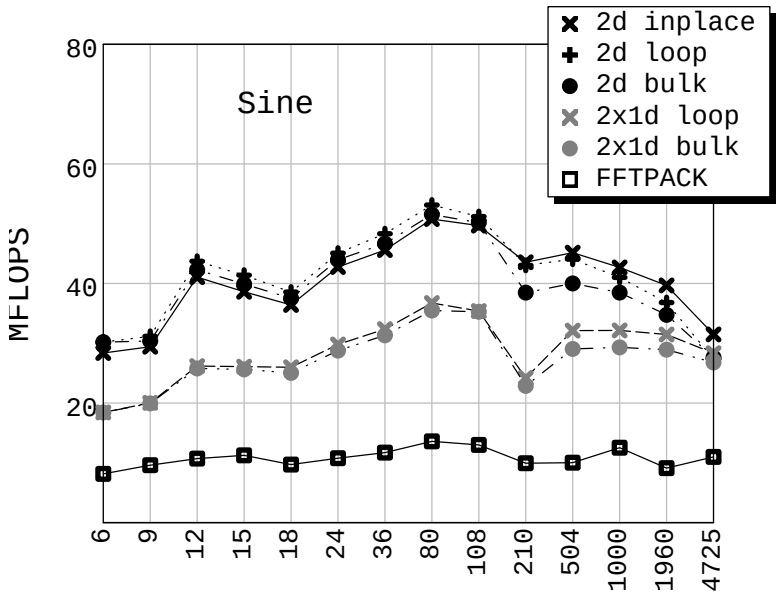

Figure A.18: Comparison of 2-d sine single precision transforms for non-powers of 2.

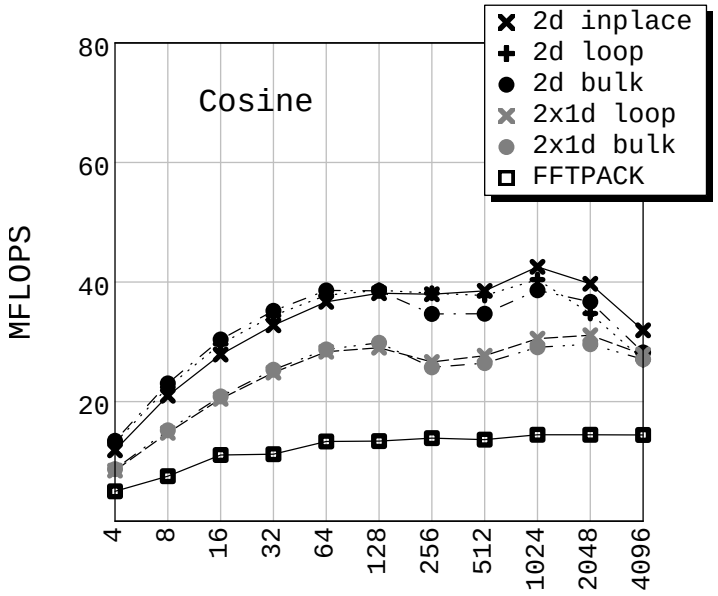

Figure A.19: Comparison of 2-d single precision cosine transforms for powers of 2.

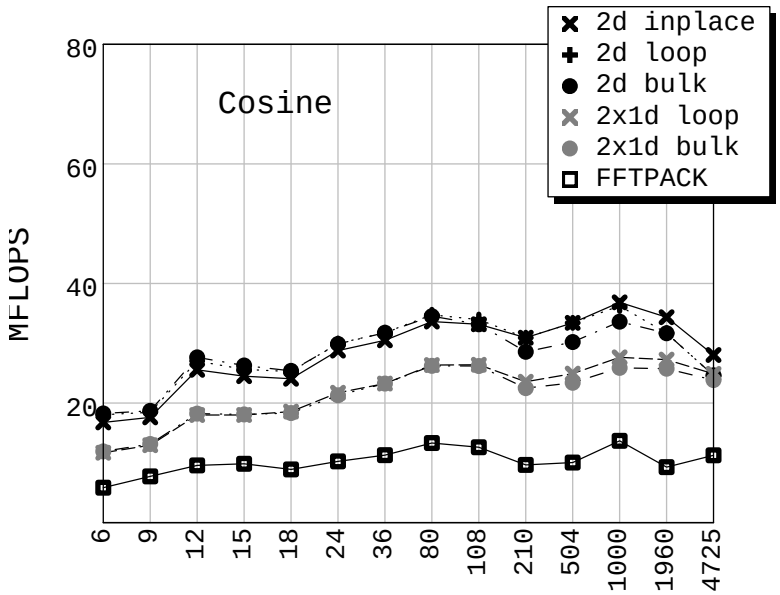

Figure A.20: Comparison of 2-d single precision cosine transforms for non-powers of 2.

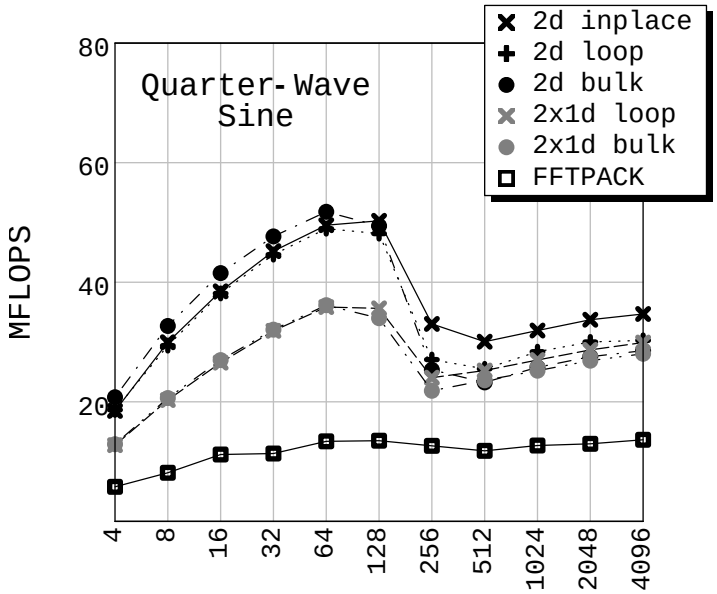

Figure A.21: Comparison of 2-d single precision quarter-wave sine transforms for powers of 2.

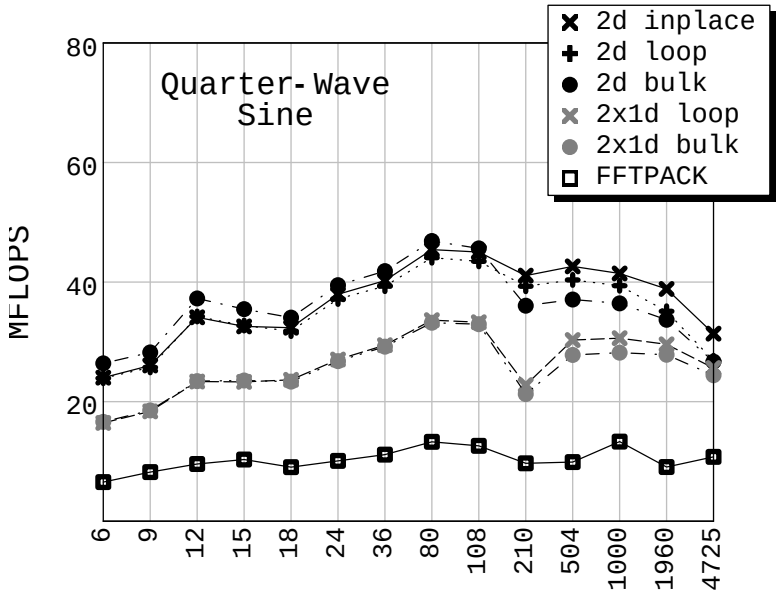

Figure A.22: Comparison of 2-d single precision quarter-wave sine transforms for non-powers of 2.

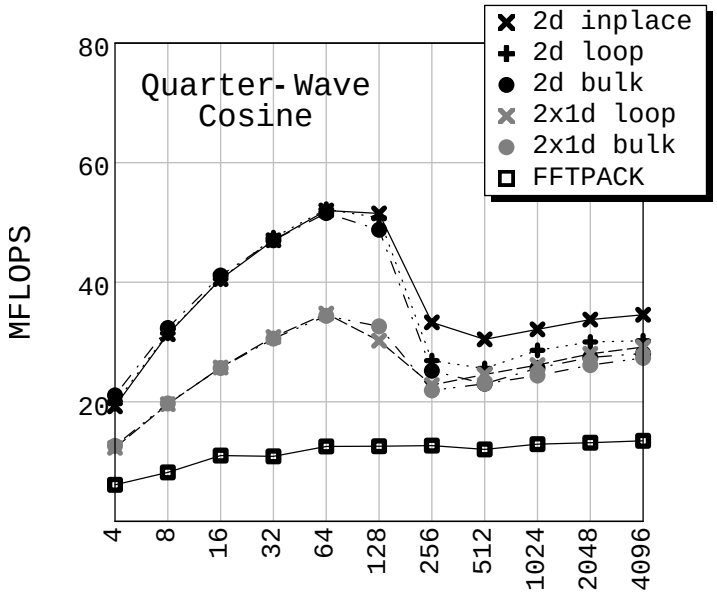

Figure A.23: Comparison of 2-d single precision quarter-wave cosine transforms for powers of 2.

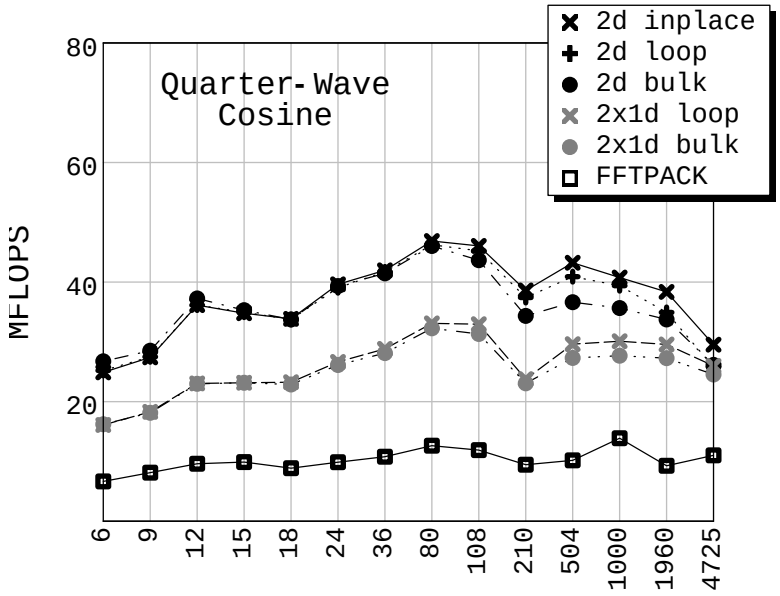

Figure A.24: Comparison of 2-d single precision quarter-wave cosine transforms for non-powers of 2.

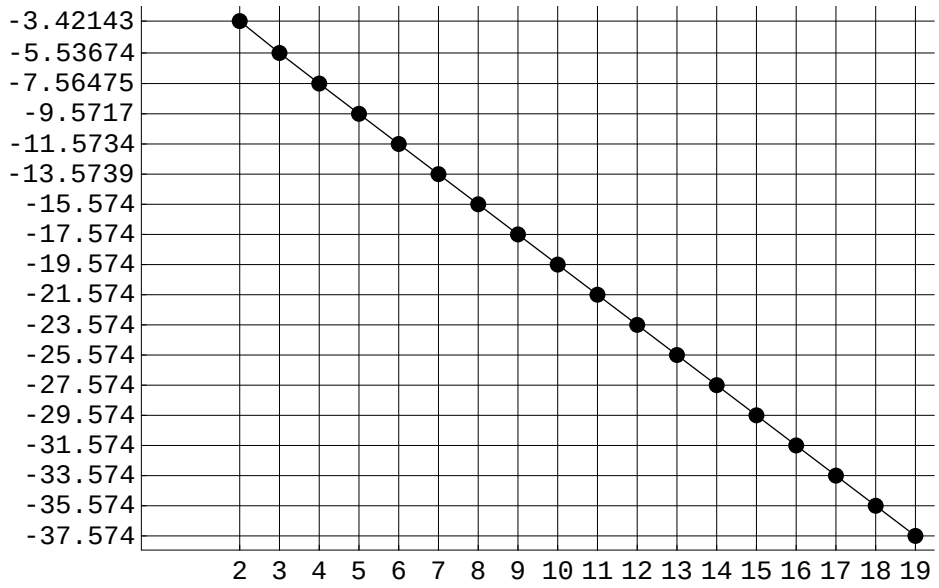

Figure A.25: Typical log-log plot of L2 error for the 1-d symmetric transforms. The x-axis show the log of the number of data points, to save space. The y-axis displays the log of the L2 error for the quarter-wave cosine transform so that the 2nd order accuracy may easily be seen. Computations were done in double precision on a nonlinear, inhomogeneous boundary conditions problem.

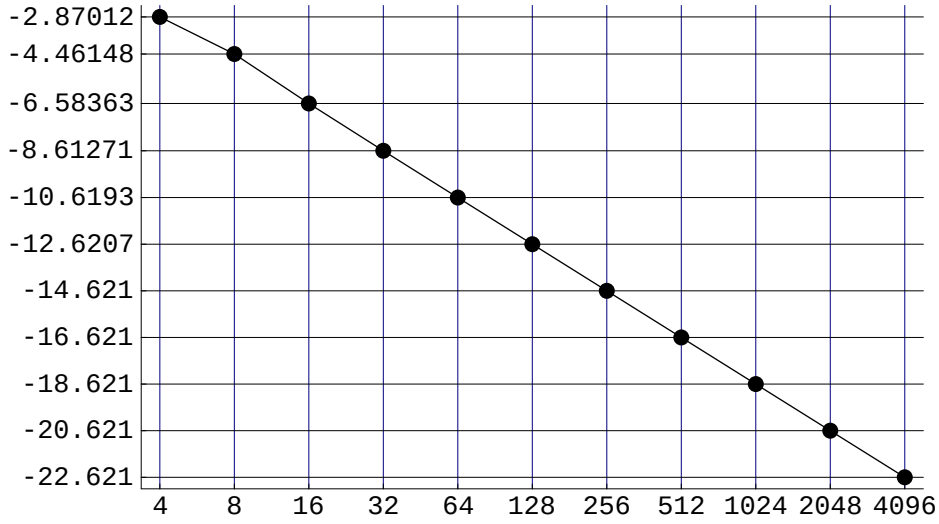

Figure A.26: Typical log-log plot of L2 error for the 2-d symmetric transforms. The x-axis show the number of data points in each dimension. The y-axis displays the log of the L2 error for the quarter-save sine transform so that the 2nd order accuracy may easily be seen. Computations were done in double precision on a nonlinear, inhomogeneous boundary conditions problem.

B Numerical discretization of the convective terms in the Navier-Stokes equations

There are many ways to write the Navier-Stokes equations. Mathematically, they are equivalent, but the specific formulation and discretization may make a difference computationally. The convective form, given in Chapter 2, is:

$$\frac{\partial \mathbf{u}}{\partial t} = -\nabla p - (\mathbf{u} \cdot \nabla)\mathbf{u} + \frac{1}{Re}\Delta \mathbf{u} \tag{B.1}$$

$$\nabla \cdot \mathbf{u} = 0 \tag{B.2}$$

A conservative formulation can be obtained by rewriting the convective terms $(\mathbf{u} \cdot \nabla)\mathbf{u}$ using the continuity equation $\nabla \cdot \mathbf{u} = 0$:

$$\frac{\partial u}{\partial t} = -\frac{\partial p}{\partial x} - \frac{\partial u^2}{\partial x} - \frac{\partial uv}{\partial y} + \frac{1}{Re}\Delta u \tag{B.3}$$

$$\frac{\partial v}{\partial t} = -\frac{\partial p}{\partial y} - \frac{\partial uv}{\partial x} - \frac{\partial v^2}{\partial y} + \frac{1}{Re}\Delta v \tag{B.4}$$

The square cylinder simulations raised some questions in my mind about the best way to deal with the convective terms, particularly near the onset of periodicity. An abbreviated test was run at $Re\,55$, where the flow should be periodic, beginning from the same initial conditions from an evolved flow at $Re\,50$ to compare several numerical options for handling the convective terms:

- central differencing, convective form
- mixed upwinding with q = 0.125, convective form
- mixed upwinding with q = 0.5, convective form
- mixed upwinding with q = 0.25, conservative form.

Mixed upwinding is nominally defined by:

$$\frac{df_n}{dx} = \frac{f_{n+1} - f_{n-1}}{2\Delta x} + \frac{q(f_{j-1} - 3f_j + 3f_{j+1} - f_{j+2})}{3\Delta x} \tag{B.5}$$

where q controls the amount of upwinding. When implemented on a staggered grid with the conservative formulation, there are choices to be made about the actual point values used since u and v are not defined on the same grid. The details are quite tedious and quite similar in concept to the presentation in Griebel [13] although not identical in detail since he does not use mixed upwinding.

Each simulation was run until the periodic flow was well established, and data was collected at 26 positions in the wake for u and v. Comparisons were made at each history point. Since the time series are out of phase, three of the time series have been shifted by integer index values in time (i.e., no interpolation was done) for a ballpark registration for visual comparison. Figure B.1 show sample time series plots, which are all quite close. The scaling in the y axis is far from uniform, so even the cases where there seems to be a large discrepancy aren't really far off since the data range is quite small (*e.g.*, the near wake plot, which shows the greatest difference).

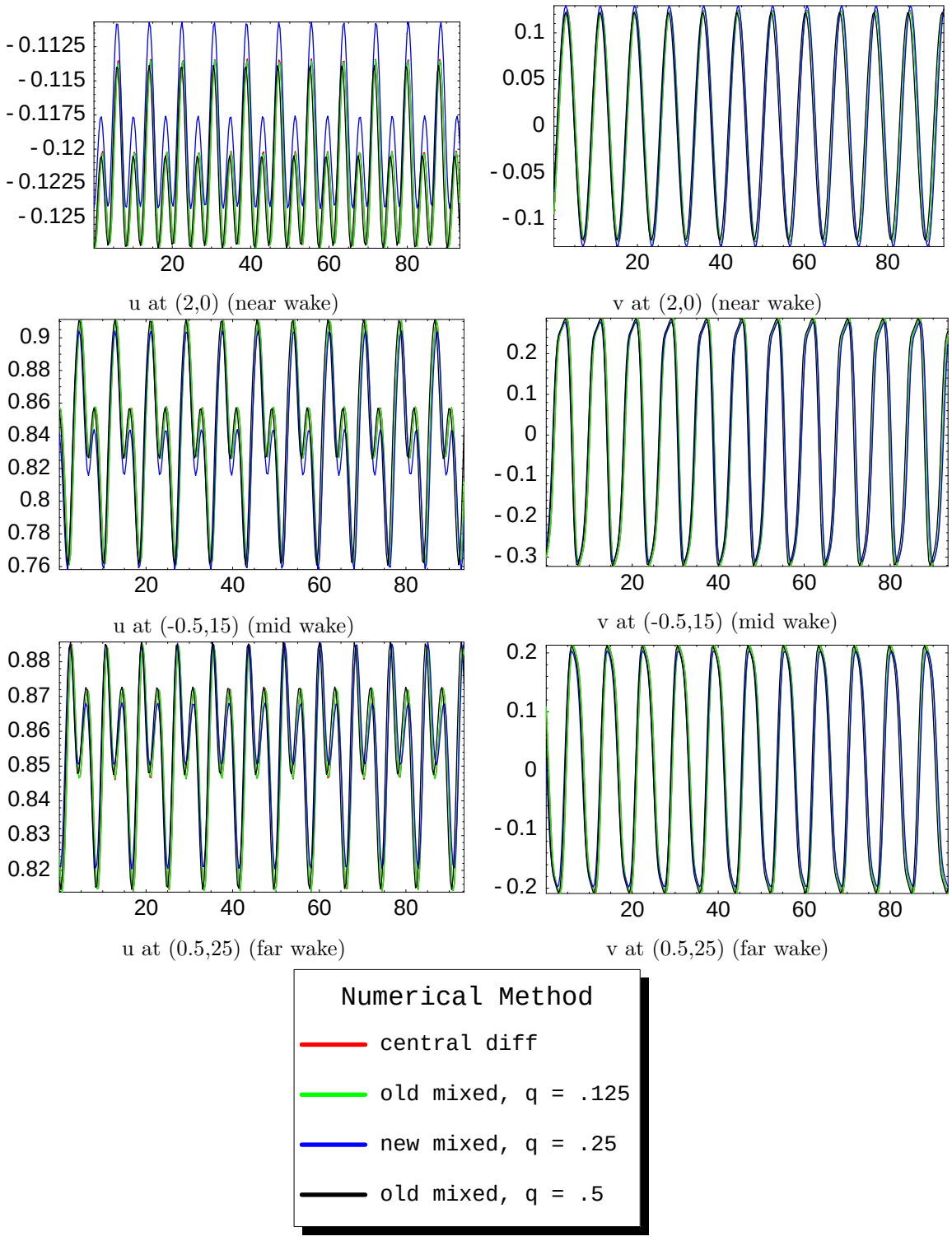

Figure B.1: Comparison of numerical methods for handling the convective terms in the Navier-Stokes equations for the wake flow past a square cylinder at $Re\,55$.

References

[1] P. Holmes, J. L. Lumley, G. Berkooz, *Turbulence, Coherent Structures, Dynamical Systems and Symmetry*, Cambridge, (1996).

[2] J. L. Lumley, "The structure of inhomogeneous turbulent flows", in *Atmospheric Turbulence and Radio Wave Propagation*, edited by A. M. Yaglom and V. L. Tararsky (Nauka, Moscow), 166-178 (1967).

[3] D. J. Tritton, *Physical Fluid Dynamics*, Oxford, 31 (1988).

[4] N. Aubry, *On the hidden beauty of the proper orthogonal decomposition*, Theoretical and Computational Fluid Dynamics, 2, 339-352 (1991).

[5] A. E. Deane, I. G. Kevrekidis, G. E. Karniadakis, S. A. Orszag, *Low-dimensional models for complex geometry flow: application to grooved channels and circular cylinders*, Physics of Fluids A, 3, 10, 2337-2354, (1991)

[6] A. Sohankar, C. Norberg, L. Davidson, *Simulation of three-dimensional flow around a square cylinder at moderate Reynolds numbers*, Physics of Fluids, 11, 2, 288-306 (1999).

[7] L. Prandtl, *Essentials of Fluid Dynamics*, New York, 188 (1952).

[8] W. Cazemier, R. W. C. P. Verstappen, A. E. P. Veldman, *Proper orthogonal decomposition and low-dimensional models for driven cavity flows*, Physics of Fluids, 10, 7, 1685-1699 (1998).

[9] B. R. Noack, H. Eckelmann, *A low-dimensional Galerkin method for the three-dimensional flow around a circular cylinder*, Physics of Fluids, 6, 124-143 (1994).

[10] E. A. Christensen, M. Brons, J. N. Sorensen, *Evaluation of proper orthogonal decomposition-based decomposition techniques applied to parameter-dependent nonturbulent flows*, SIAM Journal of Scientific Computation, 21, 4, 1419-1434 (2000).

[11] A. J. Chorin, *Numerical solution of the Navier-Stokes equations*, Mathematics of Computation, 22, 104, 745-762 (1968).

[12] R. Tenam, *Sur l'approximation de la solution des équations de Navier-Stokes par la méthode des pas fractionnaires*, Archive for Rational Mechanics and Analysis, 32, 2, 135-153 (1969).

[13] M. Griebel, T. Dormseifer, T. Neunhoeffer, *Numerical Simulation in Fluid Dynamics*, SIAM, (1998).

[14] M. Frigo, S. G. Johnson, *FFTW: An adaptive software architecture for the FFT*, Proceedings of the International Conference on Acoustics, Speech, and Signal Processing, (1998).

[15] K. Karhunen, *Zur Spektraltheorie Stochastischer Prozesse*, Ann. Acad. Sci. Fennicae, 37, (1946).

[16] M. M. Loève, *Probability Theory*, Princeton, NJ, VanNostrand (1955).

[17] Y. C. Liang, H. P. Lee, S. P. Lim, W. Z. Lin, K. H. Lee, C. G. Wu, *Proper orthogonal decomposition and its applications, part I: theory*, Journal of Sound and Vibration, 252, 3, 527-544 (2002).

[18] M. Rathinam, L. R. Petzold, *A new look at proper orthogonal decomposition*, SIAM Journal of Numerical Analysis, 41, 5, 1893-1925 (2003).

[19] C. López, E. Hernández-García, *Low-dimensional dynamical system model for observed coherent satellite data*, Physica A, 328, 233-250 (2003).

[20] M. V. Morkovin, *Recent insights into instability and transition to turbulence in open-flow systems*, ICASE report 88-44 (1988).

[21] J. M. Wallace, F. Hussain, *Coherent structures in turbulent shear flows*, Applied Mechanical Review, 43, S, part 2, S203-S209 (1990).

[22] A. J. Chorin, J. E. Marsden, *A Mathematical Introduction to Fluid Mechanics*, Springer-Verlag, New York (1998).

[23] F. Harlow, J. Welch, *Numerical calculation of time-dependent viscous incompressible flow of fluid with free surface*, Physics of Fluids, 8, 2182-2189 (1965).

[24] J. Kim, P. Moin, *Application of a fractional step method to incompressible Navier-Stokes equations*, Journal of Computational Physics, 59, 308-323 (1985).

[25] C. A. J. Fletcher, *Computational Techniques for Fluid Dynamics, I*, Springer-Verlag, (1991).

[26] J. H. Ferziger, M. Perić, *Computational Methods for Fluid Dynamics*, Springer-Verlag Berlin Heidelberg, (1997).

[27] A. Sohankar, C. Norberg, and L. Davidson, *A numerical study of unsteady two-dimensional flow around rectangular cylinders at incidence*, internal report nr. 96/25, Department of Thermo and Fluid Dynamics, Chalmers University of Technology, Gothenburg, Sweden (1996).

[28] A. Sohankar, C. Norberg, and L. Davidson, *Low Reynolds-number flow around a square cylinder at incidence: study of blockage, onset of vortex shedding and outlet boundary condition*, Int. J. Numer. Methods Fluids, 26, 39-56 (1998).

[29] W. E, J. Liu, *Vorticity boundary condition and related issues for finite difference schemes*, Journal of Computational Physics, 124, 368-382 (1996).

[30] B. Smith, P. Bjorstad, W. Gropp, *Domain Decomposition: Parallel Multilevel Methods for Elliptic Prtial Differential Equations*, Cambridge University Press (1996).

[31] R. W. Hockney,*A fast direct solution of Poisson's equation using Fourier analysis*, Journal of the Association for Computing Machinery, 12, 95-113 (1963).

[32] J. Kim and P.Moin, *Application of a fractional step method to incompressible Navier-Stokes equations*, Journal of Computational Physics, 59, 308 (1985).

[33] P. N. Swarztrauber, *Vectorizing the FFTs*, in Parallel Computations, Academic Press, New York (1982).

[34] P. N. Swarztrauber, *Fast Poisson solvers*, in MAA Studies in Numerical Analysis, Volume 24, Mathematical Association of America (1984).

[35] R. A. Sweet,*Direct methods for the solution of Poisson's equation on a staggered grid*, Journal of Computational Physics, 12, 422-428 (1973).

[36] C. Temperton,*Direct methods for the solution of the discrete Poisson equation*, Journal of Computational Physics, 31, 11-20 (1979).

[37] C. Temperton,*A generalized prime factor FFT algorithm for any n=2p3q5r*, SIAM Journal on Scientific and Statistical Computing, 13, 676-686 (1992).

[38] J.-G. Liu, Lecture notes for Computational Fluid Dynamics course given at the University of Maryland, (1999).

[39] H. Lomax, T. H. Pulliam, D. W. Zingg, *Fundamentals of Computational Fluid Dynamics*, Springer-Verlag, Berlin Heidelberg New York (2001).

[40] J. R. Koseff, R. L. Street, *Visualization studies of a shear driven three-dimensional recirculating flow*, ASME Journal of Fluids Engineering, 106, 1, 21-29 (1984).

[41] J. R. Koseff, R. L. Street, *The lid-driven cavity flow: a synthesis of qualitative and quantitive observations*, Transactions of the ASME, 106, 390-398 (1984).

[42] U. Ghia, K. N. Ghia, C. T. Shin, *High-Re solutions for incompressible flow using the Navier-Stokes equations and a multigrid method*, Journal of Computational Physics, 48, 387-411 (1982).

[43] O. Botella, R. Peyret, *Benchmark spectral results on the lid-driven cavity flow*, Computers & Fluids, 27, 4, 421-433 (1998).

[44] T. W. Pan, R. Glowinski, *A projection/wave-like equation method for the numerical simulation of incompressible viscous fluid flow modeled by the Navier-Stokes equations*, Computational Fluid Dynamics Journal, 9, 2, 28-42 (2000).

[45] R. Kupferman *A central-difference scheme for a pure stream function formulation of incompressible viscous flow*, SIAM Journal of Scientific Computing, 23, 1, 1-18 (2001).

[46] P. K. Kundu, *Fluid Mechanics*, Academic Press, San Diego (1990).

[47] C. W. Oosterlee, P. Wesseling, A. Segal, E. Brakkee, *Benchmark solutions for the incompressible Navier-Stokes equations in general co-ordinates on staggered grids*, International Journal for Numerical Methods in Fluids, 17, 301-321 (1993).

[48] L. Kaiktsis, G. E. Karniadakis, S. A. Orszag, *Onset of three-dimensionality, equilibria, and early transition in flow over a backward-facing step*, Journal of Fluid Mechanics, 231, 501-528 (1991).

[49] A. W. Runchal, *ANSWER: A benchmark study for backward-facing step*, Benchmark Problems for Heat Transfer Codes, Winter Annual Meeting ASME, Anaheim, CA, 13-20 (1992).

[50] D. Choudhury, *A numerical study of laminar flow and heat transfer in a backward-facing step using FLUENT: a finite volume code*, Benchmark Problems for Heat Transfer Codes, Winter Annual Meeting ASME, Anaheim, CA, 53-59 (1992).

[51] D. K. Gartling, *A test problem for outflow boundary conditions — flow over a backward-facing step*, International Journal for Numerical Methods in Fluids, 11, 953-967 (1990).

[52] P. M. Gresho, D. K. Gartling, J. R. Torczynski, K. A. Cliffe, K. H. Winters, T. J. Garratt, A. Spence, J. W. Goodrich, *Is the steady viscous incompressible two-dimensional flow over a backward-facing step at Re* 800 *stable?*, International Journal for Numerical Methods in Fluids, 17, 501-541 (1993).

[53] J. R. Torczynski, *A grid-refinement study of two-dimensional transient flow over a backward-facing step using a spectral element method*, Separated Flows, ASME Fluids eng Div., 149, 1-7 (1993).

[54] J. Keskar, D. A. Lyn, *COmputations of a laminar backward-facing step flow at Re* 800 *with a spectral domain decomposition method*, International Journal for Numerical Methods in Fluids, 29, 411-427 (1999).

[55] G. E. Karniadakis, G. S. Triantafyllou, *Three-dimensional dynamics and transition to turbulence in the wake of bluff bodies*, Journal of Fluid Mechanics, 238, 1-30 (1992).

[56] R. D. Blevins, *Flow-Induced Vibration*, Van Nostrand-Reinhold, New York (1990).

[57] A. Sohankar, C. Norberg, L. Davidson, *Low-Reynolds-number flow around a square cylinder at incidence: a study of blockage, onset of vortex shedding and outlet boundary conditions*, International Journal for Numerical Methods in Fluids, 26, 39-56 (1998).

[58] R. W. Davis, E. F. Moore, *A numerical study of vortex shedding from rectangles*, Journal of Fluid Mechanics, 118, 475-506 (1982).

[59] A. N. Pavlov, S. S. Sazhin, R. P. Fedorenko, M. R. Heikal, *A conservative finite difference method and its application for the analysis of a transient flow around a square prism*, International Journal of Numerical Methods for Heat and Fluid Flow, 10, 1, 6-46 (2000).

[60] J. Robichaux, S. Balachandar, S. P. Vanka, *Three-dimensional Floquet instability of the wake of square cylinder*, Physics of Fluids, 11, 3, 560-578 (1999).

[61] R. Franke, B. Chönung, *Numerical calculation of laminar vortex-shedding flow past cylinders*, Journal of Wind Engineering and Industrial Aerodynamics, 35, 237 (1990).

[62] C. Chatfield, *The Analysis of Time Series: An Introduction*, Chapman and Hall (1989).

[63] G. W. Stewart, *Introduction to Matrix Calculations*, Academic Press, New York (1973).

[64] L. Sirovich, *Turbulence and the dynamics of coherent structures part I: coherent structures*, Quarterly of Applied Mathematics, XLV, 561-571 (1987).

[65] E. J. Doedel, *AUTO 97: continuation and bifurcation software for ordinary differential equations* (1998).

[66] J. E. Marsden, M. McCracken, *The hopf bifurcation and its applications*, Springer-Verlag, Berlin, (1976).

[67] R. B. Cattell, *The Scree test for number of factors*, Multivariate Behavioral Research, 1, 140-161 (1966).

[68] G. E. Karniadakis, M. Israeli, S. A. Orszag, *High-order splitting methods for the incompressible Navier-Stokes equations*, Journal of Computational Physics, 97, 2, 414-443 (1991).

[69] M. Marion, R. Temam, *Nonlinear Galerkin Methods*, Siam Journal of Numerical Analysis, 26, 5, 1139-1157 (1989).

[70] B. Podvin, P. Le Quéré, *Low-order models for the flow in a differentially heated cavity*, Physics of Fluids, 13, 11, 3204-3214 (2001).

[71] X. Ma, G. E. Karniadakis, *A low-dimensional model for simulating 3-d cylinder flow*, Journal of Fluid Mechanics, 458, 181-190 (2002).

[72] S. Sirisup, G. E. Karniadakis, *A spectral viscosity method for correcting the long-term behavior of POD models*, Journal of Computational Physics, 194, 92-116 (2004).

[73] E. Tadmor, *Convergence of spectral methods for nonlinear conservation laws*, SIAM Journal of Numerical Analysis, 26, 1, 30-44 (1989).

[74] H. B. Keller, *Numerical solution of bifurcation and nonlinear eigenvalue problems*, 'Applications of Bifurcation Theory', P. H. Rabinowitz, ed., Academic Press, 359-384 (1977).

[75] E. J. Doedel, *Lecture notes on numerical analysis of bifurcation problems*, @ http://cmvl.cs.concordia.ca/publications.html, #16 (1997).

[76] K. T. Alligood, T. D. Sauer, J. A. Yorke, *CHAOS an introduction to dynamical systems*, Springer-Verlag, New York, (1996).

[77] P. G. Drazin, *Nonlinear Systems*, Cambridge University Press, (1992).

[78] A. Sohankar, L. Davidson, C. Norberg, *Numerical simulation of unsteady flow around a square two-dimensional cylinder*, 12^th Astraulasian Fluid Mechanics Conference, 517-520, 1995.

[79] K. M. Kelkar, S. V. Patankar, *Numerical prediction of vortex shedding behind a square cylinder*, International Journal for Numerical Methods in Fluids, 14, 327-341, 1992.

[80] M. D. Graham, I. G. Kevrekidis, *Alternative approaches to the Karhunen-Loève decomposition for model reduction and data analysis*, Computers & Chemical Engineering, 20, 5, 495-506 (1996).

[81] A. K. Bangia, P. F. Batcho, I. G. Kevrekidis, G. E. Karniadakis, *Unsteady two-dimensional flows in complex geometries: comparative bifurcation studies with global eigenfunction expansions*, SIAM Journal of Scientific Computing, 18, 3, 775-805 (1997).

[82] B. R. Noack, K. Afansiev, M. Morzynski, G. Tadmor, F. Thiele, *A hierarchy of low-dimensional models for the transient and post-transient cylinder wake*, Journal of Fluid Mechanics, 497, 335-363 (2003).

[83] B. Ahlborn, M. L. Seto, B. R. Noack, *On drag, Strouhal number and vortex-street structure*, Fluid Dynamics Research 30, 379-399 (2002).